External Control of Many-Body Quantum Systems

Dissertation
zur
Erlangung des Doktorgrades (Dr. rer. nat.)
der
Mathematisch-Naturwissenschaftlichen Fakultät
der
Rheinischen Friedrich-Wilhelms-Universität Bonn

vorgelegt von
Cătălin-Mihai Halați
aus
Reghin, Rumänien

Bonn 2021

To my parents.

Abstract

In strongly correlated many-body quantum systems, the complex interplay between a large number of degrees of freedom and the presence of various competing energy scales leads to rich phase diagrams, but also renders these systems extremely susceptible to external perturbations. Engineering couplings to external fields, or environments, offers the possibility of controlling the behavior of these quantum systems. This has opened up the door for the preparation of quantum phases of matter and light with sought-after properties, both in ultracold atoms and solid state platforms.

This thesis explores two directions for externally controlling many-body quantum systems, aiming to steer systems towards non-trivial quantum phases, or to investigate complex quantum phase transitions. First, we consider ultracold bosonic atoms coupled to a dissipative optical cavity. The interplay between the kinetic motion, atomic short range interactions and the global coupling to the lossy cavity mode provides a perfect platform for the study of many-body aspects of the self-ordering processes. In this thesis, we present several methodological developments for atoms-cavity coupled systems, going beyond the usual mean field methods. These novel methods allow us to show the crucial role of the fluctuations in the atoms-cavity coupling, which give a mixed state character to the self-organization phase transition. Furthermore, we investigate the presence of a strong symmetry which leads to the existence of conservation laws and the coexistence of multiple steady states in the open system. We analyze the many-body dynamics after slightly breaking this symmetry. Additionally, we show that by engineering the coupling to a cavity we realize a dynamically induced spin-orbit coupling. We find that a Meissner superfluid steady state exhibiting a non-trivial chiral current can be stabilized in the coupled system. Secondly, we study the excitation spectrum of the one-dimensional XXZ spin chain with a position dependent magnetic field, across a magnetic quantum phase transition. We show that at high magnetic fields the dynamics of single magnons dominate the low-frequency excitations and that states of two confined magnons are present at large frequencies. Our results are in very good agreement with measurements performed on the $BaCo_2V_2O_8$ compound in high magnetic fields.

List of publications related to this thesis

1. *Cavity-induced spin-orbit coupling in an interacting bosonic wire*
   C.-M. Halati, A. Sheikhan, and C. Kollath
   Phys. Rev. A **99**, 033604 (2019)

2. *Numerically exact treatment of many body self-organization in a cavity*
   C.-M. Halati, A. Sheikhan, H. Ritsch, and C. Kollath
   Phys. Rev. Lett. **125**, 093604 (2020)

3. *Theoretical methods to treat a single dissipative bosonic mode coupled globally to an interacting many body system*
   C.-M. Halati, A. Sheikhan, and C. Kollath
   Phys. Rev. Research **2**, 043255 (2020)

4. *Dicke transition in open many-body systems determined by fluctuation effects*
   A. V. Bezvershenko, **C.-M. Halati**, A. Sheikhan, C. Kollath, and A. Rosch
   arXiv:2012.11823, (2020)

5. *Breaking strong symmetries in dissipative quantum systems: the (non-)interacting bosonic chain coupled to a cavity*
   C.-M. Halati, A. Sheikhan, and C. Kollath
   arXiv:2102.02537, (2021)

6. *Observation of many-body magnon bound states in a transverse-field Heisenberg-Ising chain*
   Z. Wang, **C.-M. Halati**, J.-S. Bernier, A. Ponomaryov, D. Kamenskyi, D. I. Gorbunov, S. Niesen, J. M. Klopf, S. Zvyagin, T. Lorenz, A. Loidl, and C. Kollath
   in preparation

Acknowledgements

Contents

Contents

Chapter 1

Introduction

Enormous progress has been realized towards one of the central goals of modern condensed matter physics, that of realizing quantum materials [1]. An intricate balance between the competing energy scales and degrees of freedom exists in the strongly correlated many-body systems, which makes them extremely susceptible to external perturbations. Thus, one can envision the external perturbation of the microscopic interaction parameters in order to control the evolution of the quantum material towards the desired ground, or metastable state, or for inducing quantum phase transitions between competing quantum phases. This further motivates the need of an understanding of the properties of quantum materials, and the studies of the phase diagrams and the quantum critical regimes associated to the quantum phase transitions in interacting many-body quantum systems [2, 3]. A paradigmatic example are the magnetic phase transitions, in these situations the electronic degrees of freedom in the material are directly manipulated using external magnetic fields. The use of high magnetic fields have allowed the realization of phase transitions such as those between high-T_c superconducting and charge density wave ordered phases [4], or of one-dimensional quantum phase transitions [5–7] in Ising-like spin chains. Beside the fundamental interest, efforts are made in developing devices based on the exotic properties the new phases of matter [1, 8]. Furthermore, one can make use non-equilibrium phenomena in order to control the quantum states, for example by driving the system via coherent interaction of the quantum matter with light [9–13], by strongly coupling the matter degrees of freedom to quantum light [14–17], or by coupling the light to the phononic modes of the lattice [18, 19]. In particular, photoinduced enhancement of superconducting correlations has been shown [20, 21].

The philosophy of controlling quantum systems and preparing quantum states on demand is deeply ingrained in the field of ultracold quantum gases. This is in line with Feynman's vision [22] of investigating complex quantum systems by simulating them with the help of other quantum systems [23, 24]. Rapid experimental progress in techniques of cooling and trapping atoms with laser light led to remarkable possibilities of tunability and control of cold atomic gases. The milestone achievements range from the first realizations of Bose-Einstein condensation (BEC) in dilute quantum gases [25, 26], and of a degenerate quantum gas of fermions [27], to the confinement of ultracold quantum gases in tailored optical potentials [28, 29]. The versatility of these systems has allowed for the exploration of complex many-body phenom-

ena, as synthetic analogs of solid-state systems [28–31]. Numerous successful demonstrations of condensed matter phenomena has been realized [32, 33], as for example the quantum phase transition between a superfluid and a Mott-insulator [34], as predicted by the Bose-Hubbard Hamiltonian [35, 36], quantum magnetism and gauge potentials [37, 38], or topological quantum matter [39]. The long coherence times in these systems has facilitated also the study of the quantum dynamics [40–45], and the investigation of non-equilibrium processes [44, 46–49].

In the experimental realizations the system of interest is typically coupled to external environments. Having such a dissipative coupling to an environment appears as a challenge that one has to overcome in order to prepare entangled states of matter. Nevertheless, as it turns out, the non-equilibrium dissipative effects can be also utilized constructively. In this novel approach, by engineering the coupling of an open many-body system, complex quantum states can be generated [50–53]. One can tailor the interplay between the dissipative coupling to the environment and the coherent driving of the system in order to obtain the desired quantum state as a steady state, or as a state in the decoherence free subspace, of the open quantum system [53–55]. The non-equilibrium dynamics of an open system assures that the dynamics towards the steady states is exponentially fast in the presence of a dissipative gap [56], such that the steady states are stabilized against perturbations. This has been proven as a further successful approach in the quest for producing quantum materials exhibiting sought-after properties. For example, several theoretical proposals exist by now for the dissipative preparation of topological states of matter [57–63]. However, to describe these systems theoretically is very challenging. New simulation tools have been required to simulate open quantum many-body systems [64], as the methods developed for closed system cannot be easily applied.

A paradigmatic example of an open system is given by a many-body quantum system globally coupled to a dissipative quantum light field, which can be realized with ultracold atoms coupled to optical cavities [65, 66]. The potential of this platform has been highlighted with the seminal experimental demonstration of the supperradiant self-organization transition of a transversely driven BEC [67]. An interesting development in this field were the proposals of additionally confining the atomic gas with external optical lattice potentials, which leads to Hubbard models with cavity-mediated long-range interactions, for both bosons [68] and fermions [69]. The phase diagram of the extended Bose-Hubbard model with long-range interactions has been experimentally studied [70–73], showing besides the superfluid and Mott insulating phases, charge density wave and supersolid phases. Further theoretical proposals used the attractor dynamics of the open system in order to stabilize complex quantum phases [74–77], including topologically non-trivial phases [61, 78–85]. By designing specific couplings of the cavity field to the internal spin degrees of freedom of atoms, one can simulate a wide class of long-range quantum spin Hamiltonians [86–88]. This has opened the possibilities of the realization of dissipation-induced instabilities [89–91] and dynamical spin-orbit coupling [92, 93]. Recent achievements also include studies of the chaotic dynamics [94–97] and the realization of time crystals [98, 99]. A large part of the theoretical treatments of coupled atoms-cavity systems were performed, until now, in the framework of the mean field decoupling of the cavity field and the atoms [65, 66, 100, 101]. Numerous technical difficulties introduced by the atom-photon coupling are simplified in the mean field approach. However, deviations from

the mean field approach can already be found in small systems of one or two atoms, or two sites, if the exact coupling between the atomic and photonic states is fully taken into account [102–107]. This called for new methods which can also treat larger atomic ensembles globally coupled to bosonic fields, which we developed in parts of this work [108–110].

In this thesis we present two instances of quantum many-body systems with external control. First, we consider bosonic atoms confined to quasi-one-dimensional optical lattices globally coupled to the field of an optical cavity. We investigate several self-organization transitions protected by the attractor dynamics, given by the dissipative nature of the photon field. We present several novel methodological developments which allow us to identify drastic deviations from the mean field approaches extensively used in the literature. In particular, we show that the phase transitions have a *mixed state character*, being dominated by the fluctuations in the atoms-cavity coupling. Secondly, we study the $BaCo_2V_2O_8$ compound in a transverse magnetic field. At large intensities of the magnetic field this material realizes the one-dimensional XXZ spin chain model with a position dependent magnetic field. The model exhibits a phase transition as a function of the magnetic field. We show a very good agreement between experimental measurements and our numerical and analytical results.

The outline of the thesis is as follows

Chapter 2: We begin by introducing the theoretical models used for the description of the quantum many-body systems considered in this thesis. First, we present the case of ultracold atoms coupled to optical cavities. As this is a dissipative system, we offer a short introduction to the framework of Markovian open quantum systems and afterwards we sketch the derivation of the model for an one-dimensional chain of bosonic atoms globally coupled to the photonic mode. We describe the phase diagram of this system at the level of a mean field decoupling between the atoms and the cavity field, as we will contrast this to the methods which go beyond the mean field approximation later in the thesis. Secondly, we present the phase diagram of the one-dimensional XXZ spin chain model in the absence of a magnetic field and the lowest energy excitations for the different phases.

Chapter 3: One of the central elements of this thesis is the matrix product state (MPS) formalism which allows us to perform numerically exact simulations of low-dimensional many-body quantum systems. We give a short introduction into how one can find the ground state, or perform the time evolution, of a Hamiltonian system. In the second part of the chapter we go beyond the usual implementation of time-dependent matrix product state method (tMPS) approaches and develop a tMPS method for the combined atom-cavity system. This new and efficient implementation allows us to deal with the global coupled of the cavity field to the atoms, the very large dimension of the cavity Hilbert space and the dissipative nature of the system. We present extensive convergence checks of the method in order to prove its applicability to the considered systems. The second part of this chapter, which constitutes one of the main methodological developments performed in this thesis, is based upon results published in Ref. [109],

Chapter 4: In this chapter, we present one of the main analytical approaches used in this thesis, namely the many-body adiabatic elimination. This method is in essence a perturbation theory which allows us to eliminate the fast decaying subspaces of a many-body open quantum system, obtaining an effective dynamics valid at long times. After the derivation of the equations of motions for a general open system described by a Liouvillian, we extend this approach for atoms-cavity coupled systems. This is the second methodological development performed in this thesis. We consider two possible perturbations, either the kinetic energy of the atoms, or the fluctuations on top of the mean field decoupling of the cavity and the atoms, and we compute the steady state in both situations. This chapter is based upon results published in Refs. [109, 110].

Chapter 5: We present the properties of a chain of interacting bosonic atoms coupled to an optical cavity, obtained with the newly developed numerical exact and analytical methods, which go beyond the mean field description. This coupled atoms-cavity system exhibits a phase transition between a normal state and a *self-organized state*, characterized by the presence of a finite cavity occupation and the atoms forming a density wave. We observe important deviations from the mean field results in both our numerical exact time-evolution and the analytical many-body adiabatic elimination approaches. Our results show that the self-organization transition has a *mixed state character*, in contrast to the pure state transition obtained in the mean field description. In certain regimes the atoms can be described by a finite effective temperature. In particular, we show that in the self-organized phase the steady state consists in a mixture of the mean field predicted density wave states and excited states with additional defects. The deviations become even more prominent when the strength of the dissipative processes is large, in this case the atomic steady state is characterized by a very large effective temperature. This chapter is based upon results published in Refs. [108, 110].

Chapter 6: Once the bosonic atoms are non-interacting a *strong symmetry* is present in our coupled system. The existence of a symmetry in a quantum system has crucial implications on its behavior and dynamics. In dissipative quantum systems, in contrast to closed system, it is not always true that a symmetry implies a conserved quantity. Only the so-called strong symmetries lead to the existence of *multiple steady states* and conservation laws. We show with the beyond mean field methods developed in the previous chapters how the strong symmetry affects the dynamics of the atoms coupled to the cavity. We observe the phenomenon of dissipative freezing, which consists in the breaking of the conservation law at the level of single stochastic quantum trajectories in the presence of the strong symmetry. We analyze how the presence of a small interaction term breaks the strong symmetry and provokes a transition from multiple steady states to a unique steady state. This chapter is based upon results published in Ref. [111].

Chapter 7: We present a theoretical proposal in which the coupling between bosonic atoms trapped in a one-dimensional wire and the cavity is designed in such a way that a spin-orbit coupling is *dynamically induced*. The spin-orbit coupling is induced via Raman transitions between two internal states of the atoms, which employ the cavity mode and a transverse running wave

pump beam, the transitions imprint a spatial dependent phase onto the atomic wavefunction. Due to the complexity of the coupling between the atoms and the cavity field, in this chapter we take the first steps in analyzing this system, by computing the mean field phase diagram. We show that we can stabilize the exotic *Meissner superfluid* in the bosonic wire. In the Meissner phase the spin of the particles and their momentum direction are locked to each other, such that the two spins are propagating in opposite directions, giving rise to persistent chiral spin current. Our analysis is performed both in a homogeneous system, or with a parabolic trap, for experimentally feasible parameters. This chapter is based upon results published in Ref. [93].

Chapter 8: In this chapter, we investigate the one-dimensional XXZ spin chain model in the presence of a spatially dependent magnetic field with four-fold periodicity. We unveil a *quantum phase transition* as we increase the magnetic field, which we determine to belong to the Ising universality class. We perform time-dependent matrix product states simulations to compute the dynamical spin structure factor. This allows us to investigate the excitation spectrum across the phase transition. We complement our numerical simulations with analytical approaches and we identify that above the critical field the relevant excitations are single magnons and *two-magnon bound states*. We show that our theoretical results agree very well with experimental data obtained for the $BaCo_2V_2O_8$ compound in a transverse magnetic field. This chapter is based upon results soon to be published in Ref. [112].

We conclude our discussions in **Chapter 9** with a brief summary of our results and an outlook onto future research directions.

Theoretical models for quantum many-body systems

In this chapter, we give a brief presentation of the theoretical quantum many-body models we employ in this thesis. Sec. 2.1 is focused on ultracold atoms coupled to optical cavities. We present the framework of the Lindblad master equation for open quantum systems. We sketch the derivation of the model for atoms coupled to an optical cavity which we will use in Chapters 3 to 6. In Sec. 2.1.3 we discuss the mean field diagram of the model. In Sec. 2.2 we present the properties of the XXZ spin chain in zero magnetic field, which we need for our investigation of the $BaCo_2V_2O_8$ compound presented in Chap. 8.

2.1 Ultracold atoms coupled to optical cavities

2.1.1 Short introduction to open quantum systems

The paradigm of open quantum systems stems from the situation in which the quantum system of interest, S, is in contact with another system E, called the environment. One approach would be to study the full composite system, but this is usually not feasible as the environment tends to be much larger than the system of interest. For example, one could have a coupling to a reservoir with infinitely many degrees of freedom. Nevertheless, methods in which one can characterize, under certain assumptions, just the effective dynamics of the system of interest under the action of the environment exist [56]. The Hamiltonian which describes the dynamics of the full system can be written as

$$H = H_S \otimes \mathbb{1} + \mathbb{1} \otimes H_E + H_{SE}, \qquad (2.1)$$

where H_S acts on the system degrees of freedom, H_E on the environment and H_{SE} provides the coupling between the system and the environment. The evolution of the system can be now computed with the von Neumann equation for the density matrix of the full system

$$\frac{\partial}{\partial t}\rho = -\frac{i}{\hbar}\left[H, \rho\right]. \qquad (2.2)$$

We can calculate the density matrix of a sub part of the full system by performing the partial trace of the complementary part, i.e. $\rho_S = \mathrm{tr}_E(\rho)$ for the system's density matrix and $\rho_E = \mathrm{tr}_S(\rho)$ for the environment. In the case of a time-independent Hamiltonian one can write the formal solution for ρ_S by integrating Eq. (2.2) and tracing out the environment

$$\rho_S(t) = \mathrm{tr}_E\left[U(t,0)\rho(0)U(t,0)^\dagger\right], \tag{2.3}$$

with the unitary time-evolution operator $U(t,t_0) = \exp\left[-iH(t-t_0)/\hbar\right]$. As the time evolution of $\rho_S(t)$ is given by the trace over the environment, it is no longer unitary. This can be interpreted as a form of dissipation, justifying the name of open quantum system. Due to the fact that the full evolution is not feasible to be computed in most cases of interest, we would like to trace out the environment before integrating the full equation of motion, Eq. (2.2). In this approach we obtain an equation of motion containing just operators of the system S. To achieve this we make the assumption of Markovianity [56]. This can be stated as the fact that the time evolution of the open system depends only on its current state, and not on the past trajectory of the system in time. This condition is valid if the system-environment coupling induces much longer time scales than the relaxation time scales of the environment. Markovianity also implies that the environment has no "memory", such that there is no retroactive effect from previous dissipative events on the current state of the system. Thus, we can also assume that at the initial time the system and environment are decoupled, $\rho(t=0) = \rho_S(t=0) \otimes \rho_E$. These assumptions are reasonable if the environment is large enough to not be affected by the dynamics of the system. But, in general, the condition of Markovianity has to be carefully verified. In the fields of quantum optics and ultracold atoms Markovianity is usually well-fulfilled, as the main dissipation channels are photon or particle losses. The most general equation that satisfies the previous assumptions is the Markovian quantum master equation in Lindblad form, or simply the Lindblad equation, which reads [56, 113, 114]

$$\frac{\partial}{\partial t}\rho_S = \mathcal{L}(\rho_S) = -\frac{i}{\hbar}\left[H_S, \rho_S\right] + \mathcal{D}(\rho_S), \tag{2.4}$$
$$\text{with } \mathcal{D}(\rho_S) = \frac{1}{2}\sum_j \Gamma_j \left(2L_j\rho_S L_j^\dagger - L_j^\dagger L_j \rho_S - \rho_S L_j^\dagger L_j\right).$$

The Markovian time evolution is generated by the Liouvillian superoperator $\mathcal{L}$, its first term describes the unitary evolution under the system Hamiltonian and the second, the dissipator $\mathcal{D}$, the dissipative processes. L_j are called the Lindblad, or jump, operators and model the effect of the environment on the system, each corresponding to a coupling strength Γ_j. The Lindblad equation preserves the trace, hermiticity and semi-positivity of the density matrix. Thus, we are assured that the density matrix remains physical during the evolution [56]. Since in this work we are only interested in the properties of the open system, we drop the S index and use $\rho \equiv \rho_S$ from now on.

The formal solution of Eq. (2.4) can be written as

$$\rho(t) = e^{\mathcal{L}t}\rho(0). \tag{2.5}$$

The exponential in Eq. (2.6) can be computed, in principle, by going to the eigenbasis of $\mathcal{L}$, as $\mathcal{L}$ is a linear operator acting on the space of system density matrices. This implies that we can perform the time evolution by evolving the Liouvillian's eigenstates, weighted with their overlap with the initial state. Because $\mathcal{L}$ is a non-hermitian operator, its eigenvalues are in general complex. However, the form of the Lindblad equation, Eq. (2.4), leads to several restrictions on the eigenvalue spectrum. As the trace of ρ is conserved, this implies that the real part of the eigenvalues is less than or equal to zero and at least one eigenvalue is zero. Thus, there exists at least one eigenstate which satisfy the condition

$$\mathcal{L}\rho_{\text{st}} = 0. \tag{2.6}$$

These states do not evolve in time and are called *steady states*. The other eigenstates ρ_j, with the corresponding eigenvalues $\lambda_j = -\lambda_j^R + i\lambda_j^I$, which have a finite negative real part are subject to an exponential decay in time

$$\rho_j(t) = e^{-\lambda_j^R + i\lambda_j^I t}\rho_j(0) \xrightarrow{t\to\infty} 0, \quad \text{where } \lambda_j^R \in \mathbb{R}_0^+, \ \lambda_j^I \in \mathbb{R}. \tag{2.7}$$

For the unique steady state, regardless of the initial state the system always evolves towards the steady state exhibiting an attractor dynamics, exponentially fast in the presence of a dissipative gap. In contrast, in the case of multiple steady states, the long time state is determined by the overlap of the steady states with the initial state. We note that eigenstates for which $\lambda_j^R = 0$, but $\lambda_j^I \neq 0$, are also possible [115], in this case the states do not decay in time and have an oscillating phase at all times.

2.1.2 Theoretical model of ultracold atoms in optical lattices coupled to optical cavities

In the following chapters, to a large extend, we study and develop methods to investigate dissipative systems of interacting particles globally coupled to a bosonic field, as sketched in Fig. 2.1. In such a situation, the particles can for example describe atoms or electrons and the bosonic quantum field can be for example a photonic field of a cavity or a long lived phononic mode. As we saw in the previous section, these systems can be described by a Lindblad master equation for the density operator ρ, given by [56, 65, 100, 114]

$$\frac{\partial}{\partial t}\rho = -\frac{i}{\hbar}[H, \rho] + \frac{\Gamma}{2}\left(2a\rho a^\dagger - a^\dagger a\rho - \rho a^\dagger a\right), \tag{2.8}$$

where a and $a^\dagger$ are the annihilation and creation operators for the bosonic mode. The dissipative term proportional to the dissipation strength Γ describes the losses in the bosonic mode. We consider the Lindblad form of the dissipator, where the jump operator is the annihilation operator a of the bosonic mode. In a photonic cavity these can be due to the imperfections of the mirrors and for phononic modes it describes the decay into a bath of phononic modes.

In this section, we want to introduce the model of ultracold bosonic atoms confined in a one-dimensional chain coupled to an optical cavity used throughout this thesis (see Chapters 3, 4, 5 and 6) [108–111]. We sketch the derivation of the model following Ref. [100]. We note

2.1.2 Theoretical model of ultracold atoms in optical lattices coupled to optical cavities
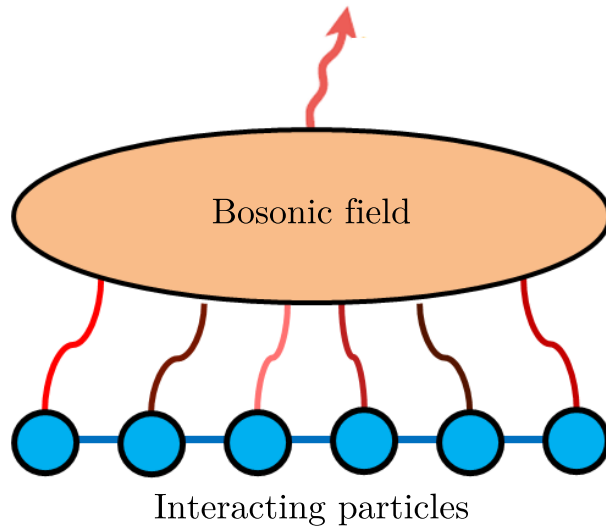
Figure 2.1: Sketch of a chain of interacting particles (e.g. atoms or electrons) coupled to a single bosonic quantum mode (cavity fields or phononic modes) . The bosonic mode has a dissipative nature and it is coupled to every site of the chain. The coupling strength can vary from site to site. ©2020 American Physical Society, published in [109].
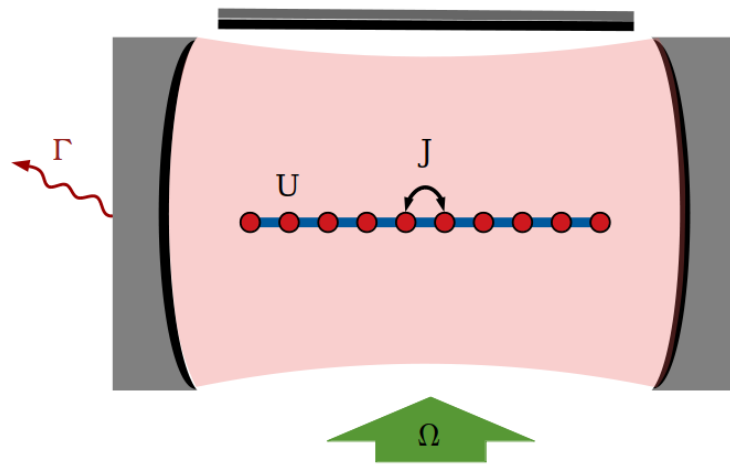
Figure 2.2: Sketch of the bosonic atoms confined in a one-dimensional chain in an optical cavity. The atoms tunnel with the amplitude J and have an on-site interaction of strength U. The coupling of the atoms to the cavity is realized with a retroreflected transverse pump beam. As the lattice spacing is commensurate with half of the wavelength of the cavity mode, the cavity field is coupled to the total imbalance between the odd and even sites of the chain. The strength of the coupling is controlled by the pump amplitude Ω. The cavity is losing photons with the dissipation strength Γ, due to the imperfections of the mirrors. ©2020 American Physical Society, published in [109].

that in Chap. 7 we consider a more complicated model where the cavity induces a dynamical spin-orbit coupling, which can be derived in a similar manner [93].

2.1 Ultracold atoms coupled to optical cavities

We start with N two-level bosonic atoms with mass m and transition frequency ω_{eg} strongly interacting with a single standing wave mode of frequency ω_c. We also consider a coherent driving of the atoms at frequency ω_p with a transverse pump beam (see Fig. 2.2). A single atom of this system can be described by a Hamiltonain in which one makes the rotating-wave and electric-dipole approximations [116] . The many particle version of the Hamiltonian using second quantization formalism, in the rotating frame of the pump laser beam, includes the following terms [100]

$$H = H_{\mathrm{a}} + H_{\mathrm{c}} + H_{\mathrm{ac}} + H_{\mathrm{ap}}. \tag{2.9}$$

The atomic Hamiltonian is given by

$$H_{\mathrm{a}} = \int d^3x \left[\psi_g^\dagger(\mathbf{x}) \left(-\frac{\hbar^2}{2m}\nabla^2 + V_g(\mathbf{x}) \right) \psi_g(\mathbf{x}) + \psi_e^\dagger(\mathbf{x}) \left(-\frac{\hbar^2}{2m}\nabla^2 + V_e(\mathbf{x}) - \hbar\Delta_a \right) \psi_e(\mathbf{x}) \right]$$
$$+ \frac{U_{\mathrm{3D}}}{2} \int d^3x \, \psi_g^\dagger(\mathbf{x})\psi_g^\dagger(\mathbf{x})\psi_g(\mathbf{x})\psi_g(\mathbf{x}), \tag{2.10}$$

where $\psi_g(\mathbf{x})$ and $\psi_e(\mathbf{x})$ denote the atomic bosonic field operator for annihilating an atom at position $\mathbf{x}$ in the ground state and the excited state, respectively. $V_g(\mathbf{x})$ and $V_e(\mathbf{x})$ are external trapping potentials for the atoms in the ground state and the excited state, respectively. $\Delta_a = \omega_p - \omega_{eg}$ is the detuning of the atomic frequency from the pump field frequency. The second line corresponds to the two-body interaction, characterized by the s-wave scattering length a_s, where $U_{\mathrm{3D}} = 4\pi a_s\hbar^2/m$. The cavity part of the Hamiltonian is

$$H_{\mathrm{c}} = \hbar\delta a^\dagger a, \tag{2.11}$$

with a detuning between the cavity mode and the transverse pump beam $\delta = \omega_{\mathrm{c}} - \omega_{\mathrm{p}}$. The coupling of the cavity field with the atoms inside the cavity is described by

$$H_{\mathrm{ac}} = -i\hbar \int d^3x \, \psi_g^\dagger(\mathbf{x})g(\mathbf{x})a^\dagger\psi_e(\mathbf{x}) + \mathrm{H.c.}, \tag{2.12}$$

where $g(\mathbf{x})$ denotes the cavity mode function. The interaction between the atoms and the pump laser beam is

$$H_{\mathrm{ap}} = -i\hbar \int d^3x \, \psi_g^\dagger(\mathbf{x})h(\mathbf{x})\psi_e(\mathbf{x}) + \mathrm{H.c.}, \tag{2.13}$$

where $h(\mathbf{x})$ represents the mode function of the transverse pump field.

We want to consider regimes with very low temperatures compared to the internal level spacing, such that the atomic excitations and spontaneous emission are negligible. In this limit one can adiabatically eliminate the excited states from the dynamics [100]. This requires large

2.1.2 Theoretical model of ultracold atoms in optical lattices coupled to optical cavities

atom-pump detunings Δ_a. By expanding the equation of motion of $\psi_e(\mathbf{x})$ in $1/\Delta_a$ one obtains

$$\psi_e(\mathbf{x}, t) = -\frac{i}{\Delta_a} \left[h(\mathbf{x}) + g(\mathbf{x})a(t) \right] \psi_g(\mathbf{x}, t), \tag{2.14}$$

where one assumes that the operators $\psi_g(\mathbf{x})$ and a vary on a much slower time scale than $1/\Delta_a$. One can insert this expression in the equations of motion for $\psi_g(\mathbf{x})$ and a and obtain that they can be described by the following effective Hamiltonian [100]

$$H_{\text{eff}} = \int d^3x \, \psi_g^\dagger(\mathbf{x}) \left\{ -\frac{\hbar^2}{2m}\nabla^2 + V_g(\mathbf{x}) + \frac{\hbar}{\Delta_a} \left[h^2(\mathbf{x}) + g^2(\mathbf{x})a^\dagger a + h(\mathbf{x})g(\mathbf{x}) \left(a + a^\dagger \right) \right] \right\} \psi_g(\mathbf{x})$$
$$+ \frac{U_{\text{3D}}}{2} \int d^3x \, \psi_g^\dagger(\mathbf{x})\psi_g^\dagger(\mathbf{x})\psi_g(\mathbf{x})\psi_g(\mathbf{x}), \tag{2.15}$$
$$+ \hbar\delta a^\dagger a.$$

In the following, we reduce the dimensionality of the system to a one-dimensional chain along the cavity axis with the help of optical lattices. The mode function of the cavity along the axis is approximated by $g(\mathbf{x}) = g(x) = g_0 \cos(kx)$, with k the cavity wavevector. As the transverse beam is a broad standing wave perpendicular to the cavity axis, it is constant for all sites of the one-dimensional lattice, $h(\mathbf{x}) = h_0 \cos(k_p y)$, with k_p the pump beam wavevector. For the trapping potential along the cavity axis we take $V_g(x) = V_0 \cos(kx)^2$, which is commensurable with the cavity mode [100]. We can now expand the atomic field operator $\psi_g(x)$ in terms of single atom Wannier functions, $w(x) = \sum_h b_j w(x - x_j)$, where we restrict ourselves just to the lowest band of the one-dimensional lattice. The operators b_j and $b_j^\dagger$ are the bosonic annihilation and creation operators of the atoms on site j. Thus, we obtain the Hamiltonian, which together with the Liovillian given in Eq. (2.8), describes the one-dimensional chain of bosonic atoms coupled to an optical cavity (sketched in Fig. 2.2) [65, 66, 100, 101]

$$H = H_{\text{c}} + H_{\text{int}} + H_{\text{kin}} + H_{\text{ac}} \tag{2.16}$$
$$H_{\text{c}} = \hbar\delta a^\dagger a,$$
$$H_{\text{int}} = \frac{U}{2} \sum_{j=1}^{L} n_j(n_j - 1),$$
$$H_{\text{kin}} = -J \sum_{j=1}^{L-1} (b_j^\dagger b_{j+1} + b_{j+1}^\dagger b_j),$$
$$H_{\text{ac}} = -\hbar\Omega(a + a^\dagger) \sum_{j=1}^{L} (-1)^j n_j,$$

where $n_j = b_j^\dagger b_j$, L denotes the number of sites of the chain and the total number of bosonic atoms is N. For the atomic part of the Hamiltonian we have H_{kin} which describes the tunneling processes of the atoms with the amplitude J and the term H_{int} representing the repulsive on-

site interaction of strength $U > 0$. H_{ac} gives the coupling between the cavity field and the total imbalance between the odd and even sites of the chain, with the effective pump amplitude Ω. This coupling is realized due to the assumed commensurability of the cavity mode with twice the periodicity of the lattice spacing within the chain [100]. We note that for simplicity in Eq. (2.16) we neglect the frequency shift of the cavity mode induced by a single atom at an antinode, this is justified for small numbers of photons in the cavity and strong lattice potentials.

The Hamiltonian, Eq. (2.16), exhibits a $\mathbb{Z}_2$ symmetry associated with the inversion of the sign of the cavity field, a, and the atomic odd-even imbalance. However, the $\mathbb{Z}_2$ symmetry is only a weak symmetry of the Liouvillian, Eq. (2.8), [115, 117] since the transformation does not commute with the jump operator a of the Lindblad equation, Eq. (2.8).

2.1.3 Phase diagram in the mean field description

For the rest of this section we present the mean field approach of eliminating the dynamics of the cavity field [65, 66, 100, 101], for the setup given in Eqs. (2.8)-(2.16). In this approach one derives an effective model for the bosonic atoms employing the adiabatic elimination of the cavity field. Due to the complexity of the models describing atoms coupled to cavities a large portion of the theoretical studies have been performed in this framework [65, 66].

This approach is based on the mean field decoupling of the cavity field and the atomic operators

$$H_{ac} = -\hbar\Omega(a + a^\dagger)\sum_{j=1}^{L}(-1)^j n_j \qquad (2.17)$$

$$\approx -\hbar\Omega(a + a^\dagger)\Delta - \hbar\Omega\langle a + a^\dagger\rangle\sum_{j=1}^{L}(-1)^j n_j + \text{const.,}$$

where we made the notation $\Delta \equiv \sum_{j=1}^{L}(-1)^j\langle n_j\rangle$. After the decoupling one can solve the equation of motion of the cavity field given by

$$i\partial_t\langle a\rangle = -\Omega\Delta + (\delta - i\Gamma/2)\langle a\rangle. \qquad (2.18)$$

A second assumption is that the cavity field has a very fast dynamics, such that we are only interested in the steady state limit of Eq. (2.18). This is obtained by imposing the condition $\partial_t\langle a\rangle = 0$. The cavity photons are obtained to be in a coherent state. Using Eqs. (2.8) and (2.16) this condition becomes

$$\alpha = \langle a\rangle = \frac{\Omega}{\delta - i\Gamma/2}\Delta. \qquad (2.19)$$

This equation relates the expectation value of the odd-even imbalance to the value of the cavity field.

After substituting the expectation value for the cavity field, Eq. (2.19), into the atomic part

of the equations of motion, we obtain an effective Hamiltonian for the atoms

$$H_{\text{eff}} = H_{\text{kin}} + H_{\text{int}} + H_{\text{imb}} \tag{2.20}$$

$$H_{\text{kin}} = -J \sum_{j=1}^{L-1} (b_j^\dagger b_{j+1} + b_{j+1}^\dagger b_j)$$

$$H_{\text{int}} = \frac{U}{2} \sum_{j=1}^{L} n_j(n_j - 1)$$

$$H_{\text{imb}} = -\hbar\Omega\,(\alpha + \alpha^*) \sum_{j=1}^{L} (-1)^j n_j.$$

We can see that this effective Hamiltonian needs to be analyzed self-consistently as it depends on the expectation value of the odd-even imbalance Δ, through the cavity field.

The usual approach is to describe the atoms by the ground state (zero-temperature state) of this effective model, Eq. (2.20) [65, 66]. Thus, in this approximation, the steady state is a pure state composed of a product state between the atomic and photonic sector

$$\rho_{\text{MF}} = |\alpha(\Delta_{\text{eff}}), \Delta_{\text{eff}}\rangle\langle\alpha(\Delta_{\text{eff}}), \Delta_{\text{eff}}|, \tag{2.21}$$

where the photonic mode is in the coherent state $\alpha(\Delta_{\text{eff}})$. The atomic state $|\Delta_{\text{eff}}\rangle$ denotes the ground state of the effective Hamiltonian with the self-consistency condition. The effective imbalance Δ_{eff} is defined as the expectation value of the odd-even imbalance in the ground state of the effective Hamiltonian.

But this is a rather arbitrary choice, as any eigenstate of the Hamiltonian would solve the mean field equation of motion for the atoms which reads

$$\frac{\partial}{\partial t}\rho^a = -\frac{i}{\hbar}\left[H_{\text{eff}}, \rho^a\right]. \tag{2.22}$$

This stems from the fact that at this level of approximation we are trying to describe an inherently open system just by an effective Hamiltonian. In order to solve these problems in this work we went beyond the mean field description by developing novel numerical and analytical methods that can deal exactly with the atoms-cavity coupling, or including the fluctuations beyond the mean field decoupling, as we will see in Chap. 3 and Chap. 4. In Chap. 5 we present our results in contrast to the mean field approach and we observe that considerable deviations appear for a wide range of parameters.

We note that the mean field approach captures the self-organization transition observed in this system [65, 66]. Thus, above a certain threshold $\Omega_{\text{MF},c}\sqrt{N}$ the cavity field $\langle a \rangle$ takes a finite value and the atoms self-organize into a density modulated pattern either on the odd or even sites of the chain. This spontaneously breaks the $\mathbb{Z}_2$ symmetry of the effective Hamiltonian. This is to be contrasted with the full open system, Eqs. (2.8)-(2.16), where we do not expect the symmetry to be broken for any finite size system, as the $\mathbb{Z}_2$ symmetry is only a weak symmetry

Figure 2.3: The mean field value of the scaled photon number, $\langle a^\dagger a\rangle/N$, as a function of the coupling strength, $\hbar\Omega\sqrt{N}/J$, for $N/L = 1/2$, $\hbar\delta/J = 2$, $U/J = 2$, and $\hbar\Gamma/J = 1$. The dashed vertical line marks the self-organization threshold.

[102, 103, 106, 118].

The sudden onset of the cavity field is also reflected in the behavior of the photon number n_{MF}, as seen in Fig. 2.3, with

$$n_{\text{MF}} = |\langle a\rangle|^2 = \frac{\Omega^2}{\delta^2 + \Gamma^2/4}\Delta_{\text{eff}}^2. \tag{2.23}$$

2.2 Properties of XXZ spin chains

In Chap. 8 we will investigate the properties of the XXZ spin chain in a transversal magnetic field, model relevant for the experimental studies of the $BaCo_2V_2O_8$ compound [5, 119, 120]. In this section, we give a short overview of the equilibrium properties of the XXZ model without a magnetic field [121, 122].

The Hamiltonian for a one-dimensional system of equally spaced spins with spin $S = 1/2$ is given by

$$H_{XXZ} = \sum_j J\left[\epsilon\big(S_j^x S_{j+1}^x + S_j^y S_{j+1}^y\big) + S_j^z S_{j+1}^z\right], \tag{2.24}$$

where we have equal interaction strengths $J\epsilon$ for the exchange couplings of neighboring spins along the x and y spin directions and an interaction strength J for the z direction. The spin$-1/2$ operators are defined as $S^\alpha = \frac{\hbar}{2}\sigma^\alpha$, with $\alpha \in \{x, y, z\}$ and σ^α are the Pauli matrices.

In the following, we present a few details regarding the ground state properties of the XXZ-model, which can be obtained analytically as the XXZ-model is solvable by Bethe-Ansatz. The phase diagram of the model exhibits three phases depending on the anisotropy $1/\epsilon$, as seen in Fig. 2.4. The system is in the gapped ferromagnetic phase (Ising FM) for $1/\epsilon < -1$,
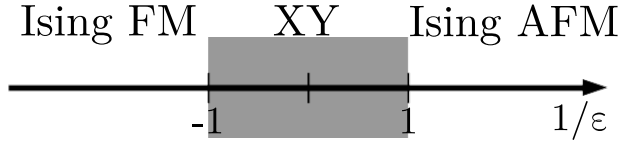
Figure 2.4: The phase diagram of the XXZ-model as a function of the anisotropy $1/\epsilon$.

the gapped antiferromagnetic phase (Ising AFM) for $1/\epsilon > 1$, or the gapless Luttinger liquid phase, also known as the XY-phase for $-1 \leq 1/\epsilon \leq 1$. We note that at the isotropic points, $1/\epsilon = \pm 1$, the system is a Heisenberg ferromagnet, or antiferromagnet, respectively.

In the Ising ferromagnetic phase, the negative anisotropy favors the parallel alignment of neighboring spins. This implies that the ground states are given by the fully polarized states in the z-direction, in two of the possible sectors [123]. For these the ground state magnetization in the z-direction is given by $\langle S^z \rangle_{gs} = \pm N/2$, with N the total number of spins. The collective low-energy excitations in this regime are the magnons. They can be thought of being a 'defect' in the fully polarized state of a spin pointing in the opposite direction with respect to the surrounding spins. The dispersion relation of the magnons is given by $E(k) = J\epsilon \left[1 - \cos(k) - (1/\epsilon + 1)\right]$ [121], yielding an approximately quadratic dispersion for small momenta on top of a gap of $|1/\epsilon| - 1$ at $k = 0$. As we approach $1/\epsilon \to -1$ the excitations become gapless. We note that we can obtain a fully polarized phase also in the presence of a strong magnetic field also for other spin directions, as we will see in Chap. 8.

In the Ising antiferromagnetic phase the positive anisotropy favors the antiparallel spin orientation of the neighboring spins. For a system of finite size, the ground state is dominated by the mixing of the two possible configurations of alternating spin orientation. But quantum fluctuations have important contributions to the ground state, as the Hamiltonian, Eq. (2.24), does not conserve the sublattice magnetization, which only takes into account the subset of either even or odd sites. For strong anisotropy, $1/\epsilon \gg 1$, the excitations on top of the antiferromagnet can be understood perturbatively by creating domain walls. In this situation, a domain wall separates regions of alternating spins by a bond with equally aligned spins. If in the ground state one spin is flipped, two domain walls arise, which can propagate during the Hamiltonian time evolution through the system. This results in a continuum in the energy spectrum. The excitation gap of the antiferromagnet opens for $1/\epsilon > 1$ and the dispersion of the excitations is linear $E(k) \sim k$ [121]. We note that for the anisotropy values considered in Chap. 8 we are in the antiferromagnetic phase at zero magnetic field.

The third phase in the phase diagram is the XY-phase appearing for small anisotropies $|1/\epsilon| \leq 1$. We can gain some intuition regarding the properties of this phase by employing the Jordan-Wigner transformation which represents the spins as free spinless fermions and perturbatively include weak nearest neighbor interactions [122]. In this framework, the ground state for $1/\epsilon = 0$ is a Fermi sea, where, if the system size is large enough, we have particle-hole excitations with energies that can be arbitrarily small, such that the spectrum is gapless. This also holds if we include small couplings in the z-direction, $|1/\epsilon| \ll 1$.

15

Numerical tensor network methods

In this chapter, we first present the formalism and theoretical background of matrix product states (MPS), which allows us to perform accurate simulations of low-dimensional many-body quantum systems [124]. In the second part we show that matrix product states will also provide us the framework for developing method suitable for the investigation of open systems with global range interactions. The main idea of matrix product states is to perform an efficient parametrization of the quantum many-body wave function, whose set of degrees of freedom is growing exponentially with the system size. We aim to capture the essential contributions by considering just the relevant subspaces of the Hilbert space, such that the representation of the state can be brought down to a polynomial complexity with respect to the system size. As we will see, if the targeted quantum state of interest is only moderately entangled upon any bipartation of the system it can be faithfully represented as a matrix product state. This is in particular true for the ground states of one-dimensional local gapped Hamiltonians which obey an area law entanglement spectrum [125], as for example in certain spin chains [126] and Hubbard models [127, 128]. The algorithm for a variational systematic ground state search has been originally formulated by S.R. White as the density matrix renormalization group (DMRG) [129]. This was later cast in the language of matrix product states. A good review can be found, for example, in Ref. [124]. One can also extend the method to study two-dimensional systems [130–132]. The further extension to time dependent phenomena (tMPS) [133–135] highlights the large class of problems that can be tackled within this framework. In this approach the subspace to which the wave function is constrained is adapted throughout the course of the time evolution. Recently, a lot of effort has been devoted to the efficient implementation of MPS techniques as open source tensor network libraries, such as ALPS [136], TeNPy [137], Open Source MPS [138], and ITensor [139]. In this work we use the ITensor [139], due to its efficient implementation and native support of the inclusion of conserved quantities, and as it offers a flexible environment for further development.

In the following, we begin by introducing the concepts on which the matrix product state formalism relies and the widely used graphical representation, Sec. 3.1.1. The most common algorithms based on MPS are presented in Sec. 3.1.2, the variational ground state search, and in Sec. 3.1.3, the time evolution presented, these already allow us to analyze the behavior of interacting complex quantum systems. In Sec. 3.2 we go a step further and we develop a tMPS
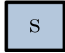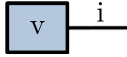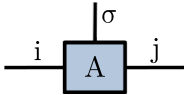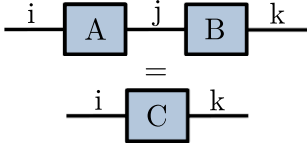
approach for dealing with the coupled atoms-cavity dissipative system, which we introduced in Sec. 2.1. This is one of the main methodological developments presented in this thesis. We explain in detail how we implemented this new algorithm in Sec. 3.2.1 and for the rest of the chapter, Sec. 3.2.2 to Sec. 3.2.6, we perform extensive convergence checks.

3.1 Background on matrix product state techniques for one-dimensional quantum systems

3.1.1 Matrix product state formalism and graphical representation

In this section, we introduce the matrix product state formalism [124] that we employ in the numerical methods used in this work. We show how to construct and compress a matrix product state (MPS), and how to compute expectation values using matrix product operators (MPO). As in the following sections we will heavily use the tensor diagram notation to describe the algorithms used, we show in Table 3.1 the relation between the basic elements of a tensor diagram and their mathematical representation.

Table 3.1: Relation between the tensor diagram elements and their mathematical representation.

Diagram	Object	Mathematical notation
s	scalar	s
v — i	vector	v_i
i — A — j	matrix	A_{ij}
i — A — j with σ	rank-3 tensor	A_{ij}^{σ}
i — A — j — B — k = i — C — k	matrix multiplication	$\sum_j A_{ij}B_{jk} = C_{ik}$

The main linear algebra tool used in MPS methods is the singular value decomposition (SVD). Its associated theorem states that any arbitrary rectangular matrix M of dimension $(m \times n)$ can be decomposed as

$$M = USV^{\dagger}, \tag{3.1}$$

where U and $V^{\dagger}$ are unitary matrices of dimension $m \times \min(m, n)$ and $\min(m, n) \times n$. S is

a diagonal matrix of dimension $\min(m,n) \times \min(m,n)$, with non-negative entries $\sqrt{\lambda_i} \geq 0$, called singular values. The Schmidt rank r of matrix M is given by the number of non-zero singular values, $\sqrt{\lambda_i} > 0$.

A first application of the SVD is to evaluate the entanglement between two parts of a quantum system by performing the Schimdt decomposition of a quantum state $|\Psi\rangle$. Let us consider a one-dimensional system, which can be divided into two subsystems A and B. The wavefunction $|\Psi\rangle$ describing the full system can be written as

$$|\Psi\rangle = \sum_{i,j} \Psi_{i,j} |i\rangle_A |j\rangle_B, \tag{3.2}$$

where $\{|i\rangle_A\}$ and $\{|j\rangle_B\}$ are the orthonormal basis of subsystem A, of dimension m, and subsystem B, of dimension n, respectively. We can rewrite the coefficients $\Psi_{i,j}$ into a matrix Ψ. By performing the singular value decomposition of the matrix Ψ we obtain

$$|\Psi\rangle = \sum_{i,j} \sum_{a=1}^{\min(m,n)} U_{i,a} S_{a,a} V_{j,a}^* |i\rangle_A |j\rangle_B \tag{3.3}$$

$$= \sum_{a=1}^{\min(m,n)} S_{a,a} \left(\sum_i U_{i,a} |i\rangle_A \right) \left(\sum_j V_{j,a}^* |j\rangle_B \right)$$

$$= \sum_{a=1}^{r} \sqrt{\lambda_a} |a\rangle_A |a\rangle_B,$$

where the sum runs only over the non-zero singular values $\sqrt{\lambda_a} > 0$, such that the upper bound is given by the rank $r \leq \min(m,n)$ of S. As the matrices U and V are unitary, the sets $\{|a\rangle_A\}$ and $\{|a\rangle_B\}$ are orthonormal basis sets in the subsystems A and B. We can observe now the relation between the Schmidt decomposition and the entanglement between the two subsystems. If the value of the Schmidt rank is $r = 1$, $|\Psi\rangle$ can be written as a product state, having no entanglement, and the entanglement between A and B is finite for larger values of the rank r. We can quantify the entanglement present between the two subsystems with the von Neumann entanglement entropy, given by

$$S_{\text{vN}} = -\sum_{a=1}^{r} \lambda_a \log(\lambda_a). \tag{3.4}$$

One can also use the Schmidt decomposition in order to approximate the quantum state $|\Psi\rangle$ with a state of a smaller rank. Thus, we want to construct a state $|\tilde{\Psi}\rangle$ of a maximal rank $D < r$, $|\tilde{\Psi}\rangle = \sum_{a=1}^{D} \sqrt{\lambda_a} |a\rangle_A |a\rangle_B$. We achieve this by minimizing the norm,

$$\left\| |\Psi\rangle - |\tilde{\Psi}\rangle \right\|^2 = 1 - \sum_{a=D}^{r} \lambda_a. \tag{3.5}$$

Where we ordered the singular values $\lambda_1 \geq \lambda_2 \geq ...$, such that we retain the largest D singular values and discard the smallest $r - D$ singular values. The approximation becomes better if λ_a decay quickly for increasing a. Thus, we can approximate our state $|\Psi\rangle$ with a state with a smaller rank at the expense of a truncation error given by sum of the smallest singular values.

Using the described tools we can now exemplify how to construct the matrix product states [124]. We start from an arbitrary quantum state for a lattice system with L sites and the dimension of the local Hilbert space d for each site

$$|\Psi\rangle = \sum_{\sigma_1,...,\sigma_L} c_{\sigma_1,...,\sigma_L} |\sigma_1, ..., \sigma_L\rangle, \tag{3.6}$$

where $\{|\sigma_j\rangle\}$ is the local basis of dimension d, and $|\vec{\sigma}\rangle \equiv |\sigma_1, ..., \sigma_L\rangle \equiv \{|\sigma_1\rangle\} \otimes ... \otimes \{|\sigma_L\rangle\}$. We have exponentially many coefficients $c_{\sigma_1,...,\sigma_L}$, which contain the information of the state. The collection of the coefficients $c_{\sigma_1,...,\sigma_L}$ can be thought of as a rank-L tensor, which we can graphically depict as in Fig. 3.1(a). The MPS representation of a state $|\Psi\rangle$ reads

$$|\Psi\rangle = \sum_{\sigma_1,...,\sigma_L} M^{\sigma_1} M^{\sigma_2} ... M^{\sigma_L} |\sigma_1, ..., \sigma_L\rangle, \tag{3.7}$$

where M^{σ_j}, $j = 1...L$, are rank-3 tensors. The contraction of the tensors results in a scalar, namely $c_{\sigma_1,...,\sigma_L}$, for each state $\{|\sigma_j\rangle\}$. The MPS representation can be constructed by performing the SVD repeatedly, starting from the left or from the right of the matrix product. This results in the so-called left-canonical or right-canonical matrix product state. In the following we will exemplify this by constructing the left-canonical matrix product state. The procedure is graphically represented in Fig. 3.1. We begin by reshaping the d^L coefficients $c_{\sigma_1,...,\sigma_L}$ into a matrix $\Psi_{\sigma_1,(\sigma_2...\sigma_L)}$ of dimensions $\left(d \times d^{L-1}\right)$ and performing the SVD of this matrix
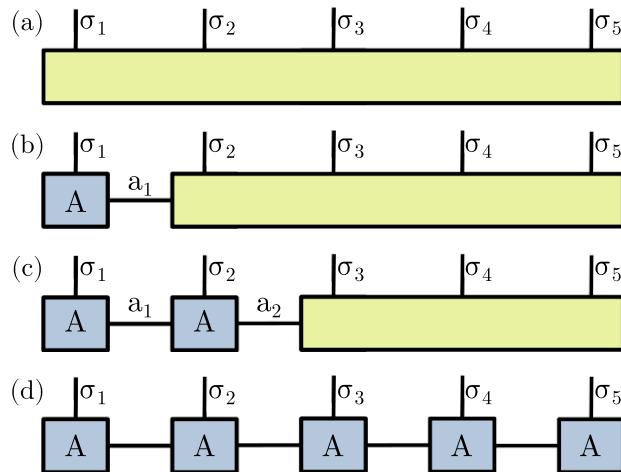
Figure 3.1: Construction of a left-canonical matrix product state by iterative applications of the singular value decomposition (SVD), see Eq. (3.10).

3.1 Background on matrix product state techniques for one-dimensional quantum systems

$$\Psi_{\sigma_1,(\sigma_2...\sigma_L)} = \sum_{a_1} U_{\sigma_1,a_1} S_{a_1,a_1} V^\dagger_{a_1,(\sigma_2...\sigma_L)} \equiv \sum_{a_1} U_{\sigma_1,a_1} c_{a_1,\sigma_2,...,\sigma_L}, \qquad (3.8)$$

where in the last equality we performed the matrix multiplication and reshaped the result back into a vector $c_{a_1,\sigma_2,...,\sigma_L}$. From this vector we construct $\Psi_{(a_1,\sigma_2),(\sigma_3...\sigma_L)} \equiv c_{a_1,\sigma_2,...,\sigma_L}$. We reshape the matrix U into a row vector A^{σ_1}, with $A^{\sigma_1}_{a_1} = U_{\sigma_1,a_1}$. After these operations we have

$$c_{\sigma_1,...,\sigma_L} = \sum_{a_1} A^{\sigma_1}_{a_1} \Psi_{(a_1\sigma_2),(\sigma_3...\sigma_L)}. \qquad (3.9)$$

Successively performing these steps, SVD and reshaping, we obtain

$$\begin{aligned}
c_{\sigma_1,...,\sigma_L} &= \sum_{a_1}\sum_{a_2} A^{\sigma_1}_{a_1} U_{(a_1\sigma_2),a_2} S_{a_2,a_2} V^\dagger_{a_2,(\sigma_3...\sigma_L)} \qquad (3.10)\\
&= \sum_{a_1}\sum_{a_2} A^{\sigma_1}_{a_1} A^{\sigma_2}_{a_1,a_2} \Psi_{(a_2\sigma_3),(\sigma_4...\sigma_L)} = ...\\
&= \sum_{a_1..a_{L-1}} A^{\sigma_1}_{a_1} A^{\sigma_2}_{a_1,a_2}...A^{\sigma_{L-1}}_{a_{L-2},a_{L-1}} A^{\sigma_L}_{a_{L-1}}\\
&= A^{\sigma_1} A^{\sigma_2}...A^{\sigma_L},
\end{aligned}$$

where A^{σ_j} is a matrix with the elements $A^{\sigma_j}_{a_{j-1},a_j} = U_{(a_{j-1}\sigma_j),a_j}$. The maximum dimensions that the collection of A-matrices can have are $(1 \times d), (d \times d^2), ..., (d^{L/2-1} \times d^{L/2}), (d^{L/2} \times d^{L/2-1}), ..., (d \times 1)$. We refer to the dimensions of these matrices, which are determined by the number of non-zero singular values in the SVD, as the bond dimension. The maximum bond dimensions are reached if in each of the singular value decompositions all singular values are non-zero. Inserting this result in Eq. (3.7), the new representation of the state reads

$$|\Psi\rangle = \sum_{\sigma_1,...,\sigma_L} A^{\sigma_1} A^{\sigma_2}...A^{\sigma_L} |\sigma_1, ..., \sigma_L\rangle, \qquad (3.11)$$

with the left normalized matrices $\sum_{\sigma_j} A^{\sigma_j\dagger} A^{\sigma_j} = \mathbb{1}$. We depict a MPS in this representation graphically as in Fig. 3.1(d).

In an analogue way, one can define a right-canonical matrix product state, by starting the
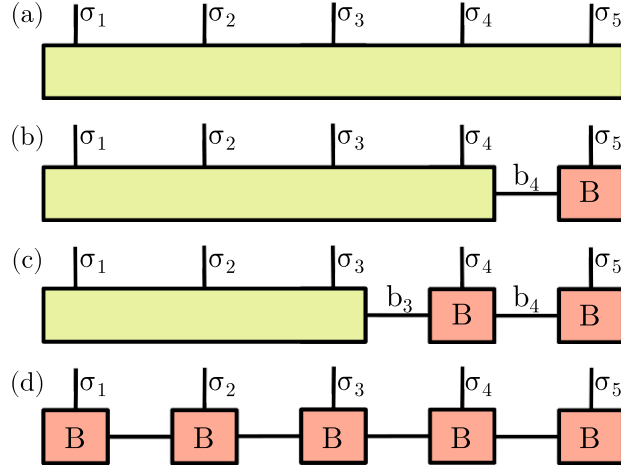
Figure 3.2: Construction of a right-canonical matrix product state by iterative appliations of the singular value decomposition (SVD), see Eq. (3.12).
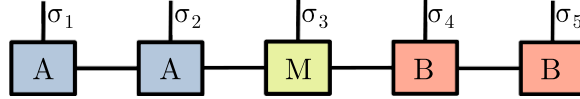
Figure 3.3: The graphical representation of the mixed canonical matrix product state, see Eq. (3.14).

reshaping procedure from the right (see Fig. 3.2)

$$
\begin{aligned}
c_{\sigma_1,\ldots,\sigma_L} &= \Psi_{(\sigma_1\ldots\sigma_{L-1}),\sigma_L,} = \ldots \\
&= \sum_{a_{L-1}} U_{(\sigma_1\ldots\sigma_{L-1}),a_{L-1}} S_{a_{L-1},a_{L-1}} V^\dagger_{a_{L-1}\sigma_L} \\
&= \sum_{a_{L-1}} \Psi_{(\sigma_1\ldots\sigma_{L-2}),(\sigma_{L-1}a_{L-1})} B^{\sigma_L}_{a_{L-1}} = \ldots \\
&= \sum_{a_1..a_{L-1}} B^{\sigma_1}_{a_1} B^{\sigma_2}_{a_1,a_2} \ldots B^{\sigma_{L-1}}_{a_{L-2},a_{L-1}} B^{\sigma_L}_{a_{L-1}} \\
&= B^{\sigma_1} B^{\sigma_2} \ldots B^{\sigma_L},
\end{aligned}
\tag{3.12}
$$

where B^{σ_j} is a matrix with the elements $B^{\sigma_j}_{a_{j-1},a_j} = V^\dagger_{a_{j-1},(\sigma_j a_j)}$. In this case the state becomes the right-canonical matrix product state

$$
|\Psi\rangle = \sum_{\sigma_1,\ldots,\sigma_L} B^{\sigma_1} B^{\sigma_2} \ldots B^{\sigma_L} |\sigma_1,\ldots,\sigma_L\rangle,
\tag{3.13}
$$

with the right normalized matrices $\sum_{\sigma_j} B^{\sigma_j} B^{\sigma_j\dagger} = \mathbb{1}$.

We can also perform a mixed decomposition from both right and left, resulting in a mixed

canonical product state

$$|\Psi\rangle = \sum_{\sigma_1,...,\sigma_L} A^{\sigma_1}...A^{\sigma_l} S B^{\sigma_{l+1}}...B^{\sigma_L} |\sigma_1,...,\sigma_L\rangle \qquad (3.14)$$

$$= \sum_{\sigma_1,...,\sigma_L} A^{\sigma_1}...A^{\sigma_{l-1}} M^{\sigma_l} B^{\sigma_{l+1}}...B^{\sigma_L} |\sigma_1,...,\sigma_L\rangle,$$

where the A matrices are left-normalized and the B matrices are right-normalized. The S matrix has the components $S_{a_l,a_l} = \sqrt{\lambda_{a_l}}$, which represent the singular values on the bond l. The mixed canonical product state is equivalent to the Schmidt decomposition of a system of length L divided into a subsystem A from site 1 to l and a subsystem B from site $l+1$ to L. We can multiply the S matrix with the matrix A^{σ_l}, obtaining a tensor, M^{σ_l}, which is not normalised on site l, representing the orthogonality center, see Fig. 3.3.

The matrices involved in the representations of a MPS can be, in principle, exponentially large, as their maximal dimension scales as $d^{L/2}$, thus their size has to be truncated in order to be feasible to perform numerical operations on them. When the singular values decay fast enough, we can perform a compression step during the SVD, by employing a cutoff D in the number of singular values kept and obtain a state that approximates $|\Psi\rangle$ the best, as in Eq. (3.5). This step can be applied iteratively for the SVDs performed at each bond $l = 1..L-1$, the error accumulated at each truncation step is given by Eq. (3.5). Thus, a MPS is characterized by the bond dimensions used for each matrix. In practice, we monitor the maximal bond dimension used in the MPS.

Now we can represent our state as a MPS, in the next step we need to see how we can apply an operator on a MPS. In this respect, we can construct matrix product operators (MPO), analogue to the procedure presented above [124].

$$\hat{O} = \sum_{\vec{\sigma},\vec{\sigma}'} c_{(\sigma_1,...,\sigma_L),(\sigma_1',...,\sigma_L')} |\vec{\sigma}\rangle\langle\vec{\sigma}'|, \qquad (3.15)$$

$$= \sum_{\vec{\sigma},\vec{\sigma}'} W^{\sigma_1,\sigma_1'}...W^{\sigma_L,\sigma_L'} |\vec{\sigma}\rangle\langle\vec{\sigma}'|,$$

where the matrices $W^{\sigma,\sigma'}$ are analogous to the matrices M^{σ}, but with two physical indices, which represent the outgoing and ingoing states.
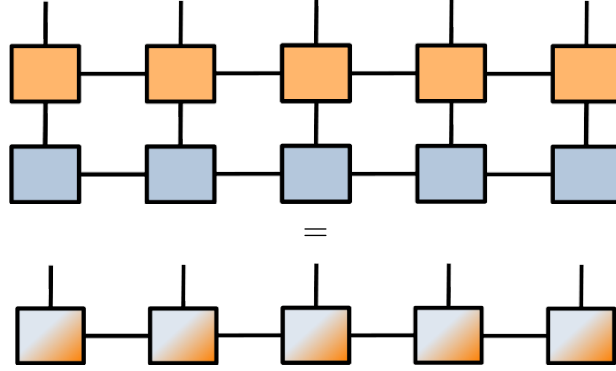
Figure 3.4: Application of a matrix product operator (MPO), to a matrix product state (MPS), as expressed in Eq. (3.16).
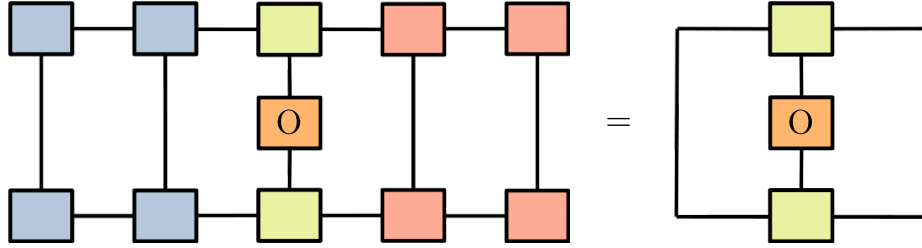
Figure 3.5: Measurement of a local observable for an MPS in the mixed-canonical representation. The blue (red) circles mark left (right) normalised tensors, while the central green tensor is *not* normalised.

When we act with a MPO onto a MPS we obtain

$$\hat{O}|\Psi\rangle = \sum_{\vec{\sigma},\vec{\sigma}'} W^{\sigma_1,\sigma_1'}...W^{\sigma_L,\sigma_L'}|\vec{\sigma}\rangle\langle\vec{\sigma}'\left(\sum_{\vec{\sigma}''} M^{\sigma_1''}...M^{\sigma_L''}|\vec{\sigma}''\rangle\right), \tag{3.16}$$

$$= \sum_{\vec{\sigma},\vec{\sigma}'} W^{\sigma_1,\sigma_1'}...W^{\sigma_L,\sigma_L'}M^{\sigma_1'}...M^{\sigma_L'}|\vec{\sigma}\rangle,$$

$$= \sum_{\vec{\sigma}}\left(\sum_{\sigma_1'} W^{\sigma_1,\sigma_1'}M^{\sigma_1'}\right)...\left(\sum_{\sigma_L'} W^{\sigma_L,\sigma_L'}M^{\sigma_L'}\right)|\vec{\sigma}\rangle,$$

$$= \sum_{\vec{\sigma}} N^{\sigma_1}...N^{\sigma_L}|\vec{\sigma}\rangle,$$

with $N^{\sigma_j}_{(b_{j-1}a_{j-1}'),(b_j a_j')} = \sum_{\sigma_j} W^{\sigma_j,\sigma_j'}_{b_{j-1},b_j} M^{\sigma_j'}_{a_{j-1}',a_j'}$ a matrix, such that the result is also a matrix product state. This is graphically depicted in Fig. 3.4. Note that the dimensions of the new matrices N are larger than the dimensions of the matrices M, such that we need to perform an additional step of SVD truncations if we want to revert the MPS to the initial bond dimensions.

In order to compute expectation values we also need to act with the adjoint to the MPS after we contract the MPS and MPO. The adjoint MPS is generically depicted graphically as a MPS for
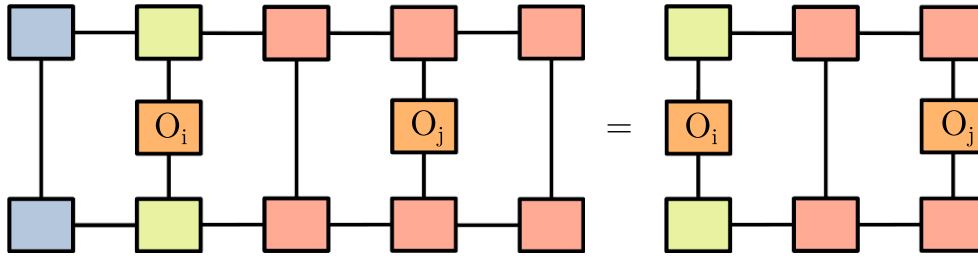
Figure 3.6: Measurement of a non-local two-point correlator in a mixed-canonical representation. The blue (red) circles mark left (right) normalised tensors.

which the physical indices are pointing in the opposite direction (as seen in Fig. 3.5 and Fig. 3.6). If the observable of interest is local, or has a limited extend, further simplifications can occur by employing the normalization properties of the different MPS representations. For example, for a local operator, as seen in Fig. 3.5 we use a mixed canonical representation [see Eq. (3.14)], where the tensor corresponding to the site on which we act with the operator is not normalized and the tensors to the left (right) are left (right) normalized. Due to the normalization conditions the contractions to the left (right) give identities and we are left only with the tensor contractions between the single site MPO and the tensors of the MPS of the same site. In the same way, for a two-point correlator we only need to consider the tensors starting from the first site on which the MPO acts and the last site, as seen in Fig. 3.6.
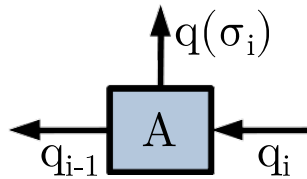
Figure 3.7: The convention used for the labels of the MPS tensors for keeping track of the quantum numbers.

Before describing the different algorithms for which we can use the MPS representation, we comment on how quantum numbers can be implemented in the structure of a MPS [139]. In the models considered in this work we deal with abelian quantum numbers. In order to keep track of the different quantum numbers, in our implementation we label our tensors with two additional labels, an incoming and outgoing one, as sketched in Fig. 3.7. Each index has a quantum number assigned and with the arrows we indicate the 'flow' of the quantum numbers. The local state on site i will change the incoming quantum number q_i by an amount $q(\sigma_i)$. Such that the arithmetic for abelian quantum numbers reduces to the local quantum number fusion rule $q_i - q(\sigma_i) = q_{i-1}$, relating the incoming and outgoing labels. Initializing the first quantum number, by convention, to $q_0 = 0$, the value of the final outgoing quantum number, q_L, will identify the considered symmetry sector. Using this procedure one can observe that the non-trivial entries in the tensors are organized in a block structure. This block structure can greatly reduce the numerical costs of the tensor operations for large tensors, which we need to perform in the algorithms that we will describe in the following.

3.1.2 Ground state search

In this section we discuss how one can use the MPS formalism in order to find the ground state of a quantum system described by a Hamiltonian, H [124]. A first question that one could raise in this regard is to ask why one should expect that a MPS is an efficient representation of a ground state. This stems from the fact that the ground states of gapped Hamiltonians with local interaction obey an entanglement area law [140]. Which implies that the entanglement entropy between two subsystems, upon a bipartition of the system, only depends on the area of the boundary, and not on the volume of the total system. For a one-dimensional system this gives that the entanglement entropy is bounded by a constant. As the entanglement is directly related to the bond dimension of the MPS, it has been shown that such low-entangled states can be efficiently represented as a MPS and the bond dimension only grows polynomially with the system size [125, 141]. In practice, one uses the MPS representation to search for the ground state also of gapless Hamiltonian, but in this cases a larger bond dimension may be needed and more attention has to be payed regarding the convergence of the algorithm.

In the following, we describe the MPS formulation of the density matrix renormalization group (DMRG) method [124]. This method has been introduced by S. R. White in 1992 for the study of the static properties of one-dimensional quantum system and was originally formulated as a variational, iterative algorithm using density matrices [129].

In order to find the ground state of the system we have to minimize the energy, given by the expectation value of the Hamiltonian, with respect to the wave function used

$$E_{\mathrm{gs}} = \min \frac{\langle \Psi | H | \Psi \rangle}{\langle \Psi | \Psi \rangle}. \tag{3.17}$$

We solve this by minimizing the following quantity

$$\langle \Psi | H | \Psi \rangle - \lambda \langle \Psi | \Psi \rangle, \tag{3.18}$$

where we have introduced the Lagrange multiplier λ. At the end of the optimization procedure $|\Psi\rangle$ will approximate the ground state wave function and λ the ground state energy. This is a very non-trivial problem, as one has to find the optimal value for all entries of the tensors of the MPS, which appear in a non-linear fashion in the quantity we want to minimize. In order to address this, we iteratively optimize one matrix M^{σ_j} at a time, while keeping all other M^{σ_i}, $i \neq j$, fixed. Afterwards, we move to the next site, 'sweeping' through the entire system. If the accuracy goal is not reached after optimizing the matrices at the edge of the system, M^{σ_L}, i.e. after performing one sweep, one performs another sweep optimizing again all the matrices, until the error goal is reached. In this work, the error goal is a 10^{-8} difference in the energy between two consecutive sweeps. Each local update is performed by constructing an effective eigenvalue equation
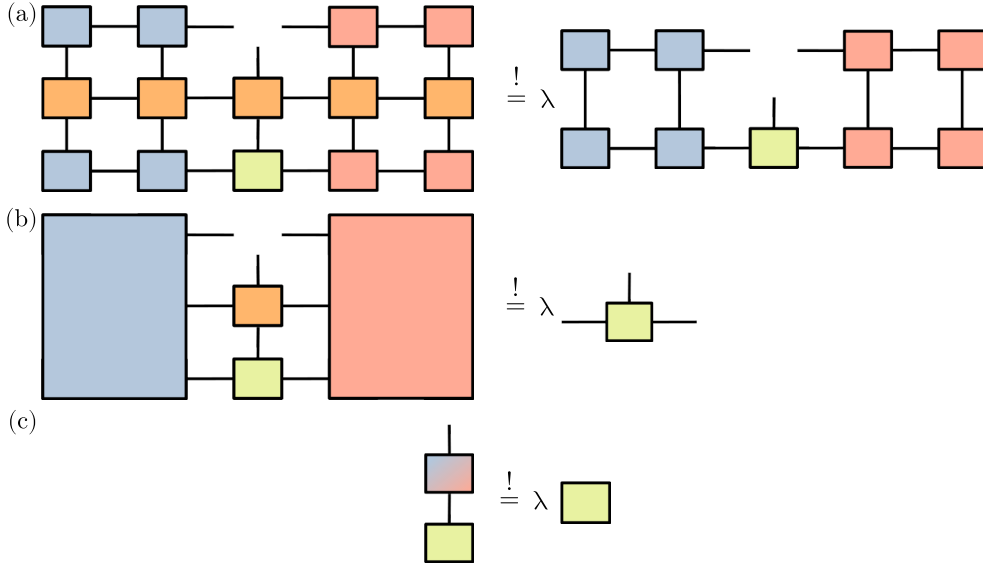
Figure 3.8: Graphical representation of the ground state search algorithm with single site optimisation. The method which reduces to an effective eigenvalue problem. (a) The original optimisation problem of Eq. (3.19). (b) Constructing the left and right tensors (L and R in blue and red respectively), using the normalisation conditions of left- (blue) and right-canonical (red) tensors, Eq. (3.20). (c) Reshaping the tensor $M^{\sigma_l}_{a_{l-1},a_l}$ into a vector $\mathbf{v} = M_{\sigma_l,a_{l-1},a_l}$ and rewriting the optimisation into an effective eigenvalue problem $H_{eff}\mathbf{v} = \lambda\mathbf{v}$, Eqs. (3.21) and (3.22).

$$\frac{\partial\langle\Psi|H|\Psi\rangle}{\partial M^{\sigma_l*}_{a_{l-1},a_l}} \overset{!}{=} \lambda\frac{\partial\langle\Psi|\Psi\rangle}{\partial M^{\sigma_l*}_{a_{l-1},a_l}}, \tag{3.19}$$

$$\sum_{\sigma_l'}\sum_{a_{l-1}',a_l'}\sum_{b_{l-1},b_l} L^{a_{l-1},a_{l-1}'}_{b_{l-1}} W^{\sigma_l,\sigma_l'}_{b_{l-1},b_l} R^{a_l,a_l'}_{b_l} M^{\sigma_l'}_{a_{l-1}',a_l'} = \lambda M^{\sigma_l}_{a_{l-1},a_l}, \tag{3.20}$$

$$\sum_{\sigma_l'}\sum_{a_{l-1}',a_l'} H^{\text{eff}}_{(\sigma_l,a_{l-1},a_l),(\sigma_l',a_{l-1}',a_l')} M_{\sigma_l',a_{l-1}',a_l'} = \lambda M_{\sigma_l,a_{l-1},a_l}, \tag{3.21}$$

$$H^{\text{eff}}\mathbf{v} = \lambda\mathbf{v}, \tag{3.22}$$

where $\mathbf{v}$ is the vector representation of M_{σ_l,a_{l-1},a_l}. The steps described above can be graphically depicted as in Fig. 3.8. In Fig. 3.8(b) we have defined the left, L, and right, R, tensors in blue and red. H_{eff} contains both the details of the original Hamiltonian in MPO form and all the MPS sites excluding site l. At this point we estimate the ground state energy with the lowest eigenvalue obtained from Eq. (3.22) and we update the local tensor $M^{\sigma_l}_{a_{l-1},a_l}$ with the corresponding eigenvector. As the dimensions of the matrices in the eigenvalue problem are, typically, too large for exact diagonalization, an iterative eigensolver that aims for the lowest eigenvalue is used. We note that the dimension of the effective Hamiltonian is $dD^2 \times dD^2$

One problem with this approach is the fact that one cannot change the bond dimension

during the sweeps. Thus, one has to choose an initial MPS with a sufficiently large bond dimension, which makes the single-site algorithm prone to getting stuck in local minima [124]. This can be remedied by performing a two-site optimization, meaning that we now iteratively optimize two matrices $M^{\sigma_l} M^{\sigma_{l+1}}$. In this case the dimension of H_{eff} is increased to $d^2 D^2 \times d^2 D^2$. This implies that the dimension of the bond l is increased up to dD, which we can truncate up to the desired new bond dimension. Thus, the advantage of the two-site algorithm is that the bond dimension can grow during the sweeps and can explore a higher-dimensional manifold of MPS states, making it less likely to get stuck in local minimum. In this work, we have used the two-site algorithm for computing ground states.

3.1.3 Time-dependent matrix product state method (tMPS)
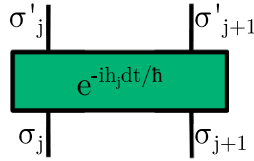
Figure 3.9: Time evolution gate, representing the bond evolution operator $e^{-iH\mathrm{d}t/\hbar}$, where the bond Hamiltonian h_j acts on sites $(j, j+1)$.

In this section, we are interested in performing the time evolution, $e^{-iHt/\hbar}$, starting from a given initial state, in the MPS representation. The time evolution is performed using the time-dependent matrix product state (tMPS) approach [124, 133–135]. This method is suitable for Hamiltonians with short range interactions, as we employ the Trotter-Suzuki decomposition [142–144] in order to decompose the time evolution operator $e^{-iHt/\hbar}$ into operations that act on just a few sites at a time.

In the following, we consider a Hamiltonian which couples only nearest neighboring sites, such that we can write our Hamiltonian as a sum over bond terms h_j acting on sites $(j, j+1)$

$$H = \sum_j h_j. \tag{3.23}$$

The first step is to discretise the time as $t = N_t \mathrm{d}t$, where N_t is the number of time steps required to evolve the system up to final time t, this evolution being described by the propagator

$$U(t) = e^{-iHt/\hbar} = \left(e^{-iH\mathrm{d}t/\hbar}\right)^{N_t}. \tag{3.24}$$

The second order Trotter-Suzuki decomposition for a single time step reads

$$U(\mathrm{d}t) = \prod_{j=1}^{L-1} e^{-ih_j \mathrm{d}t/2\hbar} \prod_{j=L-1}^{1} e^{-ih_j \mathrm{d}t/2\hbar} + \mathcal{O}\left(L\mathrm{d}t^3\right). \tag{3.25}$$

We note that different decompositions with the same order of the error are possible. We have reduced the procedure of performing a time step to the successive application of operators which
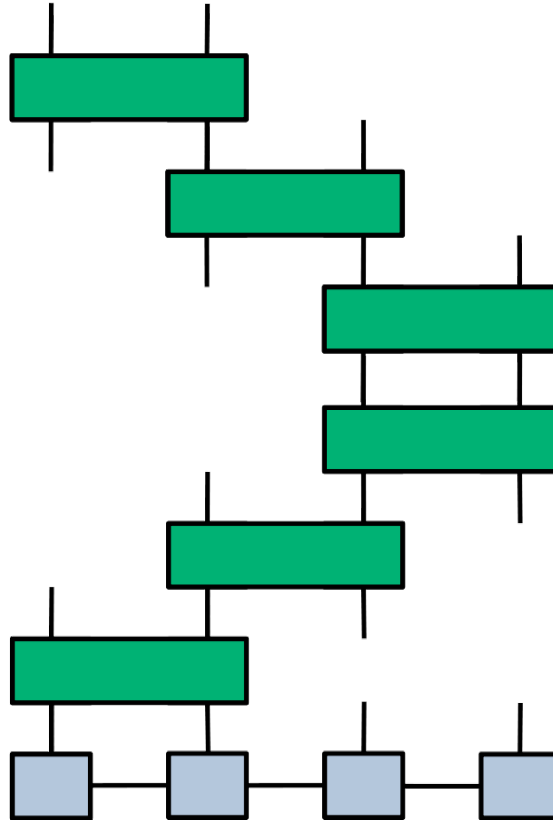
Figure 3.10: The full evolution for one time step $U(\mathrm{d}t)$ decomposed into two-site gates, for a second order Trotter-Suzuki decomposition.

act only on two adjacent site in our MPS representation, $e^{-ih_j \mathrm{d}t/2\hbar}$, which can be graphically represented as a two site gate as seen in Fig. 3.9. The full procedure of performing a single time step is depicted in Fig. 3.10. After the application of a single two site gate onto the MPS a SVD is performed in order to recast our state in the MPS form and to compress the state back to the desired bond dimension.

We can observe that the order of the error necessary to reach a time t is given by $\mathcal{O}(L\mathrm{d}t^2)$, so naively we could think that by decreasing time step we would reduce the error. However, this implies more gate applications, which results in more compression steps. Thus, one needs to pay attention to the nontrivial interplay of the two error sources, due to the finite time step and the truncation error, in order to determine the convergence of the method. Furthermore, the needed bond dimension scales exponentially with the von Neumann entropy, $D \sim \exp[S_{\mathrm{vN}}(t)]$, [145], which is restricted by the Lieb-Robinson bound to a maximally linear growth in time for local Hamiltonians [146, 147]. This implies that a MPS of a certain bond dimension D can accurately capture the time evolution only up to a certain time.

3.2 Time-dependent matrix product state (tMPS) method for combined atom-cavity systems

In this section, we describe a novel numerical exact method based on matrix product states (MPS). We developed this method to perform the quantum time evolution of the coupled cavity-atoms system described in Sec. 2.1 and it is one of the main methodological developments presented in this thesis. However, the method is very generally applicable to other many-body systems globally coupled to a dissipative bosonic mode. We follow the description of the method as we presented it in Ref. [109].

3.2.1 Details of the tMPS method for the coupled photon-atom system

In the following, we want to consider the dissipative system of atoms coupled to an optical cavity described in Sec. 2.1. This is posing several challenges for its treatment via MPS based methods. The first difficulty is due to the global coupling of the cavity mode to the interacting atoms. The second stems from the arbitrarily large dimension of the Hilbert space of the cavity field. The third challenge is the dissipative nature of the system due to the photon losses. We present in the following how our implementation overcomes all these difficulties [109]. We implement the newly developed algorithm efficiently using the ITensor library [139].

We start by describing how we deal with the dissipative aspect of the considered models in the tMPS method [64]. For the numerical simulation of a dissipative many body quantum system we need to determine the time-evolution of the density matrix given by the Lindblad equation (see Sec. 2.1). State of the art in this regard are two different routes: the first is the stochastic unraveling of the master equation using quantum trajectories [148, 149]. This approach has the advantage of simulating the time-evolution of wavefunctions instead of density matrices at the disadvantage of a stochastic sampling. The second is the purification approach which relies on the rewriting of the density matrix as a MPS with a larger dimension [150, 151].

In this work, we have implemented the stochastic unraveling of the master equation approach [109]. We note that this decision was motivated in particular by two reasons: First, already the representation of the interacting ground state of the bosonic atoms as initial state in the purification approach would have been demanding. Secondly, the additional presence of the large Hilbert space of the photons would result in an increasing in the required matrix dimensions. We take good quantum numbers into account for the atoms in our implementation of the stochastic unraveling approach, by noting that our system preserves the total number of atoms (see Sec. 2.1). So far, few efficient combinations of the stochastic unraveling of the master equation with the matrix product state methods which take conserved quantum numbers into account have been realized (see e.g. Refs. [109, 152–158]).

In the stochastic unraveling procedure, one samples the time-evolution of many quantum trajectories consisting of pure states and, in the end, the results are averaged. The probability weights in the initial density matrix determine the initial states for the trajectories. The stochastic time-evolution which is performed for each quantum trajectory is described in the following:

- A random number η is drawn from the interval $[0, 1)$.
- For each trajectory, the time evolution is performed for a time step with a non-unitary

time evolution operator, corresponding to the effective Hamiltonian,

$$\tilde{H} = H - \frac{i}{2}\hbar\Gamma a^\dagger a, \tag{3.26}$$

(see Sec. 2.1, Eq. (2.16), for full expression of H).

- Since the effective Hamiltonian is not Hermitian, this leads to a decay of the norm of the state in time. The non-unitary deterministic time evolution is performed until the norm is smaller than a threshold posed by the random number η.

- A quantum jump is performed by applying the jump operator onto the wavefunction, after which the state is normalized. In the considered case, the jump operator is the annihilation operator of the cavity field, a.

- The described procedure is repeated until the required final time is reached.

It can be shown [148, 149] that taking the Monte Carlo average over all sampled quantum trajectories the obtained time evolution is reproducing the Lindblad dynamics correctly up to the first order in the chosen time step. Many trajectories are required in order to achieve convergence in this method and, furthermore, the time step has to be chosen in such a way that it is small enough, in order to avoid multiple jumps within one time step. In our case, because the jump operator only acts on the photonic space, we need to sample several hundred trajectories, as we discuss in the Sec. 3.2.2.

In the next step, we want to perform the time evolution of one such quantum trajectory [109]. We perform the time evolution of the wave function within the MPS formalism, by representing it as a MPS [124]. We choose in the MPS representation the first site to be initially corresponding to the cavity mode and the rest to the atomic lattice using a Fock basis for each site (see Fig. 3.11). We deal with the Hilbert space of the photonic mode, which can be in principle arbitrarily large, by introducing a cutoff for its dimension. We dynamically adapt the local Hilbert space of the photonic site during the time evolution. This is done by setting a truncation goal of the photonic distribution, the details are given in Sec. 3.2.5. In order to benchmark our results we also present results in which a fixed dimension of the photonic Hilbert space is used.

Because the cavity mode is globally coupled to all the atomic sites, we cannot make the use of the tMPS implementation for short-range Hamiltonians based on the Trotter-Suzuki decomposition as it was described in Sec. 3.1.3. Thus, we develop a variant of the tMPS [109] which can tackle both the global coupling between photons and atoms and the short range interaction of the atoms into account, it is based on the dynamical deformation of the MPS structure. The dynamical deformation allows one to alter the order of the sites in the MPS representation as needed using swap gates [124, 155, 159]. MPS time evolution with swap gates has been used previously to deal with short-range interaction in two dimensional models [159], or spin-boson models [155, 160]. In contrast, our implementation can efficiently deal with interacting bosonic models globally coupled to the dissipative photonic field [109]. Based on this implementation one can adapt it for fermionic and spin systems coupled to photonic, or phononic, modes in a straightforward manner.

In the following, we describe our procedure for performing a time step dt with the effective
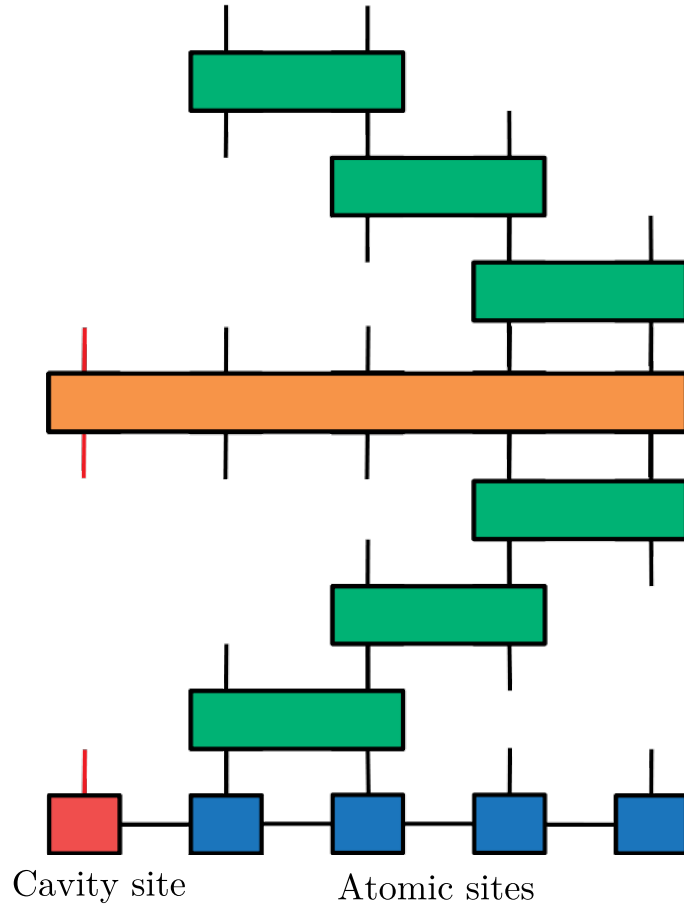
Figure 3.11: The graphical representation of one time step based on the Trotter-Suzuki decomposition described in Eq. (3.27). The first (red) site in the graphical representation of the MPS structure corresponds to the cavity mode and the rest to the atomic sites. To be noted that the cavity mode index marked with a red line has a large local dimension. Green boxes represent the application of the two site gates of the atomic terms of the time-evolution after Trotter-Suzuki decomposition followed by an SVD compression step. With orange we depict the large tensor corresponding to the time evolution of the cavity and cavity-atoms coupling terms of the Hamiltonian. Its application is detailed in Fig. 3.13. ©2020 American Physical Society, published in [109].

Hamiltonian, $\tilde{H}$, Eq. (3.26). This is based on the Trotter-Suzuki decomposition of the time evolution propagator in combination with swap gates. We split the terms in order to separate the contributions containing the cavity field operators and the remaining terms

$$e^{-\frac{i\mathrm{d}t}{\hbar}\tilde{H}} \approx \tag{3.27}$$
$$e^{-\frac{i\mathrm{d}t}{2\hbar}(H_{\mathrm{kin}}+H_{\mathrm{int}})}e^{-\frac{i\mathrm{d}t}{\hbar}\left(H_{\mathrm{ac}}+H_{\mathrm{c}}-\frac{i}{2}\hbar\Gamma a^{\dagger}a\right)}e^{-\frac{i\mathrm{d}t}{2\hbar}(H_{\mathrm{kin}}+H_{\mathrm{int}})}.$$

This decomposition is valid to the order $\mathcal{O}(\mathrm{d}t^3)$ in the time step. The evolution given by the operator $e^{-\frac{i\mathrm{d}t}{2\hbar}(H_{\mathrm{kin}}+H_{\mathrm{int}})}$ which only contains the atomic operators is computed as in the standard
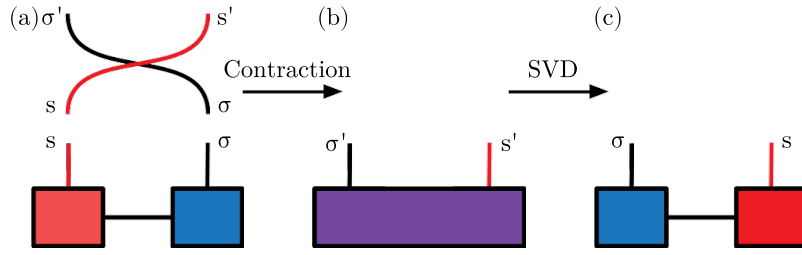
Figure 3.12: The graphical representation of the application of the swap gate procedure: (a) The two site MPS with the physical indices s, corresponding to the cavity site, and σ, corresponding to the atomic site, and the swap gate with the indices (s, σ, σ', s'). (b) The application of the swap gate onto the MPS by contracting the indices s, σ and the MPS bond index. (c) Restoring the MPS structure by performing a SVD and renaming the indices $\sigma' \to \sigma$ and $s' \to s$. ©2020 American Physical Society, published in [109].
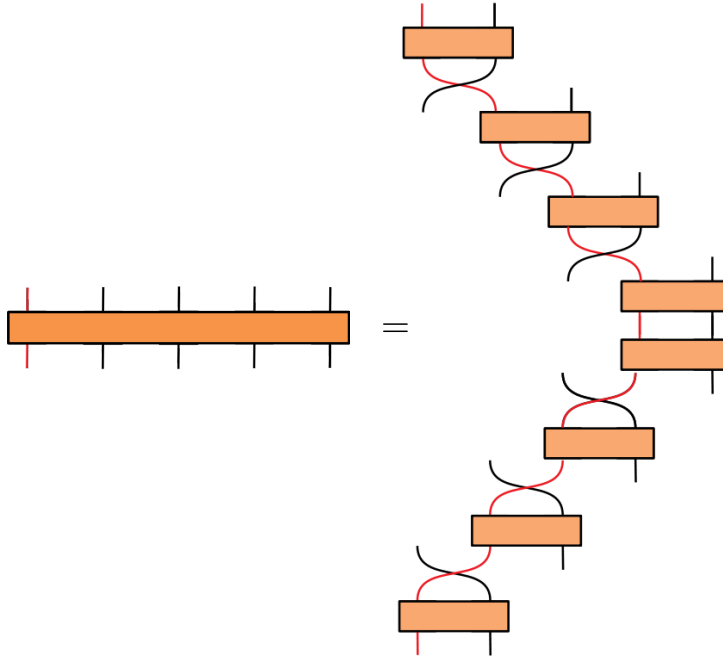
Figure 3.13: The graphical representation of application of the Trotter-Suzuki decomposition of the terms containing the cavity field, Eq. (3.28). Swap gates are needed to bring the initially distant sites close to each other. ©2020 American Physical Society, published in [109].

tMPS algorithm for short-range interactions [133, 134] by a further decomposition into two site gates (see Sec. 3.1.3). The two site gates are applied to the MPS followed by a compression step via a singular value decomposition (SVD) in the order sketched in Fig. 3.11.

For the operator which contains the global coupling to the cavity field, $e^{-\frac{idt}{\hbar}\left(H_{\mathrm{ac}}+H_{\mathrm{c}}-\frac{i}{2}\hbar\Gamma a^\dagger a\right)}$, we make use of the fact that we can decompose H_{ac} such that each term only acts on two sites

−even though distant ones−

$$e^{-\frac{idt}{\hbar}\left(H_{\mathrm{ac}}+H_{\mathrm{c}}-\frac{i}{2}\hbar\Gamma a^\dagger a\right)} = \tag{3.28}$$

$$= \prod_{j=L}^{1} e^{-\frac{idt}{2}\left\{-\Omega(a+a^\dagger)(-1)^j n_j+\frac{1}{L}\left(\delta-\frac{i}{2}\Gamma\right)a^\dagger a\right\}} \times$$

$$\prod_{j=1}^{L} e^{-\frac{idt}{2}\left\{-\Omega(a+a^\dagger)(-1)^j n_j+\frac{1}{L}\left(\delta-\frac{i}{2}\Gamma\right)a^\dagger a\right\}} + \mathcal{O}(Ldt^3).$$

Meaning that we need to apply two-site operators where the two sites are not neighbors in the initial MPS representation. In order to overcome this problem, we modify the structure of the MPS while applying the time evolution gates in such a way that the two sites on which the operator acts are brought together. This approach is implemented using swap gates, the action of the swap gates consists in the swapping of the physical indices of two neighboring MPS matrices, i.e.

$$S_{s,\sigma_i}\left(M^{\sigma_1}...M^s M^{\sigma_i}...M^{\sigma_L}\right) \tag{3.29}$$
$$= M^{\sigma_1}...(MM)^{\sigma_i,s}...M^{\sigma_L}$$
$$= M^{\sigma_1}...M^{\sigma_i} M^s...M^{\sigma_L}.$$

Here S_{s,σ_i} is the swap operator and the state $|\sigma_1,...,s,\sigma_i,...,\sigma_L\rangle$ has a weight $M^{\sigma_1}...M^s M^{\sigma_i}...M^{\sigma_L}$ in the MPS form with s the index of the cavity mode site and σ_i the index for the bosonic atoms. In Fig. 3.12 we sketch how the swap gate acts on two MPS sites and changes their order. The swap gates are constructed from two Kronecker delta functions, each between indices of the same nature, but different sites, i.e. in Fig. 3.12(a) we have a Kronecker delta from the cavity index s at the first site to the cavity index s' at the second site (red curve) and a Kronecker delta from the atomic index σ at the second site to the atomic index σ' at the first site. The next step is the application of the swap gate onto the MPS wavefunction and obtaining a two-site tensor with swapped indices [Fig. 3.12(b)]. Finally a SVD decomposition is performed to restore the MPS structure. Thus, using the swap gates we can apply the operator $e^{-\frac{idt}{\hbar}\left(H_{\mathrm{ac}}+H_{\mathrm{c}}-\frac{i}{2}\hbar\Gamma a^\dagger a\right)}$ onto the wavefunction as a series of two-site gates, as depicted in Fig. 3.13. No additional error is introduced by the application of a swap gate, except the SVD truncation error.

As we described all steps out of which our time evolution method consists, we can now evaluate the order of the errors involved. The implemented method has an error of the order $\mathcal{O}(Ldt^2)$ at a certain final time t, stemming from the Trotter-Suzuki decomposition. However, the stochastic unraveling is only valid up to first order to dt, such that we expect that this further limits the choice of the time step.

3.2.2 Numerical convergence

In this section, we discuss the convergence of the numerical method, which is controlled by several parameters [109]. Firstly, the stochastic unraveling of the master equation with quantum trajectories requires an averaging of a sufficiently large number of trajectories. Addition-
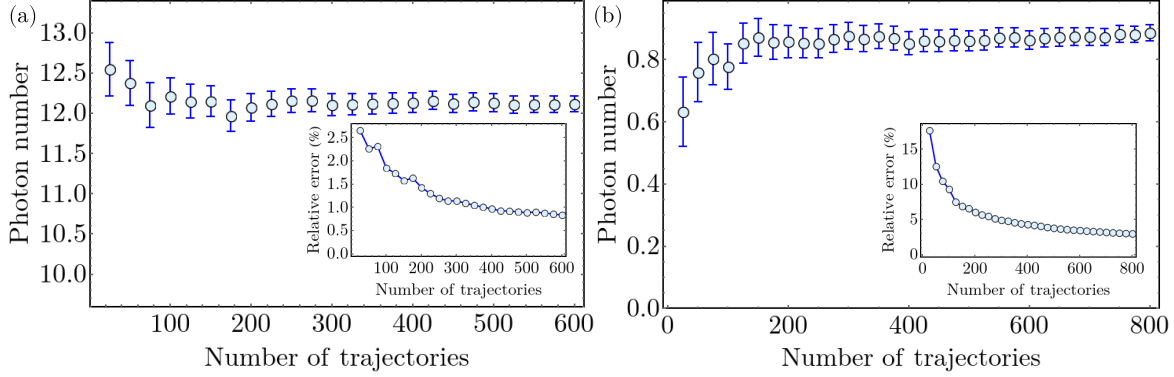
Figure 3.14: The dependence of the Monte Carlo average of the photon number as a function of the number of quantum trajectories sampled. We present the behavior for two parameter sets, $L = 10$, $N = 5$, $\hbar\delta/J = 2$, $U/J = 2$, the truncation error is $\epsilon = 10^{-12}$, (a) $\hbar\Omega\sqrt{N}/J = 3.35$, $\hbar\Gamma/J = 1$, $\mathrm{d}tJ/\hbar = 0.0125$ and (b) $\hbar\Omega\sqrt{N}/J = 4.47$, $\hbar\Gamma/J = 10$, $\mathrm{d}tJ/\hbar = 0.01$. The error bars represent the standard deviation of the mean of the Monte Carlo average and in the insets we represent the relative error as a function of the number of trajectories.

ally, the time step $\mathrm{d}t$ must be chosen small enough in order to avoid the occurrence of multiple jumps in one time step. Secondly, a different source of error comes from the Trotter-Suzuki decomposition of the time evolution operator. This also requires that the time-step $\mathrm{d}t$ is small enough. Finally, we introduce an additional error by representing our wave functions as a MPS with finite local and bond dimensions. This implies a cut-off, N_{pho}, of the local Hilbert space of the photons and in some situations also for the bosonic atoms. The procedure to dynamically adjust the cut-off, N_{pho}, will be presented in Sec. 3.2.5. Additionally, the introduction of the finite bond dimension in the MPS representation, using SVD, leads to the so-called truncation error. To control the bond dimension of the MPS we impose a truncation error goal ϵ, thus, in each compression step, after the application of a time evolution or swap gate onto the MPS, the number of states kept is such that the truncation error is smaller than ϵ. We note that as in the case of the time-dependent MPS [133, 134], the arising errors are not independent and therefore, a careful analysis needs to be performed.

In the following, we give the typical values of the convergence parameters and analyze their influence on the results. The discussion of the truncation error and the von Neumann entanglement of the trajectories is presented in Sec. 3.2.3. We note that the values of the physical parameters correspond to the model presented in Sec. 2.1 and are closely related to the ones used in Chap. 5 and Chap. 6.

Stochastic error: We want to estimate the error of having a finite number of quantum trajectories included in the Monte Carlo average, for this we compute the standard deviation of the mean for the measured expectation value of an operator $\mathcal{E}$

$$\sigma\left(\mathcal{E}(t)\right) = \sqrt{\frac{1}{R(R-1)} \sum_{r=1}^{R} \left(\langle\psi_r(t)|\mathcal{E}|\psi_r(t)\rangle - \langle\langle\mathcal{E}\rangle\rangle\right)^2}, \tag{3.30}$$
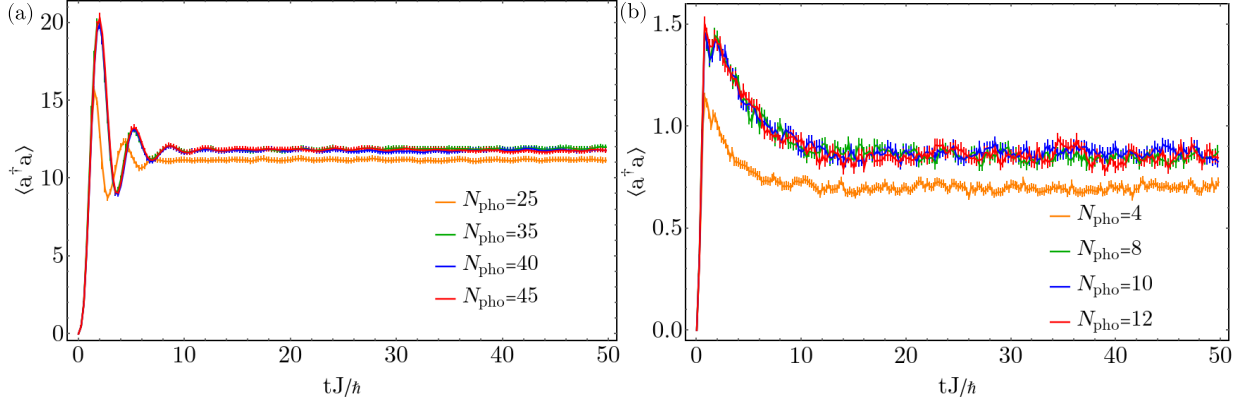
Figure 3.15: The time evolution of the photon number for different cut-offs of the photonic Hilbert space, N_{pho}. We present the behavior for two parameter sets, $L = 10$, $N = 5$, $\hbar\delta/J = 2$, $U/J = 2$, the truncation error is $\epsilon = 10^{-12}$, (a) $\hbar\Omega\sqrt{N}/J = 3.35$, $\hbar\Gamma/J = 1$, $dtJ/\hbar = 0.0125$ and (b) $\hbar\Omega\sqrt{N}/J = 4.47$, $\hbar\Gamma/J = 10$, $dtJ/\hbar = 0.01$. The error bars represent the standard deviation of the Monte Carlo average over 500 trajectories for (a), and 750 trajectories for (b). ©2020 American Physical Society, published in [109].

where R is the total number of samples, $|\psi_r(t)\rangle$ the time evolved wave function of the trajectory labeled by r, and $\langle\langle\mathcal{E}\rangle\rangle$ the statistical average over all quantum trajectories. For the numerical data presented, in this and the following chapters, we show this error as the error bars. Typically, we average over at least 500 trajectories, this ensures that for the physical parameters considered in this work the relative error in the expectation value of the photon number is smaller than 1% [see, for example, Fig. 3.14 (a)]. For the cases when the photon number is small, $\langle a^\dagger a\rangle \lesssim 1$, either at small coupling Ω or large dissipation strengths Γ, we average over 750 trajectories to obtain a relative error smaller than 3%, as the fluctuations have a greater influence [see Fig. 3.14(b)].

Cut-off of the dimension of the local Hilbert spaces: As the number of photons in the considered model is not conserved, the dimension of the local Hilbert space can be infinite and thus, a cut-off for its dimension is needed in the numerical implementation. In the following, we denote the cut-off N_{pho}, referring to the maximal number of photons that we can capture and we note that this means that we use $N_{\text{pho}} + 1$ Fock states, as we also have to include the vacuum state. In this section, we used a fixed cut-off for the photonic site, to identify more clearly the influence of the cut-off on the results. However, in Sec. 3.2.5 we present a more efficient approach by implementing an adaptive photonic local dimension, since the required cut-off can vary considerably in time and with the trajectories. Examples with different fixed cut-offs and all other convergence parameters fixed are shown in Fig. 3.15. For a given set of parameters we observe that above a certain value of the cut-off N_{pho} the average value of the photon number is only slightly varying with increasing the cut-off. In particular for the presented situation its variation for $N_{\text{pho}} \geq 35$ (or $N_{\text{pho}} \geq 8$) becomes lower that the error bars of the Monte Carlo averaging. However, choosing a too low cutoff e.g. $N_{\text{pho}} \leq 25$ (or $N_{\text{pho}} \leq 4$) in Fig. 3.15, leads to misleading results for both the time-evolution and the values reached at
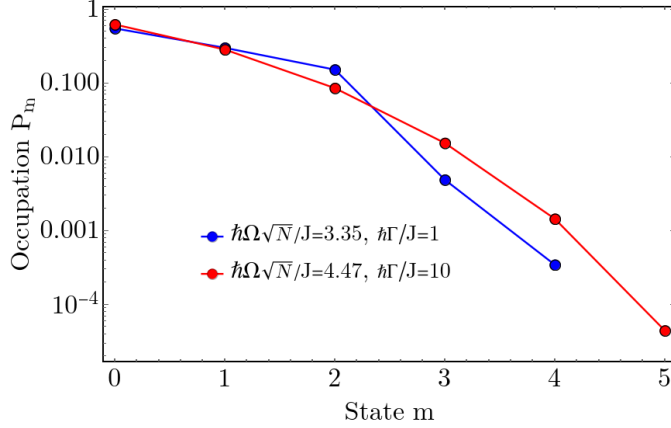
Figure 3.16: The boson number distribution, $P_m = \text{tr}\left(\langle m|\rho|m\rangle\right)$, in the middle of the chain, for site 5, at $tJ/\hbar = 49.75$. We present the behavior for two parameter sets, (red dots) $\hbar\Omega\sqrt{N}/J = 3.35$, $\hbar\Gamma/J = 1$, $\mathrm{d}tJ/\hbar = 0.0125$, $N_{\text{pho}} = 40$ and (blue dots) $\hbar\Omega\sqrt{N}/J = 4.47$, $\hbar\Gamma/J = 10$, $\mathrm{d}tJ/\hbar = 0.01$, $N_{\text{pho}} = 10$. We use $L = 10$, $N = 5$, $\hbar\delta/J = 2$, $U/J = 2$, and $\epsilon = 10^{-12}$. ©2020 American Physical Society, published in [109].

long time. We observe that because typically the photon number exhibits large increase at short times, we cannot decide the value of the cut-off just by looking at the long time values. Furthermore, the required cut-off depends very much on the physical parameters. Therefore, one needs to consider each parameter set separately, as they can result in very different values for the cut-off.

Since we consider bosonic atoms and the total number of atoms is conserved in the model, the maximal possible local dimension for the atomic sites equals the total atom number plus one for the possibility to have an empty site. We found that in many situations this very large local dimension is needed, which can strongly restrict the total number of atoms that can be efficiently simulated. However, for some physical parameter sets a reduced dimension of the local bosonic site can be taken. In Fig. 3.16 we compare the occupations of each bosonic number state for a site in the middle of the chain. We can observe that for the parameter set with $\hbar\Gamma/J = 1$ the occupations of the states with a large boson number are a few times smaller than for the parameter set with $\hbar\Gamma/J = 10$. This is due to the fact that at large dissipation strengths we expect that the atomic steady state is close to an infinite temperature state (see Chapter 4). We note that the other sites in the chain have even smaller occupations of the states with three or four bosons, for $\hbar\Gamma/J = 1$. Therefore, we can reduce the local dimension to a maximal of five instead of six states in the cases in which we consider a lower dissipation strength Γ.

Influence of the time step: Since time step controls both the convergence of the stochastic sampling process and the Trotter-Suzuki decomposition, the dependence of the results on the value of the time step can be more involved. Furthermore, as in the normal time-dependent MPS, the time step interplays with the truncation error in a non-trivial fashion. This is due to the fact that a smaller time-step requires the application of more time-evolution gates, hence more truncations, and therefore results in an increased truncation error [133]. Such that the
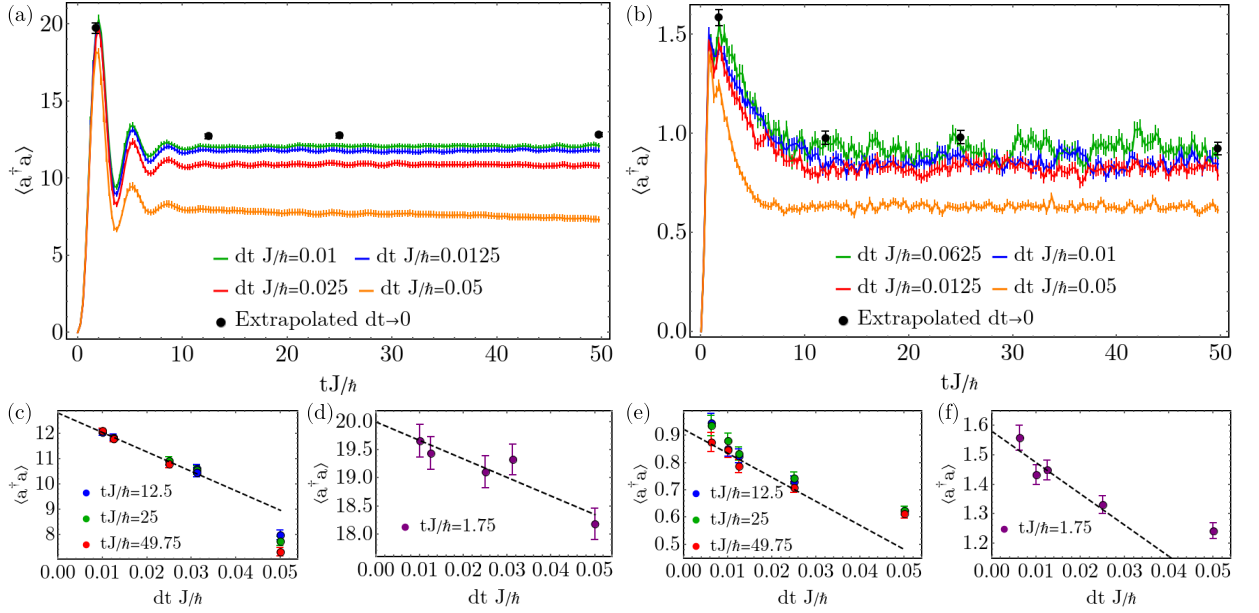
Figure 3.17: (a)-(b) The time evolution of the photon number for different time steps dt. The black dots represents the extrapolated value in the limit $dtJ \to 0$ at $tJ/\hbar \in \{1.75, 12, 25, 49.75\}$. (c)-(f) Convergence of the photon number with the time step at several chosen times. The dashed line represents a linear fit of the dependence on dtJ, for (c) and (e) the fit is done for the data taken at $tJ/\hbar = 49.75$. We present the behavior for two parameter sets, (a), (c), (d) $\hbar\Omega\sqrt{N}/J = 3.35$, $\hbar\Gamma/J = 1$, $N_{\text{pho}} = 40$ and (b), (e), (f) $\hbar\Omega\sqrt{N}/J = 4.47$, $\hbar\Gamma/J = 10$ and $N_{\text{pho}} = 10$. The error bars represent the standard deviation of the Monte Carlo average over 500 trajectories for (a), (c), (d) and 750 trajectories for (b), (e), (f). We use $L = 10$, $N = 5$, $\hbar\delta/J = 2$, $U/J = 2$, and $\epsilon = 10^{-12}$. ©2020 American Physical Society, published in [109].

values used for the time step need to be controlled very carefully depending not only on the physical timescales, but also on the other convergence parameters of the model.

In Fig. 3.17 we show an example of the dependence on the time step dt obtained fixing all other parameters. A relatively rapid convergence is seen using time steps between $dtJ/\hbar = 0.01 - 0.05$ for the considered parameters. In particular, the convergence is in agreement with the expected linear behavior in the time-step dt which suggests a well justified extrapolation method. For smaller values of Γ, here $\hbar\Gamma/J = 1$, the error induced by the time-step remains larger than the error of the statistical error, for the number of quantum trajectories considered. As we can observe that the extrapolated value lies a bit above the shown results at a finite time step at intermediate and long times. In contrast, for the case of large Γ, here $\hbar\Gamma/J = 10$, the statistical error is dominating the results and the extrapolated values are within the statistical error bars of the smallest time steps.

3.2.3 Entanglement of quantum trajectories

One of the most important convergence parameters in MPS methods is the bond dimension, m. Which corresponds to the number of states kept within the SVD compressions as we saw in
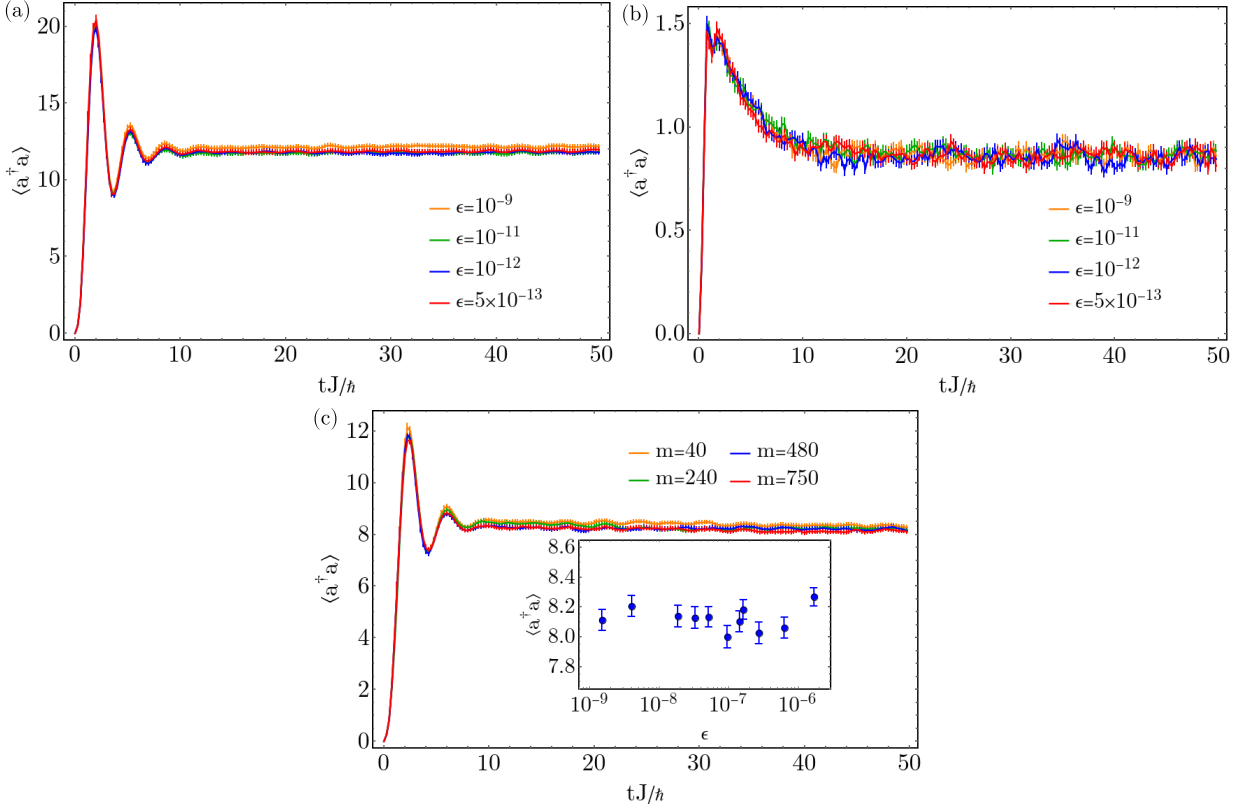
Figure 3.18: The time evolution of the photon number for different truncation errors, ϵ and bond dimensions, m. We present the behavior for three parameter sets, (a) $\hbar\Omega\sqrt{N}/J = 3.35$, $\hbar\Gamma/J = 1$, $L = 10$ sites, $N = 5$ particles, (b) $\hbar\Omega\sqrt{N}/J = 4.47$, $\hbar\Gamma/J = 10$, $L = 10$ sites, $N = 5$ particles and (c) $\hbar\Omega\sqrt{N}/J = 2.46$, $\hbar\Gamma/J = 1$, $L = 14$ sites, $N = 7$ particles. We use $\hbar\delta/J = 2$ and $U/J = 2$. In the inset of (c) the photon number is taken at $tJ/\hbar = 49.75$. The error bars represent the standard deviation of the Monte Carlo average. The numerical parameters used in the tMPS method are the following: the time step is $\mathrm{d}tJ/\hbar = 0.0125$ in (a) and (c), $\mathrm{d}tJ/\hbar = 0.01$ in (b), and the cut-off of the local dimension for the photon mode is $N_{\mathrm{pho}} = 40$ in (a), $N_{\mathrm{pho}} = 10$ in (b) and dynamically adapted in (c) (see Sec. 3.2.5). The Monte-Carlo average contains 500 trajectories for (a) and (c), and 750 trajectories for (b). ©2020 American Physical Society, published in [109].

Sec. 3.1.1. In order to control its impact, one can monitor the truncation error ϵ, representing the sum of the neglected eigenvalues of the reduced density matrix in the SVD compression. Alternatively, one can use a measure of the decay of the eigenvalues, represented by the von Neumann entropy, S_{vN}. We analyze in the following the behavior of these two quantities for different parameters [109].

We first look at the dependence on the truncation error ϵ of the SVD performed in the time-evolution gates and swap gates shown in Fig. 3.18. As the truncation error is chosen relatively small for a system size of $L = 10$ [Fig. 3.18(a)-(b)], the results only weakly depend on the value of the maximal truncation error ϵ. In the case of $L = 14$ [Fig. 3.18(c)], where we control the truncation error by using fixed bond dimensions, we can observe that the obtained photon
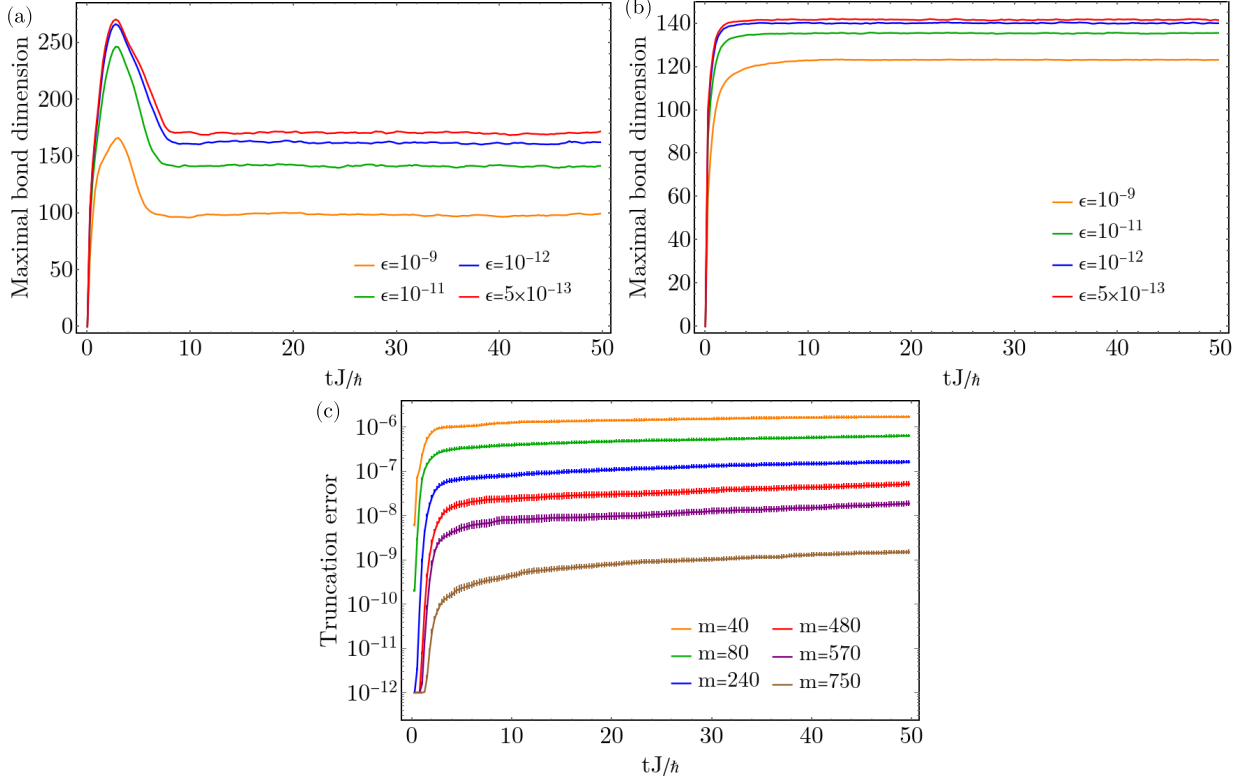
Figure 3.19: The time evolution of the maximal bond dimension for different truncation errors, ϵ (a), (b), and the time evolution of the truncation error ϵ for different bond dimensions, m. We present the behavior for three parameter sets, (a) $\hbar\Omega\sqrt{N}/J = 3.35$, $\hbar\Gamma/J = 1$, $L = 10$ sites, $N = 5$ particles, (b) $\hbar\Omega\sqrt{N}/J = 4.47$, $\hbar\Gamma/J = 10$, $L = 10$ sites, $N = 5$ particles, and (c) $\hbar\Omega\sqrt{N}/J = 2.46$, $\hbar\Gamma/J = 1$, $L = 14$ sites, $N = 7$ particles. We use $\hbar\delta/J = 2$ and $U/J = 2$. The numerical parameters used in the tMPS method are the following: the time step is $\mathrm{d}tJ/\hbar = 0.0125$ in (a) and (c), and $\mathrm{d}tJ/\hbar = 0.01$ in (b), and the cut-off of the local dimension for the photon mode is $N_{\mathrm{pho}} = 40$ in (a), $N_{\mathrm{pho}} = 10$ in (b) and dynamically adapted in (c) (see Sec. 3.2.5). The Monte-Carlo average contains 500 trajectories for (a) and (c), and 750 trajectories for (b). ©2020 American Physical Society, published in [109].

numbers are consistent with each other for a wide range of bond dimensions, except for the case with $m = 40$, which corresponds to $\epsilon \approx 10^{-6}$ at $tJ/\hbar = 49.75$. In particular, the deviations induced by the different truncation errors seem to be of the order to the statistical error. Thus, we can be confident that a truncation error of $\lesssim 10^{-7}$ provides an accurate description of the considered states in the matrix product form.

As the numerical effort of a MPS method is closely related to dimension of the matrices used, we also monitor the maximal bond dimension needed in the MPS representation in order to achieve the set truncation error goal, as depicted in Fig. 3.19 (a)-(b), or the largest truncation error obtained for a fixed bond dimension in Fig. 3.19(c). We observe that the maximal bond dimension increases considerably with lowering the truncation error. However, for the smallest chosen truncation errors the maximal bond dimension saturates. The bond dimension needed to describe the system is between 100 and 300 even for a relatively small system of size $L = 10$.
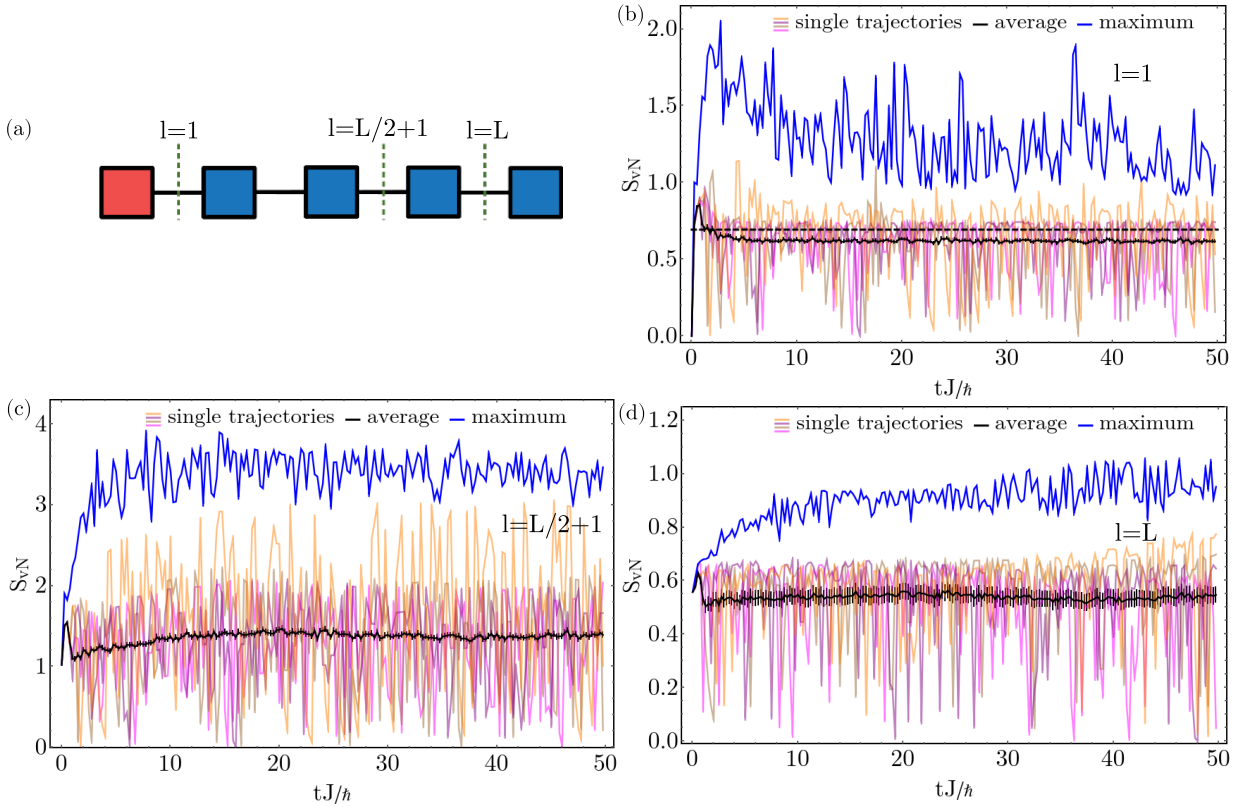
Figure 3.20: (a) The graphical representation of the MPS structure denoting the bonds for which the von Neumann entropy was computed, for a bipartition between the cavity site and the atomic sites with $l = 1$, a bipartition in the middle of the atomic chain, with one half also containing the cavity site $l = L/2 + 1$, and a bipartition between the last atomic site and the rest of the chain, $l = L$. (b)-(d) The time evolution of the von Neumann entropy, S_{vN}, of a few single trajectories, the Monte Carlo average and the maximum value over different trajectories for (b) $l = 1$, (c) $l = L/2 + 1$ and (d) $l = L$. The parameters used are $L = 10$, $N = 5$, $\hbar\delta/J = 2$, $U/J = 2$, $\hbar\Omega\sqrt{N}/J = 3.35$ and $\hbar\Gamma/J = 1$. The Monte-Carlo averages contain at least 500 trajectories. In (b) the black dashed line indicates the value $\log(2)$. ©2020 American Physical Society, published in [109].

For a system of size $L = 14$ [Fig. 3.19(c)] one needs to increase the bond dimension with more than an order of magnitude, from $m = 40$ to $m = 750$, in order to decrease the truncation error from $\epsilon \sim 10^{-6}$ to $\epsilon \sim 10^{-9}$ at long times.

In the following, in order to monitor the coupling of the photonic and atomic sectors and the correlations within the atomic chain, we turn to the von Neumann entropy of the quantum trajectories. We note that the entanglement entropy of the quantum trajectories is not a direct measure of the entanglement present in the density matrix resulting from the Monte Carlo averaging process. However, we need to make sure that our MPS method captures well the entanglement present in the trajectories and the von Neumann entropy, S_{vN}, provides valuable information in this regard.

We consider three different bipartitions of the MPS, as presented in Fig. 3.20(a), between
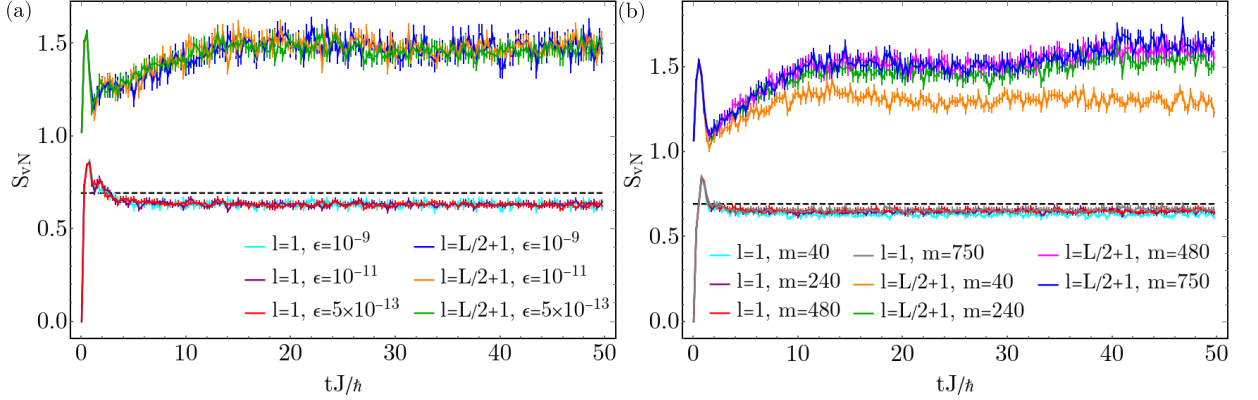
Figure 3.21: The time evolution of the von Neumman entropy S_{vN} for $l = 1$, $l = L/2 + 1$ and (a) different truncation errors and (b) bond dimensions The parameters used are $\hbar\delta/J = 2$, $U/J = 2$, (a) $\hbar\Omega\sqrt{N}/J = 3.35$, $\hbar\Gamma/J = 1$, $L = 10$ sites, $N = 5$ particles and (b) $\hbar\Omega\sqrt{N}/J = 2.46$, $\hbar\Gamma/J = 1$, $L = 14$ sites, $N = 7$ particles. The Monte-Carlo averages contain at least 500 trajectories. The black dashed line indicates the value $\log(2)$. ©2020 American Physical Society, published in [109].

the cavity site and the rest of the atomic chain, bond $l = 1$, in the middle of the atomic chain, where one half also contains the cavity site, bond $l = L/2 + 1$, and the last bond $l = L$. This is motivated by the fact that the final atomic site is the furthest apart from the cavity site, and our finding that the maximum of S_{vN} throughout the atomic chain occurs at the bond $l = L/2 + 1$. In Figs. 3.20(b)-(d) we present the time evolution of the entropy for the Monte Carlo average, the maximum entropy of the sampled quantum trajectories and for a few single trajectories, for the three considered bipartitions. We observe that for all bipartitions S_{vN} saturates to a finite value in time, both for the average and maximum values. At long times the von Neumann entropy takes finite values for all bipartitions and parameter sets considered. In Fig. 3.20(b) we see that at low dissipation strength the average entropy computed between the photon mode and the atoms ($l = 1$) becomes close to $\log(2)$ (black dashed line) at long times. This points to a coherent superposition of two states, we attribute this to a superposition of states with a different sign of the photon field [108]. The value of the entanglement within the chain is larger than $\log(2)$, signaling to contributions from several states in the superposition.

In Fig. 3.21(a) we see that the values of S_{vN} only vary within the Monte Carlo averaging uncertainty for all considered truncation errors for $L = 10$. Thus, we can be confident that our method captures the dynamics of our system correctly up to the long times considered. In the case of $L = 14$, Fig. 3.21(b), we can observe that the von Neumann entropy, S_{vN}, computed in the middle of the chain is accurately described for a bond dimension larger than $m \geq 240$. This bond dimension corresponds to $\epsilon \approx 10^{-7}$ at $tJ/\hbar = 49.75$ [Fig. 3.19(c)]. As most results in this work, including the ones presented Chapter 5 and Chapter 6, were computed with a truncation error goal of 10^{-12}, we can envision that the numerical simulations of the cavity-atoms system can be pushed towards larger systems and longer times by considering a larger truncation error.
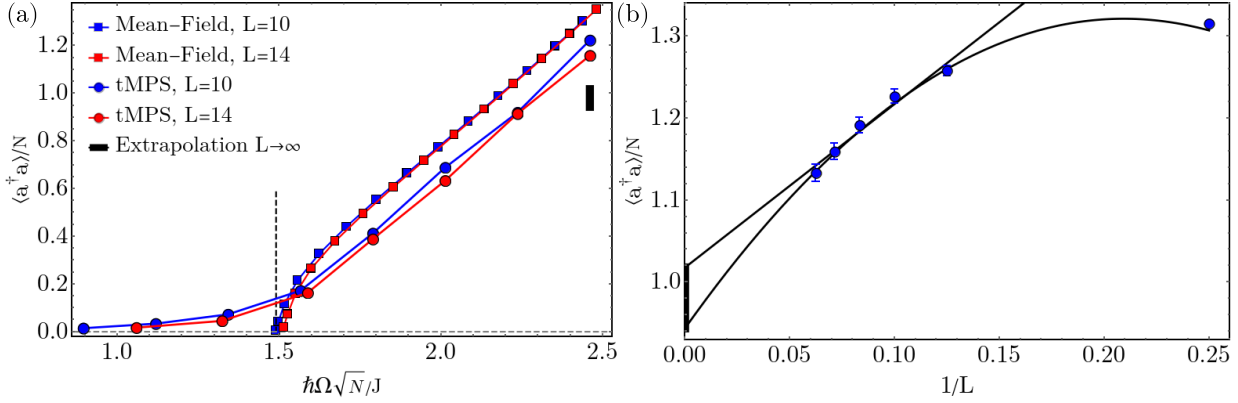
Figure 3.22: (a) The scaled photon number, $\langle a^\dagger a \rangle/N$, as a function of the scaled atoms-cavity coupling $\hbar\Omega\sqrt{N}/J$ for $L \in \{10, 14\}$. We compare our numerical results with the mean field approach. The dashed vertical line marks the self-organization threshold as obtained from the mean-field approach for $L = 10$ sites. The black vertical line represents the interval between the two possible extrapolations depicted in (b). (b) The scaled photon number, $\langle a^\dagger a \rangle/N$, as a function of the inverse system size, $1/L$, for $\hbar\Omega\sqrt{N}/J = 2.46$. The black curves represent a linear and a quadratic fit. The parameters are $n = N/L = 1/2$, $\hbar\delta/J = 2$, $U/J = 2$, $\hbar\Gamma/J = 1$, and $tJ/\hbar = 49.75$. The point for $L = 4$ is obtained by the exact diagonalization of Eqs. (2.8)-(2.16) from Sec. 2.1. The numerical parameters used in the tMPS method are the truncation error $\epsilon = 10^{-12}$ for $L = 10$ and $\epsilon = 10^{-9}$ for $L > 10$, the cut-off of the local dimension for the photon mode between 10 and 25, adapted to the average photon number, and $dtJ/\hbar = 0.0125$. The Monte-Carlo averages contain at least 500 trajectories. ©2020 American Physical Society, published in [109].

3.2.4 Finite size effects

In this subsection, we compare the values at late times for different system sizes in order to evaluate the finite size effects in our simulations [109]. We consider the values at late time, $tJ/\hbar \approx 50$, to be good approximations of the steady state values for the parameter regimes used as the considered quantities have become almost constant in time. Typically, such a regime is reached before $tJ/\hbar \approx 50$, as shown in the time evolution plots, for example Fig. 3.15 for the photon number, or Fig. 3.20 for the von Neumann entropy.

We first evaluate the finite size effects by analyzing how the transition from the normal state to the self-organized state takes place for two system sizes. In Fig. 3.22(a) we scale the photon number and the atoms-cavity coupling with the number of particles. For a comparison we show both the mean field (see Sec. 2.1) and the numerically exact tMPS method results. Only small deviations with increasing the system size are observed. In particular, in the mean field results the transition to the self-organizes phase starts later and becomes steeper with increasing system size. In the tMPS results, the rise of the photon number seems to occur for a bit larger scaled pump strength and the scaled photon number is slightly lower for $L = 14$.

The next step is to perform an extrapolation in the thermodynamic limit, $L \to \infty$, by computing the scaled photon number for multiple system size [see Fig. 3.22(b)]. We note that the point at $L = 4$ is obtained by the exact diagonalization of Eqs. (2.8)-(2.16) from Sec. 2.1 and
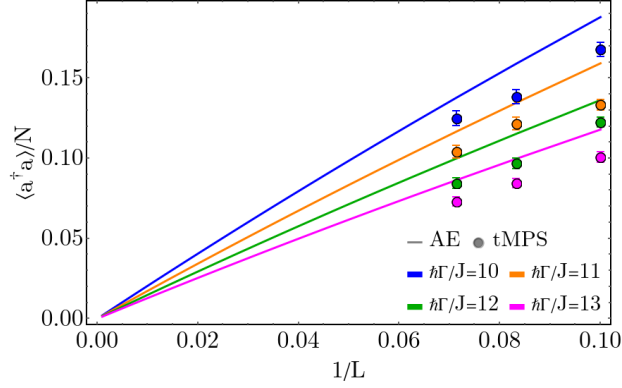
Figure 3.23: The dependence of the scaled photon number $\langle a^\dagger a \rangle/N$, on $1/L$. The parameters used are $N = L/2$ particles and $\hbar\Gamma/J \in \{10, 11, 12, 13\}$. The behavior is consistent with a L^{-1} scaling of $\langle a^\dagger a \rangle/N$. ©2020 American Physical Society, published in [109].
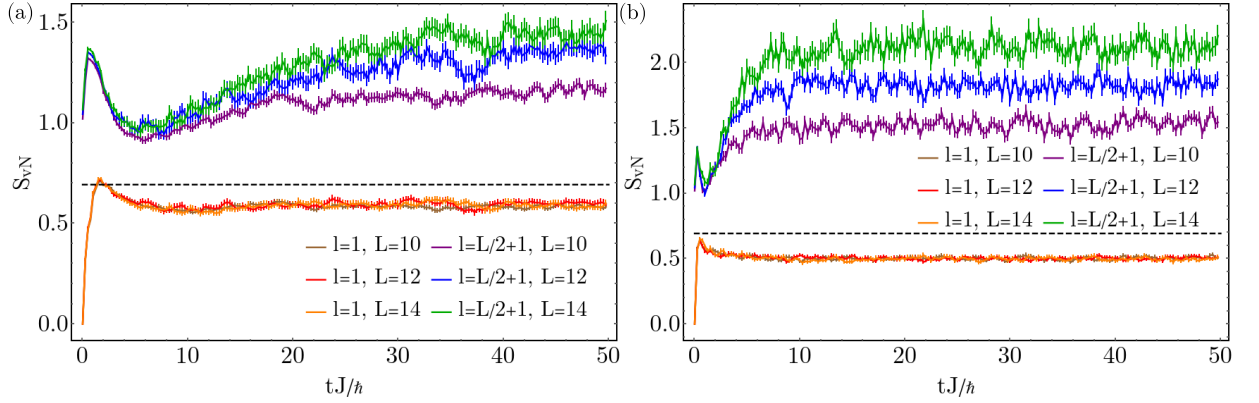
Figure 3.24: The time evolution of the von Neumman entropy, S_{vN}, of the Monte Carlo average for different system size, $L \in \{10, 12, 14\}$, for two bipartitions $l = 1$ and $l = L/2 + 1$. The parameters used are $N = L/2$, $\hbar\delta/J = 2$, $U/J = 2$, (a) $\hbar\Omega\sqrt{N}/J = 1.6$ and $\hbar\Gamma/J = 1$, (b) $\hbar\Omega\sqrt{N}/J = 4.47$ and $\hbar\Gamma/J = 13$. The Monte-Carlo averages contain at least 500 trajectories. ©2020 American Physical Society, published in [109].

taking the expectation value of the photon number in the steady state, the points for $L \geq 8$ were obtained using the tMPS method. We observe a monotonically decreasing dependence for larger L for the photon number, but the functional form of the system size dependence is not unambiguous, as both a linear fit of the points with $L \geq 8$ and a quadratic fit of all points can describe the behavior. However, as the extrapolated values are not far from the finite size results and they seems to move away from the mean field results (see black vertical line in Fig. 3.22), it leads us to the expectation that our main findings presented in Chapter 5 and Chapter 6 will remain valid for large systems [108, 109].

We further support our findings by comparing the dependence of scaled photon number with L with the many body adiabatic elimination results (method which is going to be introduced in Sec. 4.2). We perform this comparison at large dissipation strengths. We observe in

Fig. 3.23 that the agreement is very good at large dissipation strengths for all values of L and dissipation strength Γ considered. The scaled photon number is slightly decreasing for larger systems sizes in both approaches. This is consistent with the expected vanishing of the scaled photon number in the thermodynamic limit behavior for the many-body adiabatic elimination state. We note that for parameters considered together with the large dissipation strengths we are not in the self-organized state. This will be discussed further in Chapter 5.

In Fig. 3.24 we analyzed the behavior of the von Neumann entropy for different system sizes, for two different parameter sets. We see that in both cases the entanglement present in the quantum trajectories between the photon mode and the atoms remains stable for different the system sizes. This further supports the claim that a coherent superposition of two system size independent states contribute, as it is the case for the states with the different sign of the photon field [108, 109]. For the bond in the middle of the atomic chain, $l = L/2 + 1$, we observe that the value at which the entropy saturates is increasing with the system size, which indicates either that the system might be in a gapless phase, or that the system size is too small to cover the correlation length of a gapped state.

3.2.5 Dynamically adapted cut-off of the local dimension for the cavity site

As we have seen in Sec. 3.2.2, we need to be careful with respect to the cut-off of the local Hilbert space for the photons in order to obtain convergence in the numerical simulations. In particular, a sufficiently large N_{pho} is required to capture the dynamics correctly (see Fig. 3.15). Typically we take about triple the average value, this being justified by the fact that the photonic state is close to a coherent state (see Chap. 5) for which the variance of the photon number distribution is the same as its mean. Furthermore, during the time evolution the photon number often varies considerably, as for example for the case in Fig. 3.15(a). In particular, in this case at short times, $tJ/\hbar \lesssim 5$, there is a sudden increase of the number of photons in the cavity, larger than the value at late times. This implies that we need a much larger N_{pho} to accurately capture the evolution of the photonic state at short times, than we would need at later times. Therefore, we tried to optimize our implementation by adapting the local dimension for the cavity site during the time evolution [109].

The spirit of this improvement is similar with the recent developments regarding the time-dependent MPS methods with local basis optimization. Refs. [161, 162] apply the local basis optimization idea [163] to the time evolution of the Holstein model of fermions locally coupled to phononic modes. In this approach one rotates the local Hilbert space adaptively into an optimized basis that can be truncated. In our case we find that we can dynamically adapt the number of states considered, even without changing the Fock basis for the photons. It would interesting to see if one can optimize the photonic basis before the truncation step, but this is left for future implementations.

The first step in the implementation of the adaptive cut-off is to monitor the evolution of the photon number distribution, this is done by measuring the occupation P_m of the photonic Fock states with photon numbers m close to the cut-off value at each time step. The cut-off is adapted based on thresholds for the photonic state occupation. To be more precise, we use the following procedure: At a certain time in the evolution of a single quantum trajectory we have
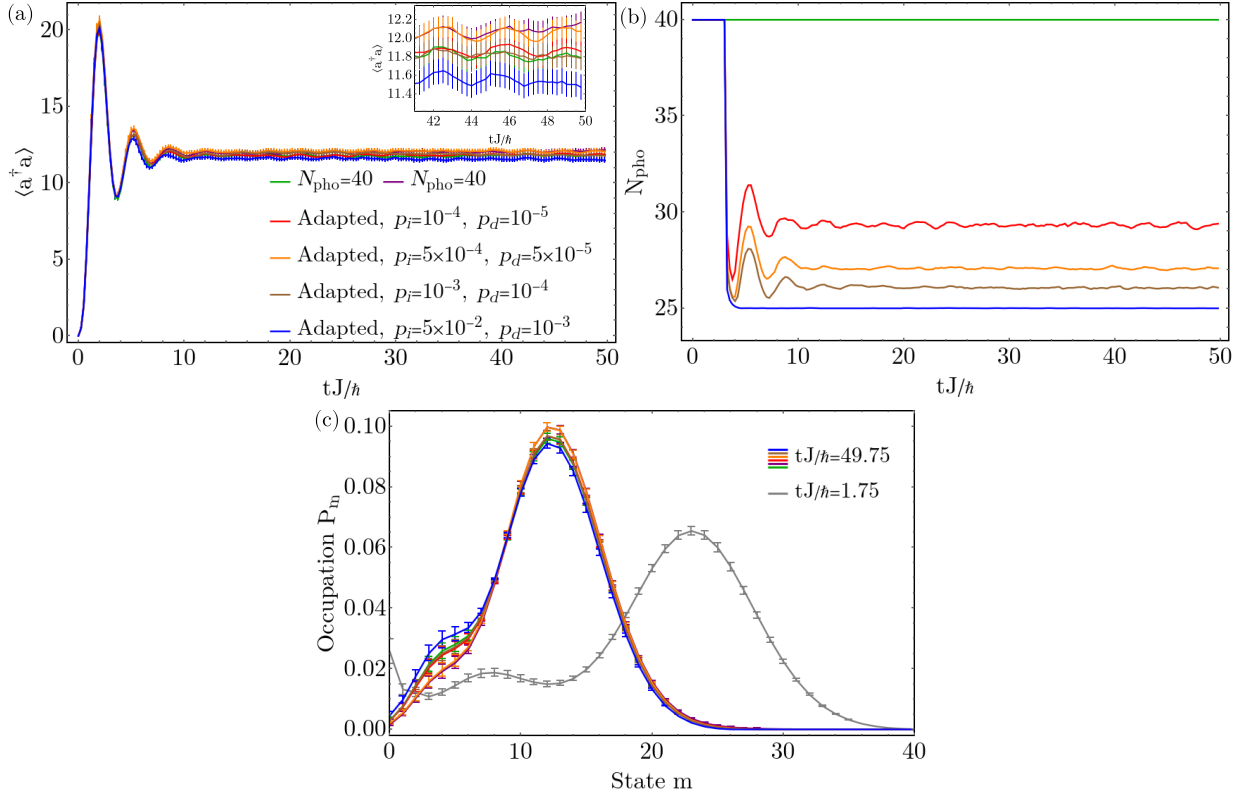
Figure 3.25: The time evolution of (a) the photon number, $\langle a^\dagger a \rangle$, and (b) N_{pho}. We compare the results corresponding to an adapted cut-off for different p_i and p_d with the Monte Carlo average of two different sets of sampled trajectories with a fixed cut-off $N_{\text{pho}} = 40$. (c) The photon number distribution, $P_m = \text{tr}\left(\langle m|\rho|m\rangle\right)$, at $tJ/\hbar = 49.75$ for the data presented in (a) and (b), and at $tJ/\hbar = 1.75$ with a fixed cut-off. The parameters used are $L = 10$, $N = 5$, $\hbar\delta/J = 2$, $U/J = 2$, $\hbar\Omega\sqrt{N}/J = 3.35$ and $\hbar\Gamma/J = 1$, time step $dtJ/\hbar = 0.0125$ and the truncation error $\epsilon = 10^{-12}$. The Monte-Carlo averages contain 500 trajectories. ©2020 American Physical Society, published in [109].

a cut-off $N_{\text{pho}}(t)$. Depending on the behavior of the photon number we need to either increase, or decrease the cut-off, thus we can encounter three different situations:

(a) The occupation $P_{N_{\text{pho}}}$ of the photonic Fock states with the largest photon number is smaller than a chosen threshold p_d. This signals that the cutoff can be decreased. In order to do this, we find the photonic Fock state $m^* \leq N_{\text{pho}}$ with the largest photon number whose occupation is above the threshold, i.e. $P_{m^*} \geq p_d$. We change the cut off of the local dimension of the cavity site of the MPS such that the maximal photon number is $N_{\text{pho}}(t + dt) = m^* + 1$ the for the time step $t + dt$.

(b) The occupation $P_{N_{\text{pho}}}$ of the photonic Fock states with the maximum photon number is larger than a second chosen threshold $p_i \geq p_d$, i.e. $P_{N_{\text{pho}}} \geq p_i$. This signals that the photon number should increase. We increase the local dimension of the cavity site of the MPS at the next time step $N_{\text{pho}}(t + dt) = N_{\text{pho}}(t) + 2$. We note that we also tried to increase the cut-off even more drastically and we obtained consistent results.
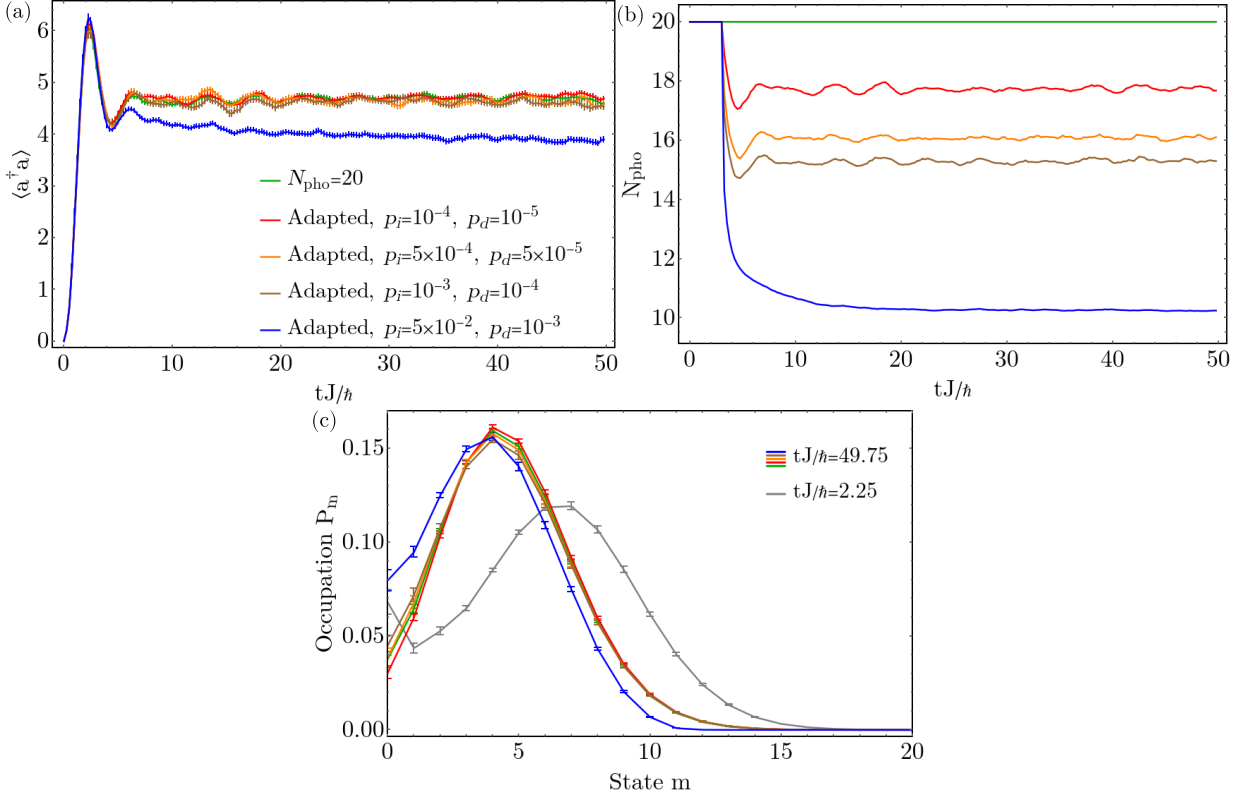
Figure 3.26: The time evolution of (a) the photon number, $\langle a^\dagger a \rangle$, and (b) N_{pho}. We compare the results corresponding to an adapted cut-off for different p_i and p_d with the Monte Carlo average of two different sets of sampled trajectories with a fixed cut-off. (c) The photon number distribution, $P_m = \text{tr}\,(\langle m|\rho|m\rangle)$, at $tJ/\hbar = 49.75$ for the data presented in (a) and (b), and at $tJ/\hbar = 2.25$ with a fixed cut-off. The parameters used are the same as Fig. 3.25, with $\hbar\Omega\sqrt{N}/J = 2.23$. ©2020 American Physical Society, published in [109].

   (c) When the occupation $P_{N_{\text{pho}}}$ of the photonic Fock states is in between the two thresholds, $p_d < P_{N_{\text{pho}}} < p_i$, we do not change the local dimension of the cavity site.

We control now the convergence of the method with the two threshold values, p_d and p_i.

    We check our procedure of adapting the local dimension for the cavity site by comparing with the results for a fixed converged cut-off, as seen in Fig. 3.25 and Fig. 3.26. In Fig. 3.25(a) and Fig. 3.26(a) we represent the Monte Carlo average of the photon number for two different sets of sampled trajectories with a fixed cut-off and the Monte Carlo average of the photon number with an adapted cut-off for different p_i and p_d. We can observe that, except for the case with $p_i = 5 \times 10^{-2}$ and $p_d = 10^{-3}$, the results for an adapted cut-off agree, within the Monte Carlo averaging error, with the ones for a fixed cut-off. The evolution in time of the cut-off can be seen in Fig. 3.25(b) and Fig. 3.26(b). We note that at short times, $tJ/\hbar < 4$, we always keep the photonic cut-off fixed and relatively large in order to capture the sudden increase in the number of photons in the cavity. But at later times we can observe that in all considered cases the cut-off is approximately 25% smaller than the initial value. As the large local dimension of

the cavity site being one of the bottlenecks of the method, this implies a significant speed up of the tMPS method. As a rough estimate, for the parameters used in Fig. 3.25 the runtime was with 50% smaller compared with the case with a fixed cut-off and for the parameters used in Fig. 3.26 with 25% smaller. We check the agreement of the entire photon number distribution in Fig. 3.25(c) and Fig. 3.26(c) by plotting the occupation of the photon number states at the final time, $tJ/\hbar = 49.75$. As in the case of the photon number average, a very good agreement is found except for the case with $p_i = 5 \times 10^{-2}$ and $p_d = 10^{-3}$. In order to show that at short times many photon number states are occupied we also plot in Fig. 3.25(c) and Fig. 3.26(c) the photon number distribution at $tJ/\hbar = 1.75$, close to the peak in the photon number. We note that we also verified the accuracy of this method at the level of single quantum trajectories, not only by analyzing the Monte Carlo average. This is an important check as in certain trajectories a sudden increase in the photon number occurs even at later times, thus, once needs to make sure that the dynamical adaptation of the cut-off can reproduce this behavior.

The improvement brought by the development presented in this section has a strong dependence on the physical parameters of the model. We have observed that it has a more important impact, roughly, when the average photon number is larger, as the difference between the maximum photon number at short times and the steady state value is larger. For example for the parameters in Fig. 3.25 we manage to lower the local dimension of the cavity site with more than 10 states compared to the fixed cut-off previously used, but for the parameters in Fig. 3.26 we have lowered the local dimension with 5 states, due to the lower photon number in the cavity.

3.2.6 Alternative MPS geometry

As we have mentioned previously we have used a MPS geometry in which the cavity site was positioned at the edge of the atomic chain, depicted in Fig. 3.20(a). Also the results presented in Chapter 5 and Chapter 6 are obtained with this geometry. The question that we try to answer in this section is whatever a different MPS geometry, in which the cavity site starts in the middle of the atomic chain [see Fig. 3.27(a)], can improve our implementation [109]. This question is motivated by the desire to minimize the occurring entanglement during the evolution of the quantum trajectories. If the cavity site is positioned in the middle of the chain the average distance between the cavity site and the atomic sites is lower, than in the case when the cavity site is at the edge of the chain. This could imply that the entanglement might be reduced and the geometry with the cavity site in the center would be a more efficient MPS representation. However, we show that in the considered cases, our approach based on swap gates is not improved this alternative geometry.

The implementation of the new position of the cavity field in the center of the atomic chain requires some adaptations compared to the implementation presented in Sec. 3.2.1. First, we slightly alter the decomposition of the time evolution with the atomic part of the Hamiltonian, given by $e^{-\frac{idt}{2\hbar}(H_{\text{kin}}+H_{\text{int}})}$, depicted in Fig. 3.11, as the atomic sites from the middle of the chain are no longer neighbors in the MPS representation. We solve this by using swap gates to bring the two atomic sites next to each other before the application of the time evolution gate. But, the main difference comes from the application of the operator $e^{-\frac{idt}{\hbar}(H_{\text{ac}}+H_{\text{c}}-\frac{i}{2}\hbar\Gamma a^{\dagger}a)}$. We use
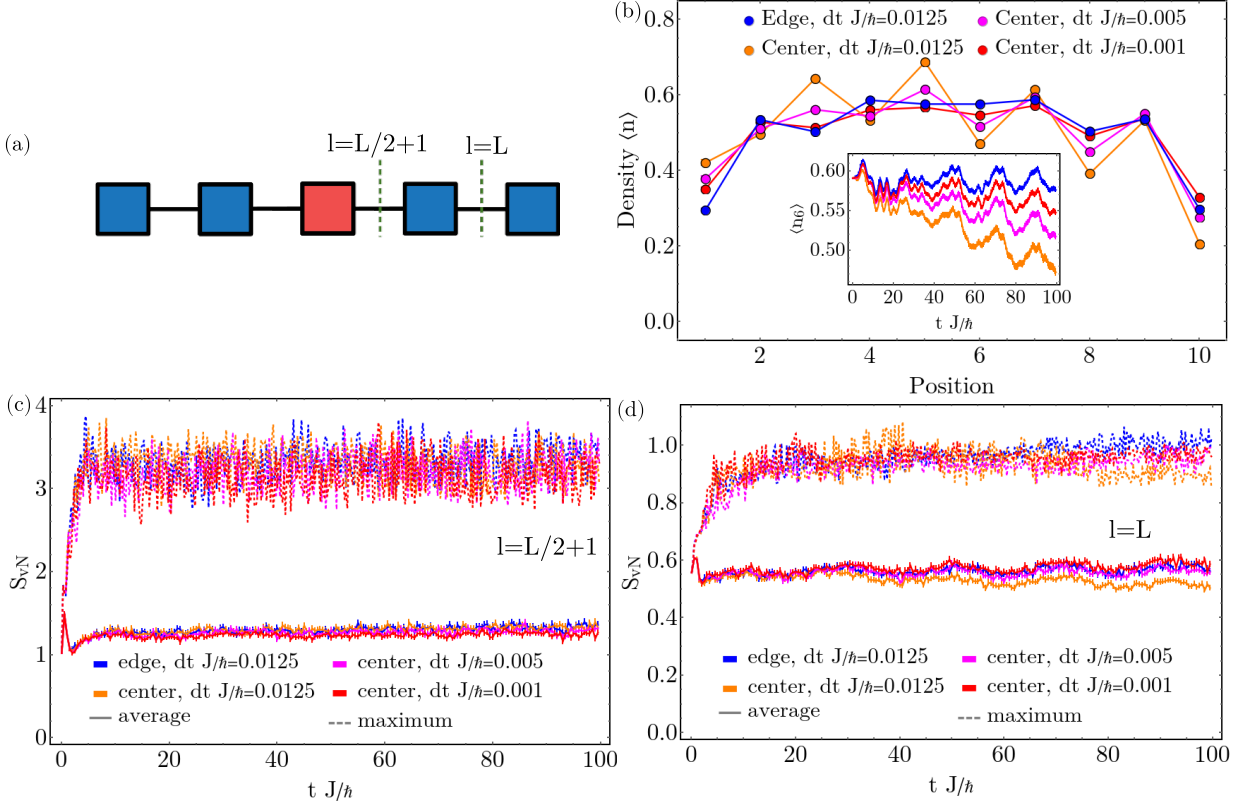
Figure 3.27: (a) The graphical representation of an alternative MPS structure with the cavity site in the middle of the chain. The bonds for which the von Neumann entropy was computed are marked. (b) The atomic density profile, $\langle n_i \rangle$, at time $tJ/\hbar = 99.75$. The inset contains the time evolution of the atomic density $\langle n_6 \rangle$. (c)-(d) The time evolution of the von Neumann entropy, S_{vN} for the Monte Carlo average and the maximum value over different trajectories for (c) $l = L/2 + 1$ and (d) $l = L$. We compare the two different MPS geometries, with the cavity site at the edge of the atomic chain and the cavity site in the middle of the chain for different time steps dt. The parameters used are $L = 10$, $N = 5$, $\hbar\delta/J = 2$, $U/J = 2$, $\hbar\Omega\sqrt{N}/J = 2.46$ and $\hbar\Gamma/J = 1$. The Monte-Carlo averages contain at least 500 trajectories. ©2020 American Physical Society, published in [109].

the decomposition that minimizes the number of swap gates used and leaves the cavity site in the center of the chain, given by

$$
e^{-\frac{idt}{\hbar}\left(H_{\mathrm{ac}}+H_{\mathrm{c}}-\frac{i}{2}\hbar\Gamma a^\dagger a\right)} = \tag{3.31}
$$

$$
= \prod_{j=1}^{L/2} e^{-\frac{idt}{2}\left[-\Omega(a+a^\dagger)(-1)^j n_j + \frac{1}{L}\left(\delta - \frac{i}{2}\Gamma\right)a^\dagger a\right]} \prod_{j=L}^{1} e^{-\frac{idt}{2}\left[-\Omega(a+a^\dagger)(-1)^j n_j + \frac{1}{L}\left(\delta - \frac{i}{2}\Gamma\right)a^\dagger a\right]} \times
$$

$$
\prod_{j=L/2+1}^{L} e^{-\frac{idt}{2}\left[-\Omega(a+a^\dagger)(-1)^j n_j + \frac{1}{L}\left(\delta - \frac{i}{2}\Gamma\right)a^\dagger a\right]} + \mathcal{O}(Ldt^2).
$$

The first thing that we can notice is that the MPS structure with the cavity site in the center the Trotter-Suzuki decomposition has a larger error compared to the one used for the geometry with the cavity site at the edge, Eq. (3.28). Thus, we expect that we need a smaller time step, dt, in this case. We note that one could use a different Trotter-Suzuki decomposition at the expense of more swap gates.

In Fig. 3.27(b) we compare the density profile at time $tJ/\hbar = 99.75$ obtained with the two geometries. We can observe that in the case with the cavity site at the center the density profile is highly asymmetric using the same time step as for the cavity site at the edge. As we expect that the density profile of the atoms to stay symmetric throughout the time evolution this signals important errors due to the time step. If we decrease the time step the density profile approaches the one obtained by the implementation with the cavity site at the edge. For a time step of $dtJ/\hbar = 10^{-3}$ the differences are within the Monte-Carlo error for short times, $tJ/\hbar \lesssim 20$, but the deviations at long time are still important, even though for the case with the cavity site at the edge the time step was more than 10 times larger. We see that the different order in the expected error due to the finite time step plays a very important role, as in order to obtain the same accuracy the implementation with the cavity site in the center needs a much smaller time step.

As the motivation for this alternative geometry was to reduce entanglement, one could naively expect that additional numerical effort induced by the smaller required time step might be compensated. We show in Figs. 3.27(c)-(d) the von Neumann entropy. For the two bipartition considered the von Neumann entropy has very similar values for the two geometries, showing no decrease in the entanglement caused by the shift of the cavity site. We attribute this to fact that the dominating contribution to entanglement could be the correlations of the atomic chain. Therefore, we also expect that the system size dependence is similar to the one found in Fig. 3.24 and, in particular, is dominated by the increase of the entanglement of the atoms.

Therefore, we can draw the conclusion that we do not expect, as long as we use swap gates, to gain a lot by using different initial geometries and we expect that this further holds for larger system sizes.

3.3 Short summary

In conclusion, we presented the basic building blocks of MPS and the algorithms for computing the ground state and the time evolution of one-dimensional systems.

In the second part of the chapter, we developed a quasi-exact tMPS method in order to determine the full quantum evolution towards the steady state of the interacting bosonic chain coupled to the cavity. This implementation deals with all the challenges posed by the atom-cavity system: We employ the stochastic unravelling of the master equation to simulate the Lindblad equation (see Sec. 2.1). The global coupling of the cavity to the atoms is tackled via the dynamical deformation of the MPS structure with swap gates. The efficient simulation of the very large photonic Hilbert space is ensured by its dynamically adapted cut-off. We analyze carefully the convergence of the method for different parameter sets and two different MPS geometries. In particular, we monitored the time dependence of the von Neumann entropy of the quantum trajectory in order to ensure that we properly capture the entanglement between

the cavity and the atoms and within the atomic chain.

The newly developed numerical method is a milestone in the field of many-body systems coupled to a dissipative bosonic mode, giving the possibility to treat them exactly. The presented algorithm is widely applicable, as it can be easily adapted to fermionic or spin many-body systems. These developments allowed us to tackle important questions regarding the self-organization phase transition and to obtain crucial deviations from the often used mean field methods, as we will see in Chap. 5 and Chap. 6.

Many-body adiabatic elimination technique for atoms-cavity coupled systems

In this chapter, we develop analytical methods which can capture the behavior of a coupled atoms-cavity dissipative system beyond the mean field approach which we discussed in Sec. 2.1. The methods which we will present are based on the many-body adiabatic elimination technique [56, 114, 164–168]. This technique is a perturbation theory for density matrices around the decoherence free subspace, where the decoherence free subspace contains the states of the unperturbed system which no longer decay under the effect of dissipation. This allows us to understand the behavior of our system close to the steady state, since for relatively long times the dynamics is dominated by virtual processes around the decoherence free subspace.

In Sec. 4.1 we present the general framework of the many-body adiabatic elimination and the effective equations of motion, which capture the quantum fluctuations around the decoherence free subspace. In the rest of the chapter, we show how to extend this method for the case of a lossy photonic mode coupled to interacting atoms. This is one of the main methodological developments presented in this thesis. In Sec. 4.2 we take the kinetic energy of the atoms as a perturbation [109] and in Sec. 4.3 the fluctuations on top of the atoms-cavity mean field decoupling [110].

4.1 Derivation of the effective equations of motion

This section gives an introduction into the many-body adiabatic elimination formalism, by deriving the perturbative equation of motion. We follow the notations and derivation of Ref. [168]. We start by considering a generic Lindblad equation

$$\frac{\partial}{\partial t}\rho = \mathcal{L}(\rho) = -\frac{i}{\hbar}\left[H_0 + H_\nu, \rho\right] + \frac{1}{2}\sum_m \Gamma_m \left(2L_m\rho L_m^\dagger - L_m^\dagger L_m \rho - \rho L_m^\dagger L_m\right), \qquad (4.1)$$

where $H_0 + H_\nu$ gives the Hamiltonian evolution and L_m are the jump operators describing the dissipation. We perform a perturbation theory by assuming that $\mathcal{V}(\rho) = -\frac{i}{\hbar}[H_\nu, \rho]$ is weak and

that we can compute the eigenvalues and the eigenvectors for $\mathcal{L}_0 = -\frac{i}{\hbar}[H_0, \cdot] + \mathcal{D}(\cdot)$,

$$\mathcal{L}_0 \rho_\lambda = (-\lambda^R + i\lambda^I)\rho_\lambda. \tag{4.2}$$

If the dissipation strength, Γ, is large enough the real part of the eigenvalues $\lambda^R \geq 0$ will either vanishing or lie in bands, separated by gaps of order $O(\Gamma)$. One can define Λ_α as the subspace of the right eigenvectors with the same λ_α^R. For $\lambda_0^R = 0$ we have the decoherence free subspace Λ_0. The states which belong to the higher subspaces $\Lambda_{\alpha \neq 0}$ will decay exponentially in time with a rate of the order $O(\Gamma)$. Thus, at long times, $t \gg \Gamma^{-1}$, the dynamics will be confined to the decoherence free subspace. To determine this effective dynamics one adiabatically eliminates the decaying subspaces $\Lambda_{\alpha \neq 0}$ and obtains [167, 168]

$$\frac{\partial}{\partial t}\rho^{\Lambda_0} = \tilde{\mathcal{L}}^{\Lambda_0}\left(\rho^{\Lambda_0}\right), \tag{4.3}$$

$$\tilde{\mathcal{L}}^{\Lambda_0} = \mathcal{L}_0^{\Lambda_0} - \sum_{\alpha \neq 0}\mathcal{V}^{\Lambda_0\Lambda_\alpha}\left(\mathcal{L}_0^{\Lambda_\alpha}\right)^{-1}\mathcal{V}^{\Lambda_\alpha\Lambda_0},$$

The projection of the density matrix into a subspace X was defined by $\rho^X = P_X(\rho)$ and the reduction of a superoperator $\mathcal{O}$ as $\mathcal{O}^{XY} = P_X\mathcal{O}P_Y$, and $\mathcal{O}^X = P_X\mathcal{O}P_X$.

If we consider the contributions only from the lowest lying subspace we can rewrite this equation as

$$\frac{\partial}{\partial t}\rho^0 = \lambda_0\rho^0 + \frac{1}{\hbar^2}P_0\left[H_\nu, \left(\mathcal{L}_0^{\Lambda_1}\right)^{-1}P_1\left[H_\nu, \rho^0\right]\right], \tag{4.4}$$

where $\rho^0 \equiv \rho^{\Lambda_0}$, P_0 and P_1 are the projectors to the decoherence free subspace and the excited subspace, respectively.

4.2 Perturbation in kinetic energy

In this section, we use the framework described in Sec. 4.1 in order to understand the long-time behavior of the coupled atom-cavity system (see Sec. 2.1) in the strongly dissipative regime. We describe how to apply the many-body adiabatic elimination formalism in the case of the photon mode coupled to the interacting atoms, by taking the kinetic energy as a perturbation. We follow Ref. [109] where we have introduced this approach, the physical results have been described in Refs. [108, 111] and will be presented in Chap. 5 and Chap. 6.

We begin by reiterating the model for coupled atoms-cavity system (see Sec. 2.1), which can be described by a Lindblad equation for the density operator ρ given by [56, 65, 100, 114]

$$\frac{\partial}{\partial t}\rho = -\frac{i}{\hbar}[H, \rho] + \frac{\Gamma}{2}\left(2a\rho a^\dagger - a^\dagger a\rho - \rho a^\dagger a\right), \tag{4.5}$$

where a and $a^\dagger$ are the annihilation and creation operators for the cavity mode. The dissipative term proportional to the dissipation strength Γ takes into account the losses from the photonic mode, due to the imperfections of the mirror.

For interacting bosons confined to a chain coupled to a single cavity mode transversely pumped with a standing-wave laser beam (see Fig. 2.2 from Sec. 2.1), the Hamiltonian has the form [65, 100, 101]

$$H = H_\text{c} + H_\text{atom} + H_\text{ac} \tag{4.6}$$
$$H_\text{c} = \hbar\delta a^\dagger a,$$
$$H_\text{atom} = H_\text{int} + H_\text{kin},$$
$$H_\text{int} = \frac{U}{2}\sum_{j=1}^{L} n_j(n_j - 1),$$
$$H_\text{kin} = -J\sum_{j=1}^{L-1}(b_j^\dagger b_{j+1} + b_{j+1}^\dagger b_j),$$
$$H_\text{ac} = -\hbar\Omega(a + a^\dagger)O, \;\; O = \sum_{j=1}^{L}(-1)^j n_j.$$

L denotes the number of sites of the chain and the total number of bosonic atoms is N. The term H_c describes the cavity mode in the rotating frame of the pump beam, with a detuning between the cavity mode, ω_c, and the transverse pump beam, ω_p, $\delta = \omega_\text{c} - \omega_\text{p}$. The operators b_j and $b_j^\dagger$ are the bosonic annihilation and creation operators of the atoms on site j and $n_j = b_j^\dagger b_j$. For the atomic part of the Hamiltonian we have the term H_kin giving the tunneling processes of the atoms with the amplitude J and the term H_int representing the repulsive on-site interaction of strength $U > 0$. The term H_ac describes the coupling between the cavity field and the total imbalance between the odd and even sites of the chain, with the effective pump amplitude Ω. We make the following notation for the expectation value of the odd-even imbalance, $\Delta = \langle O \rangle = \sum_{j=1}^{L}(-1)^j\langle n_j \rangle$. The form of the coupling is realized due to the assumed commensurability of the cavity mode with twice the periodicity of the lattice spacing within the chain [100].

We consider the kinetic energy term, H_kin, as a perturbation ($\hbar\Gamma \gg \hbar\Omega, \hbar\delta \gg J$) compared to the other terms in the Liouvillian

$$\mathcal{L}_0 = -\frac{i}{\hbar}[H_\text{c} + H_\text{int} + H_\text{ac}, \cdot] + \mathcal{D}(\cdot). \tag{4.7}$$

If we consider only contributions from the first excited subspace, Λ_1, that can be accessed via one hopping event, the effective dynamics, Eq. (4.4), for the elements of the decoherence free subspace is given by [109, 167, 168]

$$\frac{\partial}{\partial t}\rho^0 \approx \lambda_0\rho^0 + \frac{1}{\hbar^2}P_0\left[H_\text{kin}, \mathcal{L}_0^{-1}P_1\left[H_\text{kin}, \rho^0\right]\right], \tag{4.8}$$

where $\rho^0 \in \Lambda_0$ is an eigenstate of $\mathcal{L}_0$ with vanishing real part of the eigenvalue, i.e. $\mathcal{L}_0[\rho^0] = \lambda_0\rho^0$ with $\text{Re}(\lambda_0) = 0$. The operators P_0 and P_1 are the projectors onto the subspaces Λ_0 and Λ_1, respectively. In Fig. 4.1 we sketched the action of the Liouvillian $\mathcal{L}_0$ and the perturbation
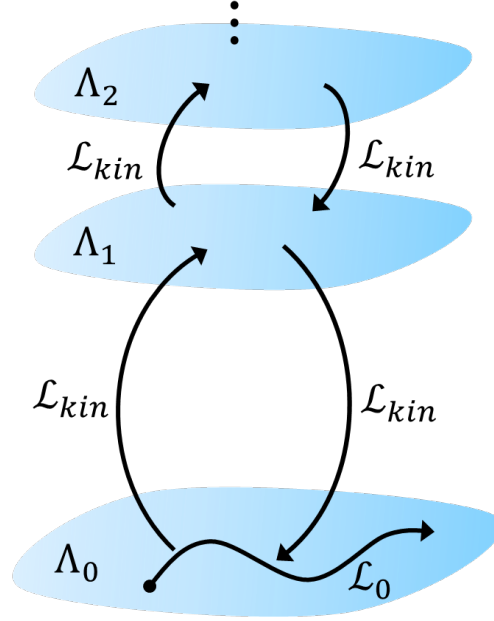
Figure 4.1: Sketch of the spectrum of the Liouvillian $\mathcal{L}_0$. The subspaces Λ_α are spanned by the eigenstates of $\mathcal{L}_0$ which have eigenvalues with the same real part. The subspace Λ_0 is the decoherence free subspace of $\mathcal{L}_0$, containing only states with a vanishing real part of the eigenvalues. While the evolution given by $\mathcal{L}_0$ is contained within a subspace, the Liovillian $\mathcal{L}_{\mathrm{kin}} = -\frac{i}{\hbar}[H_{\mathrm{kin}}, \cdot]$ can induce transitions between the different subspaces Λ_α. ©2020 American Physical Society, published in [109].

$\mathcal{L}_{\mathrm{kin}} = -\frac{i}{\hbar}[H_{\mathrm{kin}}, \cdot]$ onto the decoherence free subspace Λ_0 and two different subspaces Λ_1 and Λ_2.

Next step is to determine the elements of the decoherence free subspace Λ_0 and of the subspace Λ_1. Solving the eigenvalue equation belonging to $\mathcal{L}_0$ is already complex for the system we consider. However, we find that a set of right eigenstates of $\mathcal{L}_0$ is given by the following Ansatz

$$\rho = |\alpha(\Delta); n_1, \ldots, n_L\rangle\langle\alpha(\Delta'); n'_1, \ldots, n'_L|. \tag{4.9}$$

The atomic part is given by Fock states, with the local densities n_i and n'_i. The the odd-even imbalances are $\Delta = \sum_j (-1)^j n_j$ and $\Delta' = \sum_j (-1)^j n'_j$ and the total interaction energies are $u = \frac{U}{2}\sum_j n_j(n_j - 1)$ and $u' = \frac{U}{2}\sum_j n'_j(n'_j - 1)$. The photons are in a coherent state which depends on the atomic imbalance

$$\alpha(\Delta) = \frac{\Omega}{\delta - i\Gamma/2}\Delta, \tag{4.10}$$

We note that at this point we do not assure that these states are physical density matrices.

Inserting the state given by Eq. (4.9) in the eigenvalue equation

$$\mathcal{L}_0 \rho = \lambda \rho, \tag{4.11}$$

we obtain

$$- i \Big\{ \delta(n - m)\rho_{n,m} + \Omega \left(\Delta \sqrt{n+1}\rho_{n+1,m} + \Delta \sqrt{n}\rho_{n-1,m} - \Delta' \sqrt{m+1}\rho_{n,m+1} - \Delta' \sqrt{m}\rho_{n,m-1} \right)$$

$$\tag{4.12}$$

$$+ (u - u')\rho_{n,m} \Big\} + \frac{\Gamma}{2} \left\{ 2\sqrt{(n+1)(m+1)}\rho_{n+1,m+1} - (n+m)\rho_{n,m} \right\}$$

$$= \lambda \rho_{n,m},$$

where $\rho_{n,m}$ are the matrix elements of the photon coherent state in the Fock basis. Thus the corresponding eigenvalues for the right eigenvectors in Eq. (4.9) are given by

$$\lambda(\Delta, u, \Delta', u') = -\frac{1}{2} \frac{\Omega^2 \Gamma}{\delta^2 + \Gamma^2/4}(\Delta - \Delta')^2 \tag{4.13}$$

$$+ i \left[\frac{\Omega^2 \delta}{\delta^2 + \Gamma^2/4}(\Delta^2 - \Delta'^2) - (u - u') \right].$$

We observe that for $\Delta = \Delta'$ the real part of the eigenvalues is zero. Thus, the states in Eq. (4.9) with $\Delta = \Delta'$ lie in the decoherence free subspace of $\mathcal{L}_0$. It is interesting to note that the eigenstates with $\Delta = \Delta'$, but with different interaction energies $u \neq u'$ have purely imaginary eigenvalues. The excited subspace which can be accessed via a hopping event from the decoherence free subspace is given for the states in which $\Delta = \Delta' \pm 2$. By performing exact diagonalization of the full Liouvillian, Eqs. (4.5)-(4.6), for a small system of $N = 2$ particles in $L = 4$ sites, we observe that for large dissipation strengths the excited subspace mentioned is the lowest subspace that our perturbation couples to starting from the decoherence free subspace.

In the following, we define the two projectors from Eq. (4.8) onto the decoherence free subspace, P_0, and the excited subspace, P_1. As they mainly depend on the details of the photonic state we keep track of the atomic state only via its odd-even imbalance Δ. For P_0 we need to project states of the form $|\alpha(\Delta'), \Delta\rangle\langle\alpha(\Delta), \Delta|$ or $|\alpha(\Delta), \Delta\rangle\langle\alpha(\Delta'), \Delta|$ on the state $|\alpha(\Delta), \Delta\rangle\langle\alpha(\Delta), \Delta|$ (see Appendix A), so the action of P_0 is given by

$$P_0 \left(|\alpha(\Delta'), \Delta\rangle\langle\alpha(\Delta), \Delta| \right) = \langle\alpha(\Delta), \Delta|\alpha(\Delta'), \Delta\rangle|\alpha(\Delta), \Delta\rangle\langle\alpha(\Delta), \Delta| \tag{4.14}$$

$$= e^{-\frac{|\alpha_0|^2}{2}(\Delta - \Delta')^2}|\alpha(\Delta), \Delta\rangle\langle\alpha(\Delta), \Delta|,$$

with $\alpha_0 \equiv \frac{\Omega}{\delta - i\Gamma/2}$.

In a similar way, for P_1 we need to project states of the form $|\alpha(\Delta), \Delta'\rangle\langle\alpha(\Delta), \Delta|$ or $|\alpha(\Delta), \Delta\rangle\langle\alpha(\Delta), \Delta'|$ on the states $\{|\alpha(\Delta'), \Delta'\rangle\langle\alpha(\Delta), \Delta|, |\alpha(\Delta), \Delta\rangle\langle\alpha(\Delta'), \Delta'|\}$ (see Appendix A),

4.2 Perturbation in kinetic energy

so the action of P_1 is given by

$$P_1\left(|\alpha(\Delta), \Delta'\rangle\langle\alpha(\Delta), \Delta|\right) = \langle\alpha(\Delta'), \Delta'|\alpha(\Delta), \Delta'\rangle|\alpha(\Delta'), \Delta'\rangle\langle\alpha(\Delta), \Delta| \quad (4.15)$$

$$= e^{-\frac{|\alpha_0|^2}{2}(\Delta-\Delta')^2}|\alpha(\Delta'), \Delta'\rangle\langle\alpha(\Delta), \Delta|.$$

We are now able to write explicitly the equations of motion, Eq. (4.8), for the elements of the decoherence free subspace [109] (see Appendix A for the derivation)

$$\frac{\partial}{\partial t}\rho^0 = -i(u - u')\rho^0 + J^2 e^{-4|\alpha_0|^2}\Bigg\{ \quad (4.16)$$

$$\sum_{i \text{ odd}}\sum_{j \text{ odd}}\Bigg[-\frac{\sqrt{(n_i+1)n_{i+1}}}{\lambda(\Delta - 2, u + U(n_i - n_{i+1} + 1), \Delta, u')}\times$$

$$\left(\sqrt{(n_j'+1)n_{j+1}'}|\alpha(\Delta-2); \ldots, n_i+1, n_{i+1}-1, \ldots\rangle\langle\alpha(\Delta-2); \ldots, n_j'+1, n_{j+1}'-1, \ldots|\right.$$

$$\left. + \sqrt{(n_j'+1)n_{j-1}'}|\alpha(\Delta-2); \ldots, n_i+1, n_{i+1}-1, \ldots\rangle\langle\alpha(\Delta-2); \ldots, n_{j-1}'-1, n_j'+1, \ldots|\right)$$

$$-\frac{\sqrt{(n_i+1)n_{i-1}}}{\lambda(\Delta - 2, u + U(n_i - n_{i-1} + 1), \Delta, u')}\times$$

$$\left(\sqrt{(n_j'+1)n_{j+1}'}|\alpha(\Delta-2); \ldots, n_{i-1}-1, n_i+1, \ldots\rangle\langle\alpha(\Delta-2); \ldots, n_j'+1, n_{j+1}'-1, \ldots|\right.$$

$$\left. + \sqrt{(n_j'+1)n_{j-1}'}|\alpha(\Delta-2); \ldots, n_{i-1}-1, n_i+1, \ldots\rangle\langle\alpha(\Delta-2); \ldots, n_{j-1}'-1, n_j'+1, \ldots|\right)$$

$$-\frac{\sqrt{(n_i'+1)n_{i+1}'}}{\lambda(\Delta, u, \Delta - 2, u' + U(n_i' - n_{i+1}' + 1))}\times$$

$$\left(\sqrt{(n_j+1)n_{j+1}}|\alpha(\Delta-2); \ldots, n_j+1, n_{j+1}-1, \ldots\rangle\langle\alpha(\Delta-2); \ldots, n_i'+1, n_{i+1}'-1, \ldots|\right.$$

$$\left. + \sqrt{(n_j+1)n_{j-1}}|\alpha(\Delta-2); \ldots, n_{j+1}-1, n_j+1, \ldots\rangle\langle\alpha(\Delta-2); \ldots, n_i'+1, n_{i+1}'-1, \ldots|\right)$$

$$-\frac{\sqrt{(n_i'+1)n_{i-1}'}}{\lambda(\Delta, u, \Delta - 2, u' + U(n_i' - n_{i-1}' + 1))}\times$$

$$\left(\sqrt{(n_j+1)n_{j+1}}|\alpha(\Delta-2); \ldots, n_j+1, n_{j+1}-1, \ldots\rangle\langle\alpha(\Delta-2); \ldots, n_{i-1}'-1, n_i'+1, \ldots|\right.$$

$$\left. + \sqrt{(n_j+1)n_{j-1}}|\alpha(\Delta-2); \ldots, n_{j+1}-1, n_j+1, \ldots\rangle\langle\alpha(\Delta-2); \ldots, n_{i-1}'-1, n_i'+1, \ldots|\right)\Bigg]$$

$$+ \sum_{i \text{ odd } j \text{ even}} \left[\frac{\sqrt{(n_i+1)n_{i+1}}}{\lambda(\Delta-2, u+U(n_i-n_{i+1}+1), \Delta, u')} \times \right.$$

$$\left(\sqrt{(n_j+1)n_{j+1}} |\alpha(\Delta); \ldots, n_i+1, n_{i+1}-1, \ldots, n_j+1, n_{j+1}-1, \ldots \rangle \langle \alpha(\Delta); \ldots, n'_i, \ldots | \right.$$

$$\left. + \sqrt{(n_j+1)n_{j-1}} |\alpha(\Delta); \ldots, n_i+1, n_{i+1}-1, \ldots, n_{j-1}-1, n_j+1, \ldots \rangle \langle \alpha(\Delta); \ldots, n'_i, \ldots | \right)$$

$$+ \frac{\sqrt{(n_i+1)n_{i-1}}}{\lambda(\Delta-2, u+U(n_i-n_{i-1}+1), \Delta, u')} \times$$

$$\left(\sqrt{(n_j+1)n_{j+1}} |\alpha(\Delta); \ldots, n_{i-1}-1, n_i+1, \ldots, n_j+1, n_{j+1}-1, \ldots \rangle \langle \alpha(\Delta); \ldots, n'_i, \ldots | \right.$$

$$\left. + \sqrt{(n_j+1)n_{j-1}} |\alpha(\Delta); \ldots, n_{i-1}-1, n_i+1, \ldots, n_{j-1}-1, n_j+1, \ldots \rangle \langle \alpha(\Delta); \ldots, n'_i, \ldots | \right)$$

$$+ \frac{\sqrt{(n'_i+1)n'_{i+1}}}{\lambda(\Delta, u, \Delta-2, u'+U(n'_i-n'_{i+1}+1))} \times$$

$$\left(\sqrt{(n'_j+1)n'_{j+1}} |\alpha(\Delta); \ldots, n_i, \ldots \rangle \langle \alpha(\Delta); \ldots, n'_i+1, n'_{i+1}-1, \ldots, n'_j+1, n'_{j+1}-1, \ldots | \right.$$

$$\left. + \sqrt{(n'_j+1)n'_{j-1}} |\alpha(\Delta); \ldots, n_i, \ldots \rangle \langle \alpha(\Delta); \ldots, n'_i+1, n'_{i+1}-1, \ldots, n'_{j-1}-1, n'_j+1, \ldots | \right)$$

$$+ \frac{\sqrt{(n'_i+1)n'_{i-1}}}{\lambda(\Delta, u, \Delta-2, u'+U(n'_i-n'_{i-1}+1))} \times$$

$$\left(\sqrt{(n'_j+1)n'_{j+1}} |\alpha(\Delta); \ldots, n_i, \ldots \rangle \langle \alpha(\Delta); \ldots, n'_{i-1}-1, n'_i+1, \ldots, n'_j+1, n'_{j+1}-1, \ldots | \right.$$

$$\left. \left. + \sqrt{(n'_j+1)n'_{j-1}} |\alpha(\Delta); \ldots, n_i, \ldots \rangle \langle \alpha(\Delta); \ldots, n'_{i-1}-1, n'_i+1, \ldots, n'_{j-1}-1, n'_j+1, \ldots | \right) \right]$$

$$+ \sum_{i \text{ even } j \text{ odd}} \left[\frac{\sqrt{(n_i+1)n_{i+1}}}{\lambda(\Delta+2, u+U(n_i-n_{i+1}+1), \Delta, u')} \times \right.$$

$$\left(\sqrt{(n_j+1)n_{j+1}} |\alpha(\Delta); \ldots, n_i+1, n_{i+1}-1, \ldots, n_j+1, n_{j+1}-1, \ldots \rangle \langle \alpha(\Delta); \ldots, n'_i, \ldots | \right.$$

$$\left. + \sqrt{(n_j+1)n_{j-1}} |\alpha(\Delta); \ldots, n_i+1, n_{i+1}-1, \ldots, n_{j-1}-1, n_j+1, \ldots \rangle \langle \alpha(\Delta); \ldots, n'_i, \ldots | \right)$$

$$+ \frac{\sqrt{(n_i+1)n_{i-1}}}{\lambda(\Delta+2, u+U(n_i-n_{i-1}+1), \Delta, u')} \times$$

$$\left(\sqrt{(n_j+1)n_{j+1}} |\alpha(\Delta); \ldots, n_{i-1}-1, n_i+1, \ldots, n_j+1, n_{j+1}-1, \ldots \rangle \langle \alpha(\Delta); \ldots, n'_i, \ldots | \right.$$

$$+ \sqrt{(n_j+1)n_{j-1}}|\alpha(\Delta); \ldots, n_{i-1}-1, n_i+1, \ldots, n_{j-1}-1, n_j+1, \ldots\rangle\langle\alpha(\Delta); \ldots, n_i', \ldots|\Bigg)$$

$$+ \frac{\sqrt{(n_i'+1)n_{i+1}'}}{\lambda(\Delta, u, \Delta+2, u'+U(n_i'-n_{i+1}'+1))} \times$$

$$\Bigg(\sqrt{(n_j'+1)n_{j+1}'}|\alpha(\Delta); \ldots, n_i, \ldots\rangle\langle\alpha(\Delta); \ldots, n_i'+1, n_{i+1}'-1, \ldots, n_j'+1, n_{j+1}'-1, \ldots|$$

$$+ \sqrt{(n_j'+1)n_{j-1}'}|\alpha(\Delta); \ldots, n_i, \ldots\rangle\langle\alpha(\Delta); \ldots, n_i'+1, n_{i+1}'-1, \ldots, n_{j-1}'-1, n_j'+1, \ldots|\Bigg)$$

$$+ \frac{\sqrt{(n_i'+1)n_{i-1}'}}{\lambda(\Delta, u, \Delta+2, u'+U(n_i'-n_{i-1}'+1))} \times$$

$$\Bigg(\sqrt{(n_j'+1)n_{j+1}'}|\alpha(\Delta); \ldots, n_i, \ldots\rangle\langle\alpha(\Delta); \ldots, n_{i-1}'-1, n_i'+1, \ldots, n_j'+1, n_{j+1}'-1, \ldots|$$

$$+ \sqrt{(n_j'+1)n_{j-1}'}|\alpha(\Delta); \ldots, n_i, \ldots\rangle\langle\alpha(\Delta); \ldots, n_{i-1}'-1, n_i'+1, \ldots, n_{j-1}'-1, n_j'+1, \ldots|\Bigg)\Bigg]$$

$$+ \sum_{i \text{ even}} \sum_{j \text{ even}} \Bigg[-\frac{\sqrt{(n_i+1)n_{i+1}}}{\lambda(\Delta+2, u+U(n_i-n_{i+1}+1), \Delta, u')} \times$$

$$\Bigg(\sqrt{(n_j'+1)n_{j+1}'}|\alpha(\Delta+2); \ldots, n_i+1, n_{i+1}-1, \ldots\rangle\langle\alpha(\Delta+2); \ldots, n_j'+1, n_{j+1}'-1, \ldots|$$

$$+ \sqrt{(n_j'+1)n_{j-1}'}|\alpha(\Delta+2); \ldots, n_i+1, n_{i+1}-1, \ldots\rangle\langle\alpha(\Delta+2); \ldots, n_{j-1}'-1, n_j'+1, \ldots|\Bigg)$$

$$- \frac{\sqrt{(n_i+1)n_{i-1}}}{\lambda(\Delta+2, u+U(n_i-n_{i-1}+1), \Delta, u')} \times$$

$$\Bigg(\sqrt{(n_j'+1)n_{j+1}'}|\alpha(\Delta+2); \ldots, n_{i-1}-1, n_i+1, \ldots\rangle\langle\alpha(\Delta+2); \ldots, n_j'+1, n_{j+1}'-1, \ldots|$$

$$+ \sqrt{(n_j'+1)n_{j-1}'}|\alpha(\Delta+2); \ldots, n_{i-1}-1, n_i+1, \ldots\rangle\langle\alpha(\Delta+2); \ldots, n_{j-1}'-1, n_j'+1, \ldots|\Bigg)$$

$$- \frac{\sqrt{(n_i'+1)n_{i+1}'}}{\lambda(\Delta, u, \Delta+2, u'+U(n_i'-n_{i+1}'+1))} \times$$

$$\Bigg(\sqrt{(n_j+1)n_{j+1}}|\alpha(\Delta+2); \ldots, n_j+1, n_{j+1}-1, \ldots\rangle\langle\alpha(\Delta+2); \ldots, n_i'+1, n_{i+1}'-1, \ldots|$$

$$+ \sqrt{(n_j+1)n_{j-1}}|\alpha(\Delta+2); \ldots, n_{j-1}-1, n_j+1, \ldots\rangle\langle\alpha(\Delta+2); \ldots, n_i'+1, n_{i+1}'-1, \ldots|\Bigg)$$

$$- \frac{\sqrt{(n_i' + 1)n_{i-1}'}}{\lambda(\Delta, u, \Delta + 2, u' + U(n_i' - n_{i-1}' + 1))} \times$$

$$\left(\sqrt{(n_j + 1)n_{j+1}} |\alpha(\Delta + 2); \dots, n_j + 1, n_{j+1} - 1, \dots\rangle\langle\alpha(\Delta + 2); \dots, n_{i-1}' - 1, n_i' + 1, \dots| \right.$$

$$\left. + \sqrt{(n_j + 1)n_{j-1}} |\alpha(\Delta + 2); \dots, n_{j-1} - 1, n_j + 1, \dots\rangle\langle\alpha(\Delta + 2); \dots, n_{i-1}' - 1, n_i' + 1, \dots| \right) \Bigg] \Bigg\}.$$

In order to identify the steady states we need to solve $\frac{\partial}{\partial t}\rho^0 = 0$. By looking at the coefficients of the diagonal terms of the decoherence free subspace, $|\alpha(\Delta); n_1, \dots, n_L\rangle\langle\alpha(\Delta); n_1, \dots, n_L|$, in Eq. (4.16), we observe that their sum is zero, thus the mixed state given by

$$\rho_{\text{mix}} = \frac{1}{\mathcal{N}} \sum_{\{n_j\}} |\alpha(\Delta); n_1, \dots, n_L\rangle\langle\alpha(\Delta); n_1, \dots, n_L| \tag{4.17}$$

is a steady state of the system. Here the sum runs over all possible density configurations $\{n_j\}$ and $\mathcal{N}$ is the number of these configurations, being the number of ways one can arrange N identical particles in L sites, $\mathcal{N} = \binom{L + N - 1}{N}$.
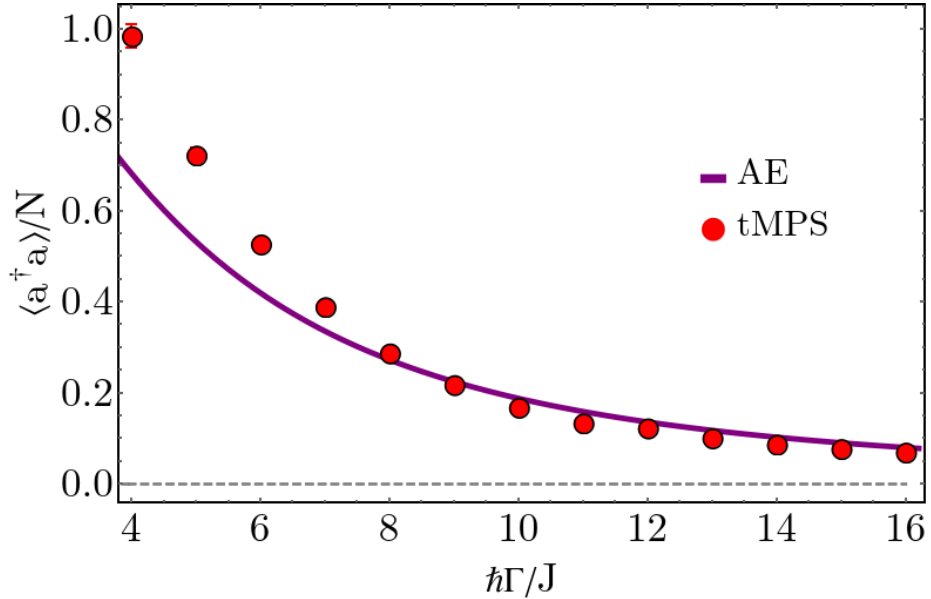
Figure 4.2: The dependence of the scaled photon number $\langle a^\dagger a\rangle/N$, on the dissipation strength, $\hbar\Gamma/J$, using tMPS and many-body adiabatic elimination (AE), for $\hbar\delta/J = 2$, $U/J = 2$ and $\hbar\Omega\sqrt{N}/J = 4.47$, $L = 10$, $N = L/2$. Figure adapted from Ref. [109].

We illustrate the range of validity of the many-body adiabatic elimination approach, by comparing its results with the numerically exact tMPS method, which we introduced and discussed in Sec. 3.2. We observe that the scaled photon number computed with ρ_{mix}, depicted in

Fig. 4.2, is in agreement with the tMPS results in the regime where the dissipation strength is larger than the other parameters, for $\hbar\Gamma/J \gtrsim 9$, and the agreement continues as we increase the dissipation strength. The properties and nature of the steady state, ρ_{mix}, will be discussed in Chap. 5. In Chap. 6 we will see how this procedure is affected by the existence of a strong symmetry in the dissipative many-body system.

In Ref. [169] the authors consider the same model, for which they obtain a state with a fully mixed atomic sector as the steady state. In contrast with our approach, they eliminate the cavity field and analyze the obtained effective Liouvillian in the atomic sector. As the effective jump operators are Hermitian in this case, it follows directly that the fully mixed state is a steady state. In our analysis we consider the full Liouvillian Eqs. (4.5) and (4.6), including the photonic degrees of freedom, the jump operator, which is annihilation operator of the cavity mode, a, is not Hermitian, thus we need to perform the many body adiabatic elimination in order to obtain insights into the nature of the steady state.

4.3 Mean field decoupling with thermal fluctuations

We follow the approach we introduced in Ref. [110] and perform a mean field decoupling of the coupling term H_{ac} [see Eq. (4.6)]. We consider the fluctuations in the coupling as the perturbation in the many-body adiabatic elimination derivation of the effective equations of motion presented in Sec. 4.1. This approach is based on a novel idea of Achim Rosch [110], which I reformulated in the framework of many-body adiabatic elimination technique. In this situation we have

$$
\begin{aligned}
H_{\text{ac}} &= H_{\text{ac}}^{MF} + \delta H_{\text{ac}} + \text{const.}, \\
H_{\text{ac}}^{\text{MF}} &= -\hbar\Omega\lambda O - \hbar\Omega(a + a^\dagger)\Delta, \\
\delta H_{\text{ac}} &= -\hbar\Omega(a + a^\dagger - \lambda)(O - \Delta),
\end{aligned}
\tag{4.18}
$$

with

$$
\begin{aligned}
\lambda &= \langle a + a^\dagger \rangle_c, \\
O &= \sum_{j=1}^{L}(-1)^j n_j, \\
\Delta &= \langle O \rangle_a.
\end{aligned}
\tag{4.19}
$$

The expectation values are taken either with respect to the the atomic density matrix, $\langle \cdot \rangle_a$, or the cavity density matrix, $\langle \cdot \rangle_c$, and they need to be evaluated self-consistently.

We note that by performing a mean field decoupling we assume a finite expectation value of the cavity field λ in the self-organized phase. This breaks the weak $\mathbb{Z}_2$ symmetry of the Liouvillian associated with the change of the sign of the cavity field (see Sec. 2.1). For any finite system size we expect that the expectation value of the cavity field is zero and only in the thermodynamic limit the weak $\mathbb{Z}_2$ symmetry is broken at the self-organization phase transition and λ acquires a finite value.

In the mean field approach the photonic mode in the superradiant phase has an expectation value $\lambda = \langle a + a^\dagger \rangle_c \sim \sqrt{L}$. The contributions of the fluctuations, δH_{ac}, are small, $\sim 1/\sqrt{L}$, but we show that they become important in the long-time limit [110] . We define the following decoupled mean-field Hamiltonians

$$H_a(\lambda) = H_{kin} + H_{int} - \hbar\Omega\lambda O, \tag{4.20}$$
$$H_{cav}(\Delta) = H_c - \hbar\Omega(a + a^\dagger)\Delta.$$

In this case our unperturbed Liouvillian is given by

$$\mathcal{L}_0\rho \equiv -\frac{i}{\hbar}\left[H_a(\lambda) + H_{cav}(\Delta), \rho\right] + \frac{\Gamma}{2}\left(2a\rho a^\dagger - a^\dagger a\rho - \rho a^\dagger a\right). \tag{4.21}$$

The solutions to the equation $\mathcal{L}_0\rho^0 = \lambda_0\rho^0$, with $\mathrm{Re}\lambda_0 = 0$, are given by the factorized states

$$\rho^0 = \rho_a^0 \otimes \rho_c^0 \tag{4.22}$$
$$\rho_a^0 = |n_1(\lambda)\rangle\langle n_2(\lambda)|,$$
$$\rho_c^0 = |\alpha(\Delta)\rangle\langle\alpha(\Delta)|,$$

where the atomic part is given all combinations of the eigenstates $H_a(\lambda)|n(\lambda)\rangle = E_n(\lambda)|n(\lambda)\rangle$ and the cavity part is in a coherent state with the field

$$\alpha(\Delta) = \frac{\Omega}{\delta - i\Gamma/2}\Delta. \tag{4.23}$$

Thus, a general state in the decoherence free subspace is

$$\rho^0 = |\alpha(\Delta)\rangle\langle\alpha(\Delta)| \cdot \rho^a(\lambda), \ \text{with } \rho^a = \sum_{n_1, n_2} c(n_1, n_2)|n_1(\lambda)\rangle\langle n_2(\lambda)|. \tag{4.24}$$

The expectation values in the definitions of λ and Δ are taken with respect to ρ_0 and are, thus, determined by the unknown parameters $c(n_1, n_2)$. Therefore the density matrix of the atomic part of the system is not uniquely fixed by the mean field master equation, $\frac{\partial}{\partial t}\rho = \mathcal{L}_0(\rho)$. As described in Sec. 2.1 the usual approach [65] was to consider simply the ground state of H_a. We resolve the arbitrariness of this choice by taking the fluctuations perturbatively into account using the perturbation

$$\mathcal{L}_1\rho = -\frac{i}{\hbar}[\delta H_{ac}, \rho]. \tag{4.25}$$

This is justified by the fact that $\mathcal{L}_1$ scales with $1/\sqrt{L}$. We expect that this is the relevant perturbation in the thermodynamic limit. The perturbative approach then determines the time

4.3 Mean field decoupling with thermal fluctuations

evolution of the density matrix [110, 167, 168]

$$\frac{\partial}{\partial t}\rho^0 = \mathcal{L}_0\rho^0 + \frac{1}{\hbar^2}P_0\left[\delta H_{\rm ac}, \mathcal{L}_0^{-1}P_1\left[\delta H_{\rm ac}, \rho^0\right]\right]. \tag{4.26}$$

where P_0 is the projection to the decoherence free subspace of $\mathcal{L}_0$ and P_1 is the projection to the first excited subspace.

In the following, we will determine the states that span the decoherence free subspace and the excited subspace, and arrive at an explicit form of the equation of motion, Eq. (4.26). In order to simplify the following calculation, we transform our basis for the cavity operators to the shifted oscillator basis and make the following notations

$$a = \tilde{a} + \alpha, \tag{4.27}$$
$$a^\dagger = \tilde{a}^\dagger + \alpha^*,$$
$$a + a^\dagger - \lambda = \tilde{a} + \tilde{a}^\dagger,$$
$$|0\rangle \equiv |\alpha\rangle,$$
$$\tilde{a}|0\rangle = 0,$$
$$|1\rangle \equiv \tilde{a}^\dagger|0\rangle, \text{ with } \langle 0|1\rangle = 0.$$

In this basis we can find some of the eigenstates of $\mathcal{L}_0$

$$\mathcal{L}_0(|n,0\rangle\langle m,0|) = -i\frac{\Delta E_{n,m}}{\hbar}|n,0\rangle\langle m,0| \tag{4.28}$$

$$\mathcal{L}_0(|m,1\rangle\langle n,0|) = \left[i\left(\frac{\Delta E_{n,m}}{\hbar} - \delta\right) - \frac{\Gamma}{2}\right]|m,1\rangle\langle n,0|,$$

$$\mathcal{L}_0(|n,0\rangle\langle m,1|) = \left[-i\left(\frac{\Delta E_{n,m}}{\hbar} - \delta\right) - \frac{\Gamma}{2}\right]|n,0\rangle\langle m,1|,$$

$$\mathcal{L}_0(|n,0\rangle\langle m,2|) = \left[-i\left(\frac{\Delta E_{n,m}}{\hbar} - 2\delta\right) - \Gamma\right]|n,0\rangle\langle m,2|,$$

$$\mathcal{L}_0(|n,0\rangle\langle m,0| - |n,1\rangle\langle m,1|) = \left(-i\frac{\Delta E_{n,m}}{\hbar} - \Gamma\right)(|n,0\rangle\langle m,0| - |n,1\rangle\langle m,1|)$$

with $\Delta E_{n,m} = E_n - E_m$ the energy difference between two atomic eigenstates. We observe that states of the form $|n,0\rangle\langle m,0|$ are spanning the decoherence free subspace, Λ_0. We note that the non-diagonal eigenstates, for $n \neq m$, which are not degenerate in energy have a purely imaginary eigenvalue. The excited subspaces are spanned by states that contain excitations in the cavity field state. Now we can compute the commutator

$$\left[\delta H_{\rm ac}, \rho^0\right] = -\hbar\Omega\left[\left(\tilde{a} + \tilde{a}^\dagger\right)\tilde{O}, \rho^0\right] \tag{4.29}$$

$$= -\hbar\Omega\sum_{n_1,n_2}c(n_1,n_2)\left[\left(\tilde{a} + \tilde{a}^\dagger\right)\tilde{O}, |n_1,0\rangle\langle n_2,0|\right]$$

$$= -\hbar\Omega \sum_{n_1,n_2} c(n_1,n_2) \left(\tilde{O}|n_1,1\rangle\langle n_2,0| - |n_1,0\rangle\langle n_2,1|\tilde{O} \right)$$

$$= -\hbar\Omega \sum_{n_1,n_2} c(n_1,n_2) \sum_m \left(\tilde{O}_{n_1,m}|m,1\rangle\langle n_2,0| - \tilde{O}_{m,n_2}|n_1,0\rangle\langle m,1| \right),$$

where $\tilde{O} = O - \Delta = O - \langle O\rangle_{\mathrm{a}}$ and $\tilde{O}_{m,n}$ its matrix elements in the eigenbasis of H_{a}. As the the states $|m,1\rangle\langle n,0|$ are already eigenstates of $\mathcal{L}_0$ in an excited subspace the projector P_1, in Eq. (4.26) becomes the identity and the action of $\mathcal{L}_0^{-1}$ gives the inverse of the eigenvalues computed in Eq. (4.28). Thus, in the next step we need to compute the action of the second commutator from Eq. (4.26)

$$\left[\left(\tilde{a} + \tilde{a}^\dagger \right) \tilde{O}, |m,1\rangle\langle n_2,0| \right] = \sum_k \left(\tilde{O}_{m,k}|k,0\rangle\langle n_2,0| + \tilde{O}_{m,k}|k,2\rangle\langle n_2,0| - \tilde{O}_{k,n_2}|m,1\rangle\langle k,1| \right),$$

(4.30)

$$\left[\left(\tilde{a} + \tilde{a}^\dagger \right) \tilde{O}, |n_1,0\rangle\langle m,1| \right] = \sum_k \left(\tilde{O}_{n_1,k}|k,1\rangle\langle m,1| - \tilde{O}_{k,m}|n_1,0\rangle\langle k,0| - \tilde{O}_{k,m}|n_1,0\rangle\langle k,2| \right).$$

We need now to determine the action of the projector P_0 on the states which are not in the decoherence free subspace. Since $|n,1\rangle\langle m,1| = |n,0\rangle\langle m,0| - (|n,0\rangle\langle m,0| - |n,1\rangle\langle m,1|)$ we obtain that

$$P_0|n,1\rangle\langle m,1| = |n,0\rangle\langle m,0|. \qquad (4.31)$$
$$P_0|n,0\rangle\langle k,2| = 0.$$

The states $|n,0\rangle\langle k,2|$ and $|n,0\rangle\langle m,0| - |n,1\rangle\langle m,1|$ are projected out by P_0 as they are eigenstates of $\mathcal{L}_0$ with non-zero real part of the eigenvalues [see Eq. (4.28)]. Using the previous results Eq. (4.26) becomes

$$\hbar\frac{\partial}{\partial t}\rho^0 = -i \sum_{n_1,n_2} \Delta E_{n_1,n_2} c(n_1,n_2)|n_1,0\rangle\langle n_2,0| \qquad (4.32)$$

$$+\hbar^2\Omega^2 \sum_{n_1,n_2} c(n_1,n_2) \sum_{m,k} \left[\frac{1}{i\left(\Delta E_{n_2,m} - \hbar\delta\right) - \hbar\Gamma/2}\tilde{O}_{n_1,m}\tilde{O}_{m,k}|k,0\rangle\langle n_2,0| \right.$$

$$-\frac{1}{i\left(\Delta E_{n_2,m} - \hbar\delta\right) - \hbar\Gamma/2}\tilde{O}_{n_1,m}\tilde{O}_{k,n_2}|m,0\rangle\langle k,0|$$

$$-\frac{1}{-i\left(\Delta E_{n_1,m} - \hbar\delta\right) - \hbar\Gamma/2}\tilde{O}_{m,n_2}\tilde{O}_{n_1,k}|k,0\rangle\langle m,0|$$

$$\left. +\frac{1}{-i\left(\Delta E_{n_1,m} - \hbar\delta\right) - \hbar\Gamma/2}\tilde{O}_{m,n_2}\tilde{O}_{k,m}|n_1,0\rangle\langle k,0| \right].$$

4.3 Mean field decoupling with thermal fluctuations

The solution for the steady state, $\frac{\partial}{\partial t}\rho^0 = 0$, is given by

$$0 = -i\Delta E_{n_1,n_2}c(n_1,n_2) + \hbar^2\Omega^2 \sum_{m,k}\left[c(k,n_2)\frac{1}{i\left(\Delta E_{n_2,m} - \hbar\delta\right) - \hbar\Gamma/2}\tilde{O}_{k,m}\tilde{O}_{m,n_1}\right.\quad(4.33)$$

$$-c(m,k)\frac{1}{i\left(\Delta E_{k,n_1} - \hbar\delta\right) - \hbar\Gamma/2}\tilde{O}_{m,n_1}\tilde{O}_{n_2,k}$$

$$-c(k,m)\frac{1}{-i\left(\Delta E_{k,n_2} - \hbar\delta\right) - \hbar\Gamma/2}\tilde{O}_{n_2,m}\tilde{O}_{k,n_1}$$

$$\left.+c(n_1,k)\frac{1}{-i\left(\Delta E_{n_1,m} - \hbar\delta\right) - \hbar\Gamma/2}\tilde{O}_{m,k}\tilde{O}_{n_2,m}\right].$$

As Eqs. (4.32)-(4.33) are obtained via a perturbative expansion they no longer assure that the solutions are physical density matrix, since the condition of positive definiteness might not be fulfilled [170]. In principle Eqs. (4.32)-(4.33) can be solved using algebraic means. However, this is a difficult task, as the number of parameters $c(n_1,n_2)$ is given by the square of the dimension atomic many-body Hilbert space.

An important simplification occurs when the atomic system described by $H_a(\lambda)$ is interacting and has the property that it thermalizes. In such a case, we can describe local observables by approximating the density matrix by a thermal state [110],

$$\rho^a \sim \exp\{-\beta H_a(\lambda)\}. \quad (4.34)$$

This argument is justified when the thermalization time of the atomic system is short compared to the time-scale induced by scattering from photon fluctuations. This is the case for the relevant observables in the thermodynamic limit $L \to \infty$. Furthermore, by considering this Ansatz the positive definiteness is automatically fulfilled. Thus, we have reduced the problem to finding the temperature, $T = 1/k_B\beta$. For this we compute the time dependence of the energy of the atomic system

$$\left\langle \frac{\partial}{\partial t}H_a \right\rangle = \text{Tr}\left(H_a\frac{\partial}{\partial t}\rho^0\right) = \quad (4.35)$$

$$\hbar\Omega^2 \sum_{n_1,n_2} c(n_1,n_2) \sum_m \left[\frac{1}{i\left(\Delta E_{n_2,m} - \hbar\delta\right) - \hbar\Gamma/2}\Delta E_{n_2,m}\right.$$

$$\left.-\frac{1}{i\left(\Delta E_{n_1,m} - \hbar\delta\right) + \hbar\Gamma/2}\Delta E_{n_1,m}\right]\tilde{O}_{m,n_2}\tilde{O}_{n_1,m}.$$

Assuming $c(n_1,n_2) = c_{n_1}\delta(n_1,n_2)$, with $c_n = e^{-\beta E_n}/Z$, with Z the partition function, then the

energy transfer becomes

$$\left\langle \frac{\partial}{\partial t} H_{\mathrm{a}} \right\rangle = \frac{\hbar \Omega^2}{Z} \sum_{n,m} |\langle n|O - \Delta|m\rangle|^2 e^{-\beta E_m} \Delta E_{n,m} \frac{\hbar \Gamma}{(\Delta E_{n,m} + \hbar \delta)^2 + (\hbar \Gamma/2)^2}. \tag{4.36}$$

We can rewrite this equation as [110]

$$\begin{aligned}
\left\langle \frac{\partial H_{\mathrm{a}}}{\partial t} \right\rangle &= 2\hbar \Omega^2 \int d\omega (1 + n_B(\hbar\omega))\,\omega \operatorname{Im}\chi^R(\omega) \delta_\Gamma(\omega + \delta), \\
\delta_\Gamma(\omega) &= \frac{\Gamma/(2\pi)}{\omega^2 + (\Gamma/2)^2}
\end{aligned} \tag{4.37}$$

where $\delta_\Gamma(\omega+\delta)$ describes the spectral function of the cavity mode broadened by the dissipation strength, Γ, and $\chi^R(\omega)$ is the retarded correlation function of the operator O calculated for a thermal state of the Hamilitonian H_{a},

$$\operatorname{Im}\chi^R(\omega) = \sum_{n,m} |\langle m|O|n\rangle|^2 \frac{e^{-\beta E_m} - e^{-\beta E_n}}{Z} \pi \delta\left(\omega - \frac{E_n - E_m}{\hbar}\right). \tag{4.38}$$

In order to determine the steady state we solve $\left\langle \frac{\partial}{\partial t} H_{\mathrm{a}} \right\rangle = 0$ and the mean field equations, Eq. (4.19), to obtain both the temperature T and the odd-even imbalance, Δ, or, equivalently, the cavity field λ. Thus, in this approach we have reduced the problem of solving the Liouville equation, Eqs. (4.5)-(4.6), to the computation of the dynamical susceptibility $\chi^R(\omega)$ and the expectation value of energy for a thermal state of the Hamiltonian $H_{\mathrm{a}}(\lambda)$ [110]. In practice, we use exact diagonalization to determine both $\left\langle \frac{\partial H_{\mathrm{a}}}{\partial t} \right\rangle$ and Δ [110]. It is important to note that the mean field approximation is valid in the thermodynamic limit, but we perform the exact diagonalization of H_{a} for rather small systems (see Sec. 5.4), which will induce finite size errors. Luckily, for the parameters considered in Chap. 5, the finite size errors are very small, as they are strongly suppressed due to the broadening induced by the dissipation and the relatively high temperatures which we will obtain.

The properties of the steady state, Eq. (4.34), and how it compares with our numerical results will be discussed in Chap. 5. In Chap. 6 we will see how this procedure is affected by the existence of a strong symmetry, which prevents the atoms from thermalizing.

4.4 Short summary

To summarize, in this chapter we described in detail two analytical approaches based on the many-body adiabatic elimination formalism capable of tackling both short and global range interactions of an interacting many-body system coupled to a single dissipative bosonic mode. This is the first time this technique has been applied to atoms-cavity systems and provides a framework for investigating a wide class of open many-body systems beyond the often employed mean field approaches. We analyzed with the newly developed analytical methods the example of a Bose-Hubbard chain coupled to an optical cavity. We will show in the following chapters that the obtained steady state in both cases has a very different nature compared to

the expected mean field state. Both methods can be generalized to higher dimensional systems relevant to experimental setups [70, 71]. In Chap. 6, we extend the methods for the case in which a strong symmetry is present in the considered open system.

The first approach is a perturbation theory in the kinetic energy and applicable for strong dissipation strength [109]. We show how to derive the steady state of the system in the limit of large dissipation strength within the many-body adiabatic elimination formalism. The resulting state is a highly mixed state and the reduced density matrix in the atomic sector corresponds to an infinite temperature state.

The second approach is a perturbation theory in the fluctuations on top of the atoms-cavity mean field decoupling. The atomic state is described by a thermal state with an effective temperature. The computation of the temperature is based on two equilibrium quantities: the thermal expectation value $\Delta = \langle O \rangle$ and the linear-response susceptibility $\chi^R(\omega)$ [110]. Thus, it can also be combined with a wide range of analytical and numerical approaches developed for closed quantum systems in equilibrium as, for example, Monte Carlo techniques.

Fluctuations effects in many-body self-organization in a cavity

In recent years, an important experimental progress was the achievement of strong coupling of quantum matter to quantum light. Realizations of such systems nowadays reach from ultracold atomic gases strongly coupled to optical cavities [65, 67, 171] to the electron gas in solids coupled to THz cavities [172–174]. These realizations have opened exciting possibilities and have allowed the studies of self-organization phenomena and dissipative phase transitions, and the stabilization of exotic quantum phases due to the coupling with the quantum light [65, 175, 176].

The element of external control in the systems where the quantum matter is coupled to a cavity is two-fold. First, we have the classical transverse pump laser beams which realize the coupling between the particles and the cavity photons. By varying the intensity of the pump beams we can change the atom-photon coupling strength. This allows one to control dissipative phase transitions and to explore different steady state phases. Secondly, the dissipative coupling of the quantum light is crucial. The open character of the system is due to the photon losses via the cavity mirrors, which couple the cavity light to an external bath of electromagnetic modes. This ensures that the stabilization of complex states of light and matter is realized via a dissipative attractor dynamics. The steady state of the open system is approached exponentially fast, in the presence of a dissipative gap, which assures stability against perturbations.

One further advantage of the coupling of quantum matter to quantum light is the presence of the cavity induced long-range interactions, which assures a fast self-organization dynamics. The cavity induced long-range interactions have been experimentally realized in atomic gases with external optical lattice potentials coupled to the optical cavities [70–72]. These systems can be described by an extended Bose-Hubbard model. In this context the effect of the long-range interactions on the superfluid to insulator transition [100, 177–186] and the out-of-equilibrium dynamics [169] have been studied.

Due to the complexity of the models required to describe the coupled atomic cavity systems, theoretical treatments were to a large extent performed using a mean field decoupling of the cavity field and the atoms [65, 66, 100, 101]. These usually assume an effective ground state for the particles, as seen in Sec. 2.1. Recently efforts are made to go beyond the mean field

description [118, 155, 187, 188]. So far the exact coupling between the atomic and photonic states has been included only for small systems of one or two atoms, or two sites [102–107], non-interacting two-level atoms [189–191], or in closed systems [192].

In the work presented in this chapter, we go beyond the mean field approximation and investigate the combined atom-cavity system with the help of the several new methods developed in this thesis. We employ the quasi-exact numerical simulations based on matrix product states (cf. Sec. 3.2) and two many-body adiabatic elimination approaches (cf. Chap. 4) [108–110]. All these methods overcome the arbitrariness of the mean field approach, either by treating the atoms-cavity coupling exactly, or by taking fluctuations induced by the light-matter coupling perturbatively into account. These methods enable us to analyze the many-body aspects of the self-ordering processes of the interacting bosonic atoms coupled to the optical cavity. We investigate the nature of the arising steady states for a wide range of parameters. We show that the admixture of excited states beyond the mean field steady state plays an important role for all parameters considered. We find that the fluctuations beyond the mean field description are crucial in order to determine the mixed state (finite temperature state) character of the self-organization phase transition and steady states. In particular, we show that, in certain regimes, the atoms are described by large effective temperatures and in the limit of very lossy cavity mirrors the atomic sector approaches the infinite temperature state. Our findings question the nature of the pure steady states and phase transitions previously predicted by the zero-temperature mean field theories [108, 110].

Throughout this chapter we present results obtained with our newly developed tMPS method for coupled cavity-atoms systems, which we described in Sec. 3.2. In Sec. 5.3 we also consider the many-body adiabatic elimination approach with the kinetic energy as a perturbation and in Sec. 5.4 the many-body adiabatic elimination approach with the fluctuations in the atom-cavity coupling as the perturbation, methods described in Chap. 4. Sec. 5.2 and Sec. 5.3 will follow the presentation given in Ref. [108] and Sec. 5.4 the results from Ref. [110]. The work presented in the current chapter (based on Refs. [108, 110]) has been performed in collaboration with Achim Rosch, Alla Bezvershenko and Helmut Ritsch. In this work, I performed the tMPS numerical simulations and derived the equations of motion, with their respective steady states, within the many-body adiabatic elimination framework. The numerical results of the mean field with thermal fluctuations represented in Fig. 5.7 and Fig. 5.8, and the analytical results from Eqs. (5.9)-(5.11) were obtained by Alla Bezvershenko and Achim Rosch [193].

5.1 Atoms-cavity coupled system

In the following, we consider the system we described in Sec. 2.1 of interacting bosons confined to a one-dimensional chain coupled to a single cavity mode and transversely pumped with a standing-wave laser beam [108] (see Fig. 2.2 in Sec. 2.1). To make this chapter self-contained we repeat briefly in the following the Lindblad equation for the density operator ρ given by [56, 65, 100, 114]

$$\frac{\partial}{\partial t}\rho = -\frac{i}{\hbar}\left[H, \rho\right] + \frac{\Gamma}{2}\left(2a\rho a^{\dagger} - a^{\dagger}a\rho - \rho a^{\dagger}a\right). \tag{5.1}$$

where the bosonic operators a and $a^\dagger$ are the annihilation and creation operators for the photon mode of the cavity and Γ the dissipation strength. The corresponding Hamiltonian is given by [65, 100, 101]

$$H = H_c + H_{\text{kin}} + H_{\text{int}} + H_{\text{ac}} \tag{5.2}$$
$$H_c = \hbar\delta a^\dagger a$$
$$H_{\text{kin}} = -J \sum_{j=1}^{L-1}(b_j^\dagger b_{j+1} + b_{j+1}^\dagger b_j)$$
$$H_{\text{int}} = \frac{U}{2} \sum_{j=1}^{L} n_j(n_j - 1)$$
$$H_{\text{ac}} = -\hbar\Omega(a + a^\dagger)O, \quad O = \sum_{j=1}^{L}(-1)^j n_j.$$

The term H_c describes the cavity mode with a detuning between the cavity mode and the transverse pump beam $\delta = \omega_c - \omega_p$, in the rotating frame of the pump beam. The operators b_j and $b_j^\dagger$ are the bosonic annihilation and creation operators of the atoms on site j and $n_j = b_j^\dagger b_j$. L denotes the number of sites of the bosonic chain and the total number of bosons is N. H_{kin} describes the tunneling processes of the atoms along the chain with the tunneling amplitude J and the term H_{int} represents the repulsive on-site interaction of strength $U > 0$. The coupling between the atoms and the cavity field is described by H_{ac}. This form of the coupling, with the effective pump amplitude Ω, stems from the assumed commensurability of the cavity mode with twice the periodicity of the lattice spacing within the chain, where $\Delta = \langle O \rangle$ is the total imbalance between the odd and even sites of the chain. In the following we scale the coupling strength as $\Omega\sqrt{N}$, in order to make our results independent of the particle number.

Whereas already to determine the time-evolution of the atomic Bose-Hubbard model alone is very involved, here additional complications arise due to the large and, in principle, unlimited dimension of the Hilbert space of the photonic mode, as we have noted in Sec. 3.2. This challenge is typically addressed by the adiabatic elimination of the cavity field, using a mean field decoupling for the atoms and the cavity mode [65], as we saw in Sec. 2.1. Within this crude approximation one obtains a zero-temperature self-organization transition. Above a certain threshold $\Omega_{\text{MF},c}\sqrt{N}$ of the pump power $\Omega\sqrt{N}$ the cavity field $\langle a \rangle$ takes a finite value, either $\pm\alpha$, and the atoms self-organize into a density modulated pattern either on the odd or even sites of the chain, depending on the sign of α. The corresponding density matrices are the ones of pure zero temperature states

$$\rho_{\text{MF}} = |\alpha(\Delta_{\text{eff}}), \Delta_{\text{eff}}\rangle\langle\alpha(\Delta_{\text{eff}}), \Delta_{\text{eff}}|, \tag{5.3}$$

with $\alpha(\Delta) = \frac{\Omega}{\delta - i\Gamma/2}\Delta$ and Δ_{eff} is the expectation value of the odd-even imbalance in the ground state of an effective atomic model, solved together with a self-consistency equation (see Sec. 2.1). For large coupling strengths $\Omega\sqrt{N}$ the effective imbalance tends towards its maximal value

$|\Delta_{\text{eff}}| \approx N$. As for our comparisons we look at the photon number, we mention that within the mean field theory, the sudden onset of the cavity field is also reflected in the behavior of the photon number n_{MF}, since $n_{\text{MF}} = |\langle a \rangle|^2 = \frac{\Omega^2}{\delta^2 + \Gamma^2/4}\Delta_{\text{eff}}^2$ [blue line in Fig. 5.1 (a)].

The appearance of two steady states with $\pm \alpha$ within the mean field analysis is due to spontaneous breaking of the $\mathbb{Z}_2$ symmetry of the Hamiltonian, Eq. (5.2), at the phase transition threshold. This $\mathbb{Z}_2$ symmetry is associated with the inversion of the sign of the cavity field, a, and the atomic odd-even imbalance, Δ. However, the $\mathbb{Z}_2$ symmetry is only a weak symmetry of the Liouvillian [115, 117], since the transformation does not commute with the jump operator a of the Lindblad equation, Eq. (5.1). Thus, for any finite system we expect a zero expectation value for the cavity field and the atomic state in a mixture of being either on the odd or on the even sites in the steady state, in the self-organized phase [102, 103, 106, 118].

In the following, we present our results in which we take the fluctuations beyond the mean field decoupling of the atom-cavity coupling into account, either exactly [108, 109] or perturbatively [110]. All these approaches offer new insights into the self-organization of interacting particles and quantum light, which we contrast with the mean field results.

The numerical tMPS results which we present in this chapter, if not stated otherwise, they are taken at long times $tJ = 49.75\hbar$. We found that these long time values are in many cases already close to the steady state values [108, 110]. As shown in Sec. 3.2 the convergence of our results is sufficient [109] for at least 500 trajectories, the truncation error goal of 10^{-12}, the time-step of $\mathrm{d}tJ/\hbar = 0.0125$ or smaller, a cut-off of the local Hilbert space of the photon mode between $N_{\text{pho}} = 55$ and $N_{\text{pho}} = 10$. The error bars in all figures in this chapter represent the standard deviation of the Monte Carlo average.

5.2 Weak dissipation regime: mixture of density wave states

We begin by analyzing the behavior of the system across the self-organization phase transition. We want to characterize the nature of the light and matter states in the presence of dissipation and identify deviations from the mean field approach. In this section, we choose a regime with relative weak dissipation strength, $\hbar\Gamma/J = 1$, which should be favorable to the mean field treatment.

We look at the photon number in the cavity as a function of the pump strength $\Omega\sqrt{N}$, as seen in Fig. 5.1 [108]. We observe the self-organization transition from an empty cavity $\langle a^\dagger a \rangle/N \approx 0$, to an occupied cavity as we increase the pump strength. In our numerical tMPS results for the photon number, depicted by red symbols in Fig. 5.1 (a), we see a smooth increase across the self-organization threshold predicted by the mean field treatment. The smooth increase is expected for the system of finite size. However, the values of our numerical results remain a bit below n_{MF} for all considered coupling strenghts, this is a first indication of deviations from the mean field state. We will show later in this section that this has its origin in the admixture of states with a reduced photon number.

In order to get more insight into the obtained photonic state, we study the phase space distribution of the cavity field, represented by the Q-function $Q(\alpha) = \text{tr}\left(\langle \alpha | \rho | \alpha \rangle \right)$, where $|\alpha\rangle$ is a photonic coherent state. We can see in Fig. 5.1(b), that for $\hbar\Omega\sqrt{N} = 1.12J$, which is below the mean field threshold $\Omega_{\text{MF},c}\sqrt{N}$, the Q-function $Q(\alpha)$ has a maximum at $\alpha = 0$ resembling
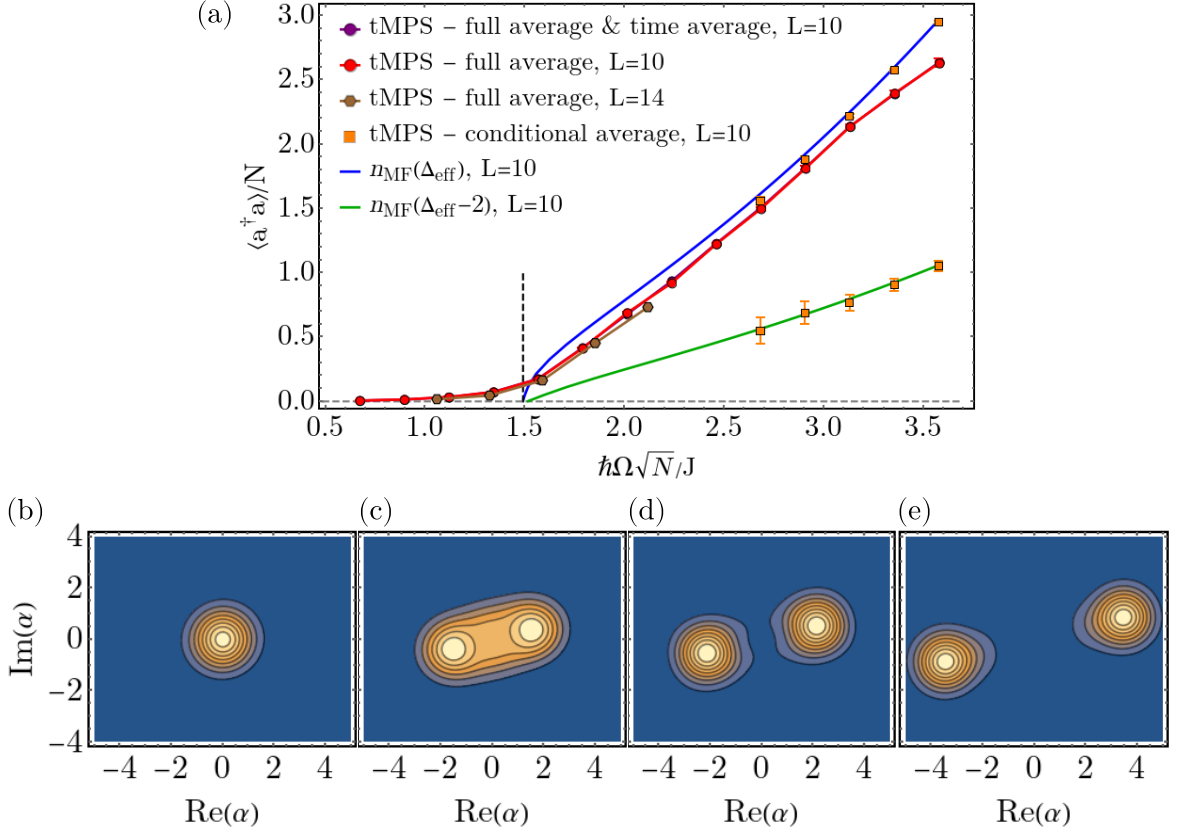
Figure 5.1: (a) The scaled photon number, $\langle a^\dagger a \rangle / N$, as a function of $\hbar\Omega\sqrt{N}/J$, for $N/L = 1/2$, $\hbar\delta/J = 2$, $U/J = 2$, and $\hbar\Gamma/J = 1$. The purple symbols (below the red symbols) represent a time average for $tJ \in (44.75\hbar, 49.75\hbar)$. For the orange symbols the trajectories are averaged depending on the final photon number. The blue (green) curves represent the mean-field value of the photon number for the imbalance Δ_{eff} ($\Delta_{\mathrm{eff}} - 2$). The vertical dashed line marks $\Omega_{\mathrm{MF},c}\sqrt{N}$. Lines joining the symbols and are guide to the eyes. (b)-(e) The Q-function for $\hbar\Omega\sqrt{N}/J \in \{1.12, 1.79, 2.24, 3.35\}$, $L = 10$, $N = 5$, $\hbar\delta/J = 2$, $U/J = 2$, $\hbar\Gamma/J = 1$, and $tJ = 49.75\hbar$. ©2019 American Physical Society, published in [108].

a coherent state with zero photons. In contrast, above the threshold ($\Omega\sqrt{N} > \Omega_{\mathrm{MF},c}\sqrt{N}$) the Q-function develops two maxima, as seen in Fig. 5.1(c). If we increase $\Omega\sqrt{N}$ further the Q-function indicates the photonic state consisting of a superposition of two states with opposite cavity fields and a small overlap, Fig. 5.1(d)-(e). This indicates that the $\mathbb{Z}_2$ is not broken at the transition. For the mean field coherent state, which breaks the $\mathbb{Z}_2$ symmetry, we would expect a single peak in Q-function centered at a finite value of the cavity field, either α or $-\alpha$. We see that the tMPS state has a dominant contribution which resembles the mixture of both mean field states. However, we observe that both peaks in $Q(\alpha)$ deviate from the circular shape expected for a coherent state and states with a lower photon number are also populated.

It is interesting now to investigate the corresponding nature of the atomic states and to determine deviations from the mean field predicted density wave [108]. Above the mean field

5.2 Weak dissipation regime: mixture of density wave states
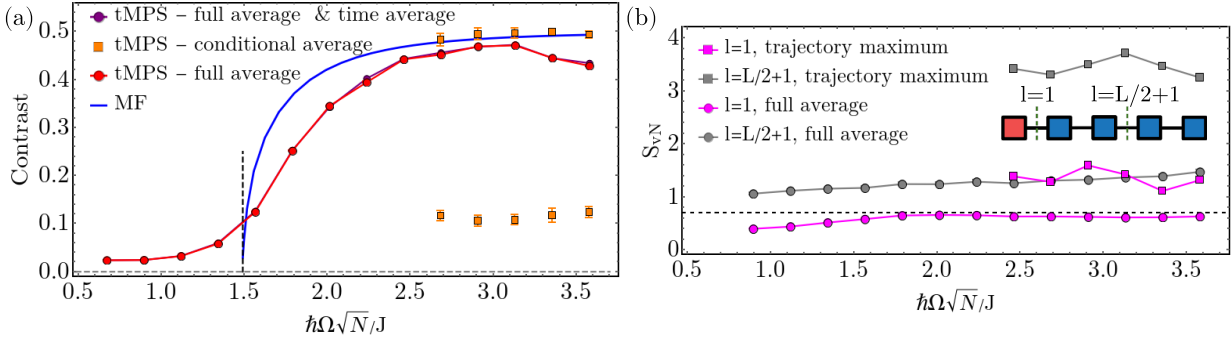
Figure 5.2: (a) The averaged contrast of the density-density correlation as a function of $\hbar\Omega\sqrt{N}/J$, for $N/L = 1/2$, $\hbar\delta/J = 2$, $U/J = 2$, and $\hbar\Gamma/J = 1$. The purple symbols (below the red symbols) represent a time average for $tJ \in (44.75\hbar, 49.75\hbar)$. For the orange symbols the trajectories are averaged depending on the final photon number. (b) The von Neumann entropy, S_{vN}, as a function of $\hbar\Omega\sqrt{N}/J$, for two bipartitions of the system, between the cavity site and atomic chain (bond $l = 1$) and in the middle of the atomic chain (bond $l = L/2 + 1$). The circles represent the average over all trajectories and the squares the maximum among the trajectories, for $L = 10$. The dashed line represents $\log(2)$. ©2019 American Physical Society, published in [108].
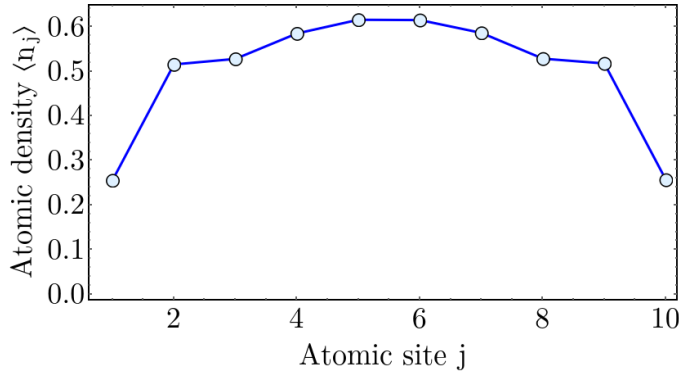
Figure 5.3: The atomic density profile for $\hbar\Omega\sqrt{N}/J = 3.35$, $L = 10$, $N = 5$, $\hbar\delta/J = 2$, $U/J = 2$, $\hbar\Gamma/J = 1$, and $tJ = 49.75\hbar$.

threshold, we observe the characteristic staggered density wave in the density-density correlations. We quantify this staggering by computing the average contrast between the maxima and the minima $\frac{1}{L-2}\sum_j \left(\langle n_j n_{j+2}\rangle - \langle n_j n_{j+1}\rangle \right)$ as a function of the scaled coupling $\Omega\sqrt{N}$, presented in Fig. 5.2(a). We see that as we increase the pump strength $\Omega\sqrt{N}$ across the self-organization threshold the staggering increases. This indicates that the density wave builds up in the system. This modulation cannot be seen in the density profile, Fig. 5.3. This further supports the fact that the $\mathbb{Z}_2$ symmetry is not broken spontaneously in our finite system and the atoms are in a mixture of either being on the odd, or the even sites. Compared to the mean field state, above the self-organization threshold the staggering contrast rises already below the mean field threshold. However, above the threshold our numerical results remain below the mean field prediction. The spatial dependence of the density density correlations $\langle n_2 n_{d+2}\rangle$ for $\hbar\Omega\sqrt{N}/J = 3.35$ and
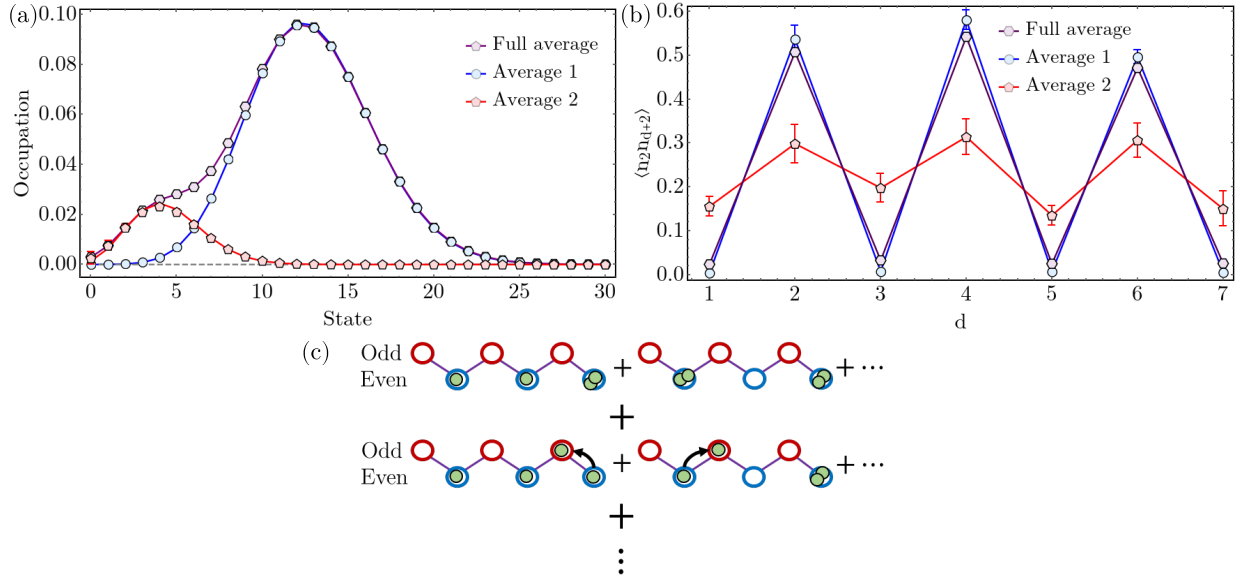
Figure 5.4: (a) Photon number distributions, $p_n = \mathrm{tr}\left(\langle n|\rho|n\rangle\right)$, and (b) the density-density correlations, $\langle n_2 n_{d+2}\rangle$, for $\hbar\Omega\sqrt{N}/J = 3.35$, $L = 10$, $N = 5$, $\hbar\delta/J = 2$, $U/J = 2$, $\hbar\Gamma/J = 1$ and $tJ = 49.75\hbar$, full average and with the trajectories averaged separately depending on the final photon number. In (a) the continuous lines show the Poisson distributions with the corresponding average photon number. (c) Sketch of the atomic sector of states with perfect imbalance, $\Delta = N$, and states with a reduced imbalance due to a defect, $\Delta = N - 2$. ©2019 American Physical Society, panels (a)-(c) published in [108].

$\hbar\Gamma/J = 1$ is shown in Fig. 5.4(b) (purple line). The fact that at odd distances the correlations are not exactly zero even at relatively large values of the pump strength hints that states without a perfect imbalance are admixed into the state.

The von Neumann entropy S_{vN} in the quantum trajectories [Fig. 5.2(b)] [109] measures the entanglement present in each trajectory. We note that the von Neumann entropy averaged over the quantum trajectories is not a measure of the entanglement present in the resulting density matrix. As we saw in Sec. 3.2, the von Neumann entropy is one of the crucial convergence parameters of MPS methods [124], since the presence of entanglement typically limits the possible compression. We observe that S_{vN} is finite and saturates in time (see Sec. 3.2) [108, 109]. Thus, we can be confident that our approach captures the dynamics of the system correctly. In Fig. 5.2(b) we see S_{vN} computed between the photon mode and the atomic chain seems to be independent of Ω above the threshold and close to $\log(2)$. We attribute this value to the coherent superposition of the two states corresponding to a different sign of the photon field in each quantum trajectory.

In order to analyze the origin of the deviations from the mean field approach we consider the single quantum trajectories sampled in our Monte Carlo procedure. We observe that the trajectories stabilize at two different photon numbers. Thus, we implemented a conditional averaging process, depending on the final photon number. The two obtained photon number distributions [Fig. 5.4(a)], agree well with a Poisson distribution with the corresponding average

photon number, as expected for a coherent state. In contrast to the full average, the expectation value averaged over the first class of trajectories of the photon number [Fig. 5.1(a)] and the staggering contrast [Fig. 5.2(a)] agree with the mean field prediction. Thus, the state resembles a good charge density wave in the first class of trajectories. This is further confirmed by the density-density correlations, which for the first class of trajectories are very close to zero at odd distances, Fig. 5.4(b).

In contrast, we attribute the second class of trajectories to states which have an additional defect due to the tunneling of an atom. In the limit of perfect imbalance $\Delta_{\text{eff}} = N$, these states would have only one atom at the "wrong" site [Fig. 5.4(b)]. More generally, the reduced average value of the photon number can be well explained assuming that the imbalance is reduced as $\Delta \approx \Delta_{\text{eff}} - 2$ [Fig. 5.1(a)]. The photon number distribution resembles a coherent state with this lower photon number [Fig. 5.4(a)]. Due to the extra defect, the contrast of the density-density staggering is reduced as seen in Fig. 5.2(a) and Fig. 5.4(b).

In certain trajectories we observe transitions between the two classes of states, characterized by the tunneling process of an atom, correlated with a sudden increase, or decrease, of the photon number. However, due to the suppression of the tunneling in the self-organized phase and the small overlap of the two corresponding photonic states for large $\Omega\sqrt{N}$ these processes become very rare. For the parameters of Fig. 5.4 we observe such transitions in the time interval $30 < tJ/\hbar < 50$ in 22 trajectories out of 600. We further note that we can distinguish between the two distributions only for $\hbar\Omega\sqrt{N}/J \geq 2.68$, as for lower pump strengths the individual quantum trajectories are too noisy due to the low photon number.

The presence of the trajectories which belong to two states different in nature strongly suggests that the numerically observed steady state is a mixture of several states with these two dominant contributions. This is further confirmed by exact diagonalization studies on small systems which show a unique steady state being the mixture of the identified states. Therefore, we identify a crucial deviation from the mean field predictions of a pure state phase transition [108].

5.3 Large dissipation regime: towards the fully mixed state

The deviations from the mean field predictions become even more prominent in the regime of strong dissipation [108]. In this regime, we can employ the many-body adiabatic elimination approach with the kinetic energy as a perturbation [109]. As we saw in Eq. (4.17) in Sec. 4.2 the steady state for finite interaction is given by

$$\rho_{\text{mix}} = \frac{1}{\mathcal{N}} \sum_{\{n_i\}} |\alpha(\Delta), n_1, \ldots, n_L\rangle\langle\alpha(\Delta), n_1, \ldots, n_L|, \tag{5.4}$$

[109]. The sum runs over all possible density configurations $\{n_i\}$ with $\mathcal{N}$ the total number of atomic configurations, and the coherent state is set by $\alpha(\Delta) = \frac{\Omega}{\delta - i\Gamma/2}\Delta$, where the value Δ is set by $\{n_i\}$. This state, ρ_{mix}, is very distinct from the mean field state and is fully mixed in the atomic sector. This very distinct nature of the steady state is also reflected in the physical observables. ρ_{mix} has a zero expectation value of the cavity field, $\langle a \rangle = 0$, capturing the weak
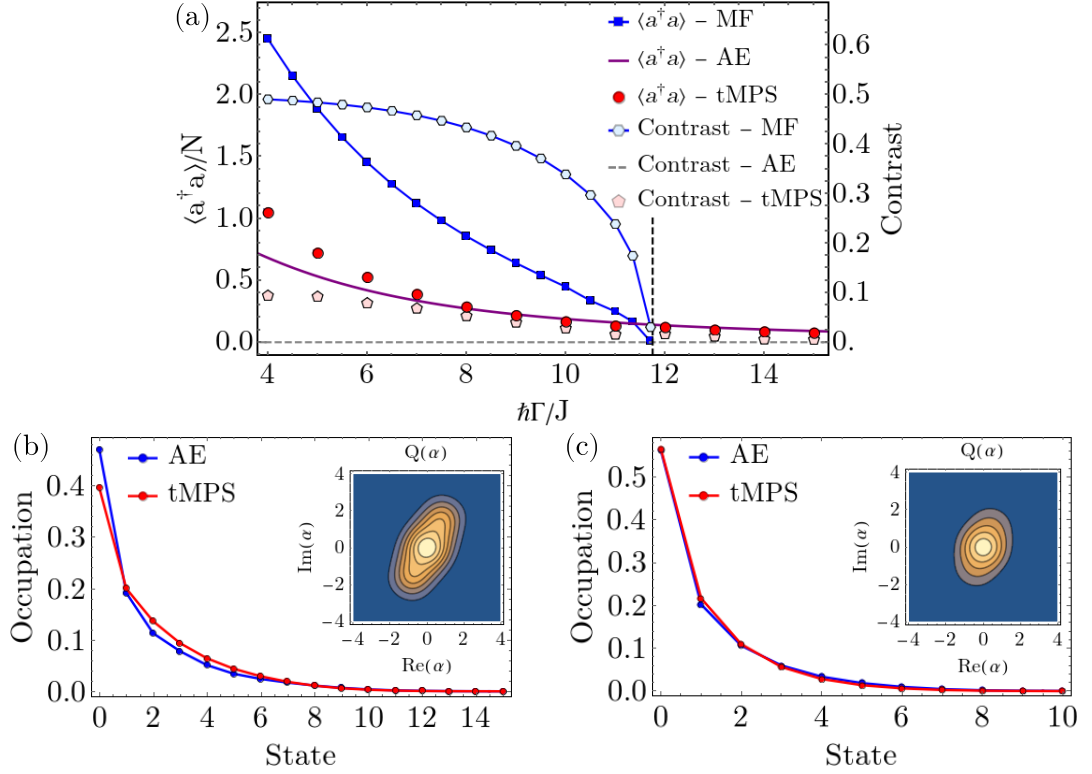
Figure 5.5: (a) The scaled photon number, $\langle a^\dagger a\rangle/N$ and the averaged contrast of the density-density correlation, $\frac{1}{L-2}\sum_j (\langle n_j n_{j+2}\rangle - \langle n_j n_{j+1}\rangle)$, as a function of $\hbar\Gamma/J$ using tMPS, mean-field (MF) and many-body adiabatic elimination (AE). (b)-(c) The full photon number distribution, $p_n = \text{tr}\,(\langle n|\rho|n\rangle)$ for (b) $\hbar\Gamma/J = 7.5$ and (c) $\hbar\Gamma/J = 10$. The insets present the corresponding Q-function determined by tMPS. The parameters are chosen to be $L = 10$, $N = 5$, $\hbar\Omega\sqrt{N}/J = 4.47$, $\hbar\delta/J = 2$, $U/J = 2$ ©2019 American Physical Society, panels (a)-(c) published in [108].

$\mathbb{Z}_2$ symmetry of the system [109], but has a finite expectation value of the photon number. The average photon number for the state ρ_{mix} is given by

$$\langle a^\dagger a\rangle = \sum_\Delta \frac{(\Omega\sqrt{N})^2}{\delta^2 + \Gamma^2/4}\frac{c_\Delta}{\mathcal{N}}\frac{\Delta^2}{N}, \tag{5.5}$$

where the sum is taken over the set $\Delta \in \{-N, -N+2, \ldots, N-2, N\}$ and c_Δ being the number of states with a certain imbalance Δ, given by

$$c_\Delta = \binom{\frac{1}{2}(L+N+\Delta)-1}{\frac{1}{2}(N+\Delta)}\binom{\frac{1}{2}(L+N-\Delta)-1}{\frac{1}{2}(N-\Delta)}. \tag{5.6}$$

In the following, we attribute the strong deviations from the mean field state to the admixture of states which correspond to more and more defects until in the limit of very large

5.3 Large dissipation regime: towards the fully mixed state
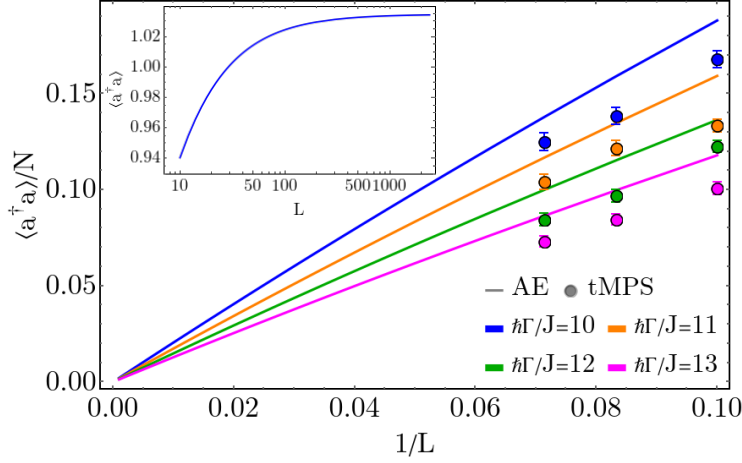
Figure 5.6: The dependence of the scaled photon number $\langle a^\dagger a \rangle/N$, on $1/L$. The parameters used are $N = L/2$ particles, $\hbar\Gamma/J \in \{10, 11, 12, 13\}$, $\hbar\delta/J = 2$, $U/J = 2$ and $\hbar\Omega\sqrt{N}/J = 4.47$. The behavior is consistent with a L^{-1} scaling of $\langle a^\dagger a \rangle/N$. In the inset we have the dependence of the photon number, $\langle a^\dagger a \rangle$, on the system size, L, which seems to saturate at large L. ©2020 American Physical Society, published in [109]

dissipation Γ the state ρ_{mix} is reached. We can observe that for a large Γ the photon number computed with tMPS deviates strongly from the mean field value, but matches fairly well with the value computed for ρ_{mix} [Fig. 5.5(a)]. In particular, whereas the mean field approach predicts that at $\hbar\Gamma/J \approx 11.6$ a transition back to the normal phase occurs, we do not observe this transition, as the photon number remains finite in the numerical results [108, 109]. The very good agreement with the adiabatic elimination results can be also seen in the distribution of the photon number [Fig. 5.5(b)-(c)]. Where at $\hbar\Gamma/J = 7.5$ still small deviations are present at low number states, the distribution for $\hbar\Gamma/J = 10$ agrees almost perfectly. The Q-function no longer has two maxima at large Γ, plotted in the insets of Figs. 5.5(b)-(c), but only one maximum at $\alpha = 0$ and a squeezed profile.

The same agreement of our numerical results and the many-body adiabatic elimination state can be seen in the staggered contrast of the density-density correlations. For ρ_{mix} the contrast in the staggering vanishes. Increasing Γ, we see that the contrast of the numerical results approaches zero, Fig. 5.5(a). Thus, at large values of the photon losses, the self-organized steady state no longer resembles a staggered density wave state. It is a mixture with a contribution from many atomic and photonic states. The steady state, ρ_{mix}, is a mixture of separable states, thus, no entanglement is present between the photons and the atoms. However, the strong cavity-atoms coupling is reflected in the fact that in each of the pure states present in the mixture the cavity field is fully determined by the atomic density profile.

In the thermodynamic limit the adiabatic elimination state, ρ_{mix}, predicts that the scaled average photon number $\langle a^\dagger a \rangle/N$ goes to zero [109]. By plotting the scaled photon number $\langle a^\dagger a \rangle/N$ at a fixed filling N/L, Fig. 5.6, we can see that this quantity vanishes as L^{-1} at large L. We observe a good agreement between ρ_{mix} and the tMPS results for different system sizes regarding the scaling. This implies that even though the scaled photon density per atom is

finite for any finite size system, it goes to zero in the thermodynamic limit, $L \to \infty$. Thus, the many-body adiabatic elimination method tells us that in the thermodynamic limit at large dissipation strengths the system is no longer in a superradiant state with a finite $\langle a^\dagger a \rangle / N$, but in a state with an average number of zero photons and a fully mixed atomic sector [109]. This is very distinct to the normal state predicted by the mean field approach. Despite the fact that in both states the average photon number vanishes, the atomic part of the mean field state is a pure state and not the infinite temperature state.

Our findings presented so far rise the question regarding the nature of phase transition in the thermodynamic limit [108, 109]. In particular, our results suggest that the nature of this transition would not correspond to a zero-temperature phase transition, but that the transition would be dominated by the admixture of excited states. We will see in the following section that the phase transition has indeed a finite temperature character. Assuming a fast thermalization of the atoms, including the fluctuations on top of the cavity-atoms mean field decoupling leads to a finite temperature character of the phase transition [110].

5.4 Thermal fluctuations in the thermodynamic limit
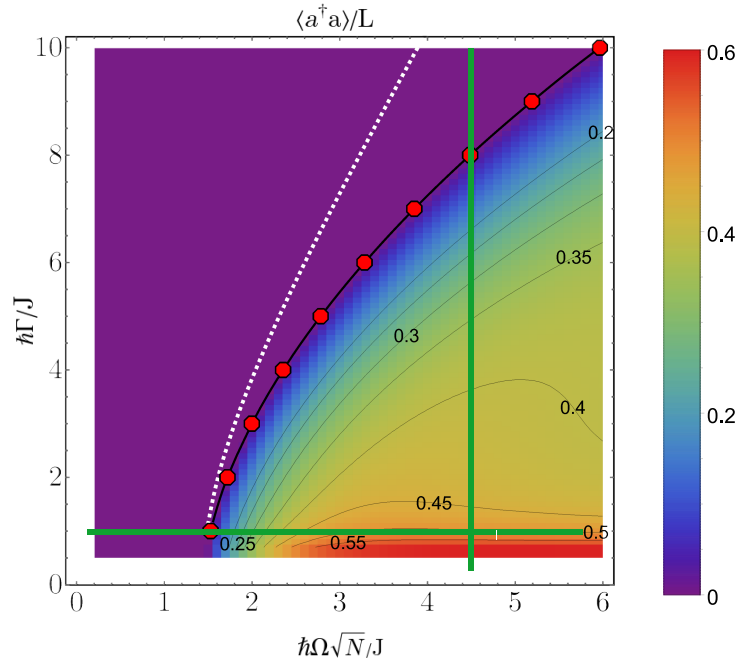
Figure 5.7: Phase diagram as function of the dissipation strength Γ and the coupling strength $\hbar\Omega\sqrt{N}/J$ for $\hbar\delta/J = 2$, $U/J = 2$, $N = L/2$. The color and contour lines encode $\langle a^\dagger a \rangle / L$, which vanishes in the disordered phase and is finite in the self-organized phase. Remarkably, the photonic density, $\langle a^\dagger a \rangle / L$, reaches the universal value $3/8 = 0.375$ deep in the ordered phase due to a heating effect, see Eq. (5.8). The dashed line corresponds to the zero temperature mean field result of the threshold. The green lines mark the cuts through the phase diagram plotted in Fig. 5.8. Figure adapted from Ref. [110].

In this section, we want to characterize the nature of the admixture of the excited states which we identified in the previous sections. For this we employ the perturbation theory in the

Figure 5.8: The dependence of the (a)-(b) photon number and (c)-(d) the effective temperature on the coupling strength and dissipation strength. The parameters considered are for $U/J = 2$, $\hbar\delta/J = 2$, $N = L/2$, $\hbar\Omega\sqrt{N}/J = 4.47$ and $\hbar\Gamma/J = 1$. We compare the results of our mean field with thermal fluctuations approach with the numerical exact tMPS results and the zero temperature mean field. The vertical dashed line corresponds to the transition threshold computed with the mean field with thermal fluctuations approach. Figure adapted from Ref. [110].

fluctuations on top of the mean field decoupling, which we developed in Sec. 4.3 [110]. In this approach we obtain that the photons are in a coherent state and we assume that the atoms in a thermal state

$$\rho_{\text{thermal}} = |\alpha(\Delta)\rangle\langle\alpha(\Delta)| \cdot \exp\{-H_{\text{a}}(\alpha)/k_B T\}, \tag{5.7}$$

where the cavity field and the temperature of the atoms are determined self-consistently from the perturbative equations of motion (see Sec. 4.3). One can observe that for $T \to 0$ one recovers the mean field state (see Sec. 2.1). In the following, we will refer to the mean field approach as the zero temperature mean field to avoid confusion.

We start by analyzing how the phase diagram changes within the mean field with thermal fluctuations approach, as presented in Fig. 5.7. In the normal phase the photon number vanishes. Once we go above the threshold, $\Omega\sqrt{N} > \Omega_c\sqrt{N}$, to the self-organized phase the photon density, $\langle a^\dagger a\rangle/L$, grows proportional to $\Omega\sqrt{N} - \Omega_c\sqrt{N}$ close to the transition. Surprisingly, we

find that the photon density saturates for large coupling strengths, $\Omega\sqrt{N} \to \infty$. Analytically, we see that deep in the superradiant phase the effects of heating compensate exactly the increase due to a higher coupling strength in the photon number [110]

$$\frac{\langle a^\dagger a \rangle}{L} \approx \frac{1}{2}n(1+n) \qquad \text{for } \Omega\sqrt{N} \to \infty, \tag{5.8}$$

such that the photon density acquires a universal value which only depends on the atomic density. For the parameters used in Fig. 5.7 we considered a density of $n = 1/2$ and, therefore, we obtain $\langle a^\dagger a \rangle/L = 3/8$. In contrast, the zero-temperature mean field theory predicts a photon number which grows quadratically with the coupling strength.

One other important deviation from the zero-temperature mean field that we observe in Fig. 5.7 is the different position of the transition threshold. We see that the critical coupling $\Omega_c\sqrt{N}$ deviates stronger from the zero temperature mean field prediction (white dashed line) as we increase the dissipation strength Γ. This explains why in the previous section we did not observe the phase transition at the value predicted by the zero-temperature mean field (see Fig. 5.5). Analytically, it can be obtaned from a high-temperature expansion for large Γ or δ that [110]

$$\Omega_c\sqrt{N} \approx \frac{\delta^2 + (\Gamma/2)^2}{\delta\sqrt{8n(1+n)}} \qquad \text{for } \hbar\Gamma \gg J, U \text{ or } \hbar\delta \gg J, U. \tag{5.9}$$

Within the zero-temperature mean field approximation, in contrast, the critical coupling is predicted to grow proportional to $\sqrt{1 + \frac{\Gamma^2}{4\delta^2}}$ instead.

In the following, we look at two cuts through the phase diagram in Fig. 5.8 [110], the parameters correspond to the two green lines in Fig. 5.7 and to the parameter sets used in Sec. 5.2 and Sec. 5.3. The photon density and the effective atomic temperatures are shown in Fig. 5.8. Upon increasing the coupling strength in the mean field with thermal fluctuations approach [see Fig. 5.8 (a)], a finite photon number $\langle a^\dagger a \rangle/L$ arises for above a critical value, which signals a transition to the self-organized phase. If we compare the behavior with the $T = 0$ mean field the increase of $\langle a^\dagger a \rangle$ is strongly suppressed for large couplings. The reason is the strong increase of the effective temperature in the ordered phase shown in Fig. 5.8 (c). Note that T is finite at the critical value of the coupling and even below the transition threshold the fluctuations beyond mean field induce a temperature of $k_B T/J \approx 1$.

The strong influence of the temperature is very evident also when we study the transition as a function of dissipation strength, in Fig. 5.8 (b) and (d). For the considered parameters, the transition to the self-organized states is considerably shifted from approximately $\hbar\Gamma/J \approx 12$ for the $T = 0$ result to $\hbar\Gamma/J \approx 8$ for the finite temperature mean-field method.

We compare the results of the mean field with thermal fluctuations approach with our numerical exact tMPS calculation for system sizes up to $L = 14$ [108–110]. Close to the transition thresholds, we find a very good agreement between the two methods, which further strengthens our previous findings that in tMPS results excited states play an important role in the steady

state. We can also extract an effective temperature from our tMPS result, as discussed in Appendix B, which reproduces in Fig. 5.8 (d) the characteristic minimum of $T(\Gamma)$ at the transition threshold, and the scaling at large Γ.

We observe that deep in the self-organized phase, for large Ω, or small Γ, we find deviations between the tMPS results and the mean field with thermal fluctuations approach. We attribute these to the fact that the mean field method characterizes the steady state in the thermodynamic limit and our tMPS results are obtained for a finite system size and time [109, 110]. As we saw in Sec. 3.2.4 as we increase the system size the photon density in the tMPS results decreases, thus we expect that for larger system sizes the agreement would become better. We note that as we consider the exact coupling in the tMPS method for any finite system size fluctuations which go beyond the ones considered in the perturbation theory on top of the mean field could play an important role at long times.

In important limits it is possible to calculate the steady-state temperature analytically, their derivation can be found in Ref. [110], and it is given by

$$
k_B T \approx \begin{cases} \frac{\hbar\delta}{\ln(1+\Gamma_0/\Gamma)} & \text{for } \hbar\Gamma \ll \hbar\delta, J, U \\ \frac{\hbar(\Gamma/2)^2+\hbar(2\lambda\Omega\sqrt{N}-\delta)^2}{4\delta} & \text{for } \hbar\Omega\sqrt{N}\lambda \gg J, U \text{ or } \hbar\delta \gg J, U \\ \frac{\hbar\kappa^2}{\delta} & \text{for } 0 < \hbar\delta \ll \hbar\Gamma, J, U \end{cases} \tag{5.10}
$$

with

$$
\Gamma_0 = \frac{2\pi\delta\,\mathrm{Im}\chi^R(\delta)}{\int_0^\infty d\omega\,\frac{\omega}{(\omega+\delta)^2}\mathrm{Im}\chi^R(\omega)}
$$

$$
\kappa^2 = \frac{\int \frac{\omega d\omega}{\omega^2+(\Gamma/2)^2}\mathrm{Im}\chi^R(\omega)}{\int \frac{\omega d\omega}{(\omega^2+(\Gamma/2)^2)^2}\mathrm{Im}\chi^R(\omega)}, \tag{5.11}
$$

where $\chi^R(\omega)$ is the retarded correlation function of the imbalance operator O, Eq. (4.38). These analytical expression can give an intuition on the behavior of the temperature shown in Figs. 5.8 (c)-(d). Thus, the strong increase of T in the ordered phase, Fig. 5.8(c), is mainly driven by the increase of coupling strength, second line of Eq. (5.10). If we go to lower values of Γ, Fig. 5.8 (d), T first decreases as $T \sim \Gamma^2$ in this regime. Then it increases again because the cavity field, $\lambda = \langle a + a^\dagger \rangle$, grows rapidly in the ordered phase. In the limits of large detuning, δ, and large dissipation strength, Γ, we find similar scalings as in previous semiclassical approaches [194–196]. Finally, for $\hbar\Gamma \lesssim J$ and $\hbar\delta = U$, a strong drop of the temperature can be seen, associated with a strong increase of photon number.

Thus, we have obtained in this section that the fluctuations in the atoms-cavity coupling determine a large temperature for the atoms throughout the phase diagram. The large temperature implies important deviations compared to the zero-temperature mean field approach. In particular, when the fluctuations effects are included, the self-organization phase transition has a finite temperature character.

5.5 Short summary

In summary, we performed the full quantum time-evolution towards the many-body steady state of a chain of interacting bosonic atoms coupled to an optical cavity. Our results show that by including the coupling between the atomic degrees of freedom and the photonic field the long time state of the system exhibits important deviations from the zero-temperature mean field approach. We observe that in the self-organized phase the steady state consists of a mixture of the mean field predicted density wave states and excited state with defects which reduce the density imbalance. Other states without density ordering become more prominent in the mixture as we increase the dissipation strength, such that in the large Γ limit the atomic sector becomes fully mixed, but with a strong coupling between the atomic and the photonic sector Furthermore, we have shown that in the thermodynamic limit the unique steady state solution can be obtained only when fluctuations effects beyond the mean field decoupling are taken into account. When the timescale for thermalization is shorter than the timescale for heating or cooling by the fluctuations of the cavity field the state of the particles can be described by an effective temperature. We obtain that for most parameters that we consider the effective temperature is large in the steady state.

Our results question the picture established by zero-temperature mean field theories which assume pure state transitions and replaces it by transitions of a mixed state character, occurring at a finite temperature in the atomic sector. We expect that many of our findings remain unaffected if instead of one-dimensional interacting bosons higher-dimensional realizations of our model [70, 71] are considered.

As the deviations from the zero-temperature mean field are consistent for a wide range of parameters, we verified that in the experimental parameter regimes of the current realizations, Refs. [70–72, 87], the predicted mixed character of the transition and steady states occurs. Thus, one can think about what are the signatures of these mixed states in the experimental measurements. A first sign of the mixed state transitions would be the observation of single experimental runs which stabilize at different photon numbers. By having access to the photon number distributions via the photons leaking out of the cavity one could observe the deviations. In particular, for ρ_{mix} the second order correlation function, $g^{(2)}(0)$, has large values, $g^{(2)}(0) > 2$, showing the importance of fluctuations in this regime. However, in order to correctly identify the mixed state character the measurement of an additional observable in the atomic sample is required, like the direct measurement of the even-odd-site imbalance, or the density-density correlations of the atoms. This can by now be measured in optical lattice experimental setups in the absence of a cavity and we expect that our findings motivate the experiments to implement this in the atoms coupled to cavity setups. Recent experiments have also analyzed the dynamics of atoms-cavity coupled systems by monitoring in real time the photons leaking out of the cavity [72, 89, 197–200].

Chapter

Symmetry effects in many-body self-organization in a cavity: breaking a strong symmetry

Symmetries play a key role in classifying and unifying the physics occurring in different microscopic systems. One of the famous examples is the universal behavior which arises at (quantum) phase transitions. This universality implies an independence from the microscopic details of the system, such that the behavior of the system can be classified by the symmetries which are spontaneously broken at the transition [2]. In a Hamiltonian system, each symmetry implies a conservation law. This has the crucial consequence for the dynamics of the system, as the long time state remembers the initial conditions. Furthermore, the conservation laws need to be considered in the construction of thermal ensembles [201]. The ensemble taking these conservation laws into account has been called the generalized Gibbs ensemble [202].

Surprisingly, in contrast to the case of closed systems, for open systems described by the dissipative Lindblad master equations $\frac{\partial}{\partial t}\rho = \mathcal{L}(\rho)$, where ρ is the density matrix and $\mathcal{L}$ the Liouvillian, a symmetry of the Liouvillian does *not always* imply a conserved quantity and multiple steady states [115, 117]. Let the Hermitian operator $\mathcal{O}$ be the generator of the symmetry $\mathcal{U} = \exp(i\phi\mathcal{O})$, with real ϕ. If the symmetry operator satisfies the condition

$$\mathcal{L}\left(\mathcal{U}\rho\mathcal{U}^{\dagger}\right) = \mathcal{U}\mathcal{L}(\rho)\mathcal{U}^{\dagger}, \tag{6.1}$$

we have only a so-called weak symmetry. The weak symmetry condition implies a block structure of Liouvillian with different symmetry sectors, but it is not sufficient to imply the existence of a conserved quantity or multiple steady states. This is in contrast to the Hamiltonian case. Additionally we need that the generator of the symmetry $\mathcal{O}$ is commuting with both the Hamiltonian and all jump operators L_m

$$[\mathcal{O}, H] = [\mathcal{O}, L_m] = 0, \tag{6.2}$$

then a so-called strong symmetry exists which implies conservation laws. For a strong sym-

metry, in each symmetry sector resulting from the block diagonalization at least one steady state exists. Thus, this gives a lower bound on the number of steady states. Furthermore, the quantity $\langle \mathcal{O} \rangle = \text{tr}(\rho O)$ is conserved,

$$\frac{\partial}{\partial t} \langle \mathcal{O} \rangle = 0. \tag{6.3}$$

In recent years a significant amount of work has been devoted to go beyond the *typical* situation of a unique steady state in experimentally relevant systems that can be described by a Lindblad master equation. Such experimental setups are very frequent in the area of quantum optics and solid state systems coupled to light. This effort led to the study of the coexistence of several steady states in such Lindblad systems [203–215]. In this context, the phenomena of bi-/meta-stability have been investigated in various systems [72, 212, 216–224]. Additionally, experiments tried to identify the coexistence of phases by the phenomenon of intermittency [210–212, 222, 225]. Intermittency implies the random switching between two distinct experimental measurement outputs in a single experimental run. However, one has to take care concerning the interpretation of the occurrence or absence of intermittency, as we will also see in this chapter. A system with a unique steady state can show intermittency if the measurement targets different diagonal components as, e.g., shown for the stochastic unravelling for the system considered in Chap. 5 [108]. Even if we have multiple steady states intermittency can be absent if the timescale for the transition between the states diverges, or in the case of disconnected multiple steady states. The latter can occur due to the presence of a strong symmetry [226].

Furthermore, by employing the symmetries of the system steady states with exotic properties have been constructed, such as steady states with η-pairing correlations [153], states with enhanced currents [227, 228], or in weakly driven systems [229]. Recently, the consequences of the weak and strong symmetries in open systems were also discussed in the context of error correction for quantum information theory [230].

We investigate in this chapter the effects of the presence of a strong symmetry on the many-body self-organization phenomena of a quantum bosonic gas coupled to a dissipative cavity (see Sec. 2.1). In this chapter, we follow the results we presented in Ref. [111]. In this work, I performed the tMPS numerical simulations and extended the many-body adiabatic elimination approach to atoms-cavity system for strong symmetries.

In Sec. 6.1 we identify the strong symmetry present in the considered system and its generators. In Sec. 6.2 we extend the many-body adiabatic elimination framework which we presented in Chap. 4 in the presence of the strong symmetry. Next, we show in Sec. 6.3 how the symmetry can lead to the occurrence of multiple dissipative phase transitions in the different symmetry sectors. Additionally, in Sec. 6.4 we show the absence of intermittency, the dissipative freezing phenomena [226], in the presence of the strong symmetry in single trajectories obtained by the stochastic unravelling of the master equation. We find that this behavior of the absence of intermittency can approximately survive for an intermediate time when adding a small symmetry breaking term in Sec. 6.5. Whereas for a larger symmetry breaking term the different symmetry sectors are no longer a good description of the system. We further investigate in Sec. 6.5 how

in the situation of the weak breaking of the strong symmetry by an additional term in the Liouvillian the unique steady state is recovered. Thus, the weak breaking causes a drastic response of the system and we analyze the timescales associated to the process of reaching the steady state.

6.1 Symmetries of the model

In this chapter, we consider the model which we introduced in Sec. 2.1, of ultracold bosons confined to a one-dimensional chain coupled to a single cavity mode and transversely pumped with a standing-wave laser beam [108, 111]. As we have already seen in the previous chapters, the dynamics of the coupled cavity-atom system is described by the Lindblad equation in which the excited internal state of the atoms is adiabatically eliminated [56, 65, 100, 108, 111, 114]

$$
\frac{\partial}{\partial t}\rho = \mathcal{L}(\rho) = -\frac{i}{\hbar}\left[H, \rho\right] + \frac{\Gamma}{2}\left(2a\rho a^\dagger - a^\dagger a\rho - \rho a^\dagger a\right), \tag{6.4}
$$

where $\mathcal{L}(\rho)$ is the Liouvillian. The bosonic operators a and $a^\dagger$ are the annihilation and creation operators for the photon mode of the cavity and Γ the dissipation strength. We consider the losses from the cavity due to the imperfections of the mirrors described by the dissipator. Compared to the previous chapter we give now the Hamiltonian in the atomic momentum basis [65, 100, 101]

$$
\begin{aligned}
H_0 =& H_\mathrm{c} + H_\mathrm{kin} + H_\mathrm{ac}, \\
H_\mathrm{c} =& \hbar\delta a^\dagger a, \\
H_\mathrm{ac} =& -\hbar\Omega(a + a^\dagger)\sum_k b_k^\dagger b_{k+\pi \,(\mathrm{mod}\ 2\pi)}, \\
H_\mathrm{kin} =& -2J\sum_k \cos(k)b_k^\dagger b_k, \\
H_\mathrm{int} =& \frac{U}{2}\sum_j n_j(n_j - 1).
\end{aligned} \tag{6.5}
$$

The cavity mode is described by the first term in H_0, in the rotating frame of the pump beam, where $\delta = \omega_c - \omega_p$ is the detuning between the cavity mode and the transverse pump beam. The operators b_k and $b_k^\dagger$ are the bosonic annihilation and creation operators of the atoms with the unitless momentum $k_j = \frac{2\pi j}{L}$ and $j = 1, \ldots, L$, assuming periodic boundary conditions. We note that in the results presented we considered open boundary conditions, the model and its symmetries for open boundary conditions are given in Appendix C. L denotes the number of sites of the bosonic chain and the total number of bosons is N. The second term gives the coupling between the atoms and the cavity field, introducing a coupling between the momentum k and $k + \pi \,(\mathrm{mod}\ 2\pi)$. These two momenta are coupled due to the periodicity of cavity mode, which has twice the periodicity of the lattice spacing of the chain. The last term describes the kinetic energy of the atoms along the chain with the tunneling amplitude J. The repulsive on-site interactions of strength $U \geq 0$ are written in position basis in the term H_int, where j

denotes the site of the chain and n_j the atomic density.

We can observe in Eq. (6.5) that in the non-interacting case, $U = 0$, only transitions between the occupation of the momenta k and $k + \pi \pmod{2\pi}$ of the atoms are possible. This implies that in the single particle case $L/2$ independent symmetry sectors exist, each spanned by the momentum states $|k_j\rangle$ and $|k_j + \pi \pmod{2\pi}\rangle$, $j = 1, \ldots, L/2$. These correspond to a strong symmetry, which has as generator the atomic number operators in each symmetry sector

$$\mathcal{O}_{k_j} = b_{k_j}^\dagger b_{k_j} + b_{k_j+\pi \; (\mathrm{mod} \; 2\pi)}^\dagger b_{k_j+\pi \; (\mathrm{mod} \; 2\pi)} \tag{6.6}$$

and their average values are conserved quantities, $m_{k_j} = \langle \mathcal{O}_{k_j} \rangle$. Due to the strong symmetry, already for a single particle multiple steady states exist.

In the case of N atoms, the symmetry sectors can be constructed from the different combinations in which one can arrange the atoms in the single particle sectors. Thus, we label each symmetry sector by $K \equiv \left(m_{k_1}, \ldots, m_{k_i}, \ldots, m_{k_{L/2}} \right)$, with $\sum_{i=1}^{L/2} m_{k_i} = N$. Even though the atoms can be arranged independently in the single particle sectors, they are coupled via the photon field.

6.2 Many-body adiabatic elimination with a strong symmetry

In Chap. 4 we described the many-body adiabatic elimination framework in the presence of interactions, which we used in Chap. 5 to determine the phase diagram of steady states in this case [108–110]. Now we want to see how these approaches change in the presence of a strong symmetry, when the dynamics decomposes in different symmetry sectors [111].

As a short reminder of Chap. 4, we decompose the Liouvillian as $\mathcal{L} = \mathcal{L}_0 - \frac{i}{\hbar}[H_\nu, \cdot]$ into an unperturbed Linbladian $\mathcal{L}_0$ and a perturbative contribution given by H_ν. We have seen that this approach captures the effective dynamics of the density matrix in the decoherence free subspace of $\mathcal{L}_0$. The resulting effective dynamics in the decoherence free subspace is given by [109, 111, 164, 165, 167, 168]

$$\frac{\partial}{\partial t}\rho^0 = \mathcal{L}_0\rho^0 + \frac{1}{\hbar^2}P_0\left[H_\nu, \mathcal{L}_0^{-1}P_1\left[H_\nu, \rho^0\right]\right], \tag{6.7}$$

where ρ^0 lies in the decoherence free subspace of $\mathcal{L}_0$ and P_0 and P_1 are the projectors onto the decoherence free subspace and the first excited subspace, respectively. In the following, we show the results of this approach in the presence of the strong symmetry [111]. In 6.2.1 we consider the perturbation as the fluctuations around the mean-field theory and in 6.2.2 the perturbation is the kinetic term of the atoms.

6.2.1 Mean field decoupling with thermal fluctuations

In the following, we follow the approach introduced in Ref. [110] and described in Sec. 4.3 for interacting particles, to deal with the non-interacting case [111]. First, we perform a mean field decoupling of the term coupling the cavity and the atoms, H_{ac}, and only consider the fluctuations in the coupling as the perturbation in the many-body adiabatic elimination derivation

6.2 Many-body adiabatic elimination with a strong symmetry

of the effective equations of motion. This gives

$$\mathcal{L}_0 = -\frac{i}{\hbar}[H_c + H_{\text{kin}} + H_{\text{ac}}^{\text{MF}}, \cdot] + \mathcal{D}(\cdot), \tag{6.8}$$
$$H_\nu \equiv \delta H_{\text{ac}}$$

where $\mathcal{D}(\rho) = \frac{\Gamma}{2}\left(2a\rho a^\dagger - a^\dagger a\rho - \rho a^\dagger a\right)$, and

$$H_{\text{ac}}^{\text{MF}} = -\hbar\Omega(\alpha + \alpha^*)\sum_k b_k^\dagger b_{\pi-k} - \hbar\Omega(a + a^\dagger)\Delta, \tag{6.9}$$

$$\delta H_{\text{ac}} = -\hbar\Omega\left(a + a^\dagger - \alpha - \alpha^*\right)\left[\sum_k b_k^\dagger b_{\pi-k} - \Delta\right].$$

As we have seen in Sec. 2.1 the mean field value $\alpha = \langle a \rangle$ depends on the mean field value of the imbalance Δ,

$$\alpha(\Delta) = \frac{\Omega}{\delta - i\Gamma/2}\Delta, \tag{6.10}$$

$$\Delta = \sum_{j=1}^{L/2}\langle \mathcal{O}_{k_j}\rangle = \sum_j(-1)^j\langle n_j\rangle.$$

At the mean field level the atomic and photonic contributions decouple beside the self-consistent determination of the parameters. Thus, an arbitrary state in the decoherence free subspace of $\mathcal{L}_0$ is given by [110, 111]

$$\rho = |\alpha(\Delta)\rangle\langle\alpha(\Delta)| \cdot \rho^b, \text{ with } \rho^b = \sum_{n,m} c_{n,m}|n(\alpha)\rangle\langle m(\alpha)|, \tag{6.11}$$

where $|n(\alpha)\rangle$ are eigenstates of the atomic mean field Hamiltonian $H_a = H_{\text{kin}} + H_{\text{ac}}^{\text{MF}}$ and the cavity is in a coherent state. If we plug in ρ given by Eq. (6.11) in Eq. (6.7) we obtain the equation of motion for the entries $c_{n,m}$ of the density matrix, as we obtained in Sec. 4.3. In order to obtain a substantial simplification, we generalize the thermal Ansatz introduced in Ref. [110] and given in Sec. 4.3. However, in the considered non-interacting case, we cannot assume that the atomic sector thermalizes as a whole, as we only have cavity mediated interactions. But we can make the assumption that the particles in each single particle symmetry sector can thermalize, such that the behavior in each single particle sector will be described by an effective inverse temperature β_j associated with this sector [111], i.e.

$$\rho^b \sim \prod_{j=1}^{L/2}\exp\left[-\beta_j H_a(k_j, \pi - k_j)\right], \text{ where} \tag{6.12}$$

$$H_a(k_j, \pi - k_j) = -\hbar\Omega(\alpha + \alpha^*)\left(b_{k_j}^\dagger b_{\pi-k_j} + b_{\pi-k_j}^\dagger b_{k_j}\right) - 2J\cos(k_j)\left(b_{k_j}^\dagger b_{k_j} - b_{\pi-k_j}^\dagger b_{\pi-k_j}\right).$$

This implies that, for the sectors chosen below in Fig. 6.1, the state from the symmetry sector $(m_{k_1} = 5)$ is described by a single temperature as all particles are in the single particle sector with momentum k_1, but the state from the symmetry sector $(m_{k_2} = 3, m_{k_4} = 2)$ is described by two temperatures as we have 3 particles in the single particle sector with momentum k_2 and 2 particles in the single particle sector with momentum k_4.

This procedure, together with the Ansatz given in Eq. (6.12), is analogous to considering the case of conservation laws in closed systems, which are described by generalized Gibbs ensembles [201, 202]. Let us note that a generalized Gibbs ensemble was previously used to describe weakly open systems in the presence of approximate conservation laws in Ref. [229].

We have reduced our problem of computing the density matrix to the determination of a smaller number of parameters, the inverse temperatures β_j. For this it is enough to consider the equations of motion of a reduced number of observables. Thus, we describe the steady state of the system with the temperatures for which the Ansatz given by Eqs. (6.11)-(6.12) satisfies the equations

$$\left\langle \frac{\partial}{\partial t} H_a(k_j, \pi - k_j) \right\rangle = 0 \tag{6.13}$$

for all momenta k_j and the mean field self-consistency condition Eq. (6.10).

6.2.2 Perturbation in kinetic energy

In this section, we consider the perturbation to be given by the kinetic energy, $H_\nu \equiv H_{\mathrm{kin}}$, as we saw in Sec. 4.2 this approach is valid in the regime $\hbar\Gamma \gg \hbar\Omega, \hbar\delta \gg J$ and we have that $\mathcal{L}_0$ is given by [109, 111]

$$\mathcal{L}_0 = -\frac{i}{\hbar}[H_c + H_{\mathrm{ac}}, \cdot] + \mathcal{D}(\cdot), \tag{6.14}$$

where we considered non-interacting atoms, with $\mathcal{D}(\rho) = \frac{\Gamma}{2}\left(2a\rho a^\dagger - a^\dagger a \rho - \rho a^\dagger a\right)$ the dissipator.

In Sec. 4.2 we obtained that states of the form $\rho = |\alpha(\Delta); \Delta, u\rangle\langle\alpha(\Delta'); \Delta', u'|$ with $\Delta = \Delta'$ lie in the decoherence free subspace of $\mathcal{L}_0$, and that the contributions which are coupled to the decoherence free subspace via the perturbation H_{kin} come from the excited subspaces spanned by the states in which $\Delta = \Delta' \pm 2$. In the case with finite interactions the mixed state given by [109]

$$\rho_{\mathrm{mix}} = \frac{1}{\mathcal{N}} \sum_{\{n_j\}} |\alpha(\Delta); n_1, \ldots, n_L\rangle\langle\alpha(\Delta); n_1, \ldots, n_L| \tag{6.15}$$

was a steady state of the system. Here $\mathcal{N}$ is the number of ways one can arrange N identical particles in L sites, $\mathcal{N} = \begin{pmatrix} L + N - 1 \\ N \end{pmatrix}$.

As we are now in the non-interacting case with the momentum labeling the different symmetry sectors, we need to initially restrict ourselves to a certain symmetry sector. In the fol-

lowing, we first compute the steady state of one particle in a certain symmetry sector and, afterwards, generalize this result to the case of N particles in a certain many-body symmetry sector. We consider a single particle in the symmetry sector $K = (m_k = 1)$, in this situation the steady state is given by [111]

$$\rho_{k,\text{st}} = \sum_{i,j \text{ odd}} \sin(ki)\sin(kj)|-\alpha;i\rangle\langle-\alpha;j| + \sum_{i,j \text{ even}} \sin(ki)\sin(kj)|\alpha;i\rangle\langle\alpha;j|. \tag{6.16}$$

The derivation of the steady states for the one particle and two particles cases can be found in Appendix C. We can observe that this state has a fully mixed atomic sector in the momentum basis.

If we generalize the one and two particle steady states (see Appendix C) to the N particle case, we obtain that for N particles the steady state will also be the fully mixed state in the different symmetry sectors. For the N particle case the symmetry sectors can be constructed from different combinations in which one can arrange the particles in the single particle sectors. Thus, the state with a fully atomic sector for N particles distributed in the $L/2$ single particle sectors, $K = \left(m_{k_1}, ..., m_{k_i}, ..., m_{k_{L/2}}\right)$, is given by [111]

$$\rho_{\text{K,st}} = \frac{1}{\mathcal{N}_0} \sum_{i_1=0}^{m_{k_1}} \cdots \sum_{i_{L/2}=0}^{m_{k_{L/2}}} |n_{k_1} = i_1, n_{\pi-k_1} = m_{k_1} - i_1; \cdots ; n_{k_{L/2}} = i_{L/2}, n_{\pi-k_{L/2}} = m_{k_{L/2}} - i_{L/2}\rangle$$

$$\langle n_{k_1} = i_1, n_{\pi-k_1} = m_{k_1} - i_1; \cdots ; n_{k_{L/2}} = i_{L/2}, n_{\pi-k_{L/2}} = m_{k_{L/2}} - i_{L/2}|,$$

with $\qquad\qquad\qquad\qquad\qquad\qquad\qquad\qquad\qquad\qquad\qquad\qquad\qquad\qquad (6.17)$

$$|n_{k_1} = i_1, n_{\pi-k_1} = m_{k_1} - i_1; \cdots ; n_{k_{L/2}} = i_{L/2}, n_{\pi-k_{L/2}} = m_{k_{L/2}} - i_{L/2}\rangle \equiv$$

$$\equiv \frac{1}{\mathcal{M}} \sum_{j_1^1, ..., j_{m_{k_1}}^1 = 0}^{L} \cdots \sum_{j_1^{L/2}, ..., j_{m_{k_{L/2}}}^{L/2} = 0}^{L} \left[\sin\left(k_1 j_1^1\right)...\sin\left(k_1 j_{m_{k_1}}^1\right)(-1)^{j_{i_1}+1+...+j_{m_{k_1}}+(m_{k_1}-i_1)}\right] \times \cdots$$

$$\times \left[\sin\left(k_{L/2} j_1^{L/2}\right)...\sin\left(k_{L/2} j_{m_{k_{L/2}}}^{L/2}\right)(-1)^{j_{i_{L/2}}+1+...+j_{m_{k_{L/2}}}+(m_{k_{L/2}}-i_{L/2})}\right] \times$$

$$\times \sqrt{(n_1)!...(n_L)!}\,|\alpha(\Delta); j_1^1, ..., j_{m_{k_1}}^1, ..., j_1^{L/2}, ..., j_{m_{k_{L/2}}}^{L/2}\rangle,$$

where n_{k_i} is the number of particles with momentum k_i, $\mathcal{N}_0 = \prod_{i=1}^{L/2}\binom{m_{k_i}+1}{m_{k_i}}$, the positions of the N particles are $j_1^1, ..., j_{m_{k_1}}^1, ..., j_1^{L/2}, ..., j_{m_{k_{L/2}}}^{L/2}$, and n_i is the occupation number of each site in real space and the even-odd imbalance is given by $\Delta = \sum_{p=1}^{m_{k_1}}(-1)^{j_p^1} + ... + \sum_{p=1}^{m_{k_{L/2}}}(-1)^{j_p^{L/2}}$, and the normalization constant is

$$\mathcal{M} = \left(\frac{L+1}{2}\right)^{N/2}\sqrt{(n_{k_1})!(n_{\pi-k_1})!...(n_{k_{L/2}})!(n_{\pi-k_{L/2}})!}. \tag{6.18}$$

Thus, we have obtained that in each symmetry sector the steady state has a fully mixed atomic sector [111], which is very different in nature compared to the steady state ρ_{mix} in the presence of interaction. In the following, we find that slightly breaking the strong symmetry can lead to drastic effects in the nature of the steady state.

6.3 Properties of the multiple steady states at $U = 0$
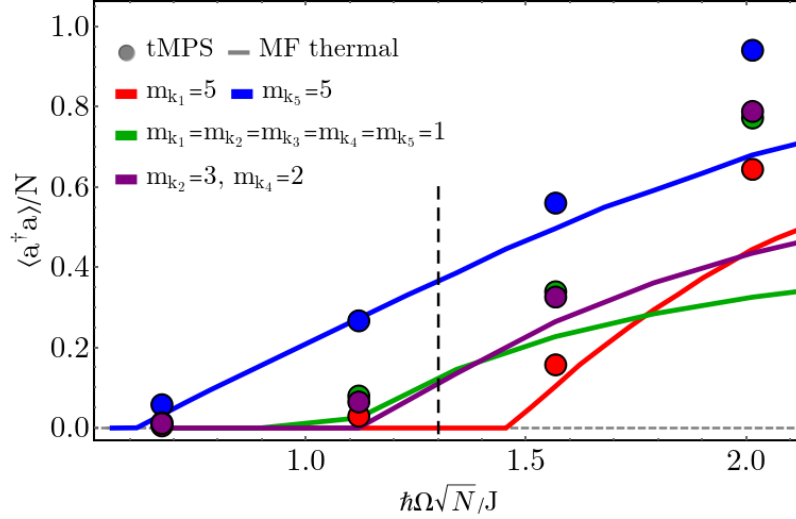
Figure 6.1: The scaled photon number, $\langle a^\dagger a \rangle / N$, as a function of $\hbar\Omega\sqrt{N}/J$, for different symmetry sectors. We compare the values obtained with tMPS at $tJ/\hbar = 200$ with the generalized Gibbs ensemble within the mean field approach including thermal fluctuations. The parameters used are $L = 10$, $N = 5$, $\hbar\delta/J = 2$, $U/J = 0$, and $\hbar\Gamma/J = 1$. At the dashed vertical line, the nature of the obtained steady states reaches from states with an empty cavity (red symbol/line) to the self-organized states (remaining ones). We note that not all possible symmetry sectors are depicted here. Figure adapted from Ref. [111].

We show in Fig. 6.1 the steady state diagram of the coupled atom cavity system using two different methods. The first method is the mean field decoupling of the atomic and the photonic sector considering the fluctuations as a perturbation together with the assumption that within each symmetry sector the atoms thermalize as described in Sec. 6.2.1 [110, 111]. For this approach we compute the photon number of the state given in Eq. (6.12).

The second approach is the time-dependent matrix product state (tMPS) method developed [109] for the numerically exact simulation of the time-evolution of the dissipative master equation, which we described in Sec. 3.2. For the time-evolution we have chosen the empty cavity and the ground state in a certain symmetry sector for the atoms as the initial state. Regarding the numerical parameters, the convergence of our results is sufficient for at least 500 quantum trajectories in the Monte Carlo sampling, the truncation error goal of 10^{-12}, the time-step of $dtJ = 0.0125\hbar$ for the parameters used in Fig. 6.1 and $dtJ = 0.00625\hbar$ for the other parameters considered in the rest of the chapter, and an adaptive cutoff of the local Hilbert space of the photon mode between $N_{\text{pho}} = 20$ and $N_{\text{pho}} = 10$. The convergence behavior for the parameters considered in this chapter is similar to the one presented in Sec. 3.2.

Both approaches give in each considered symmetry sector of the strong symmetry a transition from the empty cavity state to the self-organized state with finite cavity occupation as we increase the coupling strength. However, importantly, in each symmetry sector the transition takes place at distinct critical values of the coupling strength Ω_c. This situation could be explained by the following argument: the self-organization transition in this model arises due to the competition between the ordering of the atoms in a density wave, which is induced by interaction with the photon mode, and the kinetic energy of the atoms. As the kinetic energy depends on the momentum of the atoms and in each symmetry sector the atoms have different momenta, this gives rise to a different critical values of the coupling strength for the transition.

Thus, even if we take the same physical parameters and a fixed coupling (see vertical line in Fig. 6.1) multiple steady states arise depending on the projection of the initial state to the symmetry sectors. Each steady state can have very different nature. We observe that it can occur that one sector is still in the disordered phase with an empty cavity, whereas another sector already is deep in the self-organized phase, with a finite cavity field. This is to be contrasted to the meta-stable states arising for the weak $\mathbb{Z}_2$ symmetry present in our system (see Sec. 2.1), which are connected to a unique steady state in the case of a finite system.

6.4 Dissipative freezing

As we presented in Sec. 3.2 in our numerical simulations we deal with the dissipation by the stochastic unraveling of the master equation with quantum trajectories [111]. This allows us to study the effect of the existence of a strong symmetry in a system described by a Liouvillian on the time evolution of the quantum trajectories. Recently, the existence of the phenomenon of 'dissipative freezing' was shown in such an analysis, for systems in which the Lindblad operator is proportional to the Hamiltonian ($H \propto L$) [226]. Dissipative freezing is the phenomenon that single realizations of the quantum trajectories can break the strong symmetry. If a trajectory is purely in one symmetry sector, it will stay in that sector for the rest of the time evolution and, thus, obey the symmetry of the system. However, if one starts with an initial state such that a trajectory consists of a superposition with contributions from multiple symmetry sectors, each individual trajectory will randomly select one of the sectors and remain there for the rest of the evolution. Further, the trajectories will show no behavior of intermittency in between the different sectors. Thus, even though the expectation value of the generator of the symmetry given by Monte Carlo average is a conserved quantity, this is no longer true at the level of single trajectories. The single trajectories can break 'spontaneously' the strong symmetry of the model. This is an interesting effect which might have relevance in analyzing the single realizations of experiments. Furthermore, as the steady state is unique the interpretation of quantities measured in the quantum trajectory method which stabilize at different values does not imply different steady states.

In order to obtain further intuition in how the phenomenon of dissipative freezing occurs we look at the time-evolution of a single quantum trajectory. This is given by the following
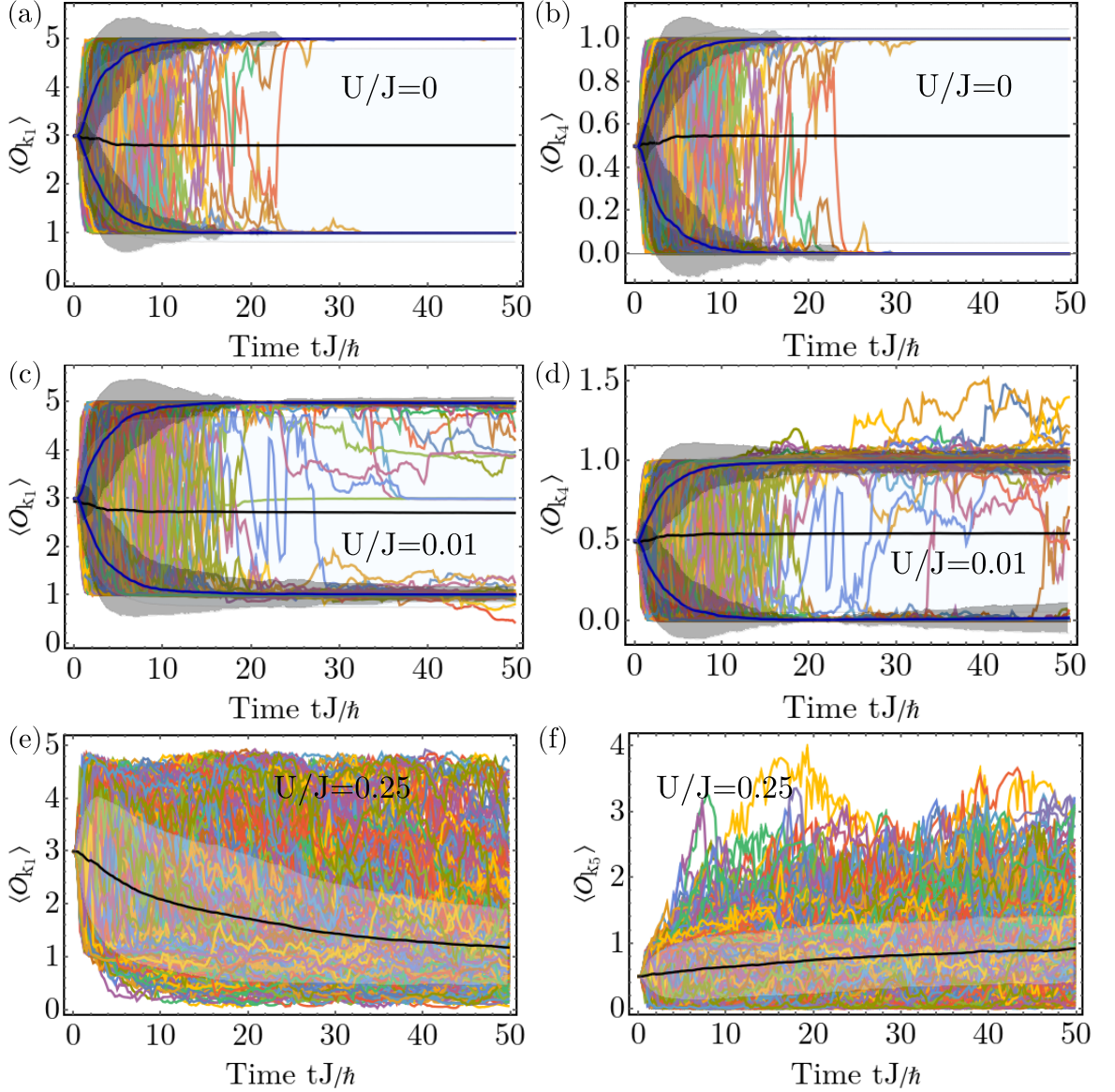
Figure 6.2: Time evolution of $\mathcal{O}_k$ for the single quantum trajectories sampled in the Monte Carlo average for different interaction strengths U, with $k = k_1$ and $k = k_4$. The initial state consists in an equal superposition between states for the sectors $(m_{k_1} = 5)$ and $(m_{k_1} = 1, m_{k_2} = 1, m_{k_3} = 1, m_{k_4} = 1, m_{k_5} = 1)$. In each panel there are 1000 trajectories plotted, the black, or blue, curves represent the Monte Carlo average, either for the full set of trajectories, or averaged separately depending on the final value, we shade the interval of one standard deviation away from the average, with light blue for the full average and light gray for the separate averages. The parameters used are $L = 10$, $N = 5$, $\hbar\delta/J = 2$, $\hbar\Omega\sqrt{N}/J = 4.47$, and $\hbar\Gamma/J = 15$. Figure adapted from Ref. [111].

time-evolution operator

$$U(t, t_0) = \frac{1}{\mathcal{M}} e^{-i\tilde{H}(t-t_N)/\hbar} \prod_{j=N}^{1} L \, e^{-i\tilde{H}(t_j - t_{j-1})/\hbar}, \tag{6.19}$$

where $\mathcal{M}$ is the normalization constant, L the jump operator, and $\{t_1, ..., t_N\}$ are the stochastically sampled times when a quantum jump occurs. The effective non-Hermitian Hamiltonian is $\tilde{H} = H - \frac{i}{2}\hbar\Gamma L^\dagger L$, as defined in Sec. 3.2. Thus the time-evolution operator also commutes with the symmetry generators, $\mathcal{O}_k$. To analyze the phenomenon of dissipative freezing we should look at the evolution of one of the symmetry generators $\mathcal{O}_k$ for a single quantum trajectory,

$$\langle \mathcal{O}_k(t) \rangle_{traj} = \langle \psi_0 | U^\dagger(t, t_0) \mathcal{O}_k U(t, t_0) | \psi_0 \rangle = \langle \psi_0 | U^\dagger(t, t_0) U(t, t_0) \mathcal{O}_k | \psi_0 \rangle, \qquad (6.20)$$

with $|\psi_0\rangle$ the initial state. If $|\psi_0\rangle$ is within one symmetry sector and is an eigenstate of $\mathcal{O}_k$, we can observe that the expectation value within the single trajectory $\langle \mathcal{O}_k(t) \rangle_{traj}$ will not evolve in time, as neither the jump operator, nor the effective Hamiltonian can change the symmetry sector. In contrast, if the initial state is taken as a superposition with contributions from more than one symmetry sector, then, in principle, both the jump operator or the evolution with the effective Hamiltonian could change the weights of the contribution of the different sectors. This implies that $\langle \mathcal{O}_k(t) \rangle_{traj}$ will evolve in time for a single quantum trajectory and only the Monte Carlo average will be constant.

In the special case in which the system satisfies $\left[H, L^\dagger L\right] = 0$ one can get a better insight as

$$U^\dagger(t, t_0) U(t, t_0) = e^{-\Gamma L^\dagger L (t - t_0)} (L^\dagger L)^n, \qquad (6.21)$$

with n the number of quantum jumps that occur up to time t. Here the evolution of $\mathcal{O}_k$ will only depend on the number of quantum jumps that occur up to time t. This includes the particular case of $L^\dagger L = \mathbb{1}$ when $U^\dagger(t, t_0) U(t, t_0) = \mathbb{1}$ and $\langle \mathcal{O}(t) \rangle_{traj}$ is trivially constant in time. This situation also includes the system considered in Ref. [226], as the authors prove that dissipative freezing always occurs if $H \propto L \propto \mathcal{O}$, as the quantum trajectory is always projected to a symmetry sector after a sufficient number of quantum jumps.

For the coupled atom-cavity system that we consider in this chapter, Eqs. (6.4)-(6.5), the condition $\left[H, L^\dagger L\right] \neq 0$ is not satisfied and the arguments given above are not directly applicable. Nevertheless, we numerically show, in Fig. 6.2(a)-(b), that even in a system that goes beyond the special case ($H \propto L$) of Ref. [226], dissipative freezing can occur [111]. In Fig. 6.2(a)-(b) we plot the expectation value of two of the generators of the strong symmetry, $\langle \mathcal{O}_{k_1} \rangle$ and $\langle \mathcal{O}_{k_4} \rangle$, in time for 1000 single trajectories. The evolution of the other symmetry generators is presented in Appendix C and supports the same conclusions. The initial state is an equal superposition of a state from the sector ($m_{k_1} = 5$) and the sector ($m_{k_1} = 1, m_{k_2} = 1, m_{k_3} = 1, m_{k_4} = 1, m_{k_5} = 1$). For the sector ($m_{k_1} = 5$) the generators of the symmetry have the values $\langle \mathcal{O}_{k_1} \rangle = 5$ and $\langle \mathcal{O}_{k_4} \rangle = 0$, and for the sector ($m_{k_1} = 1, m_{k_2} = 1, m_{k_3} = 1, m_{k_4} = 1, m_{k_5} = 1$) the values $\langle \mathcal{O}_{k_1} \rangle = 1$ and $\langle \mathcal{O}_{k_4} \rangle = 1$. At intermediate times $10\hbar \lesssim tJ \lesssim 30\hbar$ we observe that the trajectories approach one of the two sectors, signaled by the decrease of the standard deviation of the separate averages (shaded in gray). At long times, $tJ \gtrsim 40\hbar$, we can see that all trajectories evolved to one of the two symmetry sectors, as $\langle \mathcal{O}_k \rangle(t)$ equals the expected occupation in those sectors. The Monte Carlo average of the trajectories stays constant throughout the following time-evolution, up to a numerical error, showing that the strong symmetry is broken only at the level of the

quantum trajectories.

6.5 Breaking of the strong symmetry

If any finite interaction, $U > 0$, is included in the model the operators $\mathcal{O}_k$, Eq. (6.6), will no longer commute with the Hamiltonian, Eq. (6.5), which means that the strong symmetry of the Liouvillian is broken. In the following, we analyze how the system passes over from having multiple steady states in the presence of the strong symmetry to a unique steady state as the on-site interaction is slightly turned on [111]. We focus on the limit of large dissipation as in this limit we have analytical expressions of the expected steady states. For large dissipation strength the many-body adiabatic elimination with the kinetic energy as a perturbation predicts the steady state transition between the multiple steady states at $U = 0$, $\rho_{K,\text{st}}$, Eq. (6.17) derived in Sec. 6.2.2, to a single steady state ρ_{mix}, Eq. (6.15) [109].

In Fig. 6.3(a)-(b) we plot the behavior of the expectation value of the photon number and the conserved quantities of the symmetry at fixed time $tJ = 49.75\hbar$ as a function of the interaction strength U. We consider initial states in different symmetry sectors mentioned in the legend. For the considered sectors we observe that at $U = 0$ multiple steady states are obtained signaled by distinct expectation values, agreeing well with the expected values. However, as we increase the interaction strength the values of the photon number and $\langle \mathcal{O}_k \rangle$ for the different initial states start to be more and more similar until they agree with each other and with the values expected for the state ρ_{mix}, for large values of interaction U. The deviations from the predicted unique steady state ρ_{mix} for small interaction strength are due to the fact that the results are taken at a finite time for which the system has not yet reached its steady state. This can be observed in time-evolution plots given in Fig. 6.3(c)-(d) for the photon number and $\langle \mathcal{O}_k \rangle - \langle \mathcal{O}_k \rangle_{\rho_{\text{mix}}}$ for different interaction values. The expected steady state value for $\langle a^\dagger a \rangle / N$ is represented with a magenta line in Fig. 6.3(c) and $\langle \mathcal{O}_k \rangle_{\rho_{\text{mix}}} = 1$. We present the time evolution of the considered observables for other initial states in Appendix C.

In order to quantify the time-evolution we fitted the time dependence of $\langle a^\dagger a \rangle - \langle a^\dagger a \rangle_{\rho_{\text{mix}}}$ and $\langle \mathcal{O}_k \rangle - \langle \mathcal{O}_k \rangle_{\rho_{\text{mix}}}$ with an exponential function, $\propto e^{-t/\tau}$, and extracted the timescales for reaching the steady state. The fits describe very well the numerical data, which gives strong support that at infinite time the steady state is given by ρ_{mix}. Additionally, the dependence of the timescale on U is represented in Fig. 6.3(e)-(f) in log-log plots. The timescales exhibits an algebraic dependence on $1/U^2$. We compare the scaling behavior of the timescales with results from two other approaches performed for a small system of $L = 4$. First, we perform the exact diagonalization (ED) of the full Liouvillian, Eqs. (6.4)-(6.5). In this case, we compute the eigenvalues corresponding to the left eigenstates of the Liouvillian. In the second approach, we diagonalize the the many-body adiabatic elimination equations of motion, with the kinetic energy as a perturbation [109], (AE), Eq. (4.16) of Sec. 4.2. In both cases, we determine the timescale as the inverse of the real part of the first excited eigenvalue. For both approaches, we obtain an algebraic dependence $\propto U^{-\alpha}$ with $\alpha \approx 2$ confirming the tMPS results.

We observe that the timescales for $\langle \mathcal{O}_k \rangle$ are consistently larger than the timescales for the photon number. This signals that in our simulation the photon state is reaching the steady state before the atomic one. We can attribute this to the spatial extend of the atomic system.
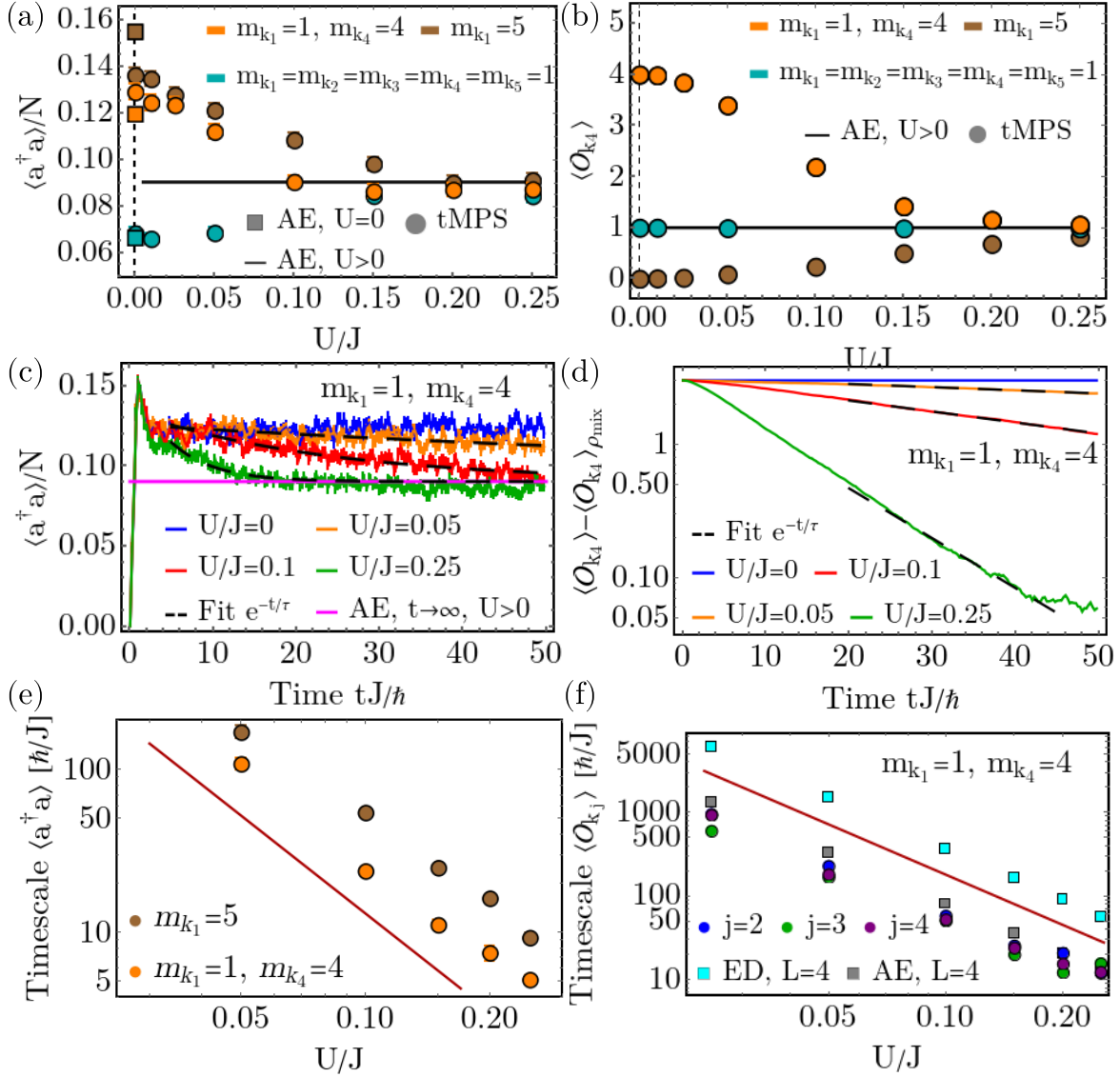
Figure 6.3: The dependence on the interaction strength U of (a) the scaled photon number, $\langle a^\dagger a \rangle / N$, and (b) the expectation value of $\mathcal{O}_{k_4}$ using tMPS at time $tJ = 49.75\hbar$ and many-body adiabatic elimination, using the kinetic energy as a perturbation (AE). The time evolution of (c) the scaled photon number, $\langle a^\dagger a \rangle / N$, and (d) the expectation value of $\mathcal{O}_{k_4}$ for different values of U. For finite U we fit the time evolution with an exponential decay (black dashed lines) the difference between the tMPS data and the expected steady state value, obtained from many-body adiabatic elimination. The timescales obtained from the exponential fits as a function of U for (e) $\langle a^\dagger a \rangle / N$ and (f) $\mathcal{O}_{k_j}$. In (f) we compare the timescales of $\mathcal{O}_{k_j}$ with the longest timescale of a small system of $N = 2$ particles in $L = 4$ system computed with exact diagonalization (ED) and many-body adiabatic elimination (AE). We fit the timescale dependence on the interaction with an algebraic decay $\propto U^{-\alpha}$ and obtain the following exponents: (e) $(m_{k_1} = 5)$, $\alpha = 1.86 \pm 0.07$; $(m_{k_1} = 1, m_{k_4} = 4)$, $\alpha = 1.73 \pm 0.08$; (f) $j = 2$, $\alpha = 1.92 \pm 0.06$; $j = 3$, $\alpha = 1.77 \pm 0.09$; $j = 4$, $\alpha = 1.78 \pm 0.03$. The red lines are a guide to the eye of an algebraic decay $\propto U^{-2}$. The parameters are chosen to be $L = 10$, $N = 5$, $\hbar\Omega\sqrt{N}/J = 4.47$, $\hbar\delta/J = 2$, and $\Gamma/J = 15$. Figure adapted from Ref. [111].

Thus, we see that the time-evolution at short times remembers well the strong symmetry and the mixing of the different symmetry sectors only occurs on timescales $\propto 1/U^2$ associated with the scattering of the atoms.

We can ask now the question regarding how the breaking of the symmetry affects the phenomenon of dissipative freezing discussed in the previous section. We analyze how this phenomenon is affected by the presence of a weak interaction, which breaks the strong symmetry. We observe in Figs. 6.2(c)-(d) (see also Appendix C) that at $U/J = 0.01$ the time evolution found for the single trajectories resembles at early time the one at $U/J = 0$. This implies that the single trajectories break the approximate strong symmetry and approach the two different symmetry sectors. At intermediate time, $20 \lesssim tJ/\hbar$, many of the quantum trajectories spend a long time near the two values expected from the $U = 0$ symmetry sectors. Only few of the trajectories directly show deviations from these values or intermittency between the values such that the phenomenon of dissipative freezing also occurs here to an approximate extend. One has to be careful not to misinterpret this absence of intermittency as the existence of multiple steady state. We observe that only starting from $U/J \gtrsim 0.25$ the effect of the strong symmetry washes out in the considered time interval.

6.6 Short summary

To summarize, our methodological developments made possible one of the first studies regarding the dynamics of a many-body open system in the presence of a strong symmetry. In this chapter, we analyzed the effects of a strong symmetry and the breaking of this symmetry on the self-organization phenomena and dynamics of a system consisting of bosonic atoms coupled to an optical cavity [111].

The strong symmetry implies the existence of multiple steady states. We showed that the dissipative phase transition to the self-organized state can occur at different thresholds in different symmetry sectors. We describe the atomic part of the steady states by generalized Gibbs ensembles. We analyzed how the nature of the steady state changes drastically when a small term that breaks the strong symmetry is introduced. The timescales towards the new unique steady state where found to be proportional to $1/U^2$, associated with the scattering between the different momentum states of the atoms. We have shown that even for a many-body system with a strong symmetry the phenomenon of dissipative freezing can occur when one considers the behavior of individual quantum trajectories. We observe that, at intermediate time, one can still identify the effect of dissipative freezing even if the strong symmetry has been slightly broken. Our work rises the open question whether a spontaneous symmetry breaking can also be observed in single trajectories of an experimental measurement. This would question the interpretation of the absence of intermittency in experimental measurements.

Chapter 7

Cavity-induced spin-orbit coupling in an interacting bosonic wire: a mean field study

In this chapter, we consider a model in which a complicated coupling between the atoms and the cavity allows for the realization of exotic phases of the atoms. Thus, in the following, we study interacting bosons confined to a one-dimensional wire, where we show that the coupling to a cavity mode can dynamically induce spin-orbit coupling [93]. The first step in the analysis is to investigate the steady state phase diagram of this model at a mean field level, as we did in Sec. 2.1 for the simpler atoms-cavity coupling. We show that at this level of approximation the dynamic stabilization of a state with a persistent chiral spin current, the Meissner superfluid, in the coupled atomic cavity system is possible. As an outlook for this chapter, the natural question arises if the non-trivial Meissner superfluid steady state survives once the fluctuations beyond the mean field are correctly taken into account with the methods we developed in Chap. 3 and Chap. 4.

In recent years, a significant amount of experimental progress has been realized in the creation of ultracold atomic gases subjected to synthetic magnetic field or spin-orbit coupling [92, 231–242]. This has opened new and exciting possibilities for the realization of exotic quantum phases such as Meissner phases or topologically non-trivial phases in a well controlled way. In the case of cold atoms loaded into an optical lattice one can use a pair of Raman beams in order to induce a tunneling process between neighboring lattice sites. If one of the Raman beams has a running wave nature the wavefunction of atoms accumulates a position dependent phase. The imprint of such a phase can be interpreted as the analog of an Aharanov-Bohm phase of charged particles in a magnetic field. In a continuum system the spin-orbit coupling of atoms has been realized using two-photon Raman transitions which couple internal states of the atoms for bosons [233, 243] and fermions [244, 245]. The realized spin-orbit coupling couples the particle's spin, which is represented by the internal state of the atoms, with its momentum, this induces chiral currents or topological effects [246, 247]. One example of such a non-trivial state is the Meissner state, which corresponds to a helical liquid. In this state

the spin and the momentum directions of the particles become locked to each other, this gives rise to the propagation of the two spins in opposite directions, which induces a chiral current [248–252].

The gauge fields which appear in high-energy and condensed-matter physics models are dynamical quantum degrees of freedom, such that going beyond the statically induced gauge fields [236–239] is of great interest. The dynamic generation of gauge fields by a cavity-assisted tunneling has been proposed for cold atoms subjected to an optical lattice, where the artificial magnetic field is induced dynamically via the feedback mechanism between the cavity field and the motion of atoms [61, 79–83, 93]. We note that a different approach for realizing dynamical gauge fields uses Floquet driving [240–242, 253]. Phases for which the cavity mediated spin-orbit coupling plays an important role have been considered for standing-wave cavities [74, 88, 254–257], or ring cavities [75, 258, 259]. Experimentally cavity mediated spin-dependent interactions [86] and spinor self-ordering of bosonic atoms coupled to a cavity [87] have been realized, which led to the demonstration of dynamical spin-orbit coupling [92]. Theoretically, the steady state phase diagram has been determined for a ladder geometry in the case of noninteracting fermions [78–80] and interacting bosons [83], where states with finite chiral currents have been found, or non-trivial topological properties in two dimensions [61].

This chapter is organized as follows, following Ref. [93], in Sec. 7.1.1 we describe the setup of the interacting bosonic wire placed into the optical cavity. In Sec. 7.1.2 we derive the mean field effective model for the atomic degrees of freedom and a stability condition by eliminating the dynamics of the cavity field. In Sec. 7.1.3 we discretize our continuum model in order to simulate the system on a lattice. Next, in Sec. 7.1.4 we present the observables of interest for the characterization of the Meissner superfluid state. We consider a set of parameters close to the ones of existing experimental setups and we show that the dynamical stabilization of the Meissner superfluid as a self-organized state with a finite cavity occupation is possible in Sec. 7.2. In this work, I derived the effective mean field model and performed the numerical ground state simulations using MPS.

7.1 Model

7.1.1 Description of the setup

In this chapter we investigate an ultracold bosonic gas placed in an optical cavity confined to a one-dimensional wire as sketched in Fig. 7.1 [93]. In order to create the spin-orbit coupling three internal states of an atom are used [see Fig. 7.1(b)]. The states from the lower energy manifold, $|\uparrow\rangle$ and $|\downarrow\rangle$, differ in energy by $\hbar\omega_z$, and can be coupled using two balanced Raman transitions. Each of the Raman transitions involves a transverse running-wave pump laser and the standing-wave cavity mode (Fig. 7.1). The transverse pump laser beams have the frequencies $\omega_{p,i=1,2}$, the Rabi frequencies $\Omega_{p,i=1,2}$ and the wave-vectors $\mathbf{k}_{p,i} = k_p\mathbf{e}_x$, along the x-direction, where the unit vectors along the three spatial directions are $\{\mathbf{e}_x, \mathbf{e}_y, \mathbf{e}_z\}$. The difference in frequency between the two pump beams is $\hbar(\omega_{p,2} - \omega_{p,1}) \approx 2\hbar\omega_z$. The cavity mode has the frequency ω_c, vacuum Rabi frequency g_0 and the wave-vector $\mathbf{k}_c = k_c\mathbf{e}_y$. As we use only one of the cavity modes, we assume that all the other cavity modes are far detuned from the possible transitions. We choose the detuning between the cavity mode and the first pump beam such
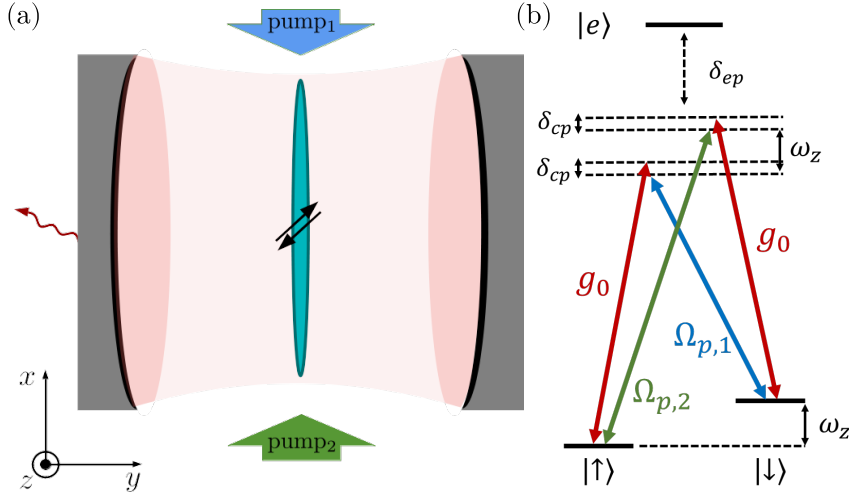
Figure 7.1: (a) Sketch of the setup. The bosonic atoms in an optical cavity are confined in a one-dimensional wire. (b) Level scheme of the cavity-induced Raman coupling: $|\uparrow\rangle$ and $|\downarrow\rangle$ denote two internal states, and $|e\rangle$ the excited internal electronic state. The energy offset between the two states is $\hbar\omega_z$. The spin-orbit coupling is realized by two Raman processes each of which involve the cavity mode with vacuum Rabi frequency g_0 and one of the two transverse running wave pump beam with Rabi frequency $\Omega_{p,i=1,2}$. δ_{ep} and δ_{cp} are the frequencies of the excited state and the cavity mode in the rotating frame. ©2019 American Physical Society, published in [93].

that it is close to the offset, $\hbar(\omega_c - \omega_{p,1}) \approx \hbar\omega_z$, furthermore the cavity and pump modes are considered to be far detuned from the internal atomic transition to the excited state, i.e. $\omega_e \gg \omega_c, \omega_{p,i=1,2}$, thus, the excited state population is negligible and can be adiabatically eliminated. In the following we will use the rotating frame with the frequency $\omega_p = (\omega_{p,2} + \omega_{p,1})/2$.

We obtain the spin-orbit coupling with the help of the cavity-induced Raman tunneling [93]. During the Raman transition a spatially dependent phase factor $e^{-i\Delta\mathbf{k}\cdot\mathbf{r}}$ is imprinted onto the atomic wavefunction, where $\Delta\mathbf{k} = k_p\mathbf{e}_x \pm k_c\mathbf{e}_y$ and $\mathbf{r} = x\mathbf{e}_x$. This corresponds to a dynamically induced spin-orbit coupling. As the cavity mode does not give a contribution, the imprinted flux is $\varphi = k_p$, defining a corresponding length-scale $l_\varphi \equiv 2\pi/\varphi$. The strength of the spin-orbit coupling can be varied, in an experimental realization, by tilting the pump beams away from the $\mathbf{e}_x$ direction.

The Hamiltonian, which describes the effective description for the atoms after the adiabatic elimination of the excited state, derived similarly to Refs. [65, 101], is given by

$$H = H_c + H_{kin} + H_{int} + H_{trap} + H_{ac} \tag{7.1}$$
$$H_c = \hbar\delta_{cp}a^\dagger a$$
$$H_{kin} = -\frac{\hbar^2}{2m}\sum_{\sigma=\uparrow,\downarrow}\int dx\,\psi_\sigma^\dagger(x)\partial_x^2\psi_\sigma(x)$$
$$H_{int} = \frac{U}{2}\sum_{\sigma=\uparrow,\downarrow}\int dx\,\psi_\sigma^\dagger(x)^2\psi_\sigma(x)^2$$

$$+ V \int dx \, \psi_\uparrow^\dagger(x)\psi_\uparrow(x)\psi_\downarrow^\dagger(x)\psi_\downarrow(x)$$

$$H_{\text{trap}} = \frac{4V_{trap}}{\mathcal{L}^2} \sum_{\sigma=\uparrow,\downarrow} \int dx \, (x-x_0)^2 \psi_\sigma^\dagger(x)\psi_\sigma(x)$$

$$H_{\text{ac}} = -\hbar\tilde{\Omega}(a+a^\dagger)(K_{\uparrow\downarrow} + K_{\uparrow\downarrow}^\dagger)$$

$$K_{\uparrow\downarrow} = \int dx \, e^{ix\varphi}\psi_\uparrow^\dagger(x)\psi_\downarrow(x).$$

H_c describes the cavity mode in the rotating frame, where $\delta_{cp} = \omega_c - \omega_p$ and a and $a^\dagger$ are the bosonic annihilation and creation operators for the cavity mode. The bosonic field operators $\psi_\sigma(x)$ and $\psi_\sigma^\dagger(x)$ are the annihilation and creation operators of the atoms in the wire for the spin state $\sigma = \uparrow, \downarrow$. The length of the one-dimensional system is denoted by $\mathcal{L}$. The total number of bosonic atoms is N, with the mean inter-particle spacing $d = \mathcal{L}/N$ and the density of the wire $\rho = d^{-1}$. H_kin describes the kinetic term for the atoms along the direction of the wire, with m the mass of the atoms. H_int gives the repulsive contact interaction, where the strength of the interaction of the atoms with the same spin is spin independent and denoted by U and between atoms with different spin is V, $(U, V > 0)$. In current experimental setups an external harmonic trapping potential is often present. We included this effect by adding the term H_trap, with $x_0 = \mathcal{L}/2$. The coupling between the atoms and the cavity field is described by H_ac, where the creation or annihilation of a cavity photon is accompanied by a spin flip. As the imprinted phase during the spin flip has a spatial dependence it follows that a dynamically induced spin-orbit coupling for the atoms is realized. We prevent a privileged spin state by coupling the spin flip in each direction to both the creation and the annihilation operators of the cavity field, using two pump laser beams [260]. The strength of this process is given by the amplitude $\tilde{\Omega} = \frac{\Omega_{p,1}g_0}{\omega_e - \omega_{p,1}}$, where g_0 is the Rabi frequency of the cavity mode. We fix the Rabi frequency of the second pump beam to $\Omega_{p,2} = \Omega_{p,1}\frac{\omega_e - \omega_{p,2}}{\omega_e - \omega_{p,1}}$, in order to realize the balanced Raman scheme.

The coupled atoms-cavity system is an open system, as we have losses due to the imperfections of the cavity mirrors. We include the dissipative nature of the cavity with a Lindblad equation, as mentioned in Sec. 2.1. The evolution of an arbitrary operator O is given by [56]

$$\frac{\partial}{\partial t}O = \frac{i}{\hbar}[H, O] + \mathcal{D}(O), \tag{7.2}$$

with the dissipator $\mathcal{D}(O) = \frac{\Gamma}{2}\left(2a^\dagger O a - O a^\dagger a - a^\dagger a O\right)$, which describes the loss of cavity photons. We mention that our model, Eqs. (7.1)-(7.2), has been recently realized experimentally in Ref. [92].

7.1.2 Mean field treatment of the cavity field

In this chapter, we adiabatically eliminate of the cavity field at a mean field level [65, 78, 83, 93]. We described this approach in Sec. 2.1 and we used it to contrast our newly developed methods presented in Chapter 5. Within this approximation, the cavity field is replaced with its steady state value, computed from the condition $\partial_t\langle a\rangle = 0$ and an effective model for the

bosonic atoms is derived. Using the equation of motion Eq. (7.2) this condition becomes

$$i\partial_t \langle a \rangle = -\tilde{\Omega} \langle K_{\uparrow\downarrow} + K_{\uparrow\downarrow}^\dagger \rangle + \left(\delta_{cp} - i\frac{\Gamma}{2} \right) \langle a \rangle = 0. \tag{7.3}$$

This relates the expectation value of the cavity field to the expectation value of the observable $K_{\uparrow\downarrow}$ by

$$\langle a \rangle = \frac{\tilde{\Omega}}{\delta_{cp} - i\frac{\Gamma}{2}} \langle K_{\uparrow\downarrow} + K_{\uparrow\downarrow}^\dagger \rangle. \tag{7.4}$$

The model exhibits a weak $\mathbb{Z}_2$ symmetry, associated with the inversion of the sign of both the cavity field, $a + a^\dagger$, and of $K_{\uparrow\downarrow} + K_{\uparrow\downarrow}^\dagger$. As we saw in Sec. 2.1 and Sec. 4.3 mean field approaches break the $\mathbb{Z}_2$ symmetry at the transition. In the following we look at the mean field solutions which have $\langle K_{\uparrow\downarrow} + K_{\uparrow\downarrow}^\dagger \rangle > 0$.

The mean field decoupling of the atomic and cavity degrees of freedom leads to the following equations of motion for the atomic operators

$$i\hbar\partial_t \langle \psi_\sigma(x) \rangle = -\frac{\hbar^2}{2m} \partial_x^2 \langle \psi_\sigma(x) \rangle + U \langle \psi_\sigma^\dagger(x) \psi_\sigma(x) \psi_\sigma(x) \rangle$$
$$+ V \langle \psi_\sigma(x) \psi_{\bar{\sigma}}^\dagger(x) \psi_{\bar{\sigma}}(x) \rangle - \hbar\tilde{\Omega} \langle a + a^\dagger \rangle e^{\pm i\varphi x} \langle \psi_{\bar{\sigma}}(x) \rangle$$
$$+ \frac{4V_{trap}}{\mathcal{L}} (x - x_0)^2 \langle \psi_\sigma(x) \rangle, \tag{7.5}$$

with $\sigma = \uparrow$ or $\downarrow$ and the sign in the exponential is positive for the spin state $\sigma = \uparrow$ and negative for $\sigma = \downarrow$. We substitute the expectation value of the cavity field, Eq. (7.4), into the equations of motion of the bosonic operators, Eq. (7.5). Thus we obtain that the effective dynamics of the atom can described by the following Hamiltonian [93]

$$H_{eff} = H_{kin} + H_{\uparrow\downarrow} + H_{int} + H_{trap} \tag{7.6}$$
$$H_{\uparrow\downarrow} = -J_{\uparrow\downarrow} (K_{\uparrow\downarrow} + K_{\uparrow\downarrow}^\dagger).$$

In this effective Hamiltonian, Eq. (7.6), $J_{\uparrow\downarrow}$ gives the amplitude of the spin-orbit coupling. $J_{\uparrow\downarrow}$ has to be computed self-consistently because it depends on the occupation of the cavity field and thus on the expectation value of $\langle K_{\uparrow\downarrow} \rangle$. The self consistency condition is given by

$$J_{\uparrow\downarrow} = A \langle K_{\uparrow\downarrow} \rangle, \text{ with } A = \frac{4\hbar\tilde{\Omega}^2 \delta_{cp}}{\delta_{cp}^2 + \Gamma^2/4}. \tag{7.7}$$

We will call A, loosely, the pump strength, since it is one of the experimental knobs used to tune A. Depending on the parameters non-trivial self consistent solutions can be typically found for a continuous range of values of A. We will obtain the solutions of this mean field as the ground state of the effective Hamiltonian, Eq. (7.6). This is a rather arbitrary choice as any eigenstate of the effective Hamiltonian would be a solution of the mean field equations of motion, as we saw

in Sec. 2.1 and Sec. 4.3, and in Ref. [110]. However, it is important to first understand the nature of the phases that can be realized in the ground state of the effective atomic Hamiltonian before considering the effects of the fluctuations beyond the mean field decoupling of the atoms and the cavity.

We determine stability of the non-trivial mean field solutions in the self-organized phase by considering perturbations around the mean field steady state [65, 83, 261]. We follow an analogous stability analysis as performed in Ref. [83]. By looking at the behavior of linear fluctuations around the stationary solutions of the equations of motion for the cavity field, Eq. (7.3), we obtain the following stability condition

$$\frac{d\langle K_{\uparrow\downarrow}\rangle}{dJ_{\uparrow\downarrow}} < \frac{1}{A}. \tag{7.8}$$

We note that for the rest of this chapter by stable solutions we mean solutions for which the condition given by Eq. (7.8) is satisfied, but which *do not* take into account the fluctuations beyond the mean field decoupling of the atoms and the cavity.

7.1.3 Discrete lattice model

As the matrix product state method for ground state search (see Sec. 3.1.2) that we want to employ to determine the self-consistent solutions is designed for discrete Hamiltonian, we discretise the spatial dimension with a spacing Δx. This maps the effective Hamiltonian, Eq. (7.6), to the corresponding model on a lattice, which reads [93]

$$H_{BH} = H_{kin} + H_{\uparrow\downarrow} + H_{int} + H_{trap} \tag{7.9}$$

$$H_{kin} = -\frac{J}{\Delta x^2} \sum_{l,\sigma=\uparrow,\downarrow} (b_{\sigma,l}^\dagger b_{\sigma,l+1} + b_{\sigma,l+1}^\dagger b_{\sigma,l})$$

$$H_{\uparrow\downarrow} = -J_{\uparrow\downarrow}(K_{\uparrow\downarrow} + K_{\uparrow\downarrow}^\dagger)$$

$$K_{\uparrow\downarrow} = \sum_l e^{i\varphi\Delta xl} b_{\uparrow,l}^\dagger b_{\downarrow,l}$$

$$H_{int} = \frac{U}{2\Delta x} \sum_{l,\sigma=\uparrow,\downarrow} n_{\sigma,l}(n_{\sigma,l} - 1) + \frac{V}{\Delta x} \sum_l n_{\uparrow,l} n_{\downarrow,l}$$

$$H_{trap} = \frac{4V_{trap}}{\mathcal{L}^2} \Delta x^2 \sum_{l,\sigma=\uparrow,\downarrow} (l - l_0)^2 n_{\sigma,l}.$$

The bosonic operators $b_{\sigma,l}$ and $b_{\sigma,l}^\dagger$ are the annihilation and creation operators of the atoms where $\sigma = \uparrow, \downarrow$ labels the legs of the ladder and $l = 1, ..., L$ the rungs of the ladder. L denotes the number of the rungs of the ladder and it is related to the physical size of the system by $L = \frac{\mathcal{L}}{\Delta x} + 1$. The operator $n_{\sigma,l} = b_{\sigma,l}^\dagger b_{\sigma,l}$ is the number operator and $J = \frac{\hbar^2}{2m}$. H_{BH} corresponds to a Bose-Hubbard ladder in a magnetic field, where the two spins states represent the two legs of the ladder and spin flip processes are equivalent to the tunneling along the rungs of the ladder.

This model has been studied previously in Refs. [262–266] and compared to our previous work from Ref. [83] on the bosonic ladder in a magnetic field, here we have the additional non-local interaction along the rungs of the ladder, given by V. The parameters of the ladder model are renormalized such that in the continuum limit, $\Delta x \to 0$, we would recover the Hamiltonian given by Eq. (7.6).

The procedure of determining the stable steady states of the model, Eq. (7.1), consists in four steps [93]:

1. First, we compute the ground state of the effective discrete model, Eq. (7.9), using a MPS method, for a fixed discrete spacing Δx and physical parameters of the continuum model: system size $\mathcal{L}$, particle number N, magnetic flux ϕ, and interactions U/J and V/J, while varying $J_{\uparrow\downarrow}/J$.

2. We compute the expectation value $\langle K_{\uparrow\downarrow}\rangle$ as a function of $J_{\uparrow\downarrow}/J$ and solve the self-consistency equation. The self-consistency condition, Eq. (7.7), can be interpreted graphically, using the reformulation

$$\frac{\langle K_{\uparrow\downarrow}\rangle}{\mathcal{L}d^{-1}} = \frac{J}{A\mathcal{L}d}\left(\frac{J_{\uparrow\downarrow}}{Jd^{-2}}\right). \tag{7.10}$$

The self-consistent solution correspond to the intersectionof the two curves. The slope of the right-hand side depends on the pump strength A. Thus, the solutions have to be determined for each value of the pump strength A.

3. The stability of the non-trivial solutions is inferred by comparing the slopes of the left-hand and right-hand sides of Eq. (7.10). The stability condition, Eq. (7.8), tells us that a solution is stable if the slope of $\langle K_{\uparrow\downarrow}\rangle$ is smaller than $\frac{J}{A\mathcal{L}d}$.

4. The last step is to verify the convergence of the results in the continuum limit $\Delta x \to 0$ by considering smaller values of Δx.

7.1.4 Observables in the Meissner phase

We show how a Meissner superfluid can be dynamically stabilized in the cavity, at mean field level, for the parameters considered in this work [93]. In this section, we describe the observables that we use to characterize the non-trivial stable steady states of the system and how we can identify them with the corresponding observables computed on the ladder. We focus the observables which can be used to characterize the properties of the Meissner superfluid. The Meissner state can be thought as a "zero momentum" state, because close to the non-interacting regime the bosonic quasiparticles are condensed in the single-particle dispersion minimum at momentum $k = 0$. It corresponds to a helical liquid, where the spin and the momentum directions of the particles lock to each other and with the two spins propagating in opposite directions [248–252], which gives rise to a chiral current.

We analyze the local densities and currents, as their configurations can point towards the Meissner or vortex nature of the chiral phases. The local density $n_\sigma(x)$, the local current $j_\sigma(x)$, and the spin flip current $j^{\uparrow\downarrow}(x)$ are defined and computed as

$$n_\sigma(x) = \psi_\sigma^\dagger(x)\psi_\sigma(x) \approx \frac{1}{\Delta x}b_{\sigma,l}^\dagger b_{\sigma,l}$$

$$j_\sigma(x) = -iJ\big[\psi_\sigma^\dagger(x)\partial_x\psi_\sigma(x) - (\partial_x\psi_\sigma^\dagger(x))\psi_\sigma(x)\big]$$

$$\approx -i\frac{J}{\Delta x^2}\Big(b_{\sigma,l}^\dagger b_{\sigma,l+1} - \text{H.c.}\Big),$$

$$j^{\uparrow\downarrow}(x) = -iJ_{\uparrow\downarrow}\Big(e^{i\varphi x}\psi_\downarrow^\dagger(x)\psi_\uparrow(x) - \text{H.c.}\Big)$$

$$\approx -i\frac{J_{\uparrow\downarrow}}{\Delta x}\Big(e^{i\varphi\Delta x l}b_{\downarrow,l}^\dagger b_{\uparrow,l} - \text{H.c.}\Big), \tag{7.11}$$

with $x = l\Delta x$. From the local currents, one can compute global observables as the chiral current J_c, which is a persistent spin current

$$J_c = \frac{1}{\mathcal{L}}\int dx\,\langle j_\uparrow(x) - j_\downarrow(x)\rangle. \tag{7.12}$$

In an infinite homogeneous system in the Meissner state we have zero spin flip currents in the bulk and a finite value of the chiral current. We compute the values of the chiral current and of the expectation value of $\langle K_{\uparrow\downarrow}\rangle$ by approximating the integrals with sums performed on the lattice, $\int dx\,O(x) \approx \Delta x\sum_l O(l\Delta x)$.

We characterize the superfluid nature of the obtained states with the help of the decay single particle correlation. An algebraic decay is a characteristic feature of the standard Luttinger liquid paradigm [122]. Here we use $\langle\psi_\sigma^\dagger(x_0)\psi_\sigma(x_0 + x)\ + \text{H.c.}\rangle \approx \langle b_{\sigma,l_0}^\dagger b_{\sigma,l_0+l} + \text{H.c.}\rangle \propto l^{-\alpha}$. In the Meissner superfluid phase the central charge c, which can be interpreted as the number of gapless modes, is $c = 1$, as this phase has a gapless symmetric sector due to the superfluid nature of the state and a gapped antisymmetric sector. We extract the central charge from the scaling of the von Neumann entropy $S_{vN}(l)$ of an embedded subsystem of length l in a system of length L. We compute $S_{vN}(l)$ for a bipartition into two subsystems of length l and $L - l$. We note that we use open boundary conditions, for which the von Neumann entropy for the ground state of gapless phases scales as [145, 267, 268]

$$S_{vN} = \frac{c}{6}\log\left(\frac{L}{\pi}\sin\frac{\pi l}{L}\right) + s_1, \tag{7.13}$$

where s_1 is a non-universal constant and we have neglected oscillatory terms [269] due to the finite size of the system and logarithmic corrections [270].

In the numerical simulations performed we observe oscillations in the local density and currents, which are algebraically decaying away from the boundaries, due to the lattice discretization and the open boundary conditions. We try to reduce the influence of these boundary effects on the computed observables, such that we extract the values of J_c and $\langle K_{\uparrow\downarrow}\rangle$ from the average around which the oscillations occur, by fitting the density and currents in the center of the system, with the oscillating function $f(x) = a + b\cos(cx + \phi)$. We observe that in the Meissner phase the amplitude of these oscillations decreases in the continuum limit and vanishes in the thermodynamic limit.

7.2 Results

In the following, we present our numerical results following Ref. [93]. They were obtained using a finite-size density matrix renormalization group (DMRG) algorithm in the MPS representation [124, 129, 271–273], implemented using the ITensor Library [139]. This method was described in Sec. 3.1.2. We compute the ground state of the discrete model Eq. (7.9) for ladders with a number of rungs between $L = 125$ and $L = 275$, depending on the chosen discretisation Δx, and with a maximal bond dimension up to 1500. This ensures that the truncation error is at most 10^{-12}. More in depth convergence checks regarding the influence of different bond dimensions are truncation errors on the observables of interest for the bosonic ladder in an artificial magnetic field are done in Ref. [274]. Since we are considering a bosonic model with finite interactions the local Hilbert space is very large, thus, a cutoff for its dimension is needed. We use a maximal local dimension of three bosons per site, justified by low density of particles on the ladder. The higher cutoff of four bosons per site gives consistent results. We make use of good quantum numbers in our implementation as the number of atoms in conserved in the considered model.

7.2.1 Identifying the stable stationary states in the homogeneous system

In the following, we solve the self-consistency condition and identify the mean field steady states which can be stabilized for different values of $J_{\uparrow\downarrow}$, for magnetic length $l_\varphi = 2\pi/\varphi = 0.8d$, interaction $U = 32.5Jd^{-1}$ and $V = 30Jd^{-1}$ in a homogeneous system, $V_{trap} = 0$ [93]. The results show that the dynamic stabilization of a Meissner superfluid state is possible. We begin by calculating the expectation value $\langle K_{\uparrow\downarrow}\rangle/\mathcal{L}d^{-1}$ in the ground state of the effective model. We determine the self-consistent solutions by intersections of this curve with the linear function $\frac{J}{A\mathcal{L}d}\left(\frac{J_{\uparrow\downarrow}}{Jd^{-2}}\right)$, as presented in Fig. 7.2(a) for $\mathcal{L} = 32d$ and different values of Δx. In order to check the stability of the solutions we compare the slopes of the two curves, Eq. (7.10). As we stated above, if the derivative of $\langle K_{\uparrow\downarrow}\rangle/\mathcal{L}d^{-1}$ is less than the slope of the linear function, the solution is stable. We observe that for the considered parameters (Fig. 7.2), we can find stable solutions for $J_{\uparrow\downarrow} \gtrsim 18.75Jd^{-2}$, for all considered values of discretization Δx.

As our simulations are for finite values of Δx, the results also imply that the stabilization of the Meissner superfluid state is possible in a system which has an underlying lattice potential, as also shown in Ref. [83] for a different set of parameters. We perform an extrapolation of our data for finite Δx in order to estimate the value of $\langle K_{\uparrow\downarrow}\rangle/\mathcal{L}d^{-1}$ in the limit $\Delta x \to 0$, this is shown in the inset of Fig. 7.2(a) for $J_{\uparrow\downarrow} = 62.5Jd^{-2}$. In the plots depicted Fig. 7.2(a) the value of $\langle K_{\uparrow\downarrow}\rangle/\mathcal{L}d^{-1}$ in the continuum limit is labeled by $\Delta x \to 0$. We see that the extrapolation $\Delta x \to 0$ also leads to a stable solution, such that we are confident that the solutions remain stable in the continuum limit, $\Delta x \to 0$.

In contrast, we observe that for small values of $J_{\uparrow\downarrow}$, marked by the grey region in our plots, we cannot make a conclusive statement about the stability, due to the fact that $\langle K_{\uparrow\downarrow}\rangle/\mathcal{L}d^{-1}$ has an almost linear behavior, as we seen in Fig. 7.2(a). This linear behavior would suggest that any small change in the numerical determination and the extrapolation could render the stable behavior unstable and vice versa. We can also obtain some information about the stability of the system in the thermodynamic limit. Thus, we performed the above procedure for different
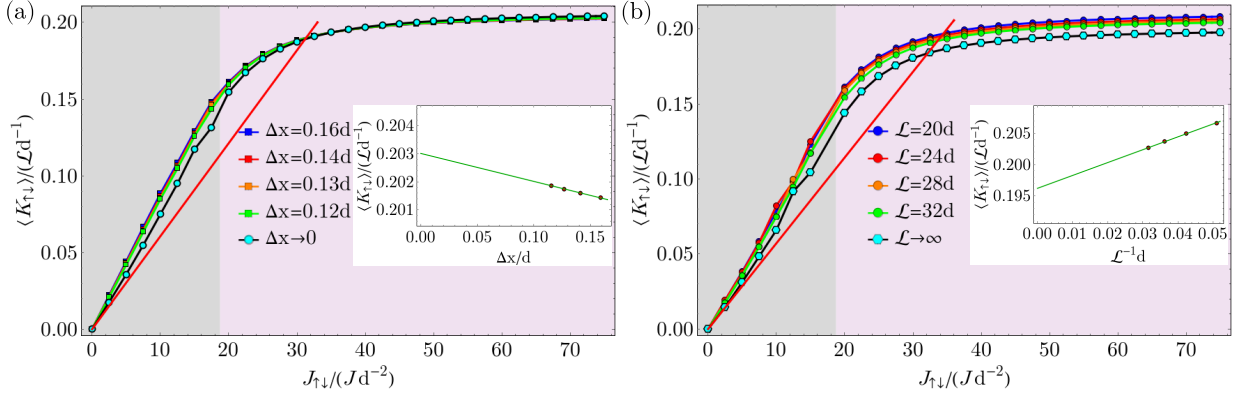
Figure 7.2: Graphical interpretation of the self-consistency condition for the parameters $l_\varphi = 0.8d$, $U = 32.5Jd^{-1}$, $V = 30Jd^{-1}$ and $V_{trap} = 0$. The expectation value $\langle K_{\uparrow\downarrow}\rangle/Ld^{-1}$ is represented for (a) $\mathcal{L} = 32d$ and multiple values of Δx, together with an extrapolation to the limit $\Delta x \to 0$, (b) for multiple system sizes in the continuum limit, and the extrapolation to the thermodynamic limit $1/\mathcal{L} \to 0$. The straight (red) lines represent the right-hand side of the self-consistency condition, Eq. (7.10), which is a linear function with slope $\frac{J}{A\mathcal{L}d}$, for one chosen value of A. The intersections of the two curves give the solutions of the self-consistency condition. In the insets the extrapolations (a) $\Delta x \to 0$ and (b) $1/\mathcal{L} \to 0$ of $\langle K_{\uparrow\downarrow}\rangle/\mathcal{L}d^{-1}$, for $J_{\uparrow\downarrow} = 62.5Jd^{-2}$, are depicted. The purple shaded area marks the regime in which for a certain value of A a stable solution can be found and the grey shaded area the regime in which our results are not accurate enough in order to determine the stability conclusively. ©2019 American Physical Society, published in [93].
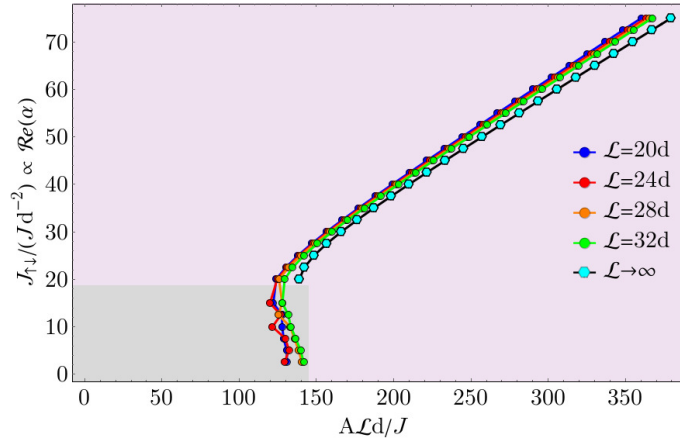
Figure 7.3: The solutions $J_{\uparrow\downarrow}/Jd^{-2}$ of the self-consistency equation which are proportional to the cavity field $Re(\alpha)$ versus the pump strength $A\mathcal{L}d/J$, for multiple $\mathcal{L}$, in the continuum and thermodynamic limits. In the grey area the stability of the solutions is not clear. ©2019 American Physical Society, published in [93].

system sizes and we performed an extrapolation to $\mathcal{L} \to \infty$, as exemplified in the inset of Fig. 7.2(b) for $J_{\uparrow\downarrow} = 62.5Jd^{-2}$. The values of $\langle K_{\uparrow\downarrow}\rangle/\mathcal{L}d^{-1}$ in the continuum limit are plotted in Fig. 7.2(b). This shows us that for $J_{\uparrow\downarrow} \gtrsim 18.75Jd^{-2}$ the self-consistent solutions remain stable

also in the thermodynamic limit.

The non-trivial stable solutions obtained in the continuum limit are plotted in Fig. 7.3, for multiple system sizes. All the nontrivial stable solutions have a finite occupation of the cavity field, independent of the discretization or system size, thus, they describe the behavior of the system in the self-organized phase. Our results suggest a sudden onset of the occupation of the cavity mode above a certain threshold of the pump strength [93], this is due to the fact that $J_{\uparrow\downarrow}/Jd^{-2}$ is proportional to the cavity field $Re(\alpha)$ [see Eqs. (7.4)-(7.7)].

7.2.2 Characterization of the Meissner superfluid steady state in the homogeneous system
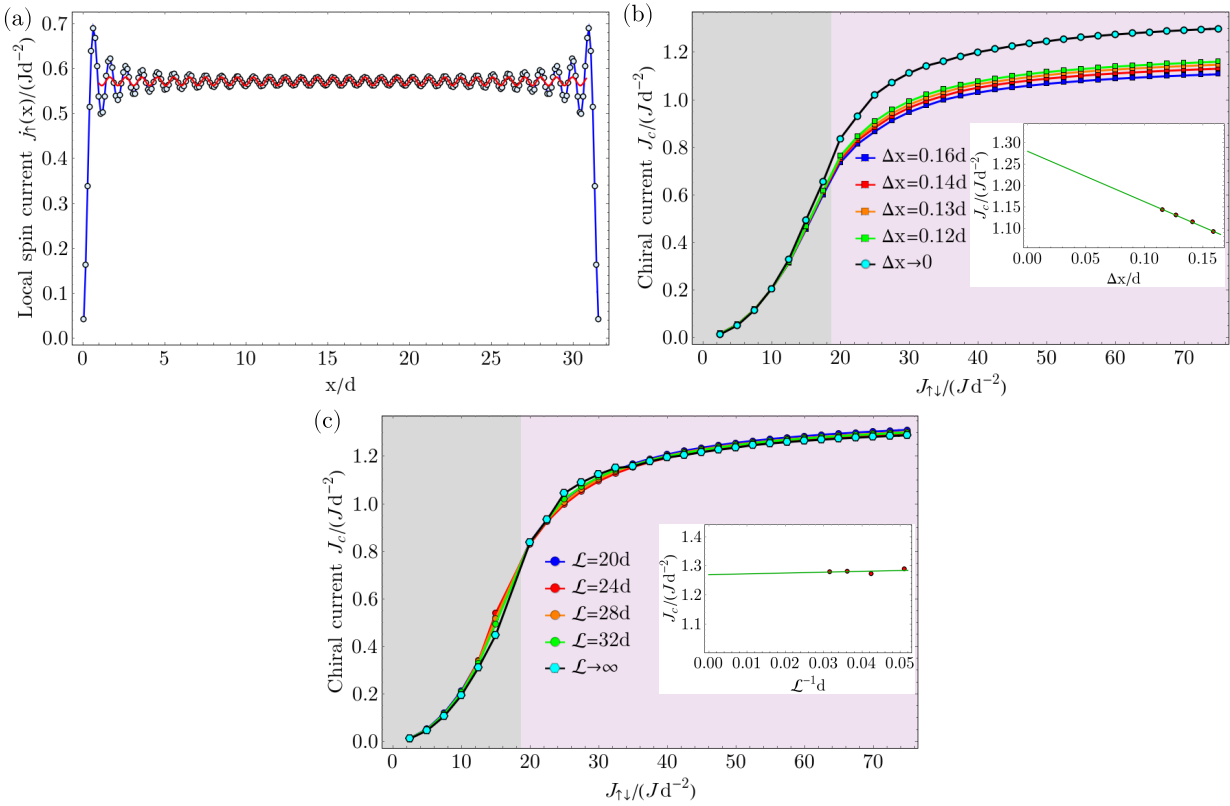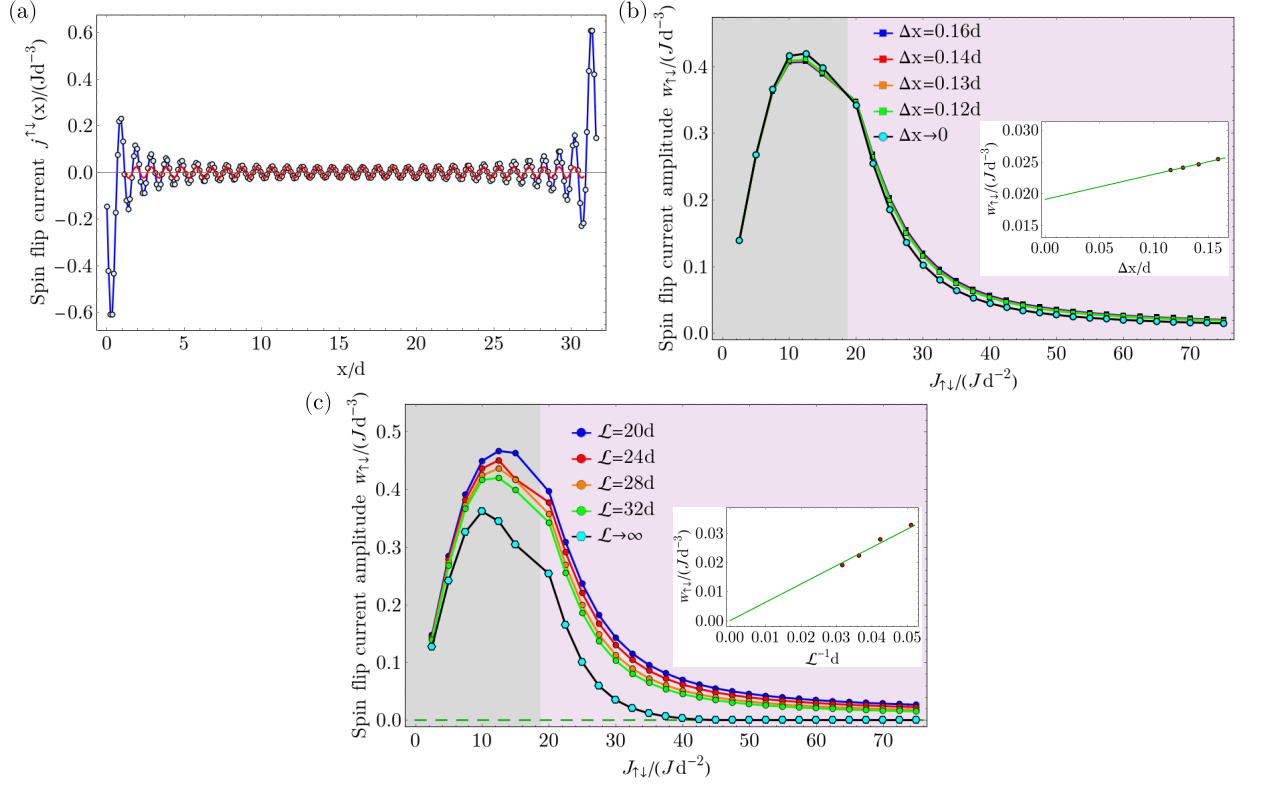

Figure 7.4: (a) The local current $j_\uparrow(x)$ for the parameters $l_\varphi = 0.8d$, $U = 32.5Jd^{-1}$, $V = 30Jd^{-1}$, $V_{trap} = 0$, $\mathcal{L} = 32d$, $J_{\uparrow\downarrow} = 62.5Jd^{-2}$ and $\Delta x = 0.12d$. The red curve represents the fit of the central part of the system, with the function $J_c/2 + a\cos(bx + \phi)$. (b) The chiral current J_c for the same parameters as a function of $J_{\uparrow\downarrow}$ for different values of the discretization and the extrapolation to the continuum limit. In the inset the extrapolation is shown for $J_{\uparrow\downarrow} = 62.5Jd^{-2}$. (c) The chiral current in the continuum limit for different system sizes and extrapolated to the thermodynamic limit. The extrapolation for $J_{\uparrow\downarrow} = 62.5Jd^{-2}$ is shown in the inset. ©2019 American Physical Society, published in [93].

We focus now on the states which are stable both in the continuum and thermodynamic limit and analyze their nature [93]. We show that the stable steady states, for $J_{\uparrow\downarrow} \gtrsim 18.75Jd^{-2}$,
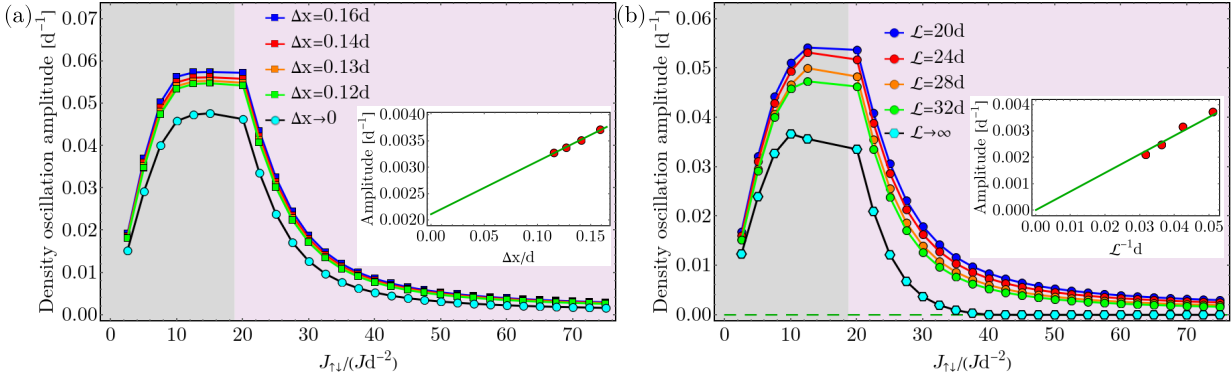
Figure 7.5: (a) The local current $j^{\uparrow\downarrow}(x)$ for the parameters $l_\varphi = 0.8d$, $U = 32.5Jd^{-1}$, $V = 30Jd^{-1}$, $V_{trap} = 0$, $\mathcal{L} = 32d$, $J_{\uparrow\downarrow} = 62.5Jd^{-2}$ and $\Delta x = 0.12d$. The red line represents the fit $w_{\uparrow\downarrow}\cos(ax + \phi)$ in the center of the system. (b) The amplitude of the oscillations in the spin flip current, $w_{\uparrow\downarrow}$, for the same parameters as a function of $J_{\uparrow\downarrow}$ for different values of the discretization and the extrapolation to the continuum limit. In the inset the extrapolation is shown for $J_{\uparrow\downarrow} = 62.5Jd^{-2}$. (c) $w_{\uparrow\downarrow}$ in the continuum limit for different system sizes and the extrapolation to the thermodynamic limit. In the inset the extrapolation is shown for $J_{\uparrow\downarrow} = 62.5Jd^{-2}$. In order to obtain an estimation of the spin flip current we enforce that it maintains a non-negative value in the $1/\mathcal{L} \to 0$ limit. ©2019 American Physical Society, published in [93].

correspond to the Meissner superfluid phase, by focusing on the behavior of the observables we introduced in Sec. 7.1.4. We observe that all stable solutions, $J_{\uparrow\downarrow} \gtrsim 18.75Jd^{-2}$, have a finite value of the chiral current, as shown in Fig. 7.4. In Fig. 7.4(a) we plot the local current along the wire for one spin state, $j_\uparrow(x)$. We exemplify here the procedure for the extraction of the value of the chiral current. We fit the oscillations, which are caused by the boundaries, in the center part of the system for each leg, with the function $J_c/2 + a\cos(bx + \phi)$. We extract the chiral current as a function of $J_{\uparrow\downarrow}$ for different values of Δx [see Fig. 7.4(b)], obtaining its behavior in the limit $\Delta x \to 0$. We observe that as we go to smaller discretizations we obtain a larger value for the chiral current, thus, we expect that it will have a finite value in the continuum. We perform this for multiple sizes of the system, as shown in Fig. 7.4(c), and we obtain consistent results, which indicates that the finite chiral current survives also in the thermodynamic limit. As we increase $J_{\uparrow\downarrow}$ and go deeper into the Meissner phase, the chiral current seems to saturate.

Figure 7.6: (a) The amplitude of the oscillations in the local density, for the parameters $l_\varphi = 0.8d$, $U = 32.5Jd^{-1}$, $V = 30Jd^{-1}$, $V_{trap} = 0$, $\mathcal{L} = 32d$ as a function of $J_{\uparrow\downarrow}$ for different values of the discretization and the extrapolation to the continuum limit. In the inset the extrapolation is shown for $J_{\uparrow\downarrow} = 62.5Jd^{-2}$. (c) The amplitude of the oscillations in the local density in the continuum limit for different system sizes and the extrapolation to the thermodynamic limit. In the inset the extrapolation is shown for $J_{\uparrow\downarrow} = 62.5Jd^{-2}$. We enforce that the extrapolated values are non-negative in the $1/\mathcal{L} \to 0$ limit.

Furthermore, the Meissner state is also characterized by balanced spin flip processes in the bulk of the system. In the lattice representation this implies that there are no currents on the rungs of the ladder. The behavior of this observable is shown in Fig. 7.5. We plot first the site-resolved spin flip current in Fig. 7.5(a), together with the fit function $w_{\uparrow\downarrow}\cos(ax + \phi)$, from which we extract the amplitude of the oscillations, $w_{\uparrow\downarrow}$. The results presented in Fig. 7.5 are computed by fitting the central $1/5$ part of the system. We note that this differs with at most 6% compared to the case if we would have considered a larger region, namely the central $2/5$ of the system, $x \in (\mathcal{L}/2 - \mathcal{L}/5, \mathcal{L}/2 + \mathcal{L}/5)$. As a function of $J_{\uparrow\downarrow}$, we observe that the amplitude of the spin flip current, $w_{\uparrow\downarrow}$, first increases with $J_{\uparrow\downarrow}$. The maximum around $J_{\uparrow\downarrow} \approx 12.5Jd^{-2}$ lies in the region where the stability is not clarified and then decreases for larger values of $J_{\uparrow\downarrow}$ [see Fig. 7.5(b)]. The finite spin flip currents at low values of $J_{\uparrow\downarrow}$ could indicate that a vortex state might be present. A phase transition may occur in the effective model between the Meissner state and a vortex state, close to the stability threshold. In Fig. 7.5(c), we extrapolate the amplitude of the spin flip current in the continuum limit and represent it as a function of $J_{\uparrow\downarrow}$ for different system sizes. In the thermodynamic limit the spin flip current vanishes deep in the Meissner phase, as expected. However, in the intermediate regime for $18.75Jd^{-2} \lesssim J_{\uparrow\downarrow} \lesssim 35Jd^{-2}$ the amplitude of the spin flip current is larger than zero in the thermodynamic limit. This might be caused by finite size effects, or the extrapolation being too rough in this regime. The amplitude of the oscillations in the particle density also goes to zero deep for large values of $J_{\uparrow\downarrow}$, after taking both the continuum and thermodynamic limit, as seen in Fig. 7.6.

Next we compute the central charge. In the Meissner superfluid the central charge has the value, $c = 1$. Our numerical data agrees with this value within the uncertainties as shown in Fig. 7.7. Furthermore, we observe that for $J_{\uparrow\downarrow} \lesssim 12.5Jd^{-2}$ the central charge has a value $c \approx 2$, which is consistent with the assumption of having a vortex state. It can be seen that close to

7.2.2 Characterization of the Meissner superfluid steady state in the homogeneous system
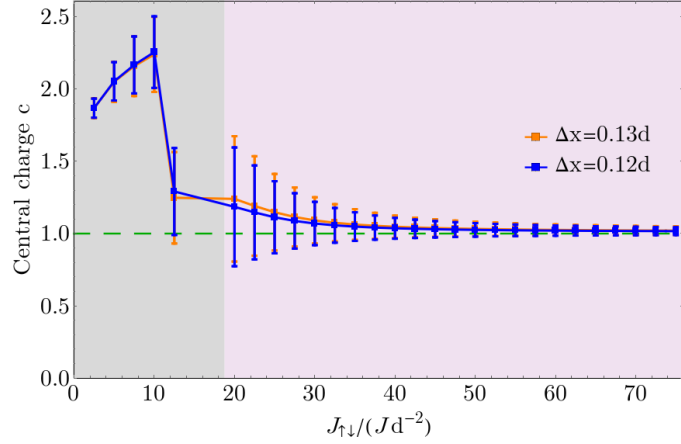
Figure 7.7: The central charge for the parameters $l_\varphi = 0.8d$, $U = 32.5d^{-1}J$, $V = 30Jd^{-1}$, $V_{trap} = 0$, $\mathcal{L} = 32d$ and multiple values of Δx, as a function of $J_{\uparrow\downarrow}$. The central charge is extracted fitting the scaling of the entanglement entropy. The errorbars represent the fit error. The dashed horizontal line indicates the constant value 1. ©2019 American Physical Society, published in [93].
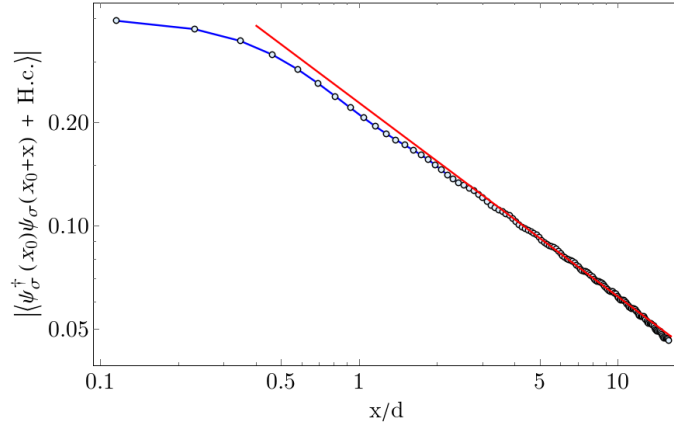

Figure 7.8: The absolute value of the single particle correlations $\langle \psi_\sigma^\dagger(x_0)\psi_\sigma(x_0 + x) + \text{H.c.} \rangle$ in a logarithmic plot for the parameters $l_\varphi = 0.8d$, $U = 32.5d^{-1}J$, $V = 30Jd^{-1}$, $V_{trap} = 0$, $\mathcal{L} = 32d$, $\Delta x = 0.12d$ for $J_{\uparrow\downarrow} = 62.5Jd^{-2}$, in the Meissner superfluid phase. The correlations show an algebraic decay with distance, which corresponds to the superfluid phase. The straight (red) line is a fit of the function $\propto x^{-\alpha}$, where $\alpha = 0.563 \pm 0.002$. ©2019 American Physical Society, published in [93].

the stability threshold both the error bars due to the fit error and the difference between the values of the central charge computed for different discretizations are larger.

The superfluid nature of the stable stationary state solutions is also confirmed by the algebraic decay of the single particle correlations, shown in Fig. 7.8 for $J_{\uparrow\downarrow} = 62.5Jd^{-2}$. We mention that, in the weakly interacting limit, a non-Luttinger liquid has been predicted [275] at the critical point of the transition between the vortex and Meissner superfluids, where an exponential decay of the single particle correlations is expected.
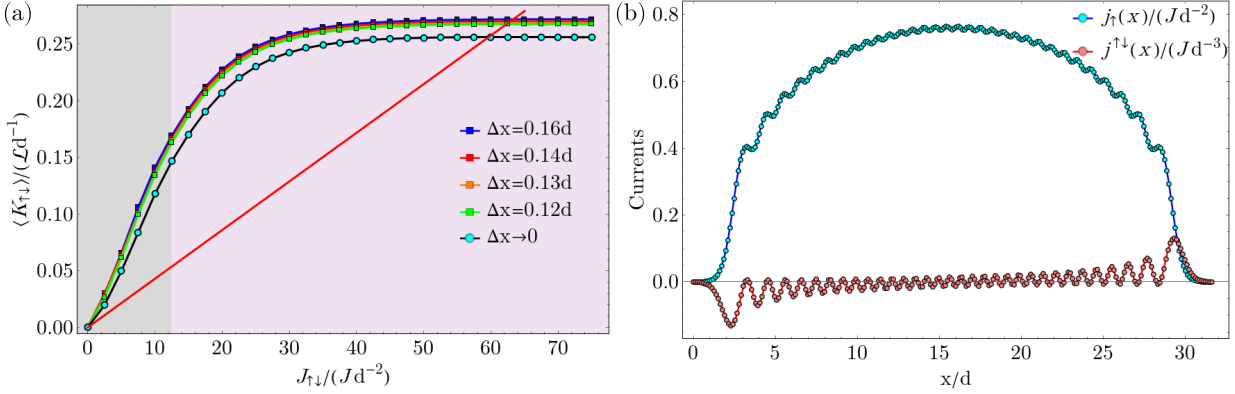
Figure 7.9: (a) Graphical interpretation of the self-consistency condition for the parameters $N = 32$, $l_\varphi = 0.8d$, $U = 32.5Jd^{-1}$, $V = 30Jd^{-1}$ and $V_{trap} = 5Jd^{-1}$. The expectation value $\langle K_{\uparrow\downarrow}\rangle/\mathcal{L}$ is represented for multiple values of Δx and an extrapolation to the limit $\Delta x \to 0$. The straight (red) line represents the right-hand side of the self-consistency condition, which is a linear function with slope $\frac{J}{A\mathcal{L}d}$. The crossings of the two curves give the solutions of the self-consistency condition. (b) The local currents $j_\uparrow(x)$ and $j^{\uparrow\downarrow}(x)$ for the same parameters and $J_{\uparrow\downarrow} = 62.5Jd^{-2}$ and $\Delta x = 0.12d$. ©2019 American Physical Society, published in [93].

7.2.3 The effect of the parabolic trap on the steady states

As an external trapping potential is common in current experimental setups we analyze the effects of the harmonic trapping H_{trap} on the dynamically organized steady states. In the following, we show that the Meissner state is stable also in the presence of a harmonic trap of strength $V_{trap} = 5Jd^{-2}$, for $l_\varphi = 0.8d$, $U = 32.5Jd^{-1}$, $V = 30Jd^{-1}$. As the trap induces a varying density, a coexistence of different states is possible across the trap. However, in determining the stability of the dynamically organized states one has to consider all regions, as $\langle K_{\uparrow\downarrow}\rangle/\mathcal{L}$, which enters the self-consistency condition, is a global observable. In the following, we focus in the characterization of the nature of the states that are present in the center of the trap, where the gradient of the trapping potential is the smallest.

In Fig. 7.9(a), the expectation value $\langle K_{\uparrow\downarrow}\rangle/\mathcal{L}$ as a function of $J_{\uparrow\downarrow}$ is plotted across the trap. The stable steady states are obtained for $J_{\uparrow\downarrow} \gtrsim 12.5Jd^{-2}$. In the following, we focus on stationary state for $J_{\uparrow\downarrow} = 62.5Jd^{-2}$. For this value the steady state is stable for all values of Δx computed and in the extrapolation to the continuum limit. Due to the trapping potential, the large oscillations at the boundaries are partially suppressed compared to the homogeneous case, as seen in Fig. 7.9(b). We identify the state realized for these parameters in the center of the trap as a Meissner superfluid, due to its finite chiral current, small values of the spin flip current and the algebraic decay of correlations (shown in Fig. 7.10). The local spin current $j_\uparrow(x)$ has a maximum in the center of the trap [Fig. 7.9(b)], different from the homogeneous case where $j_\uparrow(x)$ has a plateau-like behavior, as we can see Fig. 7.4(a). Because $j_\uparrow(x)$ and $j^{\uparrow\downarrow}(x)$ are related via a continuity equation, at the edges of the trap the spin flip current has mostly negative values, for $x \lesssim 10d$, or positive values, for $x \gtrsim 22d$. This implies that the amplitude of the oscillations of $j^{\uparrow\downarrow}(x)$ is small only in the central region of the trap. We note that the oscillations present in the
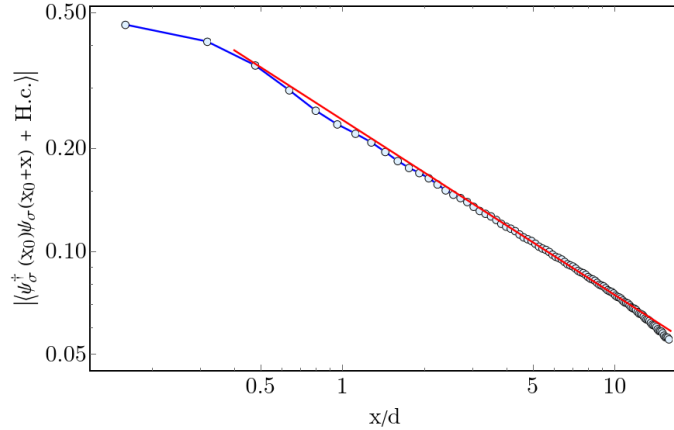
Figure 7.10: The absolute value of the single particle correlations $\langle \psi_\sigma^\dagger(x_0)\psi_\sigma(x_0 + x) + \text{H.c.}\rangle$ in a logarithmic plot for the parameters $N = 32$, $l_\varphi = 0.8d$, $U = 32.5Jd^{-1}$, $V = 30Jd^{-1}$ and $V_{trap} = 5Jd^{-1}$, $\Delta x = 0.12d$ for $J_{\uparrow\downarrow} = 62.5Jd^{-2}$, in the Meissner superfluid phase. The correlations show an algebraic decay with distance, which corresponds to the superfluid phase. The straight (red) line is a fit of the function $\propto x^{-\alpha}$, where $\alpha = 0.512 \pm 0.003$.

spin flip currents are due to the finite size of the system and boundary effects. Thus, we have shown that also in the presence of a harmonic trapping potential the dynamical stabilization of the Meissner superfluid is possible.

7.3 Comments on the experimental realization

As the parameters used in this chapter have been chosen such that they are close what is experimentally achievable, we shortly comment on the possibility of the experimental realization and how the Meissner state could be identified.

An experimental realization could use ^{87}Rb atoms in an optical cavity [67, 276, 277] subjected to additional optical lattices which confine the atoms to one-dimensional structures. Previous experiments of ultracold bosonic atoms in a cavity [65] observed the Dicke phase transition [67, 101, 171, 192, 260, 278] and an optical lattice has been added to investigate the influence of interaction [70–72]. Typical cavity parameters are $\kappa = 2\pi \times 4.5$ kHz and $g_0 = 2\pi \times 0.76$ MHz [276]. The cavity-induced spin-orbit coupling could be implemented using for example the two states from the ^{87}Rb $5S_{1/2}$ $F = 1$ manifold, $|\uparrow\rangle \equiv |F = 1, m_F = 0\rangle$ and $|\downarrow\rangle \equiv |F = 1, m_F = -1\rangle$ as used in Ref. [243]. The scattering lengths of the two ^{87}Rb states are $a_{\uparrow\uparrow} = 100.86a_B$ and $a_{\downarrow\downarrow} = 100.4a_B$ [279], with a_B the Bohr radius.

We propose different measurements in order to infer the nature of the steady state. A non-destructive measurement is the occupation of the cavity field by observing the leaking of the photons of the cavity. A finite occupation of the cavity field will identify the dynamically organized spin-orbit coupling and decide between the trivial and non-trivial steady states. In order to identify the state of the atomic component of the system, the measurement of the local density can be used to distinguish between a Meissner and a vortex state. In the Meissner case a density plateau in the center part of the wire is present, in contrast to a vortex state which

has density modulations. Furthermore, from the momentum distribution obtained in a time-of-flight experiment, one can check the dependence of the peak in the momentum distribution and the momentum transferred by the spin-orbit coupling. In Ref. [265] the connection between the peak in the momentum distribution and the imprinted phase is made in the context of bosonic ladders.

7.4 Short summary

To summarize, we show the dynamical stabilization of the Meissner superfluid of bosonic atoms confined in a one-dimensional wire coupled to an optical cavity [93]. In the proposed setup, the bosonic atoms are prepared in two hyperfine states coupled to each other via Raman transitions, which involve the creation or annihilation of a cavity photon and a position dependent momentum transfer. With this coupling a cavity mediated spin-orbit coupling is induced if a finite cavity occupation forms. Above a certain pump strength a nontrivial chiral state is realized as a steady state of the dissipative attractor dynamics. The dissipative dynamics takes place due to the leaking of photons out of the cavity mirrors.

The analysis in this chapter has been done at the level of the mean field decoupling of the cavity and the atoms. Thus, it would be interesting to see of the Meissner superfluid state survives once we include the fluctuations beyond mean field, as we performed in Chap. 5 and Chap. 6 for the models with a simpler coupling to the cavity field. This represents one of the outlooks of this chapter and will be treated in future work.

Chapter 8

Understanding the excitation spectrum across a phase transition: the XXZ-model in a transverse magnetic field

One class of quantum materials, which very often host interesting quantum states, are the low-dimensional quantum magnets [5, 122, 280–288]. Such systems show rich phase diagrams due to their enhanced quantum fluctuations, typical for low-dimensional systems. Considering the behavior of the spin degrees of freedom is often crucial to understand the properties of quantum phases with an insulating nature. In such systems, the interactions between neighboring spins are generally due to the superexchange coupling. Generically in quantum spin systems, one can couple the spin degrees of freedom of the material to an external magnetic field. Experimentally, the realization of quantum magnets that have a relatively weak magnetic exchange has opened the possibility of manipulating these systems with realizable magnetic fields. Thus, one can use the external field to induce and probe quantum phase transitions between phases with very different natures. Understanding quantum phase transitions is one of the most lively topics in condensed matter physics [2, 289–291]. Successful experimental investigations of low-dimensional magnets are, for example, the quantitative tests of Tomonaga-Luttinger liquid theory [292–294], the studies of scaling properties at quantum critical points [295, 296], or the observation of fractionalized excitations [297, 298], and other exotic excitations [6, 299, 300].

In this work, we consider the $BaCo_2V_2O_8$ compound, which exhibits several unique features [119, 120, 301–304]. This material realizes an Ising-like spin-$1/2$ chain, due to a strong Ising-like anisotropy in a XXZ-type chain. Furthermore, due to its particular crystallographic structure, applying an uniform magnetic field creates staggered fields both in the direction of the external field and perpendicular to it. This has sparked a lot of theoretical and experimental interest in this material, and in the closely related $SrCo_2V_2O_8$ compound [6, 286, 305]. For a longitudinal magnetic field [288, 306, 307], a commensurate-incommensurate phase transition has been observed [307] and high-energy many-body string excitations [288, 308]. When the field is applied transversally in the [100] crystallographic direction [5, 309], a topological quan-

tum phase transition has been seen, described by a double sine-Gordon model [310]. For a field in the [110] transversal direction, which we will consider in the following sections, it has been shown that one can use the external magnetic field to suppress the three-dimensional ordering present at small temperatures for small values of the magnetic field [7]. Thus, one can use high magnetic fields in order to access the one-dimensional physics. For this direction of the external field the low-lying excitations have been analyzed in Ref. [311], but several questions remain regarding the nature of the excitations close to the phase transition and the high-energy excitations, which we will address in this chapter [112].

In the following, we start by briefly describing the BaCo$_2$V$_2$O$_8$ compound and the XXZ-model in a transverse magnetic field used for its description (see Sec. 8.1). In Sec. 8.2 we analyze the ground state properties of the considered model using density matrix renormalization group (DMRG) simulations in the matrix product state (MPS) representation. We identify a phase transition between antiferromagnetic ordering in the z-direction and ferromagnetic ordering in the x-direction as a function of the magnetic field. In order to elucidate the mechanisms underlying the phase transitions one usually has to investigate the quantum excitations which exist around the quantum critical point. For this we compute numerically the dynamical spin structure factor from the dynamic correlations. In Sec. 8.3 we explain how we employ the time-dependent matrix product state (tMPS) method for computing the dynamic correlations and dynamical structure factor. We discuss the numerical tMPS results in Sec. 8.4. In Sec. 8.5 we develop several analytical approaches to further understand the nature of the excitations, and we compare the analytical and numerical results in Sec. 8.6. We compare our theoretical results with experimental data obtained from terahertz spectroscopy experiments [112] and we observe a very good agreement (see Sec. 8.6). In particular this allows us to identify in the experimental results high-energy two-magnon bound states [112]. Several theoretical studies exist in the literature regarding the XXZ-model in a transverse magnetic field, see for example Refs. [310, 312–314], but to our knowledge none considered both a uniform and a staggered contribution to the magnetic field as present in our analysis. This chapter is closely related to Ref. [112], in this work I performed the numerical tMPS simulations and the analytical calculations. The experimental results presented below were provided by Zhe Wang and Thomas Lorenz.

8.1 Modeling the BaCo$_2$V$_2$O$_8$ compound in a magnetic field

In this section, we describe the model of the BaCo$_2$V$_2$O$_8$ compound in a transverse magnetic field, shown in Fig. 8.1(a). The cobalt oxide BaCo$_2$V$_2$O$_8$ exhibits screw chains of Co^{2+} rotating around the four-fold **c** direction of its tetragonal structure [120, 301, 315] [see Fig. 8.1(a)]. The exchange interactions between the magnetic moments of the Co^{2+} ions can be described by an effective spin-1/2 antiferromagnetic chain model, namely the XXZ-model [119, 286, 288, 305]. Because of the crystallographic structure the magnetization local easy axes of the Co^{2+} ions are tilted from the chain **c** axis by an angle of $\theta \sim 5°$ and rotated by $90°$ when moving along the four-fold axis [119, 120]. This leads to an anisotropic g-tensor, which implies that additional effective fields are created perpendicular to an applied transverse magnetic field. In zero magnetic field, a 3D long-range antiferromagnetic ordering along the **c** axis is stabilized below the critical temperature $T_N \sim 5K$ by weak interchain couplings [301–303]. For a transverse field
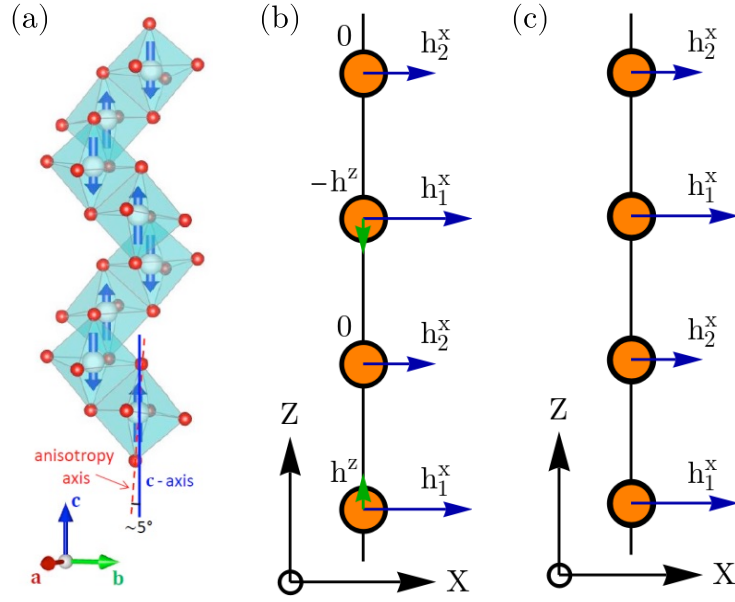
Figure 8.1: (a) The structure of a single Co^{2+} screw chain of $BaCo_2V_2O_8$, where blue and red spheres are Co and O respectively. The blue arrows show the zero-field magnetic arrangement. The local anisotropy axis is plotted with a red dashed line for the bottom CoO_6 octahedron [5]. (b)-(c) The site-dependent magnetic fields induced by a transverse external field in the direction [110], Eqs. (8.2)-(8.3). Here $h_1^x = hg_1^{xx}$, $h_2^x = hg_2^{xx}$, $h^z = hg_1^{xz} = -hg_3^{xz}$. In (b) we neglect the field in the z-direction. Panel (a) reprinted with permission from Springer Nature Customer Service Centre GmbH: Nature, Nature Physics, 14(7):716−722, Topological quantum phase transition in the Ising-like antiferromagnetic spin chain $BaCo_2V_2O_8$, Q. Faure *et al.*, © (2018).

along the crystallographic [110] direction, which will be considered in the rest of this chapter, the 3D order is destroyed at $\mu_0 H^{c,3D} = 21.4$ T [7], for the considered temperature. $H^{c,3D}$ is smaller than the corresponding one-dimensional critical field marking the end of the Néel phase, $\mu_0 H^c = 40$ T [119, 120, 316]. This will allow us to study the one-dimensional quantum phase transition in an experimentally realizable system. The effects of the coupling between different chains are negligible around the transition. In contrast, we note that for the [100] direction a phase transition occurs at lower field, $\mu_0 H^c = 10$ T. Thus, for the [100] direction, the interchain coupling plays an important role [5, 119].

The adequate model to describe the experiments we are interested in is the XXZ-model in an external magnetic field

$$H = J \sum_{j=1}^{L} \left[S_j^z S_{j+1}^z + \epsilon \left(S_j^x S_{j+1}^x + S_j^y S_{j+1}^y \right) \right] \tag{8.1}$$

$$- \sum_{j=1}^{L} \sum_{\alpha \in \{x,y,z\}} h_j^\alpha \left\{ g_j^{\alpha x} S_j^x + g_j^{\alpha y} S_j^y + g_j^{\alpha z} S_j^z \right\},$$

8.1 Modeling the $BaCo_2V_2O_8$ compound in a magnetic field

describing L spins with $S = 1/2$, see Sec. 2.2, with J the intrachain exchange interaction, ϵ the anisotropic parameter, $\mathbf{h}_j$ the magnetic field, and $g_j^{\alpha\beta}$ the elements of the g-tensor. We note that we did not include the interchain coupling between the different one-dimensional chains, as it does not play an important role for the field direction and the parameter regimes considered in the following.

In this study, we consider a transverse external field in the direction $[110]$. We take the field direction as our x-direction such that $\mathbf{h}_j = (h, 0, 0)$, corresponding to the **a+b** crystal axis [see Fig. 8.1(a)]. The z-direction in our model is along the c axis of the crystal. In this case the Hamiltonian reads [119]

$$H = J \sum_j \left[S_j^z S_{j+1}^z + \epsilon \left(S_j^x S_{j+1}^x + S_j^y S_{j+1}^y \right) \right] \tag{8.2}$$
$$- h \sum_j \left(g_j^{xx} S_j^x + g_j^{xz} S_j^z \right).$$

Here the magnetic field h has units of energy, as in the following we give the magnetic field in Tesla we can make the conversion as follows $h = \mu_B \mu_0 H$, where μ_B is the Bohr magneton, μ_0 is the vacuum permeability and the magnetic field $\mu_0 H$ has units of Tesla. The entries of the g-tensor are given by [119]

$$g_j^{xx} = \left(g_1 \cos^2 \theta + g_2 \sin^2 \theta \right) \cos^2 \left(\frac{\pi}{2}(j-1) \right) + g_3 \sin^2 \left(\frac{\pi}{2}(j-1) \right), \tag{8.3}$$
$$g_j^{xy} = 0,$$
$$g_j^{xz} = (g_2 - g_1) \cos \theta \sin \theta \cos \left(\frac{\pi}{2}(j-1) \right),$$

where θ is the tilt from the **c** axis. In all generality, the tilt θ can be site-dependent, however for the compound we consider it is uniform. g_1, g_2, and g_3 are the values of the g-tensor along the magnetic principle axes [119], and we use them as the parameters of our model. We observe that g^{xx} has different values on the odd than on the even sites, this giving a staggered contribution on top of a constant field, as we depicted in Fig. 8.1(b). The field in the z-direction has a four-fold periodicity, as g^{xz} is non-zero only on the first and third sites of the unit cell, but with different signs [see Fig. 8.1(b)].

For completeness we also give the other non-zero elements of the g-tensor which do not enter the expression of the Hamiltonian

$$g_j^{yy} = \left(g_1 \cos^2 \theta + g_2 \sin^2 \theta \right) \sin^2 \left(\frac{\pi}{2}(j-1) \right) + g_3 \cos^2 \left(\frac{\pi}{2}(j-1) \right), \tag{8.4}$$
$$g_j^{zz} = g_1 \cos^2 \theta + g_2 \sin^2 \theta,$$
$$g_j^{yz} = (g_2 - g_1) \cos \theta \sin \theta \sin \left(\frac{\pi}{2}(j-1) \right).$$

For the calculations presented in the following, we will consider the following parameters, unless stated otherwise, $g_1 = 3.5$, $g_2 = 6.1$, $g_3 = 2.1$, $\theta = 5°$, $\epsilon = 0.46$, $J = 61 k_B$, with k_B

the Boltzmann constant. We will see that this parameter set exhibits a good agreement with the experimental data. For these parameters the site dependent values in the unit cell of the g-factors are $g^{xx} = (3.52, 2.1, 3.52, 2.1)$ and $g^{xz} = (0.23, 0, -0.23, 0)$. Due to the complexity of the model it is not an easy task to find the best values of the several independent parameters for the direct comparison with the experimental results. Such that in the different studies existent in the literature, e.g. see Refs. [5, 112, 119, 311], the parameters used are slightly different depending on the observables and regimes of interest. We note that our choice of parameters shows the main features found both in the experimental terahertz spectroscopy results and the measurements of the magnetization.

8.2 Ground state properties

In this section, we look at the properties of the ground state of the Hamiltonian given in Eq. (8.2) as a function of the applied external magnetic field, in order to understand the nature of the phase transition. Our results are similar to previous studies of the ground state magnetization of the $BaCo_2V_2O_8$ compound in a transverse magnetic field [119, 311].

We compute the ground state of the model, Eq. (8.2), for a system of size $L = 200$. The results were obtained using a finite-size DMRG algorithm in the MPS representation [124, 129], implemented using the ITensor Library [139]. This method was described in Sec. 3.1.2. The convergence is ensured by a maximal bond dimension up to 300, for which the truncation error is at most 10^{-12}.

In Fig. 8.2(a) we compute the magnetization in the ground state in the direction of the field, which we define as

$$M_x = \frac{1}{L} \sum_{j=1}^{L} g_j^{xx} \langle S_j^x \rangle. \tag{8.5}$$

We observe a steady increase in the M_x as a function of the magnetic field and a saturation above the critical value $\mu_0 H_c \sim 40T$. A similar behavior is found also in the local magnetization $\langle S_j^x \rangle$, shown in Fig. 8.2(b). However, $\langle S_j^x \rangle$ for j odd is consistently larger than for j even, due to the stronger local magnetic field. Such that for j odd we observe a smoother behavior close to the transition threshold, compared to a steep increase in the magnetization on the even sites as we go near the critical point. Above the transition we see that for all sites in the unit cell $\langle S_j^x \rangle \sim 0.5$, thus we can approximate well the ground state of the system with the fully polarized state in the x-direction for large magnetic fields. In order to validate our choice of parameters we compare our ground state results with experimentally measured values [112], as presented in Fig. 8.2(a). We can observe a very good agreement for all values of the magnetic field considered, only around the phase transition threshold the experimental curve has a smoother behavior. We note that because of the fact that the model used, Eq. (8.2), has several independent parameters, one can obtain a similar agreement also for a slightly different set of parameters [112].

The local magnetization in the z-direction, $\langle S_j^z \rangle$, presented in Fig. 8.2(c), shows that the antiferromagnetic ordering in the z-direction found at zero magnetic field persists up to the phase transition threshold. The finite values of $\langle S_j^z \rangle$ for the odd sites in the unit cell for large
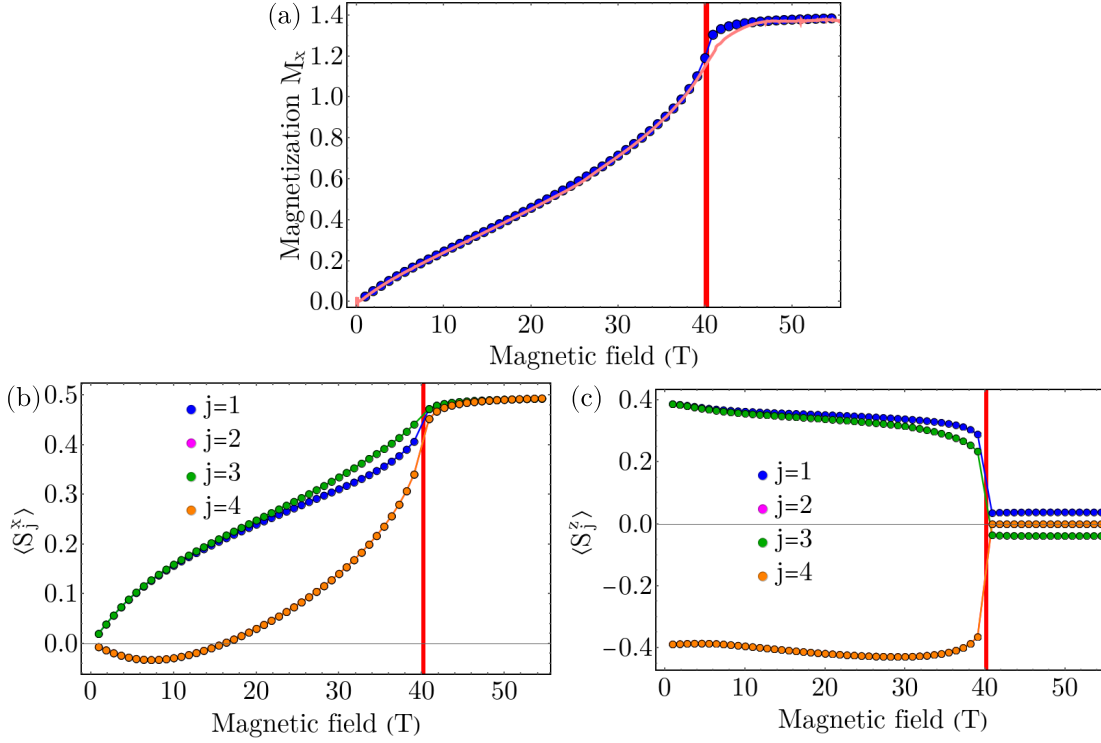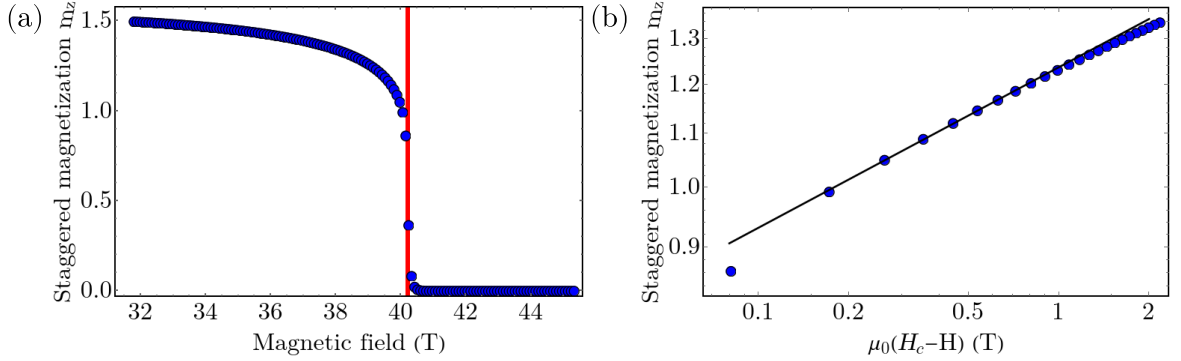
Figure 8.2: (a) The magnetization M_x as a function of the magnetic field (blue circles) in comparison with the experimentally measured magnetization line [112]. We note that from the raw experimental data we subtracted a linear contribution corresponding to the Van-Vleck susceptibility. The expectation values of the spin operators, $\langle S_j^\alpha \rangle$ for (b) $\alpha = x$ and (c) $\alpha = z$, where j represents one of the four sites of the unit cell. We note that the results for $j = 2$ are identical with the ones for $j = 4$ in panels (b) and (c). The red line represents the critical field, marking the phase transition, determined as the field for which the staggered magnetization vanishes (see Fig. 8.3). The results where obtained in the ground state for the following parameters, $L = 200$, $g_1 = 3.5$, $g_2 = 6.1$, $g_3 = 2.1$, $\theta = 5°$, $\epsilon = 0.46$, $J = 61k_B$.

magnetic field is associated to the induced magnetic field which is non-zero on these sites.

From the ground state results we see that we have a transition from an antiferromagnetic ordering in the z-direction to a ferromagnetic ordering in the x-direction as we increase the external magnetic field. This resembles the phase transition which occurs in the transverse-field Ising model. In order to understand the nature of the phase transition we look at the staggered magnetization in the z-direction, which acts as an ordered parameter for the transition. The staggered magnetization is defined as

$$m_z = \frac{1}{L} \sum_{j=1}^{L} (-1)^j \langle S_j^z \rangle. \tag{8.6}$$

We can see that for fields lower than the critical value $\mu_0 H_c \sim 40T$, Fig. 8.3(a), it has a finite value due to the antiferromagnetic ordering, and it vanishes for larger magnetic fields. Thus, the

Figure 8.3: The staggered magnetization m_z as a function of (a) the magnetic field and (b) the distance from the critical field. In (b) the black line in the log-log plot represents and algebraic fit $\propto (H_c - H)^{\beta}$, with $\beta = 0.123 \pm 0.001$ The red line represents the critical field, marking the phase transition, determined as the field for which the staggered magnetization vanishes. The results where obtained in the ground state for the following parameters, $L = 200$, $g_1 = 3.5$, $g_2 = 6.1$, $g_3 = 2.1$, $\theta = 5°$, $\epsilon = 0.46$, $J = 61k_B$.

staggered magnetization has the behavior of the order parameter for this phase transition. By looking at the algebraic scaling of m_z as a function of the distance from the critical magnetic field, depicted in Fig. 8.3(b) we obtain a exponent of $\beta = 0.123 \pm 0.001$. The value of the extracted exponent is close to the value of $1/8$ expected from a phase transition belonging to the Ising universality class [2, 310]. We note that also the situation of the transverse Ising model in a uniform magnetic field [2], and the XXZ-model with a fully staggered transverse field [310] show the same value of the exponent β and belong to the Ising universality class.

8.3 Dynamic correlations

In order to capture the properties of the quantum phase transition and the spin excitations occurring in our system, we compute in our calculations the dynamical spin structure factor. This is not only of theoretical interest, but it can be directly compared to the experimental results of the terahertz spectroscopy technique, or with other experimental methods as inelastic neutron scattering, electron spin resonance, and nuclear magnetic resonance. The first step in the calculation of the dynamical spin structure factor is to compute the two-point correlation functions at different points in time given by

$$S_{j,l}^{\alpha\beta}(t) = \langle 0|S_j^{\alpha}(t)S_l^{\beta}|0\rangle = \langle 0|e^{itH}S_j^{\alpha}e^{-itH}S_l^{\beta}|0\rangle, \tag{8.7}$$

with $|0\rangle$ the ground state of the spin chain, α and β the two spin directions. The sites for which we compute the correlations are $j = 1 \ldots L$, and $l \in \{L/2 - 1, L/2, L/2 + 1, L/2 + 2\}$, corresponding to the central 4-site unit cell. We compute numerically the correlations using the time-dependent matrix product state method (tMPS) for Hamiltonians with short range interactions [124, 133, 134] which we described in Sec. 3.1.3. We perform the time-evolution of the ground state $|0\rangle$ and the excited states $|\psi_l\rangle = S_l^{\beta}|0\rangle$ using tMPS. Afterwards the overlap of $S_j^{\alpha}|\psi_l(t)\rangle$ and $e^{-itE_0}|0\rangle$ is evaluated to obtain the correlation function from Eq. (8.25), with E_0 the ground state energy.

8.3 Dynamic correlations

The dynamical structure factor is obtained via a numerical Fourier transform to the frequency-momentum space

$$S_l^{\alpha\beta}(q,\omega) = \frac{1}{\sqrt{N_t L}} \sum_{n=0}^{N_t-1} \sum_{j=1}^{L} e^{i(\omega n \delta t - q j)} S_{j,l}^{\alpha\beta}(n\delta t), \tag{8.8}$$

with the discrete momenta $q = \frac{2\pi k}{L}$, $k = 0 \ldots L-1$ and frequencies $\omega = \frac{2\pi f}{N_t \delta t}$, with N_t the number of the time measurements and δt the time between them, $f = 0 \ldots N_t - 1$. The momentum q has the reciprocal units of the lattice spacing a, which we set to $a = 1$. In order to reduce the effects of the open boundary conditions, we apply a Gaussian filter to the correlations before the numerical Fourier transform

$$S_{j,l}^{\alpha\beta}(t)f(j) \to S_{j,l}^{\alpha\beta}(t), \text{ with } f(j) = e^{-4\left(1-\frac{2j}{L-1}\right)^2}. \tag{8.9}$$

The effect of this filter is a convolution of the correlations with a Gaussian function in momentum space. This minimizes the numerical artifacts due to the open boundary conditions, but on the same time reduces the momentum resolution. The width of the Gaussian filter was chosen to balance between these two effects.

After checking the convergence, the typical parameters used in our simulations of dynamical quantities are system sizes of $L = 124$ sites with a bond dimension up to $m = 300$ states. This ensured that the truncation error at the final time $tJ/\hbar = 110$ is $\epsilon \lesssim 10^{-7}$. We note that at large magnetic fields, above the phase transition, the truncation error at the final time is smaller, $\epsilon \lesssim 10^{-10}$. We limited the final time to be smaller than the time necessary for the excitations to reach the boundaries in order to minimize the boundary effects. The chosen time step was $dtJ/\hbar = 0.05$ and the measurements where performed every fourth time step.

In the following we want to understand better the connection between the dynamical structure factor, Eq. (8.8), and the experimental measurements, and to see which spin directions contribute most. For this we employ linear response theory [317]. In this approach, one considers that the system is subject to an external perturbation and its response is measured. The response is in general a functional of the exerted perturbation on the system, and for a sufficiently weak perturbation, one can evaluate the response from the linear terms in a perturbation theory [317].

In the experimental setup considered in the following chapter [112], the THz field is in the y-z plane, for a circular polarization this is then given by $\mathbf{h}^{\text{THz}} = (0, h^{\text{THz}}, h^{\text{THz}})$. The electromagnetic wave couples with the spin operators as

$$\sum_l \sum_{\alpha,\beta} h^{\text{THz},\alpha} g_l^{\alpha\beta} S_l^{\beta} = \tag{8.10}$$
$$= h^{\text{THz}} \sum_l \left[g_l^{zx} S_l^x + (g_l^{yy} + g_j^{zy}) S_l^y + (g_l^{yz} + g_l^{zz}) S_l^z \right]$$
$$\equiv h^{\text{THz}} \mathcal{O},$$

where $\mathcal{O} = \sum_l \left[g_l^{zx} S_l^x + (g_l^{yy} + g_j^{zy}) S_l^y + (g_l^{yz} + g_l^{zz}) S_l^z \right]$ is the operator which couples to the THz field, and we sum over the four sites of the unit cell. We look at the linear response of the system after the perturbation $H_{pert} = \mathcal{O}\, h^{\text{THz}} e^{i\omega t}$. We are interested in the change of energy of the system, as in the experiment one measures the absorption coefficient,

$$\frac{dE(t)}{dt} = i\omega \langle \mathcal{O}(t) \rangle h^{\text{THz}} e^{i\omega t}, \text{ with} \tag{8.11}$$

$$\langle O(t) \rangle = \int dt' \left[\chi_{\mathcal{O}\mathcal{O}}(t - t') h^{\text{THz}} e^{i\omega t'} + \chi_{\mathcal{O}\mathcal{O}^\dagger}(t - t') \left(h^{\text{THz}} \right)^* e^{-i\omega t'} \right].$$

Thus, the average change in energy is then given by

$$\overline{\frac{dE(t)}{dt}} = i\omega \chi_{\mathcal{O}\mathcal{O}^\dagger}(\omega) \, |h^{\text{THz}}|^2, \tag{8.12}$$

with the susceptibility

$$\chi_{\mathcal{O}\mathcal{O}^\dagger}(\omega) = -i \int dt \langle [\mathcal{O}(t), \mathcal{O}(0)] \rangle e^{i\omega t}. \tag{8.13}$$

From Eq. (8.13) we can see that, in principle, for the dynamical structure factor we need to consider all pairs of operators which appear in the commutator $[\mathcal{O}(t), \mathcal{O}(0)]$. But if we evaluate the coefficients given by the g-factors, for the parameters considered in this chapter, we observe that for the spin directions $S^y S^y$, $S^y S^z$, $S^z S^z$ the coefficients are one order of magnitude larger than in the case of the spin directions $S^x S^y$, $S^x S^z$, and two orders of magnitude compared with the case of $S^x S^x$. Thus, we expect that by computing $S_l^{\alpha\beta}(q, \omega)$, Eq. (8.8), for $\alpha, \beta \in \{y, z\}$ we can capture the main features relevant to the experimental measurements.

As we observe from Eq. (8.10) and Eq. (8.13) we have to include the g-factors to properly capture the response of the system. Thus, we modify the dynamical structure factor computed in Eq. (8.8) to

$$(gS)_l^{\alpha\beta}(q, \omega) = \frac{1}{\sqrt{N_t L}} \sum_{n=0}^{N_t-1} \sum_{j=1}^{L} e^{i(\omega n\delta t - qj)} \mathcal{G}_j^\alpha \mathcal{G}_l^\beta S_{j,l}^{\alpha\beta}(n\delta t), \tag{8.14}$$

where $\mathcal{G}_l^x = g_l^{zx}$, $\mathcal{G}_l^y = g_l^{yy} + g_l^{zy}$, $\mathcal{G}_l^z = g_l^{zz} + g_l^{yz}$. As the experimental measurements are not sensitive to the different sites of the unit cell and the spin directions, we compute the following quantity to compare with the experimental results

$$\mathcal{S}(q, \omega) = \sum_{l=L/2-1}^{L/2+2} \left[|(gS)_l^{zz}(q, \omega)|^2 + |(gS)_l^{yy}(q, \omega)|^2 + |(gS)_l^{zy}(q, \omega)|^2 + |(gS)_l^{yz}(q, \omega)|^2 \right]. \tag{8.15}$$

8.4 Numerical tMPS results

In this section, we analyze our numerical tMPS results for the dynamical structure factor $\mathcal{S}(q,\omega)$, Eq. (8.15), as presented in Fig. 8.4 and Fig. 8.5. We focus on the features which are present in the experimental results shown in Sec. 8.6, labeling them in Fig. 8.5.

In the numerical tMPS calculation of the dynamical structure factor $\mathcal{S}(q,\omega)$, Eq. (8.15), we obtain its full dependence on the momentum q and frequency ω. We show the obtained spectra in Fig. 8.4 for several values of the magnetic field. We label the three main bands which we see in Fig. 8.4 in order to better track their evolution as we vary the magnetic field. We observe that the minimum of the lowest band decreases as the transition is approached from below. This minimum reincreases as the field is increased beyond the transition. The lowest band corresponds to M'_π and $M'_{\pi/2}$ of Fig. 8.5. The shape of the second band [seen at around $\omega \approx 1.2$ THz in Fig. 8.4 (b)] seems to change quite drastically in between 20 T and 40 T. The frequency of both its peaks around $q = 0$ (M^u_0 of Fig. 8.5) and $q = \pi$ is increasing with the field, while the peak at $q = \pi/2$ ($M^u_{\pi/2}$) remains almost constant. This induces a change of curvature of the second band around $q = \pi/2$. Above the critical field, this band is shifting monotonously with the magnetic field to higher frequencies. The third band [seen in between $\omega \approx 1.5$ THz and $\omega \approx 2.4$ THz in Fig. 8.4 (b)] increases in frequency with the magnetic field, but its intensity is decreasing as we get close to the critical field, such that at $\mu_0 H = 40$ T we can only distinguish it if we increase the visibility of the high-frequency region in the density plot [Fig. 8.4 (f)]. This band corresponds to D_π in Fig. 8.5. Between 20 T and 32 T [Fig. 8.4 (b)-(d)] we can also distinguish some high-frequency features close to $q = \pi/2$ if we multiplied $\mathcal{S}(q,\omega)$ with a factor of 10 above a certain value of ω.

As the terahertz spectroscopy experiment is only sensitive to the values of momenta $q \in \{0, \pi/2, \pi\}$ [112], we analyze how the excitation modes captured by the dynamical structure factor at these values of momenta behave as a function of the magnetic field, Fig. 8.5. The main features that we can observe, also seen in the experimental data in Sec. 8.6, are the following:

- The lowest excitation mode at $q = 0$ and $q = \pi$, M'_π, which shows the gap closing at the critical value of the magnetic field, signaling the phase transition [see Fig. 8.5(a) and Fig. 8.5(c)]. We analyze later in detail the nature of this mode, above the transition it stems from the dynamics of a single mode in a staggered magnetic field.

- We observe $q = \pi/2$ a mode softening as we increase the magnetic field, $M'_{\pi/2}$, but it maintains a finite gap. The frequency of the mode increases with the magnetic field above the transition [see Fig. 8.5(b)].

- Similarly, also the frequency of the mode $M^u_{\pi/2}$ is increasing with the magnetic field above the phase transition, but under the threshold it seems to be independent of the value of the magnetic field [see Fig. 8.5(b)].

- For $q = 0$ we see a mode, M^u_0, which exhibits a relatively smooth increase in frequency with the magnetic field across the phase transition. Close in frequency is the mode D_π which has a similar behavior, but seems to be only visible up to the critical magnetic field [see Fig. 8.5(a) and Fig. 8.5(c)]. We will show that this mode corresponds to a two-magnon bound state.
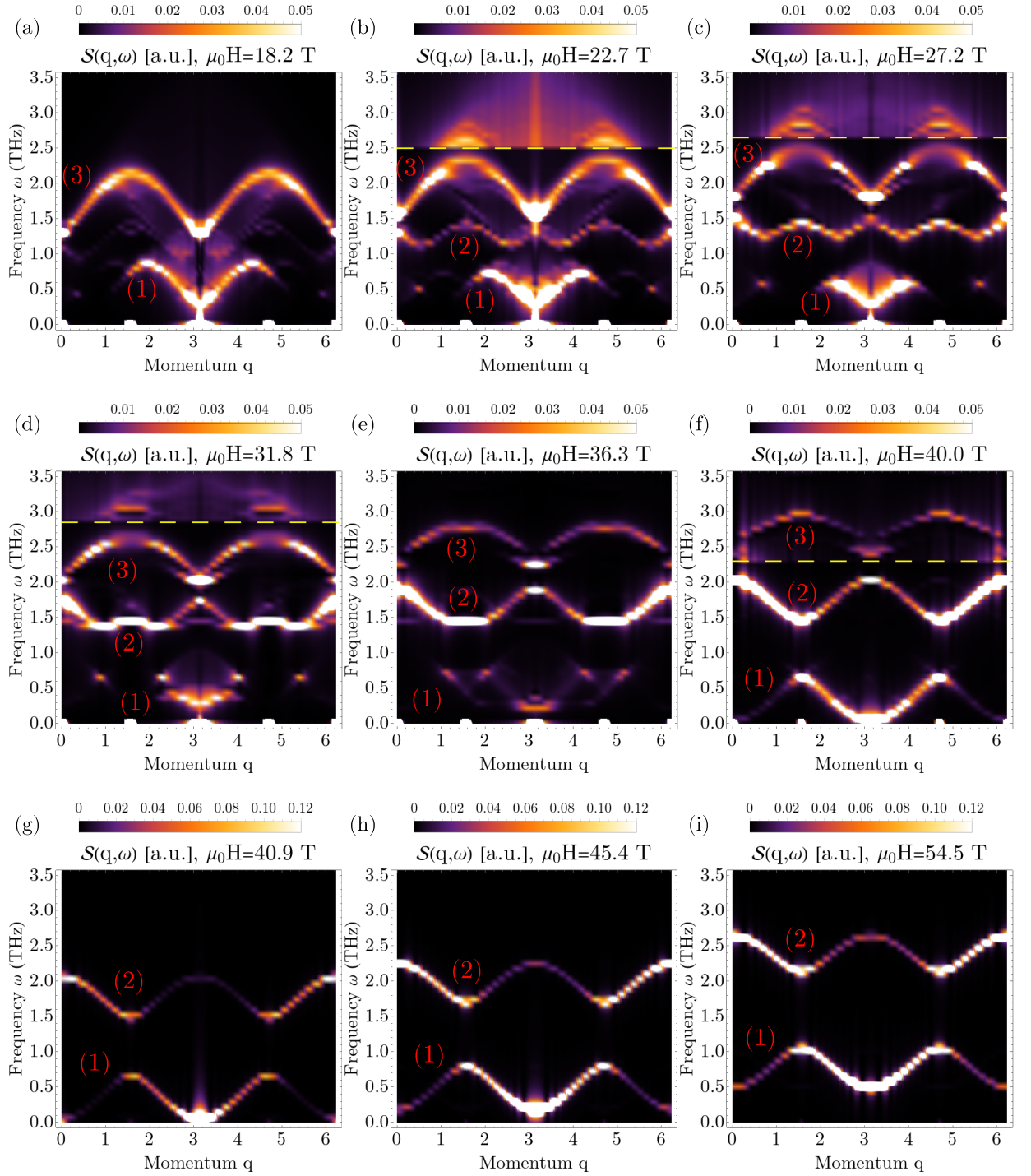
Figure 8.4: The dynamical structure factor for different values of the external magnetic field as a function of momentum q and frequency ω. In each panel we normalized the maximum of $\mathcal{S}(q,\omega)$ to 1. Above the horizontal yellow dashed line we multiplied $\mathcal{S}(q,\omega)$ with a factor of 10 in order to increase the visibility of the high-frequency modes. The results where obtained for the following parameters, $L = 124$, $g_1 = 3.5$, $g_2 = 6.1$, $g_3 = 2.1$, $\theta = 5°$, $\epsilon = 0.46$, $J = 61k_B$.
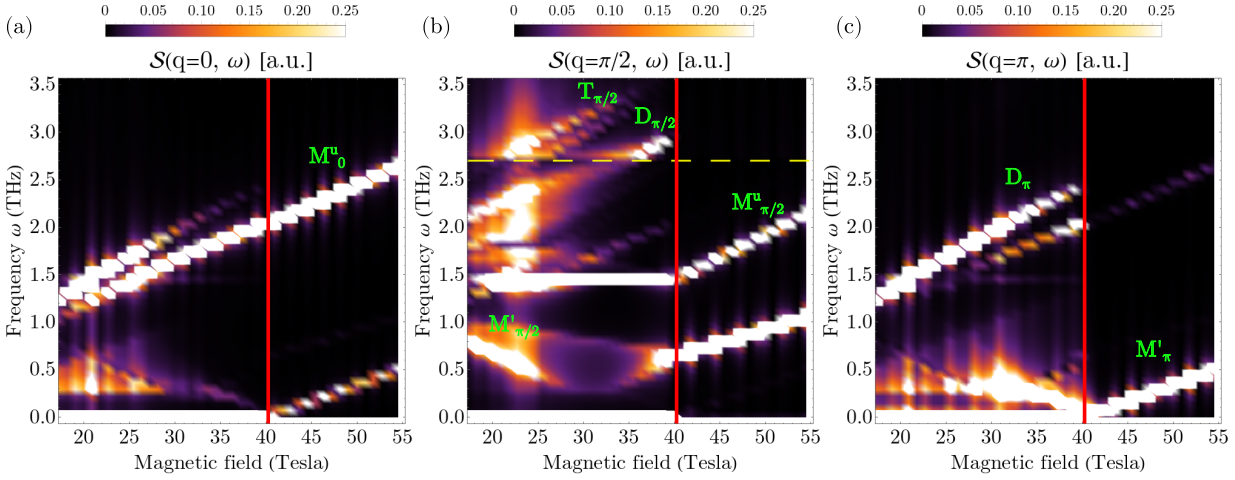
Figure 8.5: (a)-(c) The numerical results for the dynamical structure factor $\mathcal{S}(q,\omega)$, Eq. (8.15), as a function of the magnetic field for three values of the momentum, $q \in \{0, \pi/2, \pi\}$. We marked the modes that can be observed in the experimental results in Fig. 8.11 below. We normalized the maximum of $\mathcal{S}(q,\omega)$ to 1 for each considered value of the magnetic field. For $q = \pi/2$, above the horizontal yellow dashed line we multiplied $\mathcal{S}(q,\omega)$ with a factor of 5 in order to increase the visibility of the high-frequency modes. The vertical red line marks the critical magnetic field. The results where obtained for the following parameters, $L = 124$, $g_1 = 3.5$, $g_2 = 6.1$, $g_3 = 2.1$, $\theta = 5°$, $\epsilon = 0.46$, $J = 61 k_B$.

- We also capture the high-frequency modes $D_{\pi/2}$ and $T_{\pi/2}$, but they appear more faintly in the numerical data in comparison with the lower frequency features [see Fig. 8.5(b)].

Until now we observed that the model we consider, Eq. (8.2), has a complex excitation spectra, shown in Fig. 8.4 and Fig. 8.5. Thus, in the following, we want to understand the nature of the different excitations modes which we identified in our numerical tMPS simulations.

8.5 Analytical understanding of the excitations

In this section, we want to gain an analytical understanding of the nature of the features present in the dynamical structure factor which we computed in the previous section.

In Sec. 8.1 we have seen that for the parameters we consider the site dependent values in the unit cell of the g-factors are $g^{xx} = (3.52, 2.1, 3.52, 2.1)$ and $g^{xz} = (0.23, 0, -0.23, 0)$. We can observe that the values corresponding to the x-direction are one order of magnitude higher than for the z-direction. This justifies the first approximation that we make by neglecting the magnetic field induced in the z-direction from Eq. (8.2) [see Fig. 8.1(c)]. The results obtained within this approximation are, in a wide region around the transition, in good agreement with our numerical results considering all terms of the Hamiltonian, Eq. (8.2). Thus, the Hamiltonian from Eq. (8.2) becomes

$$\tilde{H} = J \sum_j \left[S_j^z S_{j+1}^z + \epsilon \left(S_j^x S_{j+1}^x + S_j^y S_{j+1}^y \right) \right] - \sum_j \left[h_u + (-1)^j h_s \right] S_j^x, \qquad (8.16)$$

where we separated the uniform part of the magnetic field $h_u = \frac{h}{2} \left(g_1^{xx} + g_2^{xx} \right)$ from the stag-

gered contribution $h_s = \frac{h}{2}\left(g_1^{xx} - g_2^{xx}\right)$. The site dependence of the magnetic field in this case is sketched in Fig. 8.1(c). We checked that the numerically computed dynamical spin structure factor for this reduced Hamiltonian reproduces all the important features we observed in Sec. 8.4.

We begin our analysis by performing a rotation to the Hamiltonian given in Eq. (8.16), in order to simplify our calculations. This rotation aligns the new z-direction along the direction of the external magnetic field

$$
\begin{aligned}
S^x &\to S^z \\
S^y &\to S^x, \\
S^z &\to S^y.
\end{aligned}
\tag{8.17}
$$

Our Hamiltonian now reads

$$
\tilde{H} = J\sum_j \left[S_j^y S_{j+1}^y + \epsilon\left(S_j^z S_{j+1}^z + S_j^x S_{j+1}^x\right)\right] - \sum_j \left[h_u + (-1)^j h_s\right] S_j^z.
\tag{8.18}
$$

8.5.1 Transverse-field Ising model

In a first approach, we aim to derive a model similar to the transverse-field Ising model [2], which one can solve exactly. This is justified by the fact that the phenomenology of the phase transition we described in Sec. 8.2 resembles the one found in the transverse-field Ising model. Thus, we expect that also the behavior of the excitations close to the transition might be well described. The main approximation that we make in this subsection is to neglect the interaction term $S_j^z S_{j+1}^z$ from Eq. (8.18). This leads to the following Hamiltonian

$$
\tilde{H}_{\mathrm{TI}} = J\sum_j \left(\epsilon S_j^x S_{j+1}^x + S_j^y S_{j+1}^y\right) - \sum_j \left[h_u + (-1)^j h_s\right] S_j^z,
\tag{8.19}
$$

which we are able to solve exactly. Compared to the usual transverse-field Ising model [2], we also consider the $S_j^y S_{j+1}^y$ term and the space dependence of the magnetic field, which will prove crucial in reproducing the features of the full model, given in Eq. (8.2). In order to find the exact spectrum of $\tilde{H}_{\mathrm{TI}}$, Eq. (8.19), we employ the Jordan-Wigner transformation [2, 318, 319]. This maps our Hamiltonian to a quadratic model of spinless fermions, which we can diagonalize. More details regarding this calculation are found in Appendix D.

In Fig. 8.6 we compare the exact spectrum of the non-interacting Hamiltonian $\tilde{H}_{\mathrm{TI}}$, Eq. (8.19) and the dynamical structure factor, $\mathcal{S}(q,\omega)$, of the full Hamiltonian, Eq. (8.2), for several values of the magnetic field. We monitor the gap corresponding to the minimum of the first band of $\tilde{H}_{\mathrm{TI}}$ and identify the critical magnetic field of the phase transition for which this gap closes. Due to the approximation we employ in the derivation of $\tilde{H}_{\mathrm{TI}}$ we obtain a lower value of the critical field than we have in the full model. To correct for this deviation we shift the results for the spectrum of $\tilde{H}_{\mathrm{TI}}$ presented in Fig. 8.6 by 16 T. We find that the behavior around the critical field is captured by $\tilde{H}_{\mathrm{TI}}$. We observe that away from the transition threshold for low values of the magnetic field, Fig. 8.6(a)-(b), $\tilde{H}_{\mathrm{TI}}$ only captures the behavior of the first band around $q = \pi$
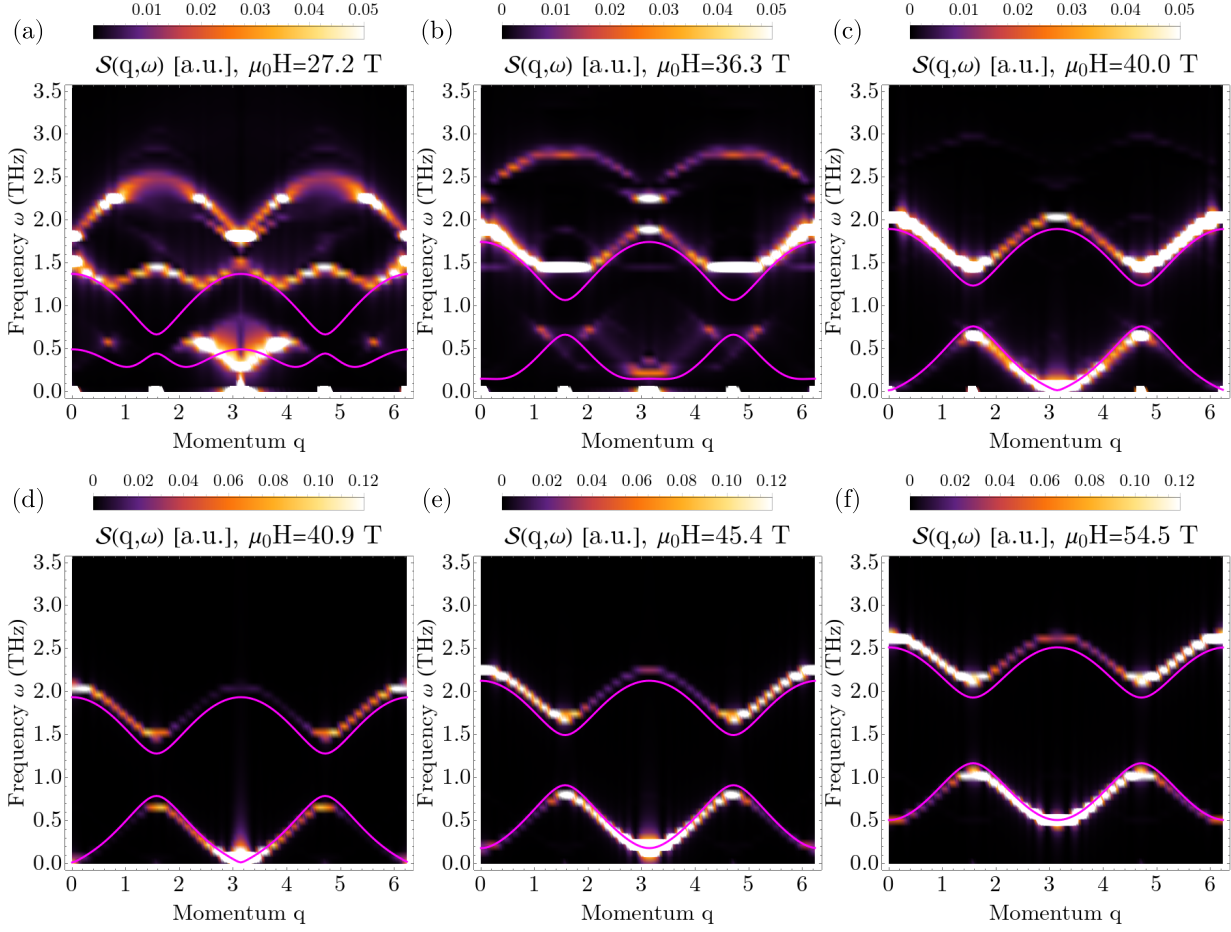
Figure 8.6: Comparison between the exact spectrum of the non-interacting Hamiltonian $\tilde{H}_{\mathrm{TI}}$, Eq. (8.19) depicted with magenta lines and the dynamical structure factor, $\mathcal{S}(q,\omega)$, of the full Hamiltonian, Eq. (8.2), for several values of the magnetic field. The spectrum of $\tilde{H}_{\mathrm{TI}}$ has been shifted with a field of 16 T in order to recover the critical field of the full model. The results where obtained for the following parameters, $L = 124$, $g_1 = 3.5$, $g_2 = 6.1$, $g_3 = 2.1$, $\theta = 5°$, $\epsilon = 0.46$, $J = 61k_B$.

and the second band for momenta close to $q = 0$ and $q = \pi$. We attribute the discrepancies mainly to the interaction term $S_j^z S_{j+1}^z$ which we neglected in $\tilde{H}_{\mathrm{TI}}$. Close to critical field the spectra of $\tilde{H}_{\mathrm{TI}}$ agrees well with the features of the dynamical structure factor of the full model [Fig. 8.6(c)-(d)], up to a small frequency shift in the second band. Moreover, the agreement remains if we increase the magnetic field to larger values, Fig. 8.6(e)-(f).

Thus, we have seen that in this approximation, neglecting the interactions in the field direction, Eq. (8.19), we can capture the behavior of the mode closing at the critical point and one of the high-energy modes present in the full calculation. In the transverse-field Ising model one can associate the excitations at low fields to domain walls in the antiferromagnetic state and at high fields to defects in the fully polarized state [2]. We expect that a similar interpretation is valid also in our case and that the two bands seen above the critical field would correspond

to the dynamics of a single magnon in the staggered magnetic field. However, we cannot find an analytical expression for the spectrum, only a numerical one. Thus, in order to gain more insights, we employ a different approximation in the following subsection to identify the nature of the excitations above the critical magnetic field.

8.5.2 Large magnetic field limit - magnon states

In the following, we focus on the regime above the phase transition threshold for large magnetic fields, $\mu_0 H \geq 40T$. In this case, the ground state of the system can be approximated well by a fully polarized state in the direction of the magnetic field, as we saw in Sec. 8.2. We rewrite Eq. (8.18) as

$$
\tilde{H} = J \sum_j \left[\epsilon S_j^z S_{j+1}^z + \frac{1}{4}(\epsilon - 1)\left(S_j^+ S_{j+1}^+ + S_j^- S_{j+1}^-\right) + \frac{1}{4}(\epsilon + 1)\left(S_j^+ S_{j+1}^- + S_j^- S_{j+1}^+\right) \right]
$$

$$
- \sum_j \left[h_u + (-1)^j h_s \right] S_j^z,
$$
(8.20)

where we used $S_j^x = \frac{1}{2}\left(S_j^+ + S_j^-\right)$ and $S_j^y = \frac{1}{2i}\left(S_j^+ - S_j^-\right)$. In the limit of large magnetic fields the ground state is approximated by the fully polarized state $|\uparrow \cdots \uparrow\rangle$ in the z-direction. In Sec. 8.3 we saw that the operators of interest in the dynamical correlations are the spin operators corresponding to the directions perpendicular on the magnetic field direction. The application of the operators S^y or S^x onto the fully polarized state will produce a spin flip defect

$$
S_i^y |\uparrow \cdots \uparrow\rangle \propto |\uparrow \cdots \downarrow \cdots \uparrow\rangle.
$$
(8.21)

This also corresponds to having a magnon excitation on top of the fully polarized state. In our analysis of the transverse-field Ising model we have seen that in this regime we expect to be able to describe the excitations as magnons, but in the Hamiltonian given in Eq. (8.20) the term $(S_j^+ S_{j+1}^+ + S_j^- S_{j+1}^-)$ does not conserve the number of defects on top of the fully polarized state. Thus, in order to restrict our analysis to sectors with well-defined numbers of defects, we neglect the term $(S_j^+ S_{j+1}^+ + S_j^- S_{j+1}^-)$ from the Hamiltonian. This is the main approximation performed in this subsection, our Hamiltonian is now given by

$$
\tilde{H}_{\text{magnon}} = J \sum_j \left[\epsilon S_j^z S_{j+1}^z + \frac{1}{4}(\epsilon + 1)\left(S_j^+ S_{j+1}^- + S_j^- S_{j+1}^+\right) \right]
$$
(8.22)

$$
- \sum_j \left[h_u + (-1)^j h_s \right] S_j^z,
$$

To consider the sectors with a fixed number of magnons it is convenient to write the Hamiltonian in terms of fermionic operator using the Jordan-Wigner transformation [2, 318, 319]

$$
S_j^z = \frac{1}{2} - c_j^\dagger c_j,
$$
(8.23)

$$S_j^+ = c_j e^{-i\pi \sum_{l=1}^{j-1} c_l^\dagger c_l},$$

$$S_j^- = e^{i\pi \sum_{l=1}^{j-1} c_l^\dagger c_l} c_j^\dagger,$$

where $c_j^\dagger$ and c_j are fermionic operators which satisfy the anticommutation relations. Using this rewriting, a magnon, or defect, at site j corresponds to the presence of a fermion at this site, and the fermionic Hamiltonian is given as

$$\tilde{H}_{\text{magnon}} = J \sum_j \left[\epsilon \left(\frac{1}{2} - c_j^\dagger c_j \right) \left(\frac{1}{2} - c_{j+1}^\dagger c_{j+1} \right) + \frac{1}{4}(\epsilon + 1)\left(c_j^\dagger c_{j+1} + c_{j+1}^\dagger c_j \right) \right] \tag{8.24}$$

$$- \sum_j \left[h_u + (-1)^j h_s \right] \left(\frac{1}{2} - c_j^\dagger c_j \right).$$

One magnon states: We first consider the case of a single magnon, corresponding to a single fermion in the Hamiltonian given in Eq. (8.24). In this case we look at how the dynamical spin structure factor captures the excitations from the ground state to the one-magnon sector

$$S_j^{\alpha,\beta}(q,\omega) \propto \sum_{e_{1m}} \langle 0|S^\alpha(q)|e_{1m}\rangle\langle e_{1m}|S_j^\beta|0\rangle \delta(\omega + E_0 - E_{1m}) \tag{8.25}$$

where $|0\rangle$ is the ground state with energy E_0, $|e_{1m}\rangle$ are the one-magnon eigenstates with the corresponding eigenenergies E_{1m}, and $S^\alpha(q) = \frac{1}{\sqrt{L}} \sum_l e^{-iql} S_l^\alpha$. The direction for which we can have the transition between the sectors are $\alpha, \beta \in \{x, y\}$, in the rotated basis, Eq. (8.17). The derivation of Eq. (8.25) for two arbitrary sectors is given in Appendix D. We can observe that $S_j^{\alpha,\beta}(q,\omega)$ can be non-zero only in the case in which $\omega + E_0 - E_{1m} = 0$, and because E_0 is a constant, this implies that we can capture the structure of $S_j^{\alpha,\beta}(q,\omega)$ by computing the dispersion relation $E_{1m}(k)$ of one magnon under the action of the Hamiltonian from Eq. (8.24).

We first compute the ground state energy of the Hamiltonian, Eq. (8.24), to obtain the energy shift. The ground state of the fermionic Hamiltonian is the state with zero fermions.

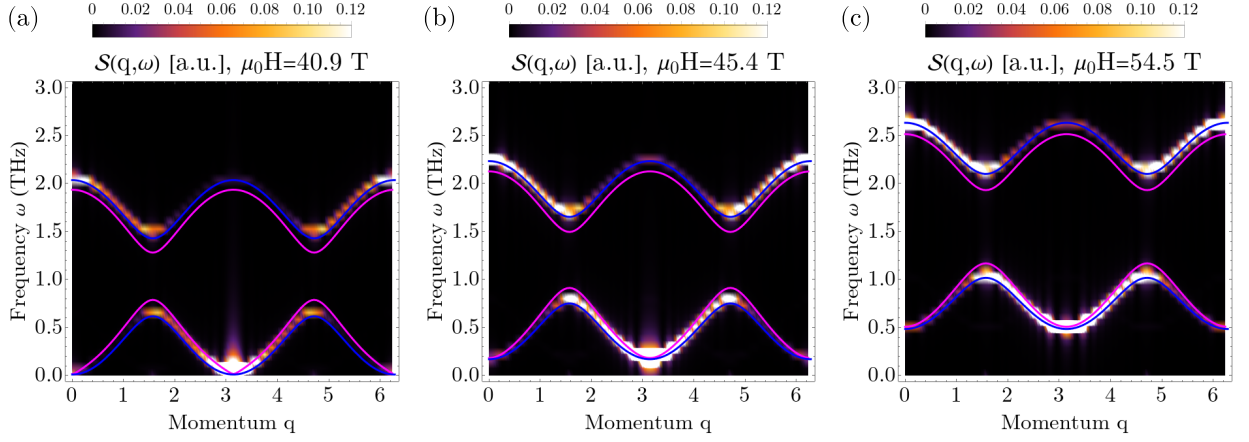$$E_0 = L\frac{J\epsilon}{4} - L\frac{h_u}{2}. \tag{8.26}$$

We can project $\tilde{H}_{\text{magnon}}$ to the subspace of a single fermion and obtain

$$\tilde{H}_{1\,\text{magnon}} - E_0 = h_u - J\epsilon + \sum_j \frac{J}{4}(\epsilon + 1)\left(c_j^\dagger c_{j+1} + c_{j+1}^\dagger c_j \right) + \sum_j (-1)^j h_s c_j^\dagger c_j. \tag{8.27}$$

The dispersion of this single particle Hamiltonian is given by

$$E_{1m}^\pm(k) = h_u - J\epsilon \pm \sqrt{\varepsilon^0(k)^2 + h_s^2} \tag{8.28}$$

Figure 8.7: Comparison between the numerical computation of the dynamical structure factor $\mathcal{S}(q, \omega)$, Eq. (8.15), for the full Hamiltonian, Eq. (8.2), the one magnon analytical dispersion (blue curves), Eq. (8.28), and the spectrum of the non-interacting Hamiltonian $\tilde{H}_{\mathrm{TI}}$ (magenta curves), Eq. (8.19), for different values of the magnetic field. The spectrum of $\tilde{H}_{\mathrm{TI}}$ has been shifted with a field of 16 T in order to recover the critical field of the full model. The results where obtained in the ground state for the following parameters, $L = 124$, $g_1 = 3.5$, $g_2 = 6.1$, $g_3 = 2.1$, $\theta = 5°$, $\epsilon = 0.46$, $J = 61k_B$.

$$= \frac{g_1^{xx} + g_2^{xx}}{2} h - J\epsilon \pm \sqrt{\left(\frac{J}{2}(1 + \epsilon)\cos(k)\right)^2 + \left(\frac{g_1^{xx} - g_2^{xx}}{2} h\right)^2},$$

where the dispersion of the kinetic part is $\varepsilon^0(k) = \frac{J}{2}(1 + \epsilon)\cos(k)$. We observe that we obtain two distinct bands due to the staggered contribution h_s to the magnetic field.

In Fig. 8.7 we compare the numerical results of the dynamical structure factor $\mathcal{S}(q, \omega)$, Eq. (8.15), which we computed for the full Hamiltonian, Eq. (8.2), and the one magnon analytical dispersion, Eq. (8.28), computed for the reduced Hamiltonian, Eq. (8.22). We observe a very good agreement for both bands, for different values of the magnetic field. Our analytical expression for the dispersion $E_{1m}^-(k)$ shows the gap at $k = 0$ closing at the a critical field very close to our full calculations and the same scaling behavior as we increase the magnetic field. Thus, the very good agreement between the two approaches, once we go above the critical value of the magnetic field, implies that the two bands what we observe in our numerical results are indeed due to having one magnon delocalized in our system. In particular, we note the importance of having a staggered contribution to the magnetic field in order to obtain two distinct bands separated by a gap. The behavior of the single magnon in the staggered magnetic field is equivalent with the dynamics of a single particle in a staggered potential, as seen from Eq. (8.27).

In the regime of high magnetic field we can compare the two analytical approaches, in Fig. 8.7 we depict the dispersion of one magnon with blue curves, Eq. (8.28), and the shifted dispersion of the transverse-field Ising model with magenta curves, Eq. (8.19). We see a good agreement of the two approaches in the shape of the two bands and their dependence of the magnetic field. The small deviations present, the shift present of the second band and the devi-
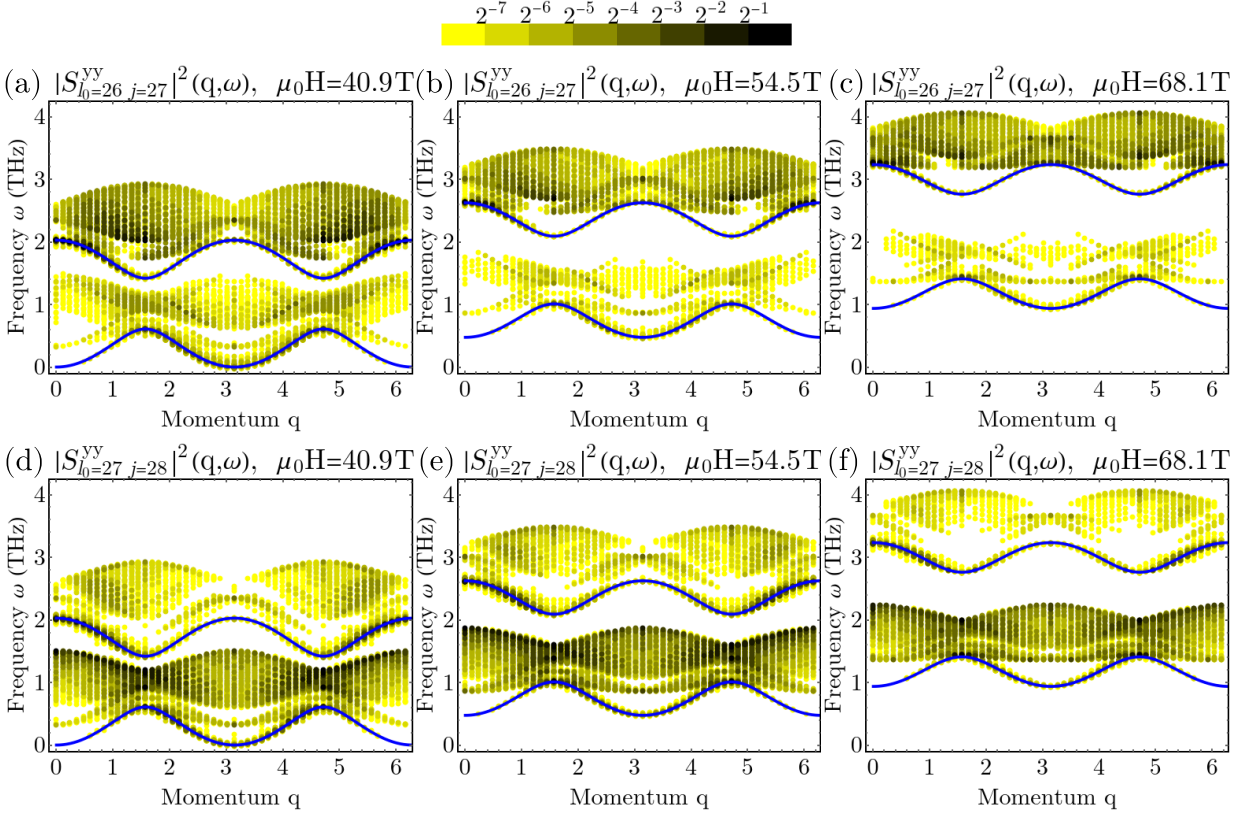
Figure 8.8: The two-magnon contribution to the dynamical structure factor, Eq. (8.29), for different magnetic fields and $l_0 \in \{26, 27\}$, we take $j = l_0 + 1$. The blue line corresponds to the single magnon dispersion, Eq. (8.28). We note that the color scale of the plotted points is logarithmic. The results where obtained for the following parameters, $L = 52$, $g_1 = 3.5$, $g_2 = 6.1$, $g_3 = 2.1$, $\theta = 5°$, $\epsilon = 0.46$, $J = 61 k_B$.

ations around $q = \pi/2$ for the lower band, we attribute to the fact that we neglected different terms in the two approaches compared to Eq. (8.18). Thus, for the transverse-field Ising model, Eq. (8.19), we neglected the interaction term $S_j^z S_{j+1}^z$, and for the single magnon dispersion we neglected the term $(S_j^+ S_{j+1}^+ + S_j^- S_{j+1}^-)$, whose contribution is most important around $q = \pi/2$.

Two magnon states: In the experimental results presented in Sec. 8.6 beside the two bands we observe in the numerical results, which we identified as being due to the single magnon dynamics, a mode at even higher frequencies is present above the critical magnetic field. As the experiment is performed at a finite temperature, contributions from excited states are already contained in the thermal equilibrium. Thus, a reasonable candidate for this higher mode would include more than one magnon. One of the simplest cases to consider is to have one magnon in the initial state and to create a second magnon via the operator we apply at time $t = 0$ in our dynamic correlation function, Eq. (8.25). This is the situation which we analyze in the following
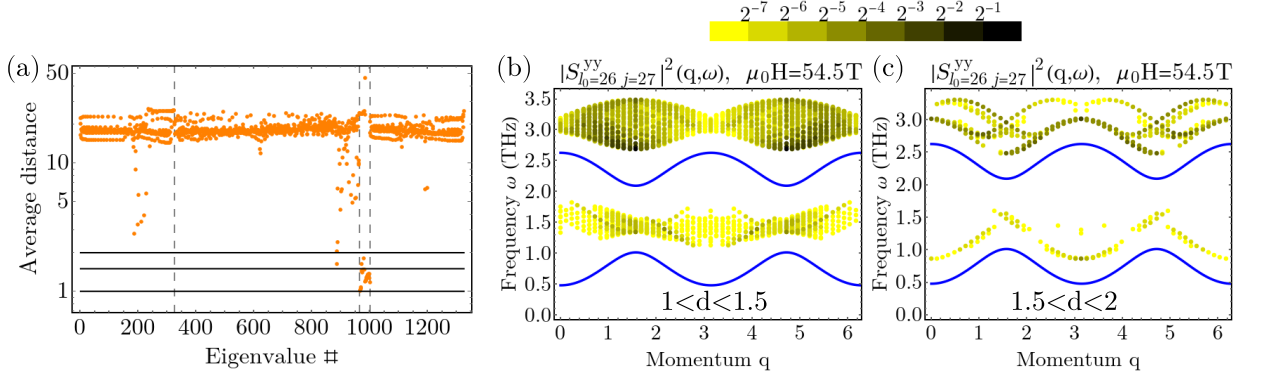
Figure 8.9: (a) The average value of the distance between the two magnons for the computed two-magnon eigenstates in a semi-log plot. The black horizontal lines are a guide to the eye for distance 1, 1.5 and 2. The gray dashed vertical lines represent the bands identified in Fig. 8.9. (b)-(c) The contribution to the dynamical structure factor of eigenstates with an average distance between the magnon of (b) $1 \leq d < 1.5$, (c) $1.5 \leq d < 2$. The blue line corresponds to the single magnon dispersion, Eq. (8.28). We note that the color scale of the plotted points is logarithmic. The results where obtained for the following parameters $\mu_0 H = 54.5$T, $L = 52$, $g_1 = 3.5$, $g_2 = 6.1$, $g_3 = 2.1$, $\theta = 5°$, $\epsilon = 0.46$, $J = 61 k_B$.

and has a contribution to the dynamical structure factor of the form

$$S_{l_0,j}^{\alpha,\beta}(q,\omega) = \sum_{e_{1m}} \sum_{e_{2m}} \langle l_0|e_{1m}\rangle \langle e_{1m}|S^\alpha(q)|e_{2m}\rangle \langle e_{2m}|S_j^\beta|l_0\rangle \delta(\omega + E_{1m} - E_{2m}), \qquad (8.29)$$

where $|l_0\rangle$ is the initial state of a localized magnon at site l_0, $|e_{1m}\rangle$ are the one-magnon eigenstates with the corresponding eigenenergies E_{1m}, $|e_{2m}\rangle$ are the two-magnon eigenstates with the corresponding eigenenergies E_{2m} and $S^\alpha(q) = \sum_l e^{-iql} S_l^\alpha$. For the calculations presented in the following, we considered $\alpha = \beta = y$ in the rotated basis. We compute the eigenstates $|e_{1m}\rangle$ and $|e_{2m}\rangle$ numerically by performing exact diagonalization of the Hamiltonian $\tilde{H}_{\text{magnon}}$, Eq. (8.22), in the subspaces of one and two-magnons.

If two magnons in the fully polarized background are far away from each other we expect that their dynamics under the Hamiltonian $\tilde{H}_{\text{magnon}}$, Eq. (8.22), to be the same as for single magnons. Such that in the non-interacting limit, where in $\tilde{H}_{\text{magnon}}$ the interaction is given by the $S_j^z S_{j+1}^z$ term, the dispersion relation for two magnons would show three bands $E_{2m} \in \{2E_{1m}^-, E_{1m}^- + E_{1m}^+, 2E_{1m}^+\}$. We note that the three bands exhibit gaps in between them only if the staggering in the magnetic field is strong enough, as the gap between E_{1m}^- and E_{1m}^+ depends on the staggering. Thus, without interaction, the main frequencies for which $S_{l_0,j}^{\alpha,\beta}(q,\omega)$, Eq. (8.29), is non-zero will be $\omega = E_{1m}^\pm$, meaning that the most important features seen in the dynamical structure factor are the same as for one magnon. This implies that $S_j^z S_{j+1}^z$ interaction term is necessary in order to observe higher mode in the dynamical structure factor beyond the single magnon bands. We would also expect this from the fact that two-magnon bound states exist at zero magnetic field on top of the ferromagnet in interacting spin chains [320].
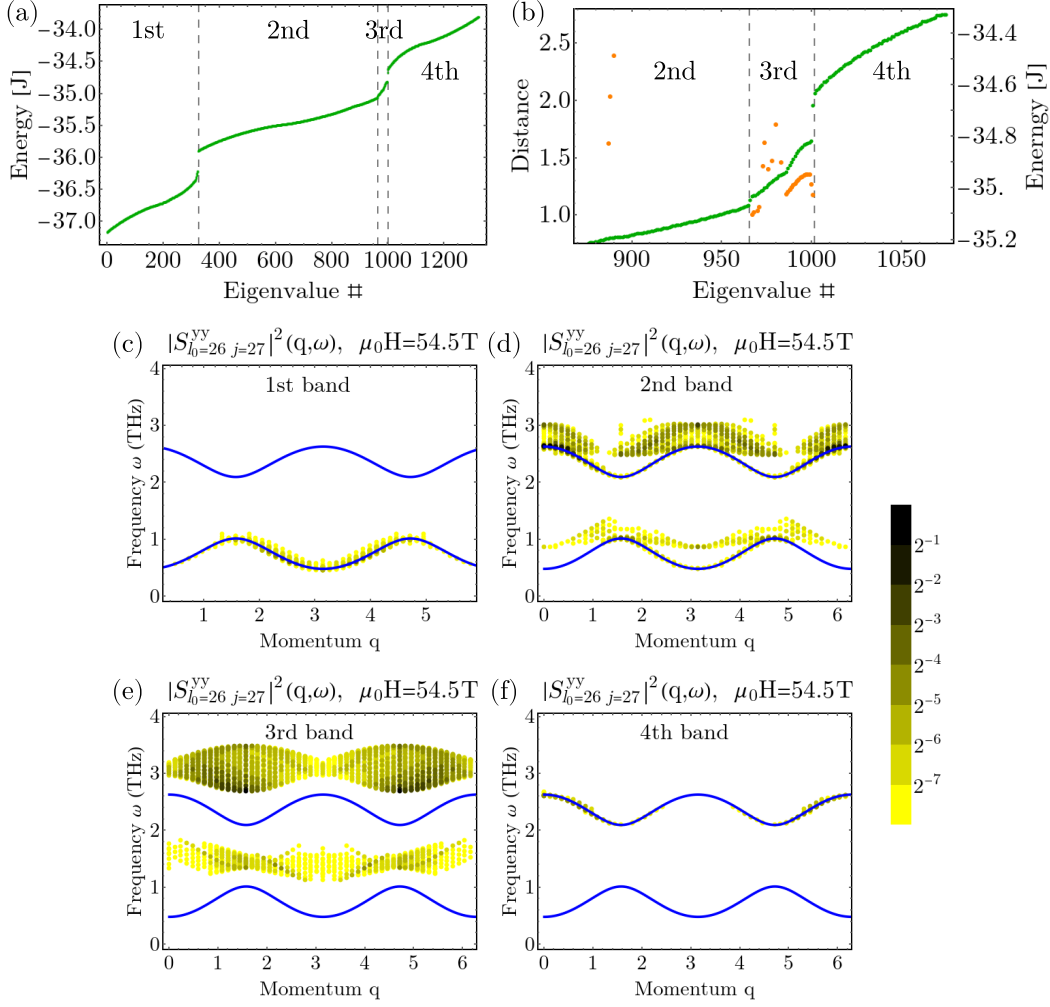
Figure 8.10: (a) The energies of the two-magnon eigenstates, we can identify four distinct bands separated by gaps. The dashed vertical lines mark the boundaries between the two-magnon bands. (b) The behavior of the energy and the average distance between the magnons around the 3rd band. (c)-(f) The contribution to the dynamical structure factor of eigenstates from each of the four bands. The blue line corresponds to the single magnon dispersion, Eq. (8.28). We note that the color scale of the plotted points is logarithmic. The results where obtained for the following parameters $\mu_0 H = 54.5$T, $L = 52$, $g_1 = 3.5$, $g_2 = 6.1$, $g_3 = 2.1$, $\theta = 5°$, $\epsilon = 0.46$, $J = 61 k_B$.

In Fig. 8.8, we plot the two-magnon contribution to the dynamical structure factor for different values of the magnetic field. For the initial state, we choose the state of a localized defect at l_0, in Fig. 8.8(a)-(c) l_0 is even, corresponding to the minima of the staggered potential, and in Fig. 8.8(d)-(f) l_0 is odd, corresponding to the maxima of the staggered potential. As we want to analyze the effects of the interaction, we create the second magnon on the next site $j = l_0 + 1$. We can observe that beside the expected bands, which show the same behavior as the single magnon dispersion, depicted with blue in Fig. 8.8, we also obtain contributions at higher fre-

quencies, or in the gap between the single magnon bands. Since our aim is to understand the high frequency modes occurring in the experimental results, in the following, we focus on the characterization of the states which have a higher frequency than the second single magnon band and look in more detail at the results for $l_0 = 26$. In particular, we will see that the intensity peak occurring for $q = 0$ or π [at $\omega \sim 3$THz for $\mu_0 H = 54.5$T in Fig. 8.8(b)], and at upper edge of the band for $q = \pi/2$ [at $\omega \sim 3.5$THz for $\mu_0 H = 54.5$T in Fig. 8.8(b)], agree well with the numerical results performed without approximations, as seen in Fig. 8.11.

In order to understand better the nature of the two magnon states of interest, in Fig. 8.9(a) we plot the average distance between the two magnons for each two-magnon eigenstates of $\tilde{H}_{\mathrm{magnon}}$, Eq. (8.22). We observe that for most eigenstates the average distance is $d \sim L/2 = 26$, showing that the magnons behave as non-interacting, but we also observe states for which the magnons are close to each other. In particular, we see that there are states for which the average distance, d is close to one, signaling that the two magnons are next to each other, thus the interaction effects play an important role. In Fig. 8.9(b)-(c), we look at the contribution to the structure factor only considering the states for which the two magnons are close to each other, either $1 < d < 1.5$, or $1.5 < d < 2$. We observe that these states contribute mostly to the high frequency features of the dynamical structure factor. This implies that the peaks in the dynamical structure factor for frequencies larger than the single magnon energy are due to states for which the two magnon are confined next to each other.

In Fig. 8.10(a) we plot the eigenenergies of the two-magnon states. As stated above, without interactions we would expect three bands, but we observe four bands. In particular, the third band, which is separated by a small gap from the second band and contains the least number of states, has mostly states for which the average distance between the two magnons is small, $d < 2$, as seen in Fig. 8.10(b). In Fig. 8.10(c)-(f) we compute the contributions of each band to the dynamical structure factor. We observe that the weight for the first and the fourth band is along the single magnon dispersions. We see that the interaction plays a role for the second band as peaks which are at a higher frequency than the single magnon bands are obtained. The third band is fully dominated by the confinement of the two magnons, as the features obtained are distinct from the single magnon bands.

We note that the staggering of the magnetic field plays a crucial role in the confining effects for the two magnons and in our ability to distinguish the high frequency band. If one would have a weaker h_s, see Eq. (8.22), the gaps we observed in Fig. 8.10 would close, we would have less states with a average distance $d < 2$ and the weight of peaks of interest for $q = 0, \pi/2, \pi$ will be much lower. In contrast, for a larger value of h_s, the gaps in the two magnon bands are larger, we have more states for which the two magnons are confined and the high energy peaks become more prominent. We present additional data to support these claims in Appendix D.

8.6 Comparison between theoretical and experimental results

In the previous section we performed several analytical calculations in different limits. We show the comparison between the full numerical results and these different analytical limits in Fig. 8.11(a)-(c). Afterwards, we compare our results with experimental results obtained using terahertz spectroscopy in magnetic fields [112] [see Fig. 8.11(d)].
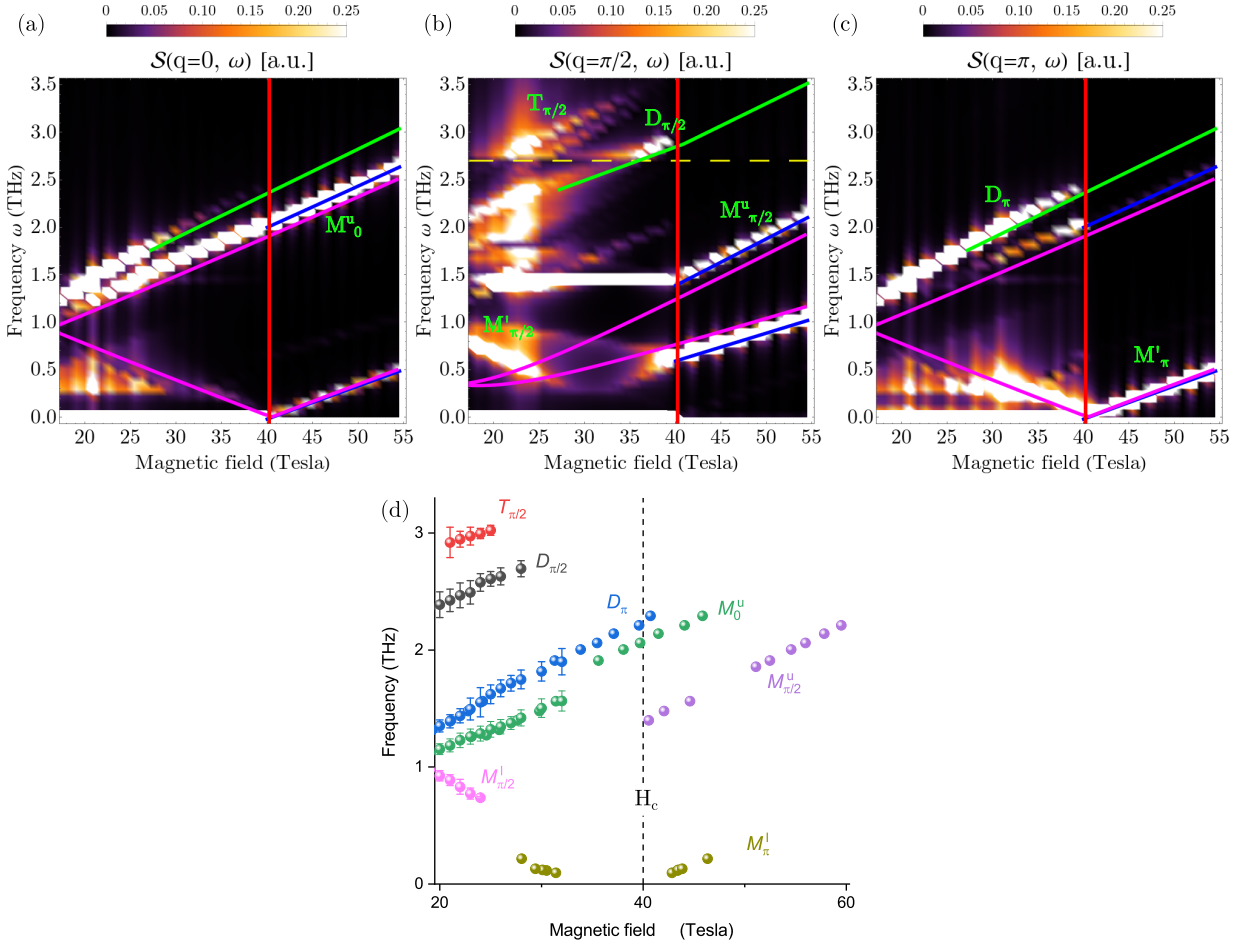
Figure 8.11: (a)-(c) Comparison between the numerical computation of the dynamical structure factor $\mathcal{S}(q,\omega)$, Eq. (8.15), for the full Hamiltonian, Eq. (8.2), and the exact spectrum of the Hamiltonian $\tilde{H}_{\mathrm{TI}}$, Eq. (8.19), (magenta curves), the one magnon analytical dispersion, Eq. (8.28), (blue curves), and the $q = \pi$ and $q = \pi/2$ peaks of the two-magnon states contribution to the dynamical structure factor (green lines). The spectrum of $\tilde{H}_{\mathrm{TI}}$ has been shifted with a field of 16 T in order to recover the critical field of the full model. The vertical red line represents the value of the critical magnetic field. For $q = \pi/2$, above the horizontal yellow dashed line we multiplied $\mathcal{S}(q,\omega)$ with a factor of 5 in order to increase the visibility of the high-frequency modes. The results where obtained for the following parameters, $L = 124$, $g_1 = 3.5$, $g_2 = 6.1$, $g_3 = 2.1$, $\theta = 5°$, $\epsilon = 0.46$, $J = 61k_B$. (d) The experimental results obtained using terahertz spectroscopy for various magnetic fields [112]. The points represent the position of the absorption peaks and the error bars their width. The momenta attributed to the different observed modes, represented with different colors, is based on the comparison with the theoretical results. The vertical black dashed line marks the critical magnetic field.

The initial approximation made was to neglect the induced magnetic field in the z direction, Eq. (8.16). From here we developed two different approaches. First, we neglected the interaction between neighboring spins in the direction of the magnetic field, in order to obtain an extension of the exactly solvable transverse-field Ising model, containing the staggered mag-

netic field, Eq. (8.19). We observe in Fig. 8.11(a)-(c) that this approach, depicted with magenta lines, captures the slopes around the closing of the gap at the critical value of the magnetic field for $q = 0$ and $q = \pi$ and of the mode M_0^u. For $q = \pi/2$ we see that the right behavior is captured only above the critical field.

In our second analytical approach, we make use of the fact that above the critical field the ground state of the system can be approximated by a fully polarized state in the direction of the external field. Thus, we derive a Hamiltonian which conserves the number of defects, or magnons, given in Eq. (8.22), but contains both the interaction between neighboring spins in the field direction and the staggering of the magnetic field. Within this approximation we could consider the contribution of the subspaces with a fixed number of magnons to the dynamical structure factor separately. We focused on the cases of one magnon and two magnons. In Fig. 8.11(a)-(c), we plot with blue lines the one magnon results and we see that they agree very well with all modes that can be identified in the full numerical calculation. A crucial ingredient in obtaining all the different modes is the presence of the staggered magnetic field. In the case of two magnons, we saw that, due to the interaction and field staggering, states in which the two magnons are confined next to each other are present. The contributions of these two-magnon bound states to the dynamical structure factor are depicted with green lines in Fig. 8.11(a)-(c). We see that they are in good agreement with high-frequency features of the numerical results.

Furthermore, we also compare our results with experimental results obtained using tera-hertz spectroscopy in magnetic fields on the $BaCo_2V_2O_8$ compound [112] , which are presented in Fig. 8.11(d). The high-field electron-spin-resonance spectroscopy in a pulsed magnetic field up to 61 T experiment was performed at Helmholtz Zentrum Dresden Rossendorf. Absorption spectra of quasi-monochromatic THz electromagnetic waves were measured as a function of the pulsed magnetic field for frequencies above 1.2 THz using a free electron laser and below 0.6 THz generated with THz transmitter sources [321, 322]. Additionaly, terahertz broad-band transmission measurements were performed for static magnetic fields up to 32 T using a Bitter electromagnet at the High Field Magnet Laboratory in Nijmegen.

We can see that all the modes observed in the experiment are very well captured by the theoretical results. We note that the attributed momenta to each mode in Fig. 8.5(a) is performed by comparison with the numerical results. For the modes present for both $q = 0$ and $q = \pi$ we attribute the momenta for which the intensity of the dynamical structure factor is higher for that certain mode. For clarity, we repeat the interpretation of the modes observed in the experimental results:

- The lowest excitation mode at $q = 0$ and $q = \pi$, M_π', exhibiting the closing of gap closing at the phase transition threshold, is well described by the shifted excitation spectrum of the transverse-field Ising model and the lower one-magnon band above the critical point.
- $M_{\pi/2}'$, which softens as we increase the magnetic field under the threshold, is continued by the lower one-magnon band for high magnetic fields.
- Above the critical magnetic field $M_{\pi/2}^u$ corresponds to the second band of the one-magnon dispersion. Similarly, for $q = 0$, M_0^u is also described by the second band of the one-magnon dispersion.
- The two-magnon bound states correspond in the experimental data to the modes D_π and

$D_{\pi/2}$.

- We expect that the features at a even higher frequency for $q = \pi/2$, marked with $T_{\pi/2}$ in Fig. 8.11, are due to states with three confined magnons [112].

We note that in the experiment the multi-magnon states at high frequencies have a larger amplitude due to the finite temperature [112].

8.7 Short summary

In this chapter, we investigated the excitation spectrum of the XXZ-model in a transverse magnetic field with a four-fold periodicity, Eq. (8.2). We show that our numerical tMPS calculations of the dynamical structure factor agree well with experimental measurements of the $BaCo_2V_2O_8$ compound in a strong magnetic field [112]. Via the application of high magnetic fields $BaCo_2V_2O_8$ effectively becomes a one-dimensional system. As we increase the external magnetic field, we unveil the presence of a phase transition between antiferromagnetic ordering in the z-direction and ferromagnetic ordering in the field direction. By performing ground state calculations we determined that the phase transition seems to belong to the universality class of the one-dimensional Ising model. We note that for magnetic fields lower than the ones studies in this chapter, $\lesssim 20$ T, three-dimensional order is dominant and one needs to include the coupling between the different one-dimensional spin chains in the theoretical analysis [5, 7].

Furthermore, through the analytical approaches we showed the importance of the presence of the staggered term originating from the four-fold periodicity of the magnetic field for recovering the features seen in the experimental results [112]. We observed that for high magnetic fields, above the critical field, the low-frequency excitations are dominated by the dynamics of single magnons present in the system under the influence of the staggered field. For large frequencies we identified the contributions stemming from states of two confined magnons, arising from the interplay of interaction effects between the magnons and the staggering of the magnetic field, in contrast to previously studied two-magnon states [320]. The understanding gained in this work opens future possibilities of designing quantum magnets with sought-after excitations.

Conclusion and Outlook

In this thesis, we investigated two classes of many-body quantum systems with external control. We showed that by the application of external fields, or by engineering a coupling with an external environment, one can steer the system towards interesting quantum phases and unveil quantum phase transitions.

The first class of many-body quantum system which we consider is that of bosonic atoms confined to low-dimensional optical lattices and globally coupled to the field of a dissipative optical cavity. Such systems show a self-organization phase transition to a non-trivial steady state protected by a dissipative attractor dynamics. Our results are obtained via two main methodological developments. We developed a time-dependent matrix product state method (tMPS) for the combined atom-cavity system. This is the first numerically exact method that can deal with a one-dimensional many-body interacting system globally coupled to a dissipative bosonic field and it is applicable to a wide class of models. It allowed us to numerically perform the full quantum evolution of ultracold interacting bosonic atoms on a chain and coupled to an optical cavity. Analytically, we extended the many-body adiabatic elimination framework to such atom-cavity systems. Within this approach, we can take into account the fluctuations of the coupling between the atoms and the photons. These two newly developed methods go beyond the extensively used mean field decoupling of the cavity and the atoms, allowing us to answer questions regarding the nature of the steady states and the phase transition. We showed that throughout the phase diagram, and, in particular, close to the phase transition threshold, the steady states have a mixed state character, in contrast to the pure steady states predicted by the often used mean field methods.

The newly developed methods made it possible to study the effects of a strong symmetry on the self-organization phase transition and the dynamics of the many-body open system of bosonic atoms coupled to the optical cavity. Multiple steady states appear due to the strong symmetry and in each symmetry sector the dissipative phase transition occurs at a different critical point. We showed that the phenomenon of dissipative freezing can occur, represented by the breaking of the conservation law at the level of individual quantum trajectories in the presence of the strong symmetry. An important contribution to the field of symmetries in open systems, which is still in its infancy, is our investigation of the dynamics of the system when a term that slightly breaks the strong symmetry is introduced. Such a symmetry breaking term

implies that the system goes from multiple steady states to a unique steady state.

We demonstrated how the dissipative character can be used for the preparation of interesting quantum states. We engineer the coupling between a one-dimensional bosonic wire and the cavity field to realize a dynamically induced spin-orbit coupling. Due to the dissipative dynamics a Meissner superfluid phase is stabilized as a steady state in the system. This states exhibits a persistent chiral spin current, with atoms in different spin states propagating in opposite directions.

Many recent exciting developments are occurring in the field of ultracold atoms coupled to optical cavities [66], with several interesting research directions. In the following, we present a short outlook into the directions for which we believe that these newly developed theoretical methods could have a strong impact. In this thesis, we mainly analyzed the nature of steady states of atom-cavity coupled systems. Thus, a natural extension of the current work would be to analyze the stability of the exotic phases predicted at a mean field level, for example, the vortex and Meissner states occurring due to the cavity-induced gauge field, or spin-orbit coupling [83, 93]. However, the novel tMPS method performs the full quantum time evolution of the coupled system, such that it is a perfect tool for the characterization of the out-of-equilibrium dynamics of both the atoms and the photons. Also the many-body adiabatic elimination approaches we developed can be employed for capturing the long-time dynamics of the system towards the steady state. Steps in the understanding of the non-equilibrium dynamics have been taken both theoretically [169, 323, 324] and in recent experimental realizations [72, 89, 197–200]. As we have seen, by coupling the atoms to a cavity mode, a global range interaction can be engineered. The atom-cavity interaction can be further controlled if one considers several cavity modes [325–327]. In such a multimode optical cavity a photon-mediated Peierls transition has been proposed [328], thus, it would be interesting to extend these results beyond mean field. The methodological developments presented here are not limited to bosonic degrees of freedom. Thus, they can be extended to consider fermionic atoms coupled to an optical cavity, as recently realized experimentally [329, 330], or towards solid-state systems of an electron gas coupled to THz cavities [14–16], or phononic modes.

The second many-body quantum system considered in this thesis is the one-dimensional XXZ spin chain model with a spatially dependent magnetic field. We show that this model describes very well the $BaCo_2V_2O_8$ compound in the high-field regime, by comparing our theoretical results with experimental data. We identified a phase transition between antiferromagnetic ordering in the z-direction and ferromagnetic ordering in the field direction as we increase the strength of the magnetic field. We employed time-dependent matrix product states (tMPS) numerical simulations to investigate the excitation spectrum across the phase transition. Our understanding of the excitations was further strengthened by analytical approaches which helped us identify that above the critical field the low-energy sector is dominated by the dynamics of single magnons in a staggered magnetic field and that for higher energies one can find two-magnon bound states.

As a first perspective, the excitations in the low-field regime of the $BaCo_2V_2O_8$ compound would be of interest, as in our work we focused on magnetic field $\gtrsim 20$ T. However, in this regime one needs to go beyond the one-dimensional XXZ-model and include the effects of

the coupling between the different one-dimensional chains. Furthermore, our study of the excitations of the spin degrees of freedom can be seen as a step towards the understanding of the interplay between the spin, charge, and phononic degrees of freedom. The coupling or competition between various orders in such quantum materials presents an avenue for manipulating their properties by means of external perturbations. For example, the phononic modes of the lattice could be excited with the help of optical pulses [18, 19, 331]. In the case of the $BaCo_2V_2O_8$ compound, the activation of a phononic mode could modify the coupling between the different one-dimensional spin chains. This could offer the possibility of performing a dimensionality quench and to analyze its subsequent non-equilibrium dynamics. These situations can be envisioned due to recent developments in the field of ultrafast spectroscopic probes [332]. Such probes offer a platform for understanding the light-matter interaction at the shortest times and a way for the study of the dynamics of charges, spins, and atoms down to femtosecond and attosecond timescales.

Appendix for Chapter 4

A.1 Explicit derivation of the equations of motion and steady state for perturbation in kinetic energy

In this section, we present the intermediate steps necessary to arrive at Eq. (4.16) from Eq. (4.8), as discussed in Sec. 4.2. We begin with a general state from the decoherence free subspace, $\rho = |\alpha(\Delta); n_1, \ldots, n_L\rangle\langle\alpha(\Delta'); n_1', \ldots, n_L'|$, Eq. (4.9), and we apply successively each operator of the second term of Eq. (4.8).

$$
\left[H_{\text{kin}}, \rho^0\right] = \tag{A.1}
$$
$$
-J\Bigg[\sum_{i \text{ odd}} \Big(\sqrt{(n_i+1)n_{i+1}}|\alpha(\Delta); \ldots, n_{i-1}, n_i+1, n_{i+1}-1, \ldots\rangle\langle\alpha(\Delta); \ldots, n_i', \ldots|
$$
$$
+ \sqrt{(n_i+1)n_{i-1}}|\alpha(\Delta); \ldots, n_{i-1}-1, n_i+1, n_{i+1}, \ldots\rangle\langle\alpha(\Delta); \ldots, n_i', \ldots|
$$
$$
- \sqrt{(n_i'+1)n_{i+1}'}|\alpha(\Delta); \ldots, n_i, \ldots\rangle\langle\alpha(\Delta); \ldots, n_{i-1}', n_i'+1, n_{i+1}'-1, \ldots|
$$
$$
- \sqrt{(n_i'+1)n_{i-1}'}|\alpha(\Delta); \ldots, n_i, \ldots\rangle\langle\alpha(\Delta); \ldots, n_{i-1}'-1, n_i'+1, n_{i+1}', \ldots|\Big)
$$
$$
+ \sum_{i \text{ even}} \Big(\sqrt{(n_i+1)n_{i+1}}|\alpha(\Delta); \ldots, n_{i-1}, n_i+1, n_{i+1}-1, \ldots\rangle\langle\alpha(\Delta); \ldots, n_i', \ldots|
$$
$$
+ \sqrt{(n_i+1)n_{i-1}}|\alpha(\Delta); \ldots, n_{i-1}-1, n_i+1, n_{i+1}, \ldots\rangle\langle\alpha(\Delta); \ldots, n_i', \ldots|
$$
$$
- \sqrt{(n_i'+1)n_{i+1}'}|\alpha(\Delta); \ldots, n_i, \ldots\rangle\langle\alpha(\Delta); \ldots, n_{i-1}', n_i'+1, n_{i+1}'-1, \ldots|
$$
$$
- \sqrt{(n_i'+1)n_{i-1}'}|\alpha(\Delta); \ldots, n_i, \ldots\rangle\langle\alpha(\Delta); \ldots, n_{i-1}'-1, n_i'+1, n_{i+1}', \ldots|\Big)\Bigg],
$$

$$
P_1\left[H_{\text{kin}}, \rho^0\right] = -Je^{-2|\alpha_0|^2}\Bigg[\tag{A.2}
$$

$$\sum_{i \text{ odd}} \left(\sqrt{(n_i+1)n_{i+1}}|\alpha(\Delta-2); \dots, n_{i-1}, n_i+1, n_{i+1}-1, \dots\rangle\langle\alpha(\Delta); \dots, n_i', \dots| \right.$$

$$+ \sqrt{(n_i+1)n_{i-1}}|\alpha(\Delta-2); \dots, n_{i-1}-1, n_i+1, n_{i+1}, \dots\rangle\langle\alpha(\Delta); \dots, n_i', \dots|$$

$$- \sqrt{(n_i'+1)n_{i+1}'}|\alpha(\Delta); \dots, n_i, \dots\rangle\langle\alpha(\Delta-2); \dots, n_{i-1}', n_i'+1, n_{i+1}'-1, \dots|$$

$$\left. - \sqrt{(n_i'+1)n_{i-1}'}|\alpha(\Delta); \dots, n_i, \dots\rangle\langle\alpha(\Delta-2); \dots, n_{i-1}'-1, n_i'+1, n_{i+1}', \dots| \right)$$

$$+ \sum_{i \text{ even}} \left(\sqrt{(n_i+1)n_{i+1}}|\alpha(\Delta+2); \dots, n_{i-1}, n_i+1, n_{i+1}-1, \dots\rangle\langle\alpha(\Delta); \dots, n_i', \dots| \right.$$

$$+ \sqrt{(n_i+1)n_{i-1}}|\alpha(\Delta+2); \dots, n_{i-1}-1, n_i+1, n_{i+1}, \dots\rangle\langle\alpha(\Delta); \dots, n_i', \dots|$$

$$- \sqrt{(n_i'+1)n_{i+1}'}|\alpha(\Delta); \dots, n_i, \dots\rangle\langle\alpha(\Delta+2); \dots, n_{i-1}', n_i'+1, n_{i+1}'-1, \dots|$$

$$\left. \left. - \sqrt{(n_i'+1)n_{i-1}'}|\alpha(\Delta); \dots, n_i, \dots\rangle\langle\alpha(\Delta+2); \dots, n_{i-1}'-1, n_i'+1, n_{i+1}', \dots| \right) \right],$$

$$\mathcal{L}_0^{-1} P_1 \left[H_{\text{kin}}, \rho^0 \right] = -J e^{-2|\alpha_0|^2} \Bigg[\tag{A.3}$$

$$\sum_{i \text{ odd}} \Bigg(\frac{\sqrt{(n_i+1)n_{i+1}}}{\lambda(\Delta-2, u+U(n_i-n_{i+1}+1), \Delta, u')} \times$$

$$|\alpha(\Delta-2); \dots, n_{i-1}, n_i+1, n_{i+1}-1, \dots\rangle\langle\alpha(\Delta); \dots, n_i', \dots|$$

$$+ \frac{\sqrt{(n_i+1)n_{i-1}}}{\lambda(\Delta-2, u+U(n_i-n_{i-1}+1), \Delta, u')} \times$$

$$|\alpha(\Delta-2); \dots, n_{i-1}-1, n_i+1, n_{i+1}, \dots\rangle\langle\alpha(\Delta); \dots, n_i', \dots|$$

$$- \frac{\sqrt{(n_i'+1)n_{i+1}'}}{\lambda(\Delta, u, \Delta-2, u'+U(n_i'-n_{i+1}'+1))} \times$$

$$|\alpha(\Delta); \dots, n_i, \dots\rangle\langle\alpha(\Delta-2); \dots, n_{i-1}', n_i'+1, n_{i+1}'-1, \dots|$$

$$- \frac{\sqrt{(n_i'+1)n_{i-1}'}}{\lambda(\Delta, u, \Delta-2, u'+U(n_i'-n_{i-1}'+1))} \times$$

$$|\alpha(\Delta); \dots, n_i, \dots\rangle\langle\alpha(\Delta-2); \dots, n_{i-1}'-1, n_i'+1, n_{i+1}', \dots| \Bigg)$$

$$+ \sum_{i \text{ even}} \Bigg(\frac{\sqrt{(n_i+1)n_{i+1}}}{\lambda(\Delta+2, u+U(n_i-n_{i+1}+1), \Delta, u')} \times$$

$$|\alpha(\Delta+2); \dots, n_{i-1}, n_i+1, n_{i+1}-1, \dots\rangle\langle\alpha(\Delta); \dots, n_i', \dots|$$

$$+ \frac{\sqrt{(n_i+1)n_{i-1}}}{\lambda(\Delta+2, u+U(n_i-n_{i-1}+1), \Delta, u')} \times$$

$$|\alpha(\Delta+2); \dots, n_{i-1}-1, n_i+1, n_{i+1}, \dots\rangle\langle\alpha(\Delta); \dots, n_i', \dots|$$

A.1 Explicit derivation of the equations of motion and steady state for perturbation in kinetic energy

$$
-\frac{\sqrt{(n'_i+1)n'_{i+1}}}{\lambda(\Delta,u,\Delta+2,u'+U(n'_i-n'_{i+1}+1))}\times
$$

$$
|\alpha(\Delta);\dots,n_i,\dots\rangle\langle\alpha(\Delta+2);\dots,n'_{i-1},n'_i+1,n'_{i+1}-1,\dots|
$$

$$
-\frac{\sqrt{(n'_i+1)n'_{i-1}}}{\lambda(\Delta,u,\Delta+2,u'+U(n'_i-n'_{i-1}+1))}\times
$$

$$
\left.\left.|\alpha(\Delta);\dots,n_i,\dots\rangle\langle\alpha(\Delta+2);\dots,n'_{i-1}-1,n'_i+1,n'_{i+1},\dots|\right)\right],
$$

$$
P_0\left[H_{\text{kin}},\mathcal{L}_0^{-1}P_1\left[H_{\text{kin}},\rho^0\right]\right]=J^2 e^{-4|\alpha_0|^2}\Bigg\{ \tag{A.4}
$$

$$
\sum_{i\text{ odd}}\sum_{j\text{ odd}}\Bigg[-\frac{\sqrt{(n_i+1)n_{i+1}}}{\lambda(\Delta-2,u+U(n_i-n_{i+1}+1),\Delta,u')}\times
$$

$$
\left(\sqrt{(n'_j+1)n'_{j+1}}|\alpha(\Delta-2);\dots,n_i+1,n_{i+1}-1,\dots\rangle\langle\alpha(\Delta-2);\dots,n'_j+1,n'_{j+1}-1,\dots|\right.
$$

$$
\left.+\sqrt{(n'_j+1)n'_{j-1}}|\alpha(\Delta-2);\dots,n_i+1,n_{i+1}-1,\dots\rangle\langle\alpha(\Delta-2);\dots,n'_{j-1}-1,n'_j+1,\dots|\right)
$$

$$
-\frac{\sqrt{(n_i+1)n_{i-1}}}{\lambda(\Delta-2,u+U(n_i-n_{i-1}+1),\Delta,u')}\times
$$

$$
\left(\sqrt{(n'_j+1)n'_{j+1}}|\alpha(\Delta-2);\dots,n_{i-1}-1,n_i+1,\dots\rangle\langle\alpha(\Delta-2);\dots,n'_j+1,n'_{j+1}-1,\dots|\right.
$$

$$
\left.+\sqrt{(n'_j+1)n'_{j-1}}|\alpha(\Delta-2);\dots,n_{i-1}-1,n_i+1,\dots\rangle\langle\alpha(\Delta-2);\dots,n'_{j-1}-1,n'_j+1,\dots|\right)
$$

$$
-\frac{\sqrt{(n'_i+1)n'_{i+1}}}{\lambda(\Delta,u,\Delta-2,u'+U(n'_i-n'_{i+1}+1))}\times
$$

$$
\left(\sqrt{(n_j+1)n_{j+1}}|\alpha(\Delta-2);\dots,n_j+1,n_{j+1}-1,\dots\rangle\langle\alpha(\Delta-2);\dots,n'_i+1,n'_{i+1}-1,\dots|\right.
$$

$$
\left.+\sqrt{(n_j+1)n_{j-1}}|\alpha(\Delta-2);\dots,n_{j+1}-1,n_j+1,\dots\rangle\langle\alpha(\Delta-2);\dots,n'_i+1,n'_{i+1}-1,\dots|\right)
$$

$$
-\frac{\sqrt{(n'_i+1)n'_{i-1}}}{\lambda(\Delta,u,\Delta-2,u'+U(n'_i-n'_{i-1}+1))}\times
$$

$$
\left(\sqrt{(n_j+1)n_{j+1}}|\alpha(\Delta-2);\dots,n_j+1,n_{j+1}-1,\dots\rangle\langle\alpha(\Delta-2);\dots,n'_{i-1}-1,n'_i+1,\dots|\right.
$$

$$+ \sqrt{(n_j+1)n_{j-1}}|\alpha(\Delta-2);\ldots,n_{j+1}-1,n_j+1,\ldots\rangle\langle\alpha(\Delta-2);\ldots,n'_{i-1}-1,n'_i+1,\ldots|\Big)\Big]$$

$$+\sum_{i\text{ odd }j\text{ even}}\Bigg[\frac{\sqrt{(n_i+1)n_{i+1}}}{\lambda(\Delta-2,u+U(n_i-n_{i+1}+1),\Delta,u')}\times$$

$$\Bigg(\sqrt{(n_j+1)n_{j+1}}|\alpha(\Delta);\ldots,n_i+1,n_{i+1}-1,\ldots,n_j+1,n_{j+1}-1,\ldots\rangle\langle\alpha(\Delta);\ldots,n'_i,\ldots|$$

$$+\sqrt{(n_j+1)n_{j-1}}|\alpha(\Delta);\ldots,n_i+1,n_{i+1}-1,\ldots,n_{j-1}-1,n_j+1,\ldots\rangle\langle\alpha(\Delta);\ldots,n'_i,\ldots|\Bigg)$$

$$+\frac{\sqrt{(n_i+1)n_{i-1}}}{\lambda(\Delta-2,u+U(n_i-n_{i-1}+1),\Delta,u')}\times$$

$$\Bigg(\sqrt{(n_j+1)n_{j+1}}|\alpha(\Delta);\ldots,n_{i-1}-1,n_i+1,\ldots,n_j+1,n_{j+1}-1,\ldots\rangle\langle\alpha(\Delta);\ldots,n'_i,\ldots|$$

$$+\sqrt{(n_j+1)n_{j-1}}|\alpha(\Delta);\ldots,n_{i-1}-1,n_i+1,\ldots,n_{j-1}-1,n_j+1,\ldots\rangle\langle\alpha(\Delta);\ldots,n'_i,\ldots|\Bigg)$$

$$+\frac{\sqrt{(n'_i+1)n'_{i+1}}}{\lambda(\Delta,u,\Delta-2,u'+U(n'_i-n'_{i+1}+1))}\times$$

$$\Bigg(\sqrt{(n'_j+1)n'_{j+1}}|\alpha(\Delta);\ldots,n_i,\ldots\rangle\langle\alpha(\Delta);\ldots,n'_i+1,n'_{i+1}-1,\ldots,n'_j+1,n'_{j+1}-1,\ldots|$$

$$+\sqrt{(n'_j+1)n'_{j-1}}|\alpha(\Delta);\ldots,n_i,\ldots\rangle\langle\alpha(\Delta);\ldots,n'_i+1,n'_{i+1}-1,\ldots,n'_{j-1}-1,n'_j+1,\ldots|\Bigg)$$

$$+\frac{\sqrt{(n'_i+1)n'_{i-1}}}{\lambda(\Delta,u,\Delta-2,u'+U(n'_i-n'_{i-1}+1))}\times$$

$$\Bigg(\sqrt{(n'_j+1)n'_{j+1}}|\alpha(\Delta);\ldots,n_i,\ldots\rangle\langle\alpha(\Delta);\ldots,n'_{i-1}-1,n'_i+1,\ldots,n'_j+1,n'_{j+1}-1,\ldots|$$

$$+\sqrt{(n'_j+1)n'_{j-1}}|\alpha(\Delta);\ldots,n_i,\ldots\rangle\langle\alpha(\Delta);\ldots,n'_{i-1}-1,n'_i+1,\ldots,n'_{j-1}-1,n'_j+1,\ldots|\Bigg)\Bigg]$$

$$+\sum_{i\text{ even }j\text{ odd}}\Bigg[\frac{\sqrt{(n_i+1)n_{i+1}}}{\lambda(\Delta+2,u+U(n_i-n_{i+1}+1),\Delta,u')}\times$$

$$\Bigg(\sqrt{(n_j+1)n_{j+1}}|\alpha(\Delta);\ldots,n_i+1,n_{i+1}-1,\ldots,n_j+1,n_{j+1}-1,\ldots\rangle\langle\alpha(\Delta);\ldots,n'_i,\ldots|$$

$$+\sqrt{(n_j+1)n_{j-1}}|\alpha(\Delta);\ldots,n_i+1,n_{i+1}-1,\ldots,n_{j-1}-1,n_j+1,\ldots\rangle\langle\alpha(\Delta);\ldots,n'_i,\ldots|\Bigg)$$

$$+\frac{\sqrt{(n_i+1)n_{i-1}}}{\lambda(\Delta+2,u+U(n_i-n_{i-1}+1),\Delta,u')}\times$$

A.1 Explicit derivation of the equations of motion and steady state for perturbation in kinetic energy

$$
\left(\sqrt{(n_j+1)n_{j+1}} |\alpha(\Delta); \ldots, n_{i-1}-1, n_i+1, \ldots, n_j+1, n_{j+1}-1, \ldots\rangle\langle\alpha(\Delta); \ldots, n_i', \ldots| \right.
$$

$$
\left. + \sqrt{(n_j+1)n_{j-1}} |\alpha(\Delta); \ldots, n_{i-1}-1, n_i+1, \ldots, n_{j-1}-1, n_j+1, \ldots\rangle\langle\alpha(\Delta); \ldots, n_i', \ldots| \right)
$$

$$
+ \frac{\sqrt{(n_i'+1)n_{i+1}'}}{\lambda(\Delta, u, \Delta+2, u'+U(n_i'-n_{i+1}'+1))} \times
$$

$$
\left(\sqrt{(n_j'+1)n_{j+1}'} |\alpha(\Delta); \ldots, n_i, \ldots\rangle\langle\alpha(\Delta); \ldots, n_i'+1, n_{i+1}'-1, \ldots, n_j'+1, n_{j+1}'-1, \ldots| \right.
$$

$$
\left. + \sqrt{(n_j'+1)n_{j-1}'} |\alpha(\Delta); \ldots, n_i, \ldots\rangle\langle\alpha(\Delta); \ldots, n_i'+1, n_{i+1}'-1, \ldots, n_{j-1}'-1, n_j'+1, \ldots| \right)
$$

$$
+ \frac{\sqrt{(n_i'+1)n_{i-1}'}}{\lambda(\Delta, u, \Delta+2, u'+U(n_i'-n_{i-1}'+1))} \times
$$

$$
\left(\sqrt{(n_j'+1)n_{j+1}'} |\alpha(\Delta); \ldots, n_i, \ldots\rangle\langle\alpha(\Delta); \ldots, n_{i-1}'-1, n_i'+1, \ldots, n_j'+1, n_{j+1}'-1, \ldots| \right.
$$

$$
\left. \left. + \sqrt{(n_j'+1)n_{j-1}'} |\alpha(\Delta); \ldots, n_i, \ldots\rangle\langle\alpha(\Delta); \ldots, n_{i-1}'-1, n_i'+1, \ldots, n_{j-1}'-1, n_j'+1, \ldots| \right) \right]
$$

$$
+ \sum_{i \text{ even}} \sum_{j \text{ even}} \left[-\frac{\sqrt{(n_i+1)n_{i+1}}}{\lambda(\Delta+2, u+U(n_i-n_{i+1}+1), \Delta, u')} \times \right.
$$

$$
\left(\sqrt{(n_j'+1)n_{j+1}'} |\alpha(\Delta+2); \ldots, n_i+1, n_{i+1}-1, \ldots\rangle\langle\alpha(\Delta+2); \ldots, n_j'+1, n_{j+1}'-1, \ldots| \right.
$$

$$
\left. + \sqrt{(n_j'+1)n_{j-1}'} |\alpha(\Delta+2); \ldots, n_i+1, n_{i+1}-1, \ldots\rangle\langle\alpha(\Delta+2); \ldots, n_{j-1}'-1, n_j'+1, \ldots| \right)
$$

$$
- \frac{\sqrt{(n_i+1)n_{i-1}}}{\lambda(\Delta+2, u+U(n_i-n_{i-1}+1), \Delta, u')} \times
$$

$$
\left(\sqrt{(n_j'+1)n_{j+1}'} |\alpha(\Delta+2); \ldots, n_{i-1}-1, n_i+1, \ldots\rangle\langle\alpha(\Delta+2); \ldots, n_j'+1, n_{j+1}'-1, \ldots| \right.
$$

$$
\left. + \sqrt{(n_j'+1)n_{j-1}'} |\alpha(\Delta+2); \ldots, n_{i-1}-1, n_i+1, \ldots\rangle\langle\alpha(\Delta+2); \ldots, n_{j-1}'-1, n_j'+1, \ldots| \right)
$$

$$
- \frac{\sqrt{(n_i'+1)n_{i+1}'}}{\lambda(\Delta, u, \Delta+2, u'+U(n_i'-n_{i+1}'+1))} \times
$$

$$
\left(\sqrt{(n_j+1)n_{j+1}} |\alpha(\Delta+2); \ldots, n_j+1, n_{j+1}-1, \ldots\rangle\langle\alpha(\Delta+2); \ldots, n_i'+1, n_{i+1}'-1, \ldots| \right.
$$

$$+ \sqrt{(n_j + 1)n_{j-1}}|\alpha(\Delta + 2); \ldots, n_{j-1} - 1, n_j + 1, \ldots\rangle\langle\alpha(\Delta + 2); \ldots, n'_i + 1, n'_{i+1} - 1, \ldots|\Big)$$

$$- \frac{\sqrt{(n'_i + 1)n'_{i-1}}}{\lambda(\Delta, u, \Delta + 2, u' + U(n'_i - n'_{i-1} + 1))} \times$$

$$\Big(\sqrt{(n_j + 1)n_{j+1}}|\alpha(\Delta + 2); \ldots, n_j + 1, n_{j+1} - 1, \ldots\rangle\langle\alpha(\Delta + 2); \ldots, n'_{i-1} - 1, n'_i + 1, \ldots|$$

$$+ \sqrt{(n_j + 1)n_{j-1}}|\alpha(\Delta + 2); \ldots, n_{j-1} - 1, n_j + 1, \ldots\rangle\langle\alpha(\Delta + 2); \ldots, n'_{i-1} - 1, n'_i + 1, \ldots|\Big)\Big]\Big\},$$

from where Eq. (4.16) follows.

Finally, we want to check that the state given by Eq. (4.17) is the steady state of Eq. (4.16). In order to show this, we rewrite Eq. (4.16) by separating the diagonal states of the decoherence free subspace, $\rho^0 = |\alpha(\Delta); n_1, \ldots, n_L\rangle\langle\alpha(\Delta); n_1, \ldots, n_L|$, from the rest.

$$\sum_{i \text{ odd}} \Big(- \frac{(n_i + 1)n_{i+1}}{\lambda(\Delta - 2, u + U(n_i - n_{i+1} + 1), \Delta, u)} \times \tag{A.5}$$

$$|\alpha(\Delta - 2); \ldots, n_i + 1, n_{i+1} - 1, \ldots\rangle\langle\alpha(\Delta - 2); \ldots, n_i + 1, n_{i+1} - 1, \ldots|$$

$$- \frac{(n_i + 1)n_{i-1}}{\lambda(\Delta - 2, u + U(n_i - n_{i-1} + 1), \Delta, u)} \times \tag{A.6}$$

$$|\alpha(\Delta - 2); \ldots, n_{i-1} - 1, n_i + 1, \ldots\rangle\langle\alpha(\Delta - 2); \ldots, n_{i-1} - 1, n_i + 1, \ldots|$$

$$- \frac{(n_i + 1)n_{i+1}}{\lambda(\Delta, u, \Delta - 2, u + U(n_i - n_{i+1} + 1))} \times \tag{A.7}$$

$$|\alpha(\Delta - 2); \ldots, n_i + 1, n_{i+1} - 1, \ldots\rangle\langle\alpha(\Delta - 2); \ldots, n_i + 1, n_{i+1} - 1, \ldots|$$

$$- \frac{\sqrt{(n_i + 1)n_{i-1}}}{\lambda(\Delta, u, \Delta - 2, u + U(n_i - n_{i-1} + 1))} \times \tag{A.8}$$

$$|\alpha(\Delta - 2); \ldots, n_{i+1} - 1, n_i + 1, \ldots\rangle\langle\alpha(\Delta - 2); \ldots, n_{i-1} - 1, n_i + 1, \ldots|\Big)$$

$$+ \sum_{i \text{ odd}} \Big(\frac{(n_i + 1)n_{i+1}}{\lambda(\Delta - 2, u + U(n_i - n_{i+1} + 1), \Delta, u)} \times \tag{A.9}$$

$$|\alpha(\Delta); \ldots, n_i, \ldots\rangle\langle\alpha(\Delta); \ldots, n_i, \ldots|$$

$$+ \frac{(n_i + 1)n_{i-1}}{\lambda(\Delta - 2, u + U(n_i - n_{i-1} + 1), \Delta, u)} \times \tag{A.10}$$

$$|\alpha(\Delta); \ldots, n_i, \ldots\rangle\langle\alpha(\Delta); \ldots, n_i, \ldots|$$

$$+ \frac{(n_i + 1)n_{i+1}}{\lambda(\Delta, u, \Delta - 2, u + U(n_i - n_{i+1} + 1))} \times \tag{A.11}$$

A.1 Explicit derivation of the equations of motion and steady state for perturbation in kinetic energy

$$|\alpha(\Delta); \ldots, n_i, \ldots\rangle\langle\alpha(\Delta); \ldots, n_i, \ldots|$$

$$+ \frac{(n_i + 1)n_{i-1}}{\lambda(\Delta, u, \Delta - 2, u + U(n_i - n_{i-1} + 1))} \times \tag{A.12}$$

$$\left. |\alpha(\Delta); \ldots, n_i, \ldots\rangle\langle\alpha(\Delta); \ldots, n_i, \ldots| \right)$$

$$+ \sum_{i \text{ even}} \left(\frac{(n_i + 1)n_{i+1}}{\lambda(\Delta + 2, u + U(n_i - n_{i+1} + 1), \Delta, u)} \times \right. \tag{A.13}$$

$$|\alpha(\Delta); \ldots, n_i, \ldots\rangle\langle\alpha(\Delta); \ldots, n_i, \ldots|$$

$$+ \frac{(n_i + 1)n_{i-1}}{\lambda(\Delta + 2, u + U(n_i - n_{i-1} + 1), \Delta, u)} \times \tag{A.14}$$

$$|\alpha(\Delta); \ldots, n_i, \ldots\rangle\langle\alpha(\Delta); \ldots, n_i, \ldots|$$

$$+ \frac{(n_i + 1)n_{i+1}}{\lambda(\Delta, u, \Delta + 2, u + U(n_i - n_{i+1} + 1))} \times \tag{A.15}$$

$$|\alpha(\Delta); \ldots, n_i, \ldots\rangle\langle\alpha(\Delta); \ldots, n_i, \ldots|$$

$$+ \frac{(n_i + 1)n_{i-1}}{\lambda(\Delta, u, \Delta + 2, u + U(n_i - n_{i-1} + 1))} \times \tag{A.16}$$

$$\left. |\alpha(\Delta); \ldots, n_i, \ldots\rangle\langle\alpha(\Delta); \ldots, n_i, \ldots| \right)$$

$$+ \sum_{i \text{ even}} \left(-\frac{(n_i + 1)n_{i+1}}{\lambda(\Delta + 2, u + U(n_i - n_{i+1} + 1), \Delta, u)} \times \right. \tag{A.17}$$

$$|\alpha(\Delta + 2); \ldots, n_i + 1, n_{i+1} - 1, \ldots\rangle\langle\alpha(\Delta + 2); \ldots, n_i + 1, n_{i+1} - 1, \ldots|$$

$$- \frac{(n_i + 1)n_{i-1}}{\lambda(\Delta + 2, u + U(n_i - n_{i-1} + 1), \Delta, u)} \times \tag{A.18}$$

$$|\alpha(\Delta + 2); \ldots, n_{i-1} - 1, n_i + 1, \ldots\rangle\langle\alpha(\Delta + 2); \ldots, n_{i-1} - 1, n_i + 1, \ldots|$$

$$- \frac{(n_i + 1)n_{i+1}}{\lambda(\Delta, u, \Delta + 2, u + U(n_i - n_{i+1} + 1))} \times \tag{A.19}$$

$$|\alpha(\Delta + 2); \ldots, n_i + 1, n_{i+1} - 1, \ldots\rangle\langle\alpha(\Delta + 2); \ldots, n_i + 1, n_{i+1} - 1, \ldots|$$

$$- \frac{(n_i + 1)n_{i-1}}{\lambda(\Delta, u, \Delta + 2, u + U(n_i - n_{i-1} + 1))} \times \tag{A.20}$$

$$\left. |\alpha(\Delta + 2); \ldots, n_{i-1} - 1, n_i + 1, \ldots\rangle\langle\alpha(\Delta + 2); \ldots, n_{i-1} - 1, n_i + 1, \ldots| \right)$$

$$+ \left(\text{off-diagonal terms} \right) = 0.$$

One can observe that the coefficients are canceling in pairs, thus, (A.5) has the same value with opposite sign compared with (A.9), (A.6) with (A.10), (A.7) with (A.11), (A.8) with (A.12),
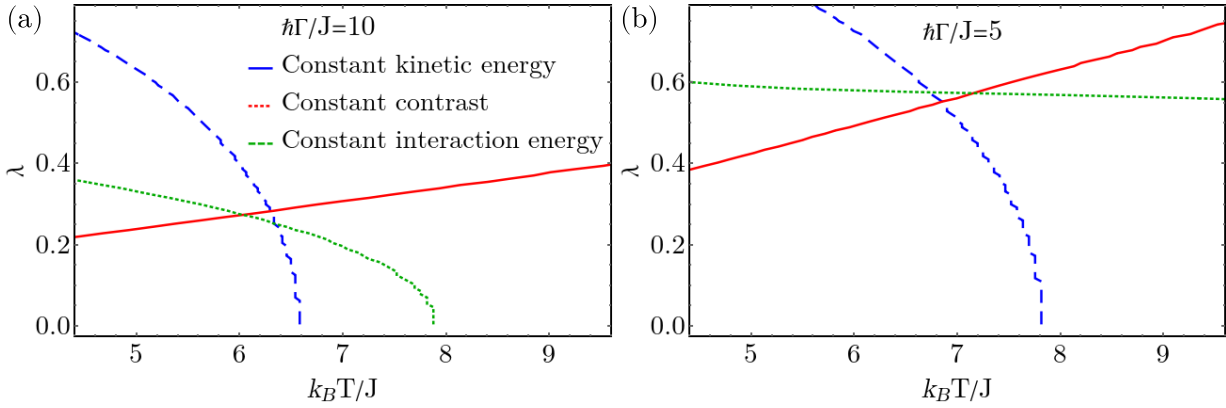
(A.13) with (A.17), (A.14) with (A.18), (A.15) with (A.19), and (A.16) with (A.20). This means that the state give by Eq. (4.17) has the eigenvalue zero and is indeed the steady state of our system.

Appendix B

Appendix for Chapter 5

B.1 Characterizing the tMPS results with a finite temperature

Figure B.1: Extraction of the effective temperature from the tMPS data for the parameters $L = 10$, $N = 5$, $\hbar g/J = 4.47$, $\hbar\delta/J = 2$, $U/J = 2$, $\hbar\Gamma/J \in \{5, 10\}$, $tJ = 49.75\hbar$. The lines in the T-λ plane are for constant kinetic energy, (a) $E_{\text{kin}}/J = -1.85$ and (b) $E_{\text{kin}}/J = -1.56$, contrast of the density-density correlations, (a) $\frac{1}{L-2} \sum_j \left(\langle n_j n_{j+2} \rangle - \langle n_j n_{j+1} \rangle\right) = 0.09$ and (b) $\frac{1}{L-2} \sum_j \left(\langle n_j n_{j+2} \rangle - \langle n_j n_{j+1} \rangle\right) = 0.03$, interaction energy, (a) $E_{\text{int}}/J = 2.75$ and (b) $E_{\text{int}}/J = 3.25$. Panel (a) is published in Ref. [110]

In order to the compare the values of the effective temperature obtained in the perturbation theory on top the mean field approach we need to extract an effective temperature that can describe the tMPS results, see Fig. 5.8(d) of Sec. 5.4. Thus, we try to find the temperature, T, and cavity field, λ, which determine the density matrix $\rho(T, \lambda) \sim |\alpha(\lambda)\rangle\langle\alpha(\lambda)| e^{-H_b(\lambda)/k_B T}$, by requiring the thermal density matrix to approximately describe the tMPS results. For this we employ the following procedure. We first compute the expectation values of three important observables of the atomic sector with tMPS, the kinetic energy, $E_{\text{kin}} = -J \sum_{j=1}^{L-1} \langle b_j^\dagger b_{j+1} + b_{j+1}^\dagger b_j \rangle$, the contrast of the density-density correlations, $\frac{1}{L-2} \sum_{j=1}^{L-2} \left(\langle n_j n_{j+2} \rangle - \langle n_j n_{j+1} \rangle\right)$ and interaction energy, $E_{\text{int}} = \frac{U}{2} \sum_{j=1}^{L} \langle n_j(n_j - 1) \rangle$.

In the next step we compute the expectation values of the mentioned observables using

148

$\rho(T, \lambda)$ and identify the points for which we obtain the same values as in tMPS. In Fig. B.1, we observe that in the T-λ plane for each observable we find a curve along which the expectation value agrees with tMPS. Thus, by finding the intersection point of the three curves we obtain the values of T and λ for which $\rho(T, \lambda)$ approximates the tMPS state.

As we observe that these curves do not intersect each other in a unique point, but rather in three distinct ones, we define the area of the triangle as a measure the errors involved in the determination of the effective temperature, see Fig. B.1. Note that the cavity field λ used as a parameter in this procedure does not agree with the tMPS photon number, as in the full quantum evolution the cavity field is not restricted to a coherent state. We note that for $\hbar\Gamma/J \lesssim 5$ this procedure gives unreliable results as the intersection points are far from each other.

Appendix C

$$\text{Appendix} \quad \text{C}$$

Appendix for Chapter 6

C.1 Open boundary conditions

In Chap. 6 the Liouvillian describing the system, given by Eqs.(6.4)-(6.5), was written in momentum space, the real space Hamiltonian is given in Sec. 2.1.

In our numerical simulations for finite size systems we used open boundary conditions. In the analytical many-body adiabatic elimination calculations, presented in Chap. 6 and this Appendix, we also use open boundary condition for a direct correspondence. In this case one uses the Fourier sine transform, defined by

$$b_k = \sqrt{\frac{2}{L+1}} \sum_{j=1}^{L} b_j \sin(kj), \tag{C.1}$$

$$b_k^\dagger = \sqrt{\frac{2}{L+1}} \sum_{j=1}^{L} b_j^\dagger \sin(kj),$$

and the unitless momenta are given by $k = \frac{\pi m}{L+1}$ and $m = 1, \ldots, L$. In this case we also have $L/2$ independent symmetry sectors for a single particle, but each is spanned by the momentum states $|k_j\rangle$ and $|\pi - k_j\rangle$, $j = 1, \ldots, L/2$. As the momenta k_j are in the interval $[0, \pi]$, the values $\pi - k_j$ will always be inside the first Brillouin zone. We can write the symmetry generator as

$$\mathcal{O}_{k_j} = b_{k_j}^\dagger b_{k_j} + b_{\pi-k_j}^\dagger b_{\pi-k_j}. \tag{C.2}$$

C.2 Explicit derivation of the steady states for the one and two particles cases for perturbation in kinetic energy

In the following we show explicitly how to compute the steady states with the procedure described in Sec. 6.2.2 for the single particle and two particle cases. In this section we take $\hbar = 1$.

C.2.1 The single particle case

For a single particle in the symmetry sector $K = (m_k = 1)$ a general state in the dissipation free subspace which is restricted to this symmetry sector has the form

$$\rho_k(b) = \sum_{i,j \text{ odd}} \left(\frac{1}{2} + b\right) \sin(ki)\sin(kj)|-\alpha; i\rangle\langle-\alpha; j| \tag{C.3}$$

$$+ \sum_{i,j \text{ even}} \left(\frac{1}{2} - b\right) \sin(ki)\sin(kj)|\alpha; i\rangle\langle\alpha; j|,$$

with b a real parameter, i and j the positions of the particle, and $\alpha = \frac{\Omega}{\delta - i\Gamma/2}$ the cavity field.

The equation of motion for a state $\rho_0 = |\pm\alpha; i\rangle\langle\pm\alpha; j|$, with i and j both even or both odd, from the dissipation free subspace, obtained with the many-body adiabatic elimination is given by

$$\frac{\partial}{\partial t}|\pm\alpha; i\rangle\langle\pm\alpha; j| = P_0 \left[H_{\text{kin}}, \mathcal{L}_0^{-1} P_1 \left[H_{\text{kin}}, |\pm\alpha; i\rangle\langle\pm\alpha; j|\right]\right] \tag{C.4}$$

$$= \frac{J^2}{\lambda_0} e^{-4|\alpha|^2} \Big(4|\pm\alpha; i\rangle\langle\pm\alpha; j| - 2|\mp\alpha; i+1\rangle\langle\mp\alpha; j+1| - 2|\mp\alpha; i+1\rangle\langle\mp\alpha; j-1|$$

$$- 2|\mp\alpha; i-1\rangle\langle\mp\alpha; j+1| - 2|\mp\alpha; i-1\rangle\langle\mp\alpha; j-1| + |\pm\alpha; i+2\rangle\langle\pm\alpha; j|$$

$$+ |\pm\alpha; i-2\rangle\langle\pm\alpha; j| + |\pm\alpha; i\rangle\langle\pm\alpha; j+2| + |\pm\alpha; i\rangle\langle\pm\alpha; j-2|\Big),$$

with $\lambda_0 = -\frac{2\Omega^2\Gamma}{\delta^2 + \Gamma^2/4}$. This allows us to write the equation of motion for the state $\rho_k(b)$, from which we observe that for $b = 0$ we obtain the steady state, $\frac{\partial}{\partial t}\rho_{k,\text{st}} = 0$, for the one particle case

$$\rho_{k,\text{st}} = \sum_{i,j \text{ odd}} \sin(ki)\sin(kj)|-\alpha; i\rangle\langle-\alpha; j| + \sum_{i,j \text{ even}} \sin(ki)\sin(kj)|\alpha; i\rangle\langle\alpha; j|. \tag{C.5}$$

One can see that this state has a fully mixed atomic sector in the momentum basis.

C.2.2 The two particle case

We now consider two particles in the sector $K = (m_{k_1} = 1, m_{k_2} = 1)$. The basis in the dissipation free subspace in the considered symmetry sector is spanned by

$$\sigma_0 = 4(s_3 - s_4 - s_5 + s_6), \tag{C.6}$$
$$\sigma_1 = 4(s_1 + s_2 - s_3 + 2s_4 + 2s_5 - s_6),$$
$$\sigma_2 = 4(s_1 + s_2 - s_3 - s_6),$$
$$\sigma_3 = 4(s_1 - s_2 + s_4 - s_5),$$
$$\sigma_4 = 4(-s_3 - s_4 + s_5 + s_6),$$
$$\sigma_5 = 4(s_1 - s_2 + s_3 - s_6),$$

151

C.2 Explicit derivation of the steady states for the one and two particles cases for perturbation in kinetic energy

where we defined the states

$$s_1 = \sum_{i_1,i_2,j_1,j_2 \text{ odd}} \sin(k_1 i_1)\sin(k_1 j_1)\sin(k_2 i_2)\sin(k_2 j_2)\sqrt{n_{i_1} n_{j_1}}|-\alpha; i_1, i_2\rangle\langle-\alpha; j_1, j_2|, \quad \text{(C.7)}$$

$$s_2 = \sum_{i_1,i_2,j_1,j_2 \text{ even}} \sin(k_1 i_1)\sin(k_1 j_1)\sin(k_2 i_2)\sin(k_2 j_2)\sqrt{n_{i_1} n_{j_1}}|\alpha; i_1, i_2\rangle\langle\alpha; j_1, j_2|,$$

$$s_3 = \sum_{\substack{i_1,j_1 \text{ odd} \\ i_2,j_2 \text{ even}}} \sin(k_1 i_1)\sin(k_1 j_1)\sin(k_2 i_2)\sin(k_2 j_2)\sqrt{n_{i_1} n_{j_1}}|0; i_1, i_2\rangle\langle0; j_1, j_2|,$$

$$s_4 = \sum_{\substack{i_2,j_1 \text{ odd} \\ i_1,j_2 \text{ even}}} \sin(k_1 i_1)\sin(k_1 j_1)\sin(k_2 i_2)\sin(k_2 j_2)\sqrt{n_{i_1} n_{j_1}}|0; i_1, i_2\rangle\langle0; j_1, j_2|,$$

$$s_5 = \sum_{\substack{i_1,j_2 \text{ odd} \\ i_2,j_1 \text{ even}}} \sin(k_1 i_1)\sin(k_1 j_1)\sin(k_2 i_2)\sin(k_2 j_2)\sqrt{n_{i_1} n_{j_1}}|0; i_1, i_2\rangle\langle0; j_1, j_2|,$$

$$s_6 = \sum_{\substack{i_2,j_2 \text{ odd} \\ i_1,j_1 \text{ even}}} \sin(k_1 i_1)\sin(k_1 j_1)\sin(k_2 i_2)\sin(k_2 j_2)\sqrt{n_{i_1} n_{j_1}}|0; i_1, i_2\rangle\langle0; j_1, j_2|,$$

with i_1, i_2, j_1 and j_2 the positions of the two particles, and n_i the number of particles at site i, and the cavity field is $\alpha = \frac{2\Omega}{\delta - i\Gamma/2}$

In the following, we give the equations of motion for the states $|\pm\alpha; i_1, i_2\rangle\langle\pm\alpha; j_1, j_2|$ and $|0; i_1, i_2\rangle\langle0; j_1, j_2|$ for two particles

$$\frac{\partial}{\partial t}|\pm\alpha; i_1, i_2\rangle\langle\pm\alpha; j_1, j_2| = P_0\left[H_{\text{kin}}, \mathcal{L}_0^{-1} P_1\left[H_{\text{kin}}, |\pm\alpha; i_1, i_2\rangle\langle\pm\alpha; j_1, j_2|\right]\right] \quad \text{(C.8)}$$

$$= J^2 e^{-4|\alpha_0|^2}\left[\frac{\sqrt{(n_{i_1+1}+1)n_{i_1}}}{\lambda_1^*}\left(\sqrt{n_{i_1}(n_{i_1+1}+1)}|\pm\alpha; i_1, i_2\rangle\langle\pm\alpha; j_1, j_2|\right.\right.$$

$$- \sqrt{(n_{j_1+1}+1)n_{j_1}}|0; i_1+1, i_2\rangle\langle0; j_1+1, j_2|$$

$$+ \sqrt{(n_{i_1+2}+1)(n_{i_1+1}+1)}|\pm\alpha; i_1+2, i_2\rangle\langle\pm\alpha; j_1, j_2|$$

$$- \sqrt{(n_{j_1-1}+1)n_{j_1}}|0; i_1+1, i_2\rangle\langle0; j_1-1, j_2|$$

$$- \sqrt{(n_{j_2+1}+1)n_{j_2}}|0; i_1+1, i_2\rangle\langle0; j_1, j_2+1|$$

$$\left.- \sqrt{(n_{j_2-1}+1)n_{j_2}}|0; i_1+1, i_2\rangle\langle0; j_1, j_2-1|\right)$$

$$+\frac{\sqrt{(n_{i_1-1}+1)n_{i_1}}}{\lambda_1^*}\left(\sqrt{n_{i_1}(n_{i_1-1}+1)}|\pm\alpha; i_1, i_2\rangle\langle\pm\alpha; j_1, j_2|\right.$$

$$- \sqrt{(n_{j_1+1}+1)n_{j_1}}|0; i_1-1, i_2\rangle\langle0; j_1+1, j_2|$$

$$+ \sqrt{(n_{i_1-2}+1)(n_{i_1-1}+1)}|\pm\alpha; i_1-2, i_2\rangle\langle\pm\alpha; j_1, j_2|$$

$$- \sqrt{(n_{j_1-1}+1)n_{j_1}}|0; i_1-1, i_2\rangle\langle0; j_1-1, j_2|$$

$$
\begin{aligned}
&- \sqrt{(n_{j_2+1}+1)n_{j_2}}|0;i_1-1,i_2\rangle\langle 0;j_1,j_2+1| \\
&\left. - \sqrt{(n_{j_2-1}+1)n_{j_2}}|0;i_1-1,i_2\rangle\langle 0;j_1,j_2-1| \right) \\
+&\frac{\sqrt{(n_{i_2+1}+1)n_{i_2}}}{\lambda_1^*}\left(\sqrt{n_{i_2}(n_{i_2+1}+1)}|\pm\alpha;i_1,i_2\rangle\langle\pm\alpha;j_1,j_2| \right. \\
&- \sqrt{(n_{j_1+1}+1)n_{j_1}}|0;i_1,i_2+1\rangle\langle 0;j_1+1,j_2| \\
&+ \sqrt{(n_{i_2+2}+1)(n_{i_2+1}+1)}|\pm\alpha;i_1,i_2+2\rangle\langle\pm\alpha;j_1,j_2| \\
&- \sqrt{(n_{j_1-1}+1)n_{j_1}}|0;i_1,i_2+1\rangle\langle 0;j_1-1,j_2| \\
&- \sqrt{(n_{j_2+1}+1)n_{j_2}}|0;i_1,i_2+1\rangle\langle 0;j_1,j_2+1| \\
&\left. - \sqrt{(n_{j_2-1}+1)n_{j_2}}|0;i_1,i_2+1\rangle\langle 0;j_1,j_2-1| \right) \\
+&\frac{\sqrt{(n_{i_2-1}+1)n_{i_2}}}{\lambda_1^*}\left(\sqrt{n_{i_2}(n_{i_2-1}+1)}|\pm\alpha;i_1,i_2\rangle\langle\pm\alpha;j_1,j_2| \right. \\
&- \sqrt{(n_{j_1+1}+1)n_{j_1}}|0;i_1,i_2-1\rangle\langle 0;j_1+1,j_2| \\
&+ \sqrt{(n_{i_2-2}+1)(n_{i_2-1}+1)}|\pm\alpha;i_1,i_2-2\rangle\langle\pm\alpha;j_1,j_2| \\
&- \sqrt{(n_{j_1-1}+1)n_{j_1}}|0;i_1,i_2-1\rangle\langle 0;j_1-1,j_2| \\
&- \sqrt{(n_{j_2+1}+1)n_{j_2}}|0;i_1,i_2-1\rangle\langle 0;j_1,j_2-1| \\
&\left. - \sqrt{(n_{j_2-1}+1)n_{j_2}}|0;i_1,i_2-1\rangle\langle 0;j_1,j_2-1| \right) \\
-&\frac{\sqrt{(n_{j_1+1}+1)n_{j_1}}}{\lambda_1}\left(\sqrt{(n_{i_1+1}+1)n_{i_1}}|0;i_1+1,i_2\rangle\langle 0;j_1+1,j_2| \right. \\
&+ \sqrt{(n_{i_1-1}+1)n_{i_1}}|0;i_1-1,i_2\rangle\langle 0;j_1+1,j_2| \\
&+ \sqrt{(n_{i_2+1}+1)n_{i_2}}|0;i_1,i_2+1\rangle\langle 0;j_1+1,j_2| \\
&+ \sqrt{(n_{i_2-1}+1)n_{i_2}}|0;i_1,i_2-1\rangle\langle 0;j_1+1,j_2| \\
&- \sqrt{n_{j_1}(n_{j_1+1}+1)}|\pm\alpha;i_1,i_2\rangle\langle\pm\alpha;j_1,j_2| \\
&\left. - \sqrt{(n_{j_1+2}+1)(n_{j_1+1}+1)}|\pm\alpha;i_1,i_2\rangle\langle\pm\alpha;j_1+2,j_2| \right) \\
-&\frac{\sqrt{(n_{j_1-1}+1)n_{j_1}}}{\lambda_1}\left(\sqrt{(n_{i_1+1}+1)n_{i_1}}|0;i_1+1,i_2\rangle\langle 0;j_1-1,j_2| \right. \\
&+ \sqrt{(n_{i_1-1}+1)n_{i_1}}|0;i_1-1,i_2\rangle\langle 0;j_1-1,j_2| \\
&+ \sqrt{(n_{i_2+1}+1)n_{i_2}}|0;i_1,i_2+1\rangle\langle 0;j_1-1,j_2| \\
&+ \sqrt{(n_{i_2-1}+1)n_{i_2}}|0;i_1,i_2-1\rangle\langle 0;j_1-1,j_2| \\
&- \sqrt{n_{j_1}(n_{j_1-1}+1)}|\pm\alpha;i_1,i_2\rangle\langle\pm\alpha;j_1,j_2| \\
&\left. - \sqrt{(n_{j_1-2}+1)(n_{j_1-1}+1)}|\pm\alpha;i_1,i_2\rangle\langle\pm\alpha;j_1-2,j_2| \right)
\end{aligned}
$$

$$-\frac{\sqrt{(n_{j_2+1}+1)n_{j_2}}}{\lambda_1}\Big(\sqrt{(n_{i_1+1}+1)n_{i_1}}|0;i_1+1,i_2\rangle\langle 0;j_1,j_2+1|$$

$$+\sqrt{(n_{i_1-1}+1)n_{i_1}}|0;i_1-1,i_2\rangle\langle 0;j_1,j_2+1|$$

$$+\sqrt{(n_{i_2+1}+1)n_{i_2}}|0;i_1,i_2+1\rangle\langle 0;j_1,j_2+1|$$

$$+\sqrt{(n_{i_2-1}+1)n_{i_2}}|0;i_1,i_2-1\rangle\langle 0;j_1,j_2+1|$$

$$-\sqrt{n_{j_2}(n_{j_2+1}+1)}|\pm\alpha;i_1,i_2\rangle\langle\pm\alpha;j_1,j_2|$$

$$-\sqrt{(n_{j_2+2}+1)(n_{j_2+1}+1)}|\pm\alpha;i_1,i_2\rangle\langle\pm\alpha;j_1,j_2+2|\Big)$$

$$-\frac{\sqrt{(n_{j_2-1}+1)n_{j_2}}}{\lambda_1}\Big(\sqrt{(n_{i_1+1}+1)n_{i_1}}|0;i_1+1,i_2\rangle\langle 0;j_1,j_2-1|$$

$$+\sqrt{(n_{i_1-1}+1)n_{i_1}}|0;i_1-1,i_2\rangle\langle 0;j_1,j_2-1|$$

$$+\sqrt{(n_{i_2+1}+1)n_{i_2}}|0;i_1,i_2+1\rangle\langle 0;j_1,j_2-1|$$

$$+\sqrt{(n_{i_2-1}+1)n_{i_2}}|0;i_1,i_2-1\rangle\langle 0;j_1,j_2-1|$$

$$-\sqrt{n_{j_2}(n_{j_2-1}+1)}|\pm\alpha;i_1,i_2\rangle\langle\pm\alpha;j_1,j_2|$$

$$-\sqrt{(n_{j_2-2}+1)(n_{j_2-1}+1)}|\pm\alpha;i_1,i_2\rangle\langle\pm\alpha;j_1,j_2-2|\Big)\Bigg],$$

$$\frac{\partial}{\partial t}|0;i_1,i_2\rangle\langle 0;j_1,j_2| = P_0\left[H_{\text{kin}},\mathcal{L}_0^{-1}P_1\left[H_{\text{kin}},|0;i_1,i_2\rangle\langle 0;j_1,j_2|\right]\right] \tag{C.9}$$

$$= J^2 e^{-4|\alpha_0|^2}\Bigg[\frac{\sqrt{(n_{i_1+1}+1)n_{i_1}}}{\lambda_1}\Big(\sqrt{n_{i_1}(n_{i_1+1}+1)}|0;i_1,i_2\rangle\langle 0;j_1,j_2|$$

$$+\sqrt{(n_{i_1+2}+1)(n_{i_1+1}+1)}|0;i_1+2,i_2\rangle\langle 0;j_1,j_2|$$

$$+\sqrt{(n_{i_2+1}+1)n_{i_2}}|0;i_1+1,i_2+1\rangle\langle 0;j_1,j_2|$$

$$+\sqrt{(n_{i_2-1}+1)n_{i_2}}|0;i_1+1,i_2-1\rangle\langle 0;j_1,j_2|$$

$$-\sqrt{(n_{j_1+1}+1)n_{j_1}}|(-1)^{i_1+1}\alpha;i_1+1,i_2\rangle\langle(-1)^{j_1+1}\alpha;j_1+1,j_2|$$

$$-\sqrt{(n_{j_1-1}+1)n_{j_1}}|(-1)^{i_1+1}\alpha;i_1+1,i_2\rangle\langle(-1)^{j_1-1}\alpha;j_1-1,j_2|$$

$$-\sqrt{(n_{j_2+1}+1)n_{j_2}}|(-1)^{i_1+1}\alpha;i_1+1,i_2\rangle\langle(-1)^{j_2+1}\alpha;j_1,j_2+1|$$

$$-\sqrt{(n_{j_2-1}+1)n_{j_2}}|(-1)^{i_1+1}\alpha;i_1+1,i_2\rangle\langle(-1)^{j_2-1}\alpha;j_1,j_2-1|\Big)$$

$$+\frac{\sqrt{(n_{i_1-1}+1)n_{i_1}}}{\lambda_1}\Big(\sqrt{n_{i_1}(n_{i_1-1}+1)}|0;i_1,i_2\rangle\langle 0;j_1,j_2|$$

$$+\sqrt{(n_{i_1-2}+1)(n_{i_1-1}+1)}|0;i_1-2,i_2\rangle\langle 0;j_1,j_2|$$

$$+\sqrt{(n_{i_2+1}+1)n_{i_2}}|0;i_1-1,i_2+1\rangle\langle 0;j_1,j_2|$$

$$+\sqrt{(n_{i_2-1}+1)n_{i_2}}|0;i_1-1,i_2-1\rangle\langle 0;j_1,j_2|$$

$$
\begin{aligned}
&- \sqrt{(n_{j_1+1}+1)n_{j_1}}|(-1)^{i_1-1}\alpha; i_1-1, i_2\rangle\langle(-1)^{j_1+1}\alpha; j_1+1, j_2| \\
&- \sqrt{(n_{j_1-1}+1)n_{j_1}}|(-1)^{i_1-1}\alpha; i_1-1, i_2\rangle\langle(-1)^{j_1-1}\alpha; j_1-1, j_2| \\
&- \sqrt{(n_{j_2+1}+1)n_{j_2}}|(-1)^{i_1-1}\alpha; i_1-1, i_2\rangle\langle(-1)^{j_2+1}\alpha; j_1, j_2+1| \\
&- \sqrt{(n_{j_2-1}+1)n_{j_2}}|(-1)^{i_1-1}\alpha; i_1-1, i_2\rangle\langle(-1)^{j_2-1}\alpha; j_1, j_2-1|\Big) \\
&+ \frac{\sqrt{(n_{i_2+1}+1)n_{i_2}}}{\lambda_1}\Big(\sqrt{n_{i_2}(n_{i_2+1}+1)}|0; i_1, i_2\rangle\langle 0; j_1, j_2| \\
&\qquad + \sqrt{(n_{i_2+2}+1)(n_{i_2+1}+1)}|0; i_1, i_2+2\rangle\langle 0; j_1, j_2| \\
&\qquad + \sqrt{(n_{i_1+1}+1)n_{i_1}}|0; i_1+1, i_2+1\rangle\langle 0; j_1, j_2| \\
&\qquad + \sqrt{(n_{i_1-1}+1)n_{i_1}}|0; i_1-1, i_2+1\rangle\langle 0; j_1, j_2| \\
&\qquad - \sqrt{(n_{j_1+1}+1)n_{j_1}}|(-1)^{i_2+1}\alpha; i_1, i_2+1\rangle\langle(-1)^{j_1+1}\alpha; j_1+1, j_2| \\
&\qquad - \sqrt{(n_{j_1-1}+1)n_{j_1}}|(-1)^{i_2+1}\alpha; i_1, i_2+1\rangle\langle(-1)^{j_1-1}\alpha; j_1-1, j_2| \\
&\qquad - \sqrt{(n_{j_2+1}+1)n_{j_2}}|(-1)^{i_2+1}\alpha; i_1, i_2+1\rangle\langle(-1)^{j_2+1}\alpha; j_1, j_2+1| \\
&\qquad - \sqrt{(n_{j_2-1}+1)n_{j_2}}|(-1)^{i_2+1}\alpha; i_1, i_2+1\rangle\langle(-1)^{j_2-1}\alpha; j_1, j_2-1|\Big) \\
&+ \frac{\sqrt{(n_{i_2-1}+1)n_{i_2}}}{\lambda_1}\Big(\sqrt{n_{i_2}(n_{i_2-1}+1)}|0; i_1, i_2\rangle\langle 0; j_1, j_2| \\
&\qquad + \sqrt{(n_{i_2-2}+1)(n_{i_2-1}+1)}|0; i_1, i_2-2\rangle\langle 0; j_1, j_2| \\
&\qquad + \sqrt{(n_{i_1+1}+1)n_{i_1}}|0; i_1+1, i_2-1\rangle\langle 0; j_1, j_2| \\
&\qquad + \sqrt{(n_{i_1-1}+1)n_{i_1}}|0; i_1-1, i_2-1\rangle\langle 0; j_1, j_2| \\
&\qquad - \sqrt{(n_{j_1+1}+1)n_{j_1}}|(-1)^{i_2-1}\alpha; i_1, i_2-1\rangle\langle(-1)^{j_1+1}\alpha; j_1+1, j_2| \\
&\qquad - \sqrt{(n_{j_1-1}+1)n_{j_1}}|(-1)^{i_2-1}\alpha; i_1, i_2-1\rangle\langle(-1)^{j_1-1}\alpha; j_1-1, j_2| \\
&\qquad - \sqrt{(n_{j_2+1}+1)n_{j_2}}|(-1)^{i_2-1}\alpha; i_1, i_2-1\rangle\langle(-1)^{j_2+1}\alpha; j_1, j_2+1| \\
&\qquad - \sqrt{(n_{j_2-1}+1)n_{j_2}}|(-1)^{i_2-1}\alpha; i_1, i_2-1\rangle\langle(-1)^{j_2-1}\alpha; j_1, j_2-1|\Big) \\
&- \frac{\sqrt{(n_{j_1+1}+1)n_{j_1}}}{\lambda_1^*}\Big(-\sqrt{n_{j_1}(n_{j_1+1}+1)}|0; i_1, i_2\rangle\langle 0; j_1, j_2| \\
&\qquad - \sqrt{(n_{j_1+2}+1)(n_{j_1+1}+1)}|0; i_1, i_2\rangle\langle 0; j_1+2, j_2| \\
&\qquad - \sqrt{(n_{j_2+1}+1)n_{j_2}}|0; i_1, i_2\rangle\langle 0; j_1+1, j_2+1| \\
&\qquad - \sqrt{(n_{j_2-1}+1)n_{j_2}}|0; i_1, i_2\rangle\langle 0; j_1+1, j_2-1| \\
&\qquad + \sqrt{(n_{i_1+1}+1)n_{i_1}}|(-1)^{i_1+1}\alpha; i_1+1, i_2\rangle\langle(-1)^{j_1+1}\alpha; j_1+1, j_2| \\
&\qquad + \sqrt{(n_{i_1-1}+1)n_{i_1}}|(-1)^{i_1-1}\alpha; i_1-1, i_2\rangle\langle(-1)^{j_1+1}\alpha; j_1+1, j_2|
\end{aligned}
$$

$$+ \sqrt{(n_{i_2+1}+1)n_{i_2}}|(-1)^{i_2+1}\alpha; i_1, i_2+1\rangle\langle(-1)^{j_1+1}\alpha; j_1+1, j_2|$$

$$+ \sqrt{(n_{i_2-1}+1)n_{i_2}}|(-1)^{i_2-1}\alpha; i_1, i_2-1\rangle\langle(-1)^{j_1+1}\alpha; j_1+1, j_2|\Big)$$

$$- \frac{\sqrt{(n_{j_1-1}+1)n_{j_1}}}{\lambda_1^*}\Big(- \sqrt{n_{j_1}(n_{j_1-1}+1)}|0; i_1, i_2\rangle\langle0; j_1, j_2|$$

$$- \sqrt{(n_{j_1-2}+1)(n_{j_1-1}+1)}|0; i_1, i_2\rangle\langle0; j_1-2, j_2|$$

$$- \sqrt{(n_{j_2+1}+1)n_{j_2}}|0; i_1, i_2\rangle\langle0; j_1-1, j_2+1|$$

$$- \sqrt{(n_{j_2-1}+1)n_{j_2}}|0; i_1, i_2\rangle\langle0; j_1-1, j_2-1|$$

$$+ \sqrt{(n_{i_1+1}+1)n_{i_1}}|(-1)^{i_1+1}\alpha; i_1+1, i_2\rangle\langle(-1)^{j_1-1}\alpha; j_1-1, j_2|$$

$$+ \sqrt{(n_{i_1-1}+1)n_{i_1}}|(-1)^{i_1-1}\alpha; i_1-1, i_2\rangle\langle(-1)^{j_1-1}\alpha; j_1-1, j_2|$$

$$+ \sqrt{(n_{i_2+1}+1)n_{i_2}}|(-1)^{i_2+1}\alpha; i_1, i_2+1\rangle\langle(-1)^{j_1-1}\alpha; j_1-1, j_2|$$

$$+ \sqrt{(n_{i_2-1}+1)n_{i_2}}|(-1)^{i_2-1}\alpha; i_1, i_2-1\rangle\langle(-1)^{j_1-1}\alpha; j_1-1, j_2|\Big)$$

$$- \frac{\sqrt{(n_{j_2+1}+1)n_{j_2}}}{\lambda_1^*}\Big(- \sqrt{n_{j_2}(n_{j_2+1}+1)}|0; i_1, i_2\rangle\langle0; j_1, j_2|$$

$$- \sqrt{(n_{j_2+2}+1)(n_{j_2+1}+1)}|0; i_1, i_2\rangle\langle0; j_1, j_2+2|$$

$$- \sqrt{(n_{j_1+1}+1)n_{j_1}}|0; i_1, i_2\rangle\langle0; j_1+1, j_2+1|$$

$$- \sqrt{(n_{j_1-1}+1)n_{j_1}}|0; i_1, i_2\rangle\langle0; j_1-1, j_2+1|$$

$$+ \sqrt{(n_{i_1+1}+1)n_{i_1}}|(-1)^{i_1+1}\alpha; i_1+1, i_2\rangle\langle(-1)^{j_2+1}\alpha; j_1, j_2+1|$$

$$+ \sqrt{(n_{i_1-1}+1)n_{i_1}}|(-1)^{i_1-1}\alpha; i_1-1, i_2\rangle\langle(-1)^{j_2+1}\alpha; j_1, j_2+1|$$

$$+ \sqrt{(n_{i_2+1}+1)n_{i_2}}|(-1)^{i_2+1}\alpha; i_1, i_2+1\rangle\langle(-1)^{j_2+1}\alpha; j_1, j_2+1|$$

$$+ \sqrt{(n_{i_2-1}+1)n_{i_2}}|(-1)^{i_2-1}\alpha; i_1, i_2-1\rangle\langle(-1)^{j_2+1}\alpha; j_1, j_2+1|\Big)$$

$$- \frac{\sqrt{(n_{j_2-1}+1)n_{j_2}}}{\lambda_1^*}\Big(- \sqrt{n_{j_2}(n_{j_2-1}+1)}|0; i_1, i_2\rangle\langle0; j_1, j_2|$$

$$- \sqrt{(n_{j_2-2}+1)(n_{j_2-1}+1)}|0; i_1, i_2\rangle\langle0; j_1, j_2-2|$$

$$- \sqrt{(n_{j_1+1}+1)n_{j_1}}|0; i_1, i_2\rangle\langle0; j_1+1, j_2-1|$$

$$- \sqrt{(n_{j_1-1}+1)n_{j_1}}|0; i_1, i_2\rangle\langle0; j_1-1, j_2-1|$$

$$+ \sqrt{(n_{i_1+1}+1)n_{i_1}}|(-1)^{i_1+1}\alpha; i_1+1, i_2\rangle\langle(-1)^{j_2-1}\alpha; j_1, j_2-1|$$

$$+ \sqrt{(n_{i_1-1}+1)n_{i_1}}|(-1)^{i_1-1}\alpha; i_1-1, i_2\rangle\langle(-1)^{j_2-1}\alpha; j_1, j_2-1|$$

$$+ \sqrt{(n_{i_2+1}+1)n_{i_2}}|(-1)^{i_2+1}\alpha; i_1, i_2+1\rangle\langle(-1)^{j_2-1}\alpha; j_1, j_2-1|$$

$$+ \sqrt{(n_{i_2-1}+1)n_{i_2}}|(-1)^{i_2-1}\alpha; i_1, i_2-1\rangle\langle(-1)^{j_2-1}\alpha; j_1, j_2-1|\Big)\Bigg],$$

where $\lambda_1 = -\frac{2\Omega^2\Gamma}{\delta^2+\Gamma^2/4} + i\frac{4\Omega^2\delta}{\delta^2+\Gamma^2/4}$. The next step consists in deriving the equations of motion for the states $\sigma_1, ..., \sigma_6$. From this one can obtain the steady state solution to be

$$
\begin{aligned}
\rho_{k_1,k_2,\text{st}} =& \frac{1}{2}\sigma_0 + \frac{1}{4}\sigma_1, \\
=& \sum_{i_1,i_2,j_1,j_2 \text{ odd}} \sin(k_1 i_1)\sin(k_1 j_1)\sin(k_2 i_2)\sin(k_2 j_2)\sqrt{n_{i_1}n_{j_1}}|-\alpha;i_1,i_2\rangle\langle-\alpha;j_1,j_2| \\
&+ \sum_{i_1,i_2,j_1,j_2 \text{ even}} \sin(k_1 i_1)\sin(k_1 j_1)\sin(k_2 i_2)\sin(k_2 j_2)\sqrt{n_{i_1}n_{j_1}}|\alpha;i_1,i_2\rangle\langle\alpha;j_1,j_2| \\
&+ \sum_{\substack{i_1,j_1 \text{ odd} \\ i_2,j_2 \text{ even}}} \sin(k_1 i_1)\sin(k_1 j_1)\sin(k_2 i_2)\sin(k_2 j_2)\sqrt{n_{i_1}n_{j_1}}|0;i_1,i_2\rangle\langle0;j_1,j_2| \\
&+ \sum_{\substack{i_2,j_2 \text{ odd} \\ i_1,j_1 \text{ even}}} \sin(k_1 i_1)\sin(k_1 j_1)\sin(k_2 i_2)\sin(k_2 j_2)\sqrt{n_{i_1}n_{j_1}}|0;i_1,i_2\rangle\langle0;j_1,j_2|.
\end{aligned}
\tag{C.10}
$$

We observe that we obtain the same state as in Eq. (6.17) for $N = 2$, which justifies our generalization. If we trace out the photon states we obtain a fully mixed atomic sector

$$
\begin{aligned}
\text{tr}_{\text{photons}}\rho_{k_1,k_2,\text{st}} =& \frac{1}{4}(|k_1,k_2\rangle\langle k_1,k_2| + |k_1,\pi-k_2\rangle\langle k_1,\pi-k_2| \\
&+ |\pi-k_1,k_2\rangle\langle\pi-k_1,k_2| + |\pi-k_1,\pi-k_2\rangle\langle\pi-k_1,\pi-k_2|).
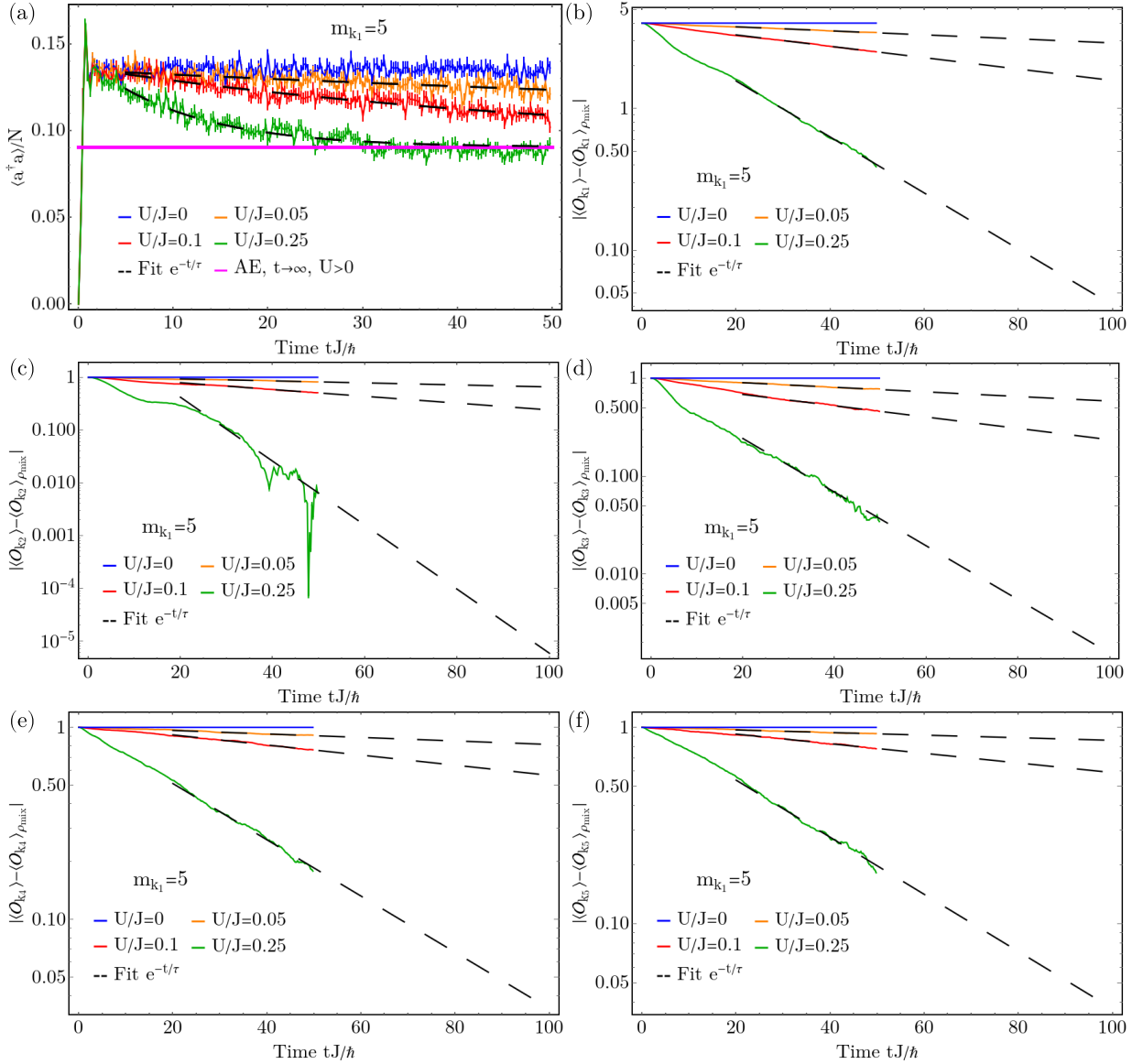\end{aligned}
\tag{C.11}
$$

C.3 Further comparisons with the numerical exact tMPS

In Figs. C.1-C.4 we present additional data complementing Fig. 6.3. We compare the many-body adiabatic elimination results taking the kinetic term as the perturbation and the numerical exact tMPS results at large dissipation strengths.

In Fig. C.1 and Fig. C.2 we show the time evolution of the scaled photon number, $\langle a^\dagger a\rangle/N$, and of the conserved quantities, $\langle\mathcal{O}_{k_j}\rangle$, for two additional symmetry sectors. The dissipation strength has been chosen large, $\hbar\Gamma/J = 15$, such that we can compare to the results of the many body adiabatic elimination with the kinetic term as the perturbation. We see a similar behavior as for the symmetry sector presented in Fig. 6.3, such that, at finite interaction, the late time behavior is nicely described by an exponential decay towards the many-body adiabatic elimination state, ρ_{mix}, given in Eq. (6.15). We perform an exponential fit for $\langle\mathcal{O}_{k_j}\rangle - \langle\mathcal{O}_{k_j}\rangle_{\rho_{\text{mix}}}$, $\propto e^{-t/\tau}$. We observe that the fit works very well in most cases supporting the decay towards the steady state ρ_{mix}. The decay time τ gives the timescale for reaching the steady state. The deviations that we see in the curves for the strongest interaction are of the order of the statistical uncertainty of the Monte Carlo sampling of the different trajectories. The timescales corresponding to Fig. C.1 are shown in Fig. 6.3, for the photon number, and in Fig. C.3, for the conserved quantities, and show the decay of $\tau \propto 1/U^2$.

In Fig. C.4, we look at the finite time value at time $tJ = 49.75\hbar$ of the scaled photon number, $\langle a^\dagger a\rangle/N$, and all conserved quantities, $\langle\mathcal{O}_{k_j}\rangle$, as a function of the interaction strength
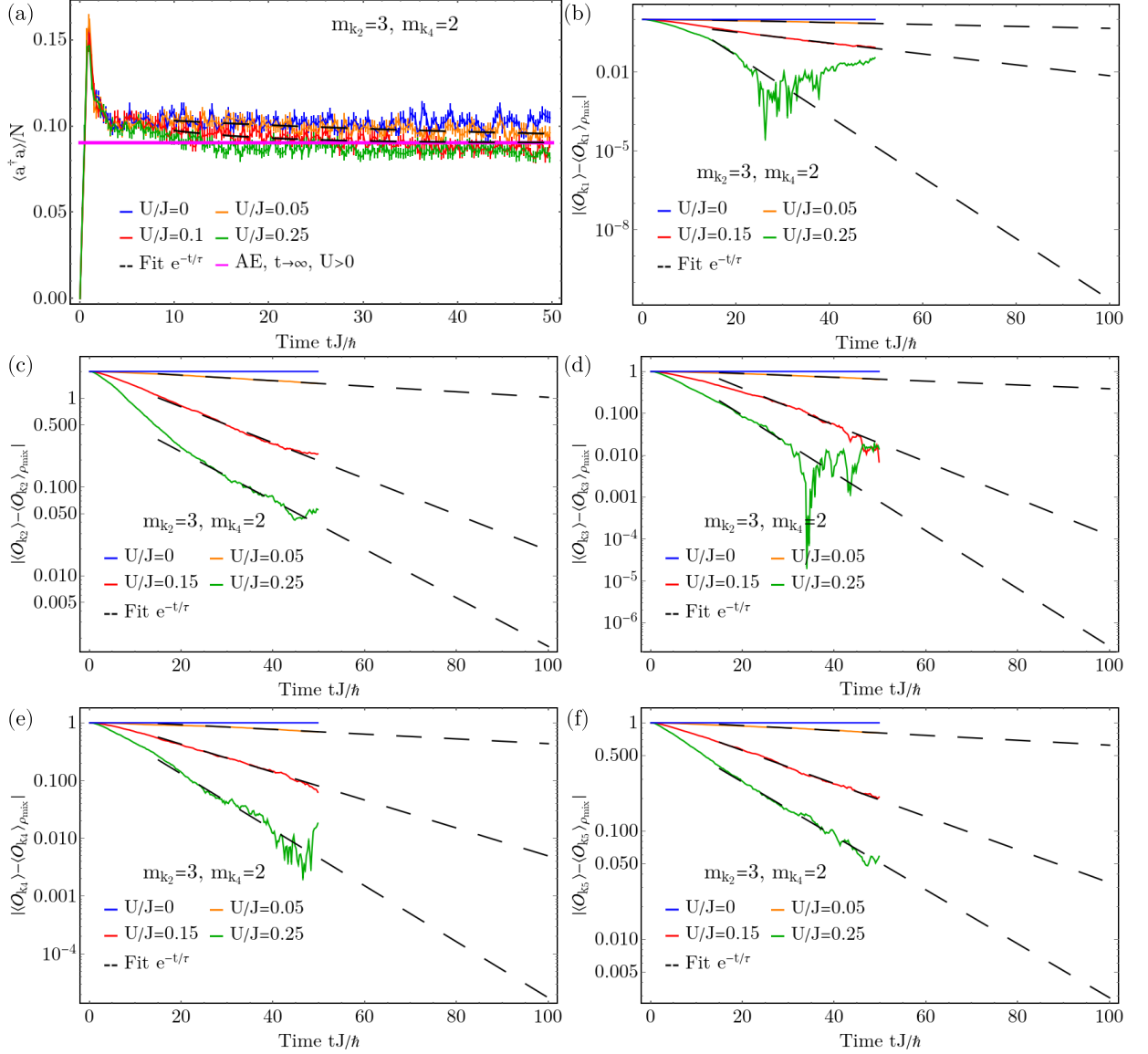
Figure C.1: The time evolution of (a) the scaled photon number, $\langle a^\dagger a\rangle/N$, and [(b)-(f)] the expectation value of $\mathcal{O}_{k_j}$ for different values of U. For finite U we fit the time evolution with an exponential decay (black dashed lines) the difference between the tMPS data and the expected steady state value, obtained from many-body adiabatic elimination. The parameters are chosen to be $L = 10$, $N = 5$, $\hbar\Omega\sqrt{N}/J = 4.47$, $\hbar\delta/J = 2$, $\Gamma/J = 15$, and the symmetry sector $(m_{k_1} = 5)$. Figure adapted from Ref. [111].

for different symmetry sectors. Part of the data presented is overlapping with the data in Fig. 6.3 (a) and (b), but here additional symmetry sectors are shown and all conserved quantities $\langle\mathcal{O}_{k_j}\rangle$.

In the presence of the strong symmetry, at $U = 0$ (marked by a dashed vertical line in Fig. C.4), we compare the tMPS results with the expectations value computed with the state $\rho_{K,st}$, Eq. (6.17), and the obtained agreement is very good in all sectors. We note that we observe that for the state $\rho_{K,st}$ the expectation of the photon number depends only on the distribution of

Figure C.2: The time evolution of (a) the scaled photon number, $\langle a^\dagger a \rangle / N$, and [(b)-(f)] the expectation value of $\mathcal{O}_{k_j}$ for different values of U. For finite U we fit the time evolution with an exponential decay (black dashed lines) the difference between the tMPS data and the expected steady state value, obtained from many-body adiabatic elimination. The parameters are chosen to be $L = 10$, $N = 5$, $\hbar\Omega\sqrt{N}/J =$ 4.47, $\hbar\delta/J = 2$, $\Gamma/J = 15$, and the symmetry sector $(m_{k_2} = 3, m_{k_4} = 2)$. Figure adapted from Ref. [111].

the particles in the single particle sectors and not the particular momentum values the particles have, i.e. the sectors $(m_{k_1} = 5)$ and $(m_{k_5} = 5)$ have the same photon number. If we look at finite interaction, we expect an agreement between the tMPS results and the state ρ_{mix}, Eq. (6.15), as we can see for $U/J \gtrsim 0.2$. The deviations at lower U we attribute to the fact that the numerical results are taken at finite time and the steady state has not yet been reached, as we can observe
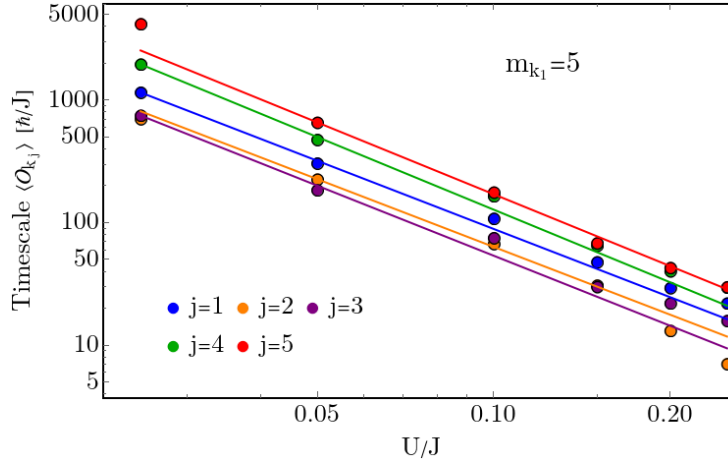
Figure C.3: The timescales obtained from the exponential fits of $\mathcal{O}_{k_j}$ as a function of U, for the data presented in Fig. C.1. The lines represent a fit of the timescale dependence on the interaction with an algebraic decay $\propto U^{-\alpha}$, we obtain the following exponents: $j = 1$, $\alpha = 1.85 \pm 0.05$; $j = 2$, $\alpha = 1.84 \pm 0.07$; $j = 3$, $\alpha = 1.90 \pm 0.09$; $j = 4$, $\alpha = 1.97 \pm 0.06$; $j = 1$, $\alpha = 1.95 \pm 0.04$. The parameters are chosen to be $L = 10$, $N = 5$, $\hbar\Omega\sqrt{N}/J = 4.47$, $\hbar\delta/J = 2$, and $\Gamma/J = 15$. Figure adapted from Ref. [111].

in Figs. C.1, C.2. This is a reasonable assumption since the exponential fit in Fig. C.1 and Fig. C.2 is approaching the correct steady state value.

C.4 Dissipative freezing

In Fig. C.5 we extend the data presented in Fig. 6.2, by plotting the expectation value of all the generators of the strong symmetry, $\langle \mathcal{O}_{k_j} \rangle$, $j = 1..5$, in time for 1000 single trajectories. We take as the initial state an equal superposition of a state from the sector $(m_{k_1} = 5)$ and the sector $(m_{k_1} = 1, m_{k_2} = 1, m_{k_3} = 1, m_{k_4} = 1, m_{k_5} = 1)$. We observe in the first column of Fig. C.5 that the phenomenon of dissipative freezing can be identified in the evolution of each of the symmetry generators, as for times $tJ \gtrsim 40\hbar$, all trajectories evolved to one of the two symmetry sectors and the Monte Carlo average of the trajectories stays constant throughout the following time-evolution. By slightly turning on the interaction and breaking the strong symmetry, as seen second column of Fig. C.5 for $U/J = 0.01$, at short and intermediate time scales the behavior of the quantum trajectories is very similar to dissipative freezing. Thus we can infer that the approximate strong symmetry still affects the short-time dynamics. When we increase the interaction even further, $U/J \geq 0.05$, the mixing of the trajectories starts earlier and the dissipative freezing effects are washed out.
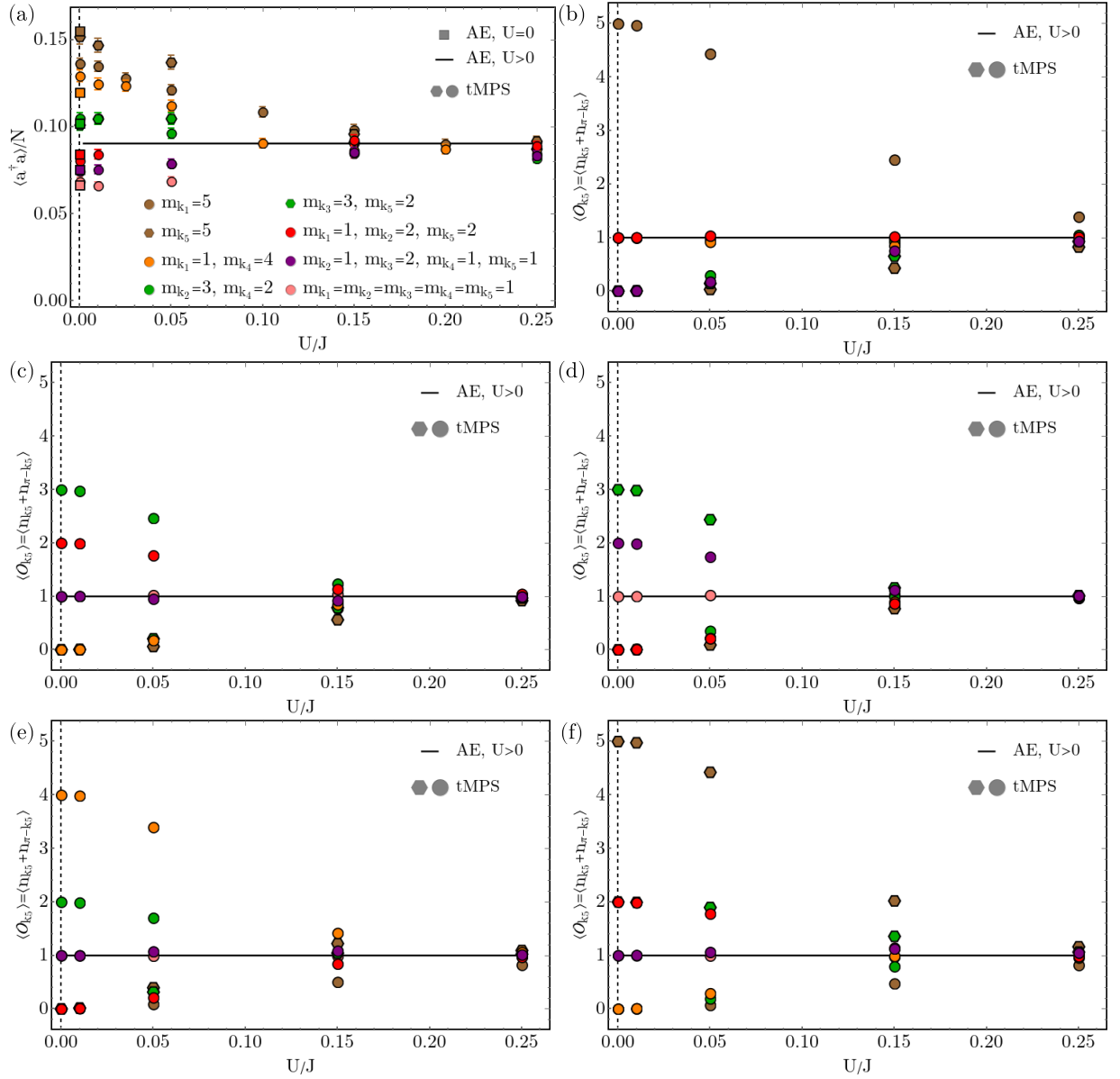
Figure C.4: The dependence on the interaction strength U of (a) the scaled photon number, $\langle a^\dagger a \rangle / N$, and [(b)-(f)] the expectation value of $\mathcal{O}_{k_j}$, $j = 1..5$ using tMPS at time $tJ = 49.75\hbar$ and many-body adiabatic elimination (AE), for different symmetry sectors. The symbols identifying each symmetry sector are consistent in all panels. The parameters are chosen to be $L = 10$, $N = 5$, $\hbar\Omega\sqrt{N}/J = 4.47$, $\hbar\delta/J = 2$, and $\Gamma/J = 15$. Figure adapted from Ref. [111].
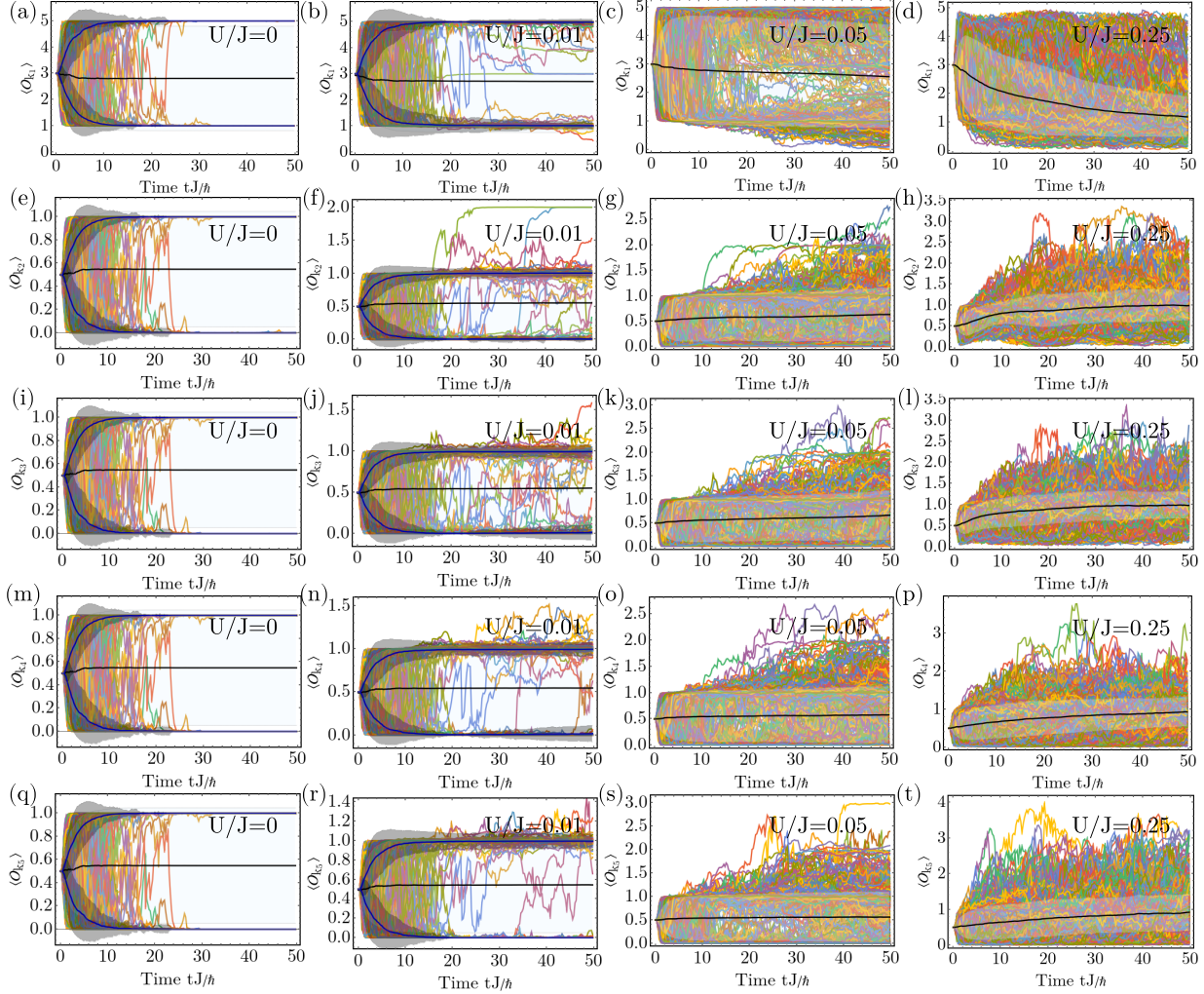
Figure C.5: Time evolution of $\mathcal{O}_k$ for the single quantum trajectories sampled in the Monte Carlo average for different interaction strengths U. The initial state consists in an equal superposition between states for the sectors $(m_{k_1} = 5)$ and $(m_{k_1} = 1, m_{k_2} = 1, m_{k_3} = 1, m_{k_4} = 1, m_{k_5} = 1)$. In each panel there are 1000 trajectories plotted, the black, or blue, curves represent the Monte Carlo average, either for the full set of trajectories, or averaged separately depending on the final value, we shade the interval of one standard deviation away from the average, with light blue for the full average and light gray for the separate averages. The parameters used are $L = 10$, $N = 5$, $\hbar\delta/J = 2$, $\hbar\Omega\sqrt{N}/J = 4.47$, and $\hbar\Gamma/J = 15$. The standard deviation is defined as $\sigma(\mathcal{O}_k(t)) = \sqrt{\frac{1}{R}\sum_{r=1}^{R}\left(\langle\psi_r(t)|\mathcal{O}_k|\psi_r(t)\rangle - \langle\langle\mathcal{O}_k\rangle\rangle\right)^2}$, where R is the total number of trajectories, $|\psi_r(t)\rangle$ the time-evolved wave function of the trajectory labeled by r and $\langle\langle\mathcal{O}_k\rangle\rangle$ the statistical average over all trajectories. Figure adapted from Ref. [111].

Appendix D

$$\text{Appendix} \quad \mathbf{D}$$

Appendix for Chapter 8

D.1 Exact spectrum of the transverse-field Ising model

In this section, we want to find the exact spectrum of $\tilde{H}_{\mathrm{TI}}$, Eq. (8.19). For this we employ the Jordan-Wigner transformation [2, 318, 319], which maps models with spin-$1/2$ degrees of freedom to spinless fermions. In order to do this, we first write $\tilde{H}_{\mathrm{TI}}$ as

$$\tilde{H}_{\mathrm{TI}} = \frac{J}{4} \sum_j \left[(1+\epsilon) \left(S_j^+ S_{j+1}^- + S_j^- S_{j+1}^+ \right) - (1-\epsilon) \left(S_j^+ S_{j+1}^+ + S_j^- S_{j+1}^- \right) \right] \tag{D.1}$$
$$- \sum_j \left[h_u + (-1)^j h_s \right] S_j^z,$$

where we used $S_j^x = \frac{1}{2} \left(S_j^+ + S_j^- \right)$ and $S_j^y = \frac{1}{2i} \left(S_j^+ - S_j^- \right)$. The Jordan-Wigner transformation is defined as

$$S_j^z = \frac{1}{2} - c_j^\dagger c_j, \tag{D.2}$$
$$S_j^+ = c_j e^{-i\pi \sum_{l=1}^{j-1} c_l^\dagger c_l},$$
$$S_j^- = e^{i\pi \sum_{l=1}^{j-1} c_l^\dagger c_l} c_j^\dagger,$$

where $c_j^\dagger$ and c_j are fermionic operators which satisfy the anticommutation rules $\{c_l, c_j^\dagger\} = \delta_{l,j}$ and $\{c_l^\dagger, c_j^\dagger\} = \{c_l, c_j\} = 0$. Using this our Hamiltonian becomes a quadratic Hamiltonian in the fermionic operators

$$\tilde{H}_{\mathrm{TI}} = \frac{J}{4} \sum_j \left[(1+\epsilon) \left(c_j^\dagger c_{j+1} + c_{j+1}^\dagger c_j \right) - (1-\epsilon) \left(c_j^\dagger c_{j+1}^\dagger + c_{j+1} c_j \right) \right] \tag{D.3}$$
$$+ \sum_j \left[h_u + (-1)^j h_s \right] \left(c_j^\dagger c_j - \frac{1}{2} \right).$$

D.1 Exact spectrum of the transverse-field Ising model

We can observe that the fermionic Hamiltonian has terms as $c_j^\dagger c_{j+1}^\dagger$ that violate the conservation of the fermion number. This implies that the total magnetization in the field direction is not conserved. Spins can be flipped in pairs under the time evolution. Thus, the eigenstates of $\tilde{H}_{\mathrm{TI}}$ will not have have a definite fermion number. But as the Hamiltonian is quadratic we can diagonalize it by going to momentum space and performing an unitary transformation. In momentum space the Hamiltonian is given by

$$\tilde{H}_{\mathrm{TI}} = \frac{J(1+\epsilon)}{4} \sum_{-\pi \leq k \leq \pi} \cos(k) c_k^\dagger c_k - \frac{J(1-\epsilon)}{4} \sum_{-\pi \leq k \leq \pi} i\sin(k) \left(c_k^\dagger c_{-k}^\dagger - c_{-k} c_k \right) \qquad (\text{D.4})$$
$$+ h_u \sum_{-\pi \leq k \leq \pi} c_k^\dagger c_k + h_s \sum_{-\pi \leq k \leq \pi} c_k^\dagger c_{k-\pi},$$

where we used the transformation $c_j = \frac{1}{\sqrt{L}} \sum_k e^{ikj} c_k$ and the the values of the momenta are $k \in \left\{ -\pi + \frac{2\pi j}{L} \mid j = 1...L-1 \right\}$. In order to properly count the operators appearing in Eq. (D.4) we need to fold our Brillouin zone such that $0 \leq k \leq \pi/2$,

$$\tilde{H}_{\mathrm{TI}} = \frac{J(1+\epsilon)}{2} \sum_{0 \leq k \leq \pi/2} \cos(k) \left(c_k^\dagger c_k + c_{-k}^\dagger c_{-k} - c_{k-\pi}^\dagger c_{k-\pi} - c_{\pi-k}^\dagger c_{\pi-k} \right) \qquad (\text{D.5})$$
$$- \frac{J(1-\epsilon)}{4} \sum_{0 \leq k \leq \pi/2} i\sin(k) \left(c_k^\dagger c_{-k}^\dagger - c_{-k}^\dagger c_k^\dagger - c_{k-\pi}^\dagger c_{\pi-k}^\dagger + c_{\pi-k}^\dagger c_{k-\pi}^\dagger \right)$$
$$- \frac{J(1-\epsilon)}{4} \sum_{0 \leq k \leq \pi/2} i\sin(k) \left(c_k c_{-k} - c_{-k} c_k - c_{k-\pi} c_{\pi-k} + c_{\pi-k} c_{k-\pi} \right)$$
$$+ h_u \sum_{0 \leq k \leq \pi/2} \left(c_k^\dagger c_k + c_{-k}^\dagger c_{-k} + c_{k-\pi}^\dagger c_{k-\pi} + c_{\pi-k}^\dagger c_{\pi-k} \right)$$
$$+ h_s \sum_{0 \leq k \leq \pi/2} \left(c_k^\dagger c_{k-\pi} + c_{-k}^\dagger c_{\pi-k} + c_{k-\pi}^\dagger c_k + c_{\pi-k}^\dagger c_{-k} \right).$$

We can recast this Hamiltonian in a matrix form as

$$\tilde{H}_{\mathrm{TI}} = \sum_{0 \leq k \leq \pi/2} \psi^\dagger M_k \psi, \qquad (\text{D.6})$$

with $\psi^\dagger = \begin{pmatrix} c_k^\dagger & c_{-k}^\dagger & c_{k-\pi}^\dagger & c_{\pi-k}^\dagger & c_k & c_{-k} & c_{k-\pi} & c_{\pi-k} \end{pmatrix}$ and the entries of the 8×8 matrix M_k taken from Eq. (D.5). As the analytically determination the eigenvalues of M_k is not an easy task, we numerically diagonalize M_k in order to obtain the dispersion relations presented in Sec. 8.5.1.

D.2 Contributions to the dynamical structure factor from excitations contained in a symmetry sector

In this section, we want to determine the contributions to the dynamical structure factor given by the excitations contained in a symmetry sector of the Hamiltonian. For this we assume that the Hamiltonian has an underlying symmetry which constrains the dynamics to different symmetry sectors and that the operators considered in the correlation function can induce transitions between these sectors. In the following we consider two such sectors of the Hamiltonian, which we will denote by s_1 and s_2. We start from Eq. (8.8)

$$S_{l_0,l}^{\alpha\beta}(q,\omega) = \frac{1}{\sqrt{N_t L}} \sum_t \sum_j e^{i(\omega t - qj)} \langle l_0 | e^{itH} S_j^\alpha e^{-itH} S_l^\beta | l_0 \rangle \tag{D.7}$$

$$= \frac{1}{\sqrt{N_t}} \sum_t e^{i\omega t} \langle l_0 | e^{itH} S^\alpha(q) e^{-itH} S_l^\beta | l_0 \rangle,$$

where $|l_0\rangle$ is an initial state from sector s_1 and $S^\alpha(q) = \frac{1}{\sqrt{L}} \sum_l e^{-iql} S_l^\alpha$. We make use of the Lehmann representation [333] by inserting the identity operators corresponding to each sector and write $S_{l_0,l}^{\alpha\beta}(q,\omega)$ as

$$S_{l_0,l}^{\alpha,\beta}(q,\omega) = \sum_{e_{s_1}} \sum_{e_{s_2}} \langle l_0 | e_{s_1} \rangle \langle e_{s_1} | S^\alpha(q) | e_{s_2} \rangle \langle e_{s_2} | S_l^\beta | l_0 \rangle \frac{1}{\sqrt{N_t}} \sum_t e^{i\omega t} e^{itE_{s_1}} e^{itE_{s_2}}, \tag{D.8}$$

where $|e_{s_1}\rangle$ are the eigenstates from sector s_1, with the corresponding eigenenergies E_{s_1}, $|e_{s_2}\rangle$ are the eigenstates from sector s_2, with the corresponding eigenenergies E_{s_2}. If we perform the sum over t we obtain a δ function for the energy

$$S_{l_0,l}^{\alpha,\beta}(q,\omega) = \sum_{e_{s_1}} \sum_{e_{s_2}} \langle l_0 | e_{s_1} \rangle \langle e_{s_1} | S^\alpha(q) | e_{s_2} \rangle \langle e_{s_2} | S_l^\beta | l_0 \rangle \delta(\omega + E_{s_1} - E_{s_2}). \tag{D.9}$$

Thus, we arrive at the expression which we use in Sec. 8.5.2 giving the contributions to the structure factor for transition between two sectors s_1 and s_2.

D.3 Additional data for two-magnon states

In Fig. D.1 we present result for a weaker staggering compared to the results presented in Sec. 8.5.2. We observe that no gaps can be distinguished in the two-magnon eigenenergies, Fig. D.1(e), and we have less states with a average distance $d < 2$, see Fig. D.1(d). This leads to a reduced weight of peaks of interest for $q = 0, \pi/2, \pi$, Fig. D.1 (a)-(c).

In contrast, in Fig. D.2 we present result for a stronger staggering compared to the results presented in Sec. 8.5.2. We observe that larger gaps can be distinguished in the two-magnon eigenenergies, Fig. D.2(e), and we have more states with a average distance $d < 2$, see Fig. D.2(d). This leads to an increased weight of the features present at high frequency in the dynamical structure factor.

In Fig. D.3 we plot the the two-magnon contribution to the dynamical structure factor,
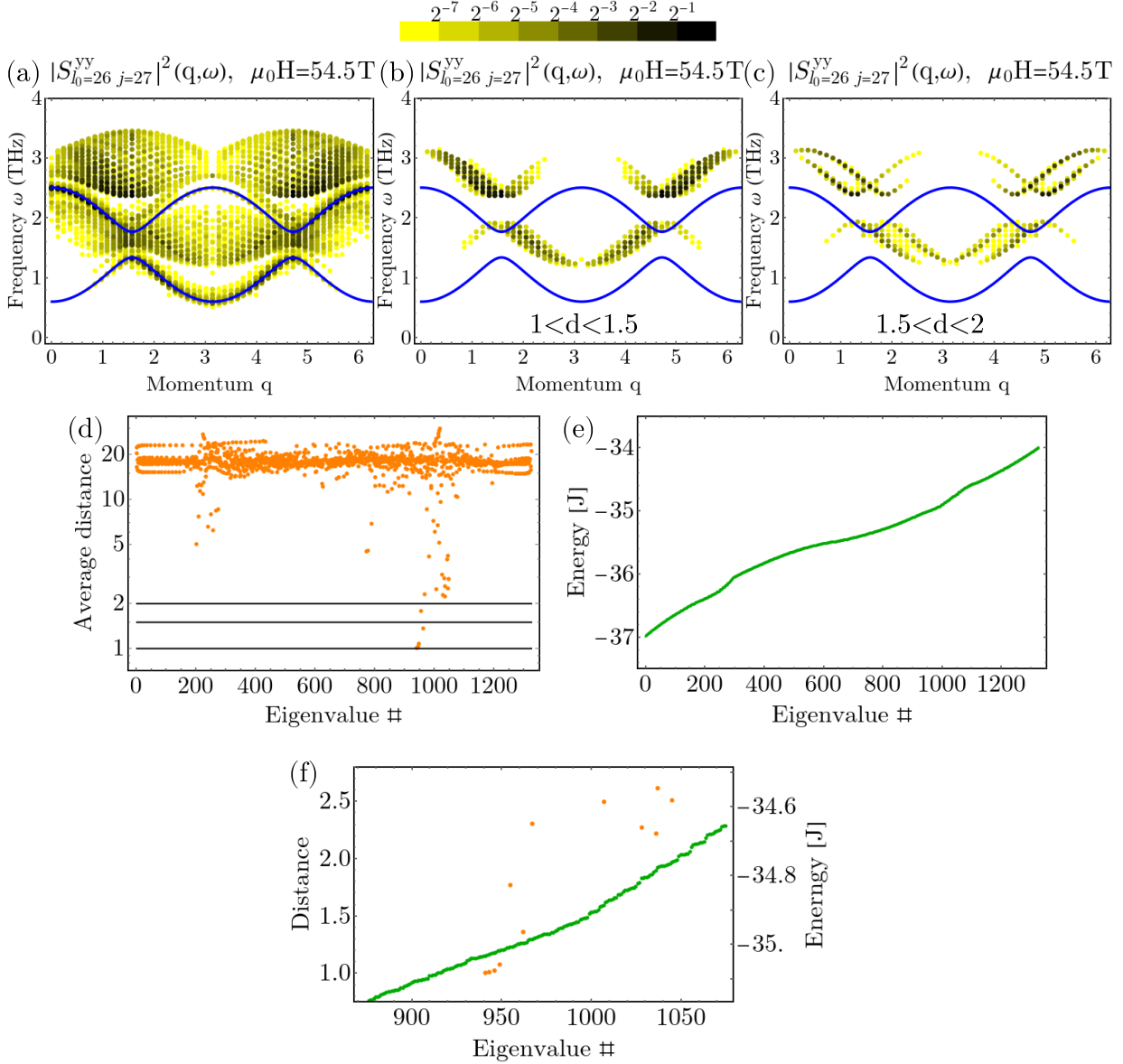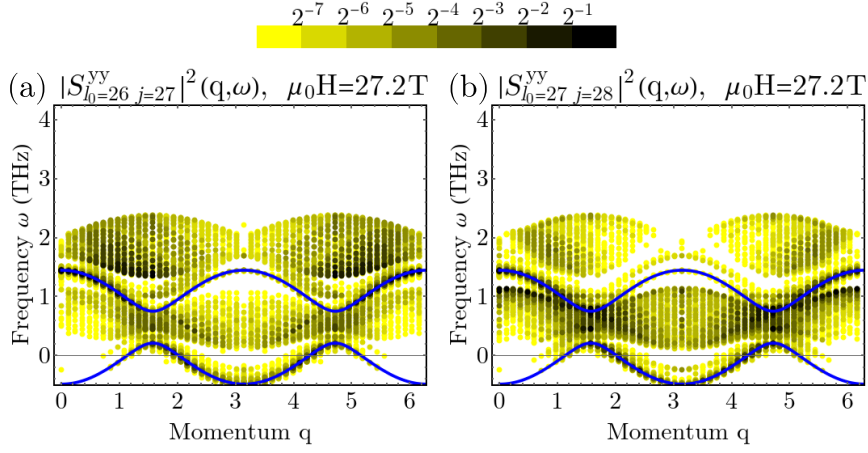
Figure D.1: (a) The two-magnon contribution to the dynamical structure factor for $l_0 = 26$ and $j = 27$ in the case of less staggering, $g^{xx} = (3.09, 2.53, 3.09, 2.53)$. (b)-(c) The contribution to the dynamical structure factor of eigenstates with an average distance between the magnon of (b) $1 \leq d < 1.5$, (c) $1.5 \leq d < 2$. The blue line corresponds to the single magnon dispersion, Eq. (8.28). We note that the color scale of the plotted points is logarithmic. (d) The average value of the distance between the two magnons for the computed two-magnon eigenstates in a semi-log plot. The black horizontal lines are a guide to the eye for distance 1, 1.5 and 2. (e) The energies of the two-magnon eigenstates, we can identify four distinct bands separated by gaps. (f) The behavior of the energy and the average distance between the magnons. The results where obtained in the ground state for the following parameters $\mu_0 H = 54.5$T, $L = 52$, $\epsilon = 0.46$, $J = 61 k_B$.
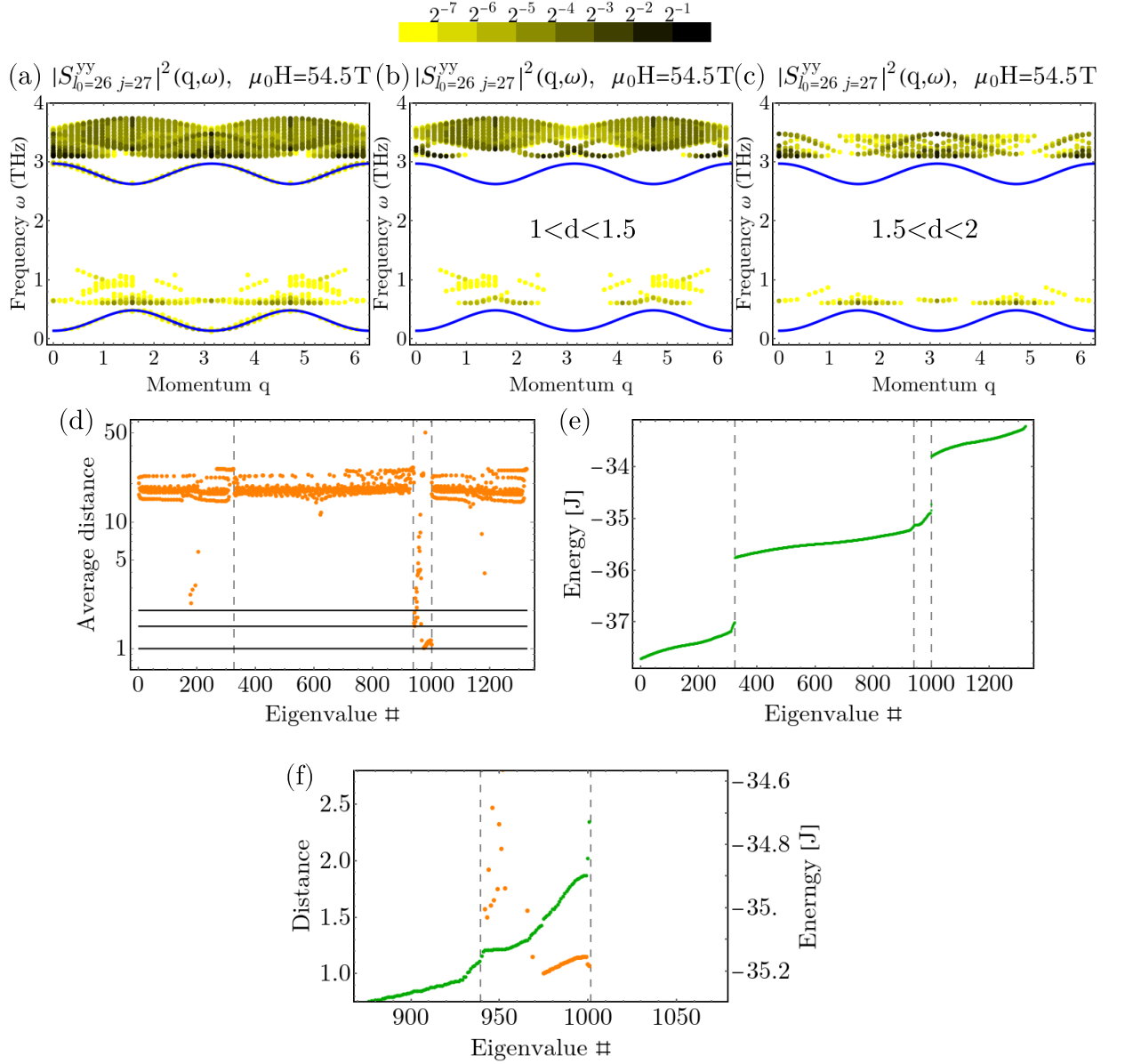
Figure D.2: (a) The two-magnon contribution to the dynamical structure factor for $l_0 = 26$ and $j = 27$ in the case of stronger staggering, $g^{xx} = (4.21, 1.4, 4.21, 1.4)$. (b)-(c) The contribution to the dynamical structure factor of eigenstates with an average distance between the magnon of (b) $1 \leq d < 1.5$, (c) $1.5 \leq d < 2$. The blue line corresponds to the single magnon dispersion, Eq. (8.28). We note that the color scale of the plotted points is logarithmic. (d) The average value of the distance between the two magnons for the computed two-magnon eigenstates in a semi-log plot. The black horizontal lines are a guide to the eye for distance 1, 1.5 and 2. The dashed vertical lines mark the two-magnon bands separated by gaps. (e) The energies of the two-magnon eigenstates, we can identify four distinct bands separated by gaps. (f) The behavior of the energy and the average distance between the magnons around the third band. The results where obtained in the ground state for the following parameters $\mu_0 H = 54.5\text{T}$, $L = 52$, $\epsilon = 0.46$, $J = 61 k_B$.

D.3 Additional data for two-magnon states

Figure D.3: The two-magnon contribution to the dynamical structure factor, Eq. (8.29), for $\mu_0 H = 27.2$T and $l_0 \in \{26, 27\}$, we take $j = l_0 + 1$. The blue line corresponds to the single magnon dispersion, Eq. (8.28). We note that the color scale of the plotted points is logarithmic. The results where obtained in the ground state for the following parameters, $L = 52$, $g_1 = 3.5$, $g_2 = 6.1$, $g_3 = 2.1$, $\theta = 5°$, $\epsilon = 0.46$, $J = 61k_B$.

Eq. (8.29), for a magnetic field value $m_0 H = 27.2$ T, lower than the critical field. In this regime the approximations employed in the derivation of $\tilde{H}_{\text{magnon}}$, Eq. (8.22), are no longer justified. But as most high frequency modes in the numerical data for the full Hamiltonian, Eq (8.2), and in the experimental data seem to have a smooth behavior across the phase transition, we perform exact diagonalization in the subspaces with a fixed number of magnons also at lower field to extract the position of the high frequency peaks. We can see in Fig. D.3 that the high frequency features resemble well the ones obtained in Fig. 8.8.

List of Tables

List of Figures

List of Figures

Bibliography

[1] D. N. Basov, R. D. Averitt, and D. Hsieh. Towards properties on demand in quantum materials. *Nature Materials*, 16(11):1077–1088, Nov 2017.

[2] S. Sachdev. *Quantum phase transition*. Cambridge University Press, 1999.

[3] Piers Coleman and Andrew J. Schofield. Quantum criticality. *Nature*, 433(7023):226–229, Jan 2005.

[4] S. Gerber, H. Jang, H. Nojiri, S. Matsuzawa, H. Yasumura, D. A. Bonn, R. Liang, W. N. Hardy, Z. Islam, A. Mehta, S. Song, M. Sikorski, D. Stefanescu, Y. Feng, S. A. Kivelson, T. P. Devereaux, Z.-X. Shen, C.-C. Kao, W.-S. Lee, D. Zhu, and J.-S. Lee. Three-dimensional charge density wave order in YBa2Cu3O6.67 at high magnetic fields. *Science*, 350(6263):949–952, 2015.

[5] Quentin Faure, Shintaro Takayoshi, Sylvain Petit, Virginie Simonet, Stéphane Raymond, Louis-Pierre Regnault, Martin Boehm, Jonathan S. White, Martin Månsson, Christian Rüegg, Pascal Lejay, Benjamin Canals, Thomas Lorenz, Shunsuke C. Furuya, Thierry Giamarchi, and Béatrice Grenier. Topological quantum phase transition in the Ising-like antiferromagnetic spin chain BaCo2V2O8. *Nature Physics*, 14(7):716–722, Jul 2018.

[6] Zhe Wang, Jianda Wu, Wang Yang, Anup Kumar Bera, Dmytro Kamenskyi, A. T. M. Nazmul Islam, Shenglong Xu, Joseph Matthew Law, Bella Lake, Congjun Wu, and Alois Loidl. Experimental observation of Bethe strings. *Nature*, 554(7691):219–223, Feb 2018.

[7] Zhe Wang, T. Lorenz, D. I. Gorbunov, P. T. Cong, Y. Kohama, S. Niesen, O. Breunig, J. Engelmayer, A. Herman, Jianda Wu, K. Kindo, J. Wosnitza, S. Zherlitsyn, and A. Loidl. Quantum Criticality of an Ising-like Spin-$1/2$ Antiferromagnetic Chain in a Transverse Magnetic Field. *Phys. Rev. Lett.*, 120:207205, May 2018.

[8] Yoshinori Tokura, Masashi Kawasaki, and Naoto Nagaosa. Emergent functions of quantum materials. *Nature Physics*, 13(11):1056–1068, Nov 2017.

[9] Takashi Oka and Hideo Aoki. Photovoltaic Hall effect in graphene. *Phys. Rev. B*, 79:081406, Feb 2009.

[10] Jun-ichi Inoue and Akihiro Tanaka. Photoinduced Transition between Conventional and Topological Insulators in Two-Dimensional Electronic Systems. *Phys. Rev. Lett.*, 105:017401, Jun 2010.

[11] N.H. Lindner, G. Refael, and V. Galitski. Floquet topological insulator in semiconductor quantum wells. *Nature Physics*, 7:490, 2011.

[12] M. Nuske, L. Broers, B. Schulte, G. Jotzu, S. A. Sato, A. Cavalleri, A. Rubio, J. W. McIver, and L. Mathey. Floquet dynamics in light-driven solids. *Phys. Rev. Research*, 2:043408, Dec 2020.

[13] A. de la Torre, D. M. Kennes, M. Claassen, S. Gerber, J. W. McIver, and M. A. Sentef. Nonthermal pathways to ultrafast control in quantum materials. *arXiv:2103.14888*, 2021.

[14] Kankan Cong, Qi Zhang, Yongrui Wang, G. Timothy Noe, Alexey Belyanin, and Junichiro Kono. Dicke superradiance in solids. *J. Opt. Soc. Am. B*, 33(7):C80–C101, Jul 2016.

Bibliography

[15] Anton Frisk Kockum, Adam Miranowicz, Simone De Liberato, Salvatore Savasta, and Franco Nori. Ultrastrong coupling between light and matter. *Nature Reviews Physics*, 1(1):19–40, Jan 2019.

[16] P. Forn-Díaz, L. Lamata, E. Rico, J. Kono, and E. Solano. Ultrastrong coupling regimes of light-matter interaction. *Rev. Mod. Phys.*, 91:025005, Jun 2019.

[17] Yuto Ashida, Ata ç İmamoğlu, Jérôme Faist, Dieter Jaksch, Andrea Cavalleri, and Eugene Demler. Quantum Electrodynamic Control of Matter: Cavity-Enhanced Ferroelectric Phase Transition. *Phys. Rev. X*, 10:041027, Nov 2020.

[18] M. Först, C. Manzoni, S. Kaiser, Y. Tomioka, Y. Tokura, R. Merlin, and A. Cavalleri. Nonlinear phononics as an ultrafast route to lattice control. *Nature Physics*, 7(11):854–856, Nov 2011.

[19] Alaska Subedi, Andrea Cavalleri, and Antoine Georges. Theory of nonlinear phononics for coherent light control of solids. *Phys. Rev. B*, 89:220301, Jun 2014.

[20] M. Mitrano, A. Cantaluppi, D. Nicoletti, S. Kaiser, A. Perucchi, S. Lupi, P. Di Pietro, D. Pontiroli, M. Riccò, S. R. Clark, D. Jaksch, and A. Cavalleri. Possible light-induced superconductivity in K3C60 at high temperature. *Nature*, 530(7591):461–464, Feb 2016.

[21] B. Liu, M. Först, M. Fechner, D. Nicoletti, J. Porras, T. Loew, B. Keimer, and A. Cavalleri. Pump Frequency Resonances for Light-Induced Incipient Superconductivity in $YBa_2Cu_3O_{6.5}$. *Phys. Rev. X*, 10:011053, Mar 2020.

[22] Richard P. Feynman. Simulating physics with computers. *International Journal of Theoretical Physics*, 21(6):467–488, Jun 1982.

[23] I. M. Georgescu, S. Ashhab, and Franco Nori. Quantum simulation. *Rev. Mod. Phys.*, 86:153–185, Mar 2014.

[24] Ehud Altman, Kenneth R. Brown, Giuseppe Carleo, Lincoln D. Carr, Eugene Demler, Cheng Chin, Brian DeMarco, Sophia E. Economou, Mark A. Eriksson, Kai-Mei C. Fu, Markus Greiner, Kaden R.A. Hazzard, Randall G. Hulet, Alicia J. Kollár, Benjamin L. Lev, Mikhail D. Lukin, Ruichao Ma, Xiao Mi, Shashank Misra, Christopher Monroe, Kater Murch, Zaira Nazario, Kang-Kuen Ni, Andrew C. Potter, Pedram Roushan, Mark Saffman, Monika Schleier-Smith, Irfan Siddiqi, Raymond Simmonds, Meenakshi Singh, I.B. Spielman, Kristan Temme, David S. Weiss, Jelena Vucković, Vladan Vuletić, Jun Ye, and Martin Zwierlein. Quantum Simulators: Architectures and Opportunities. *PRX Quantum*, 2:017003, Feb 2021.

[25] M. H. Anderson, J. R. Ensher, M. R. Matthews, C. E. Wieman, and E. A. Cornell. Observation of Bose-Einstein condensation in a dilute atomic vapor. *Science*, 269(0):198, 1995.

[26] K. B. Davis, M. O. Mewes, M. R. Andrews, N. J. van Druten, D. S. Durfee, D. M. Kurn, and W. Ketterle. Bose-Einstein Condensation in a Gas of Sodium Atoms. *Phys. Rev. Lett.*, 75:3969–3973, Nov 1995.

[27] B. DeMarco and D. S. Jin. Onset of Fermi Degeneracy in a Trapped Atomic Gas. *Science*, 285(5434):1703–1706, 1999.

[28] Maciej Lewenstein, Anna Sanpera, Veronica Ahufinger, Bogdan Damski, Aditi Sen(De),

and Ujjwal Sen. Ultracold atomic gases in optical lattices: mimicking condensed matter physics and beyond. *Advances in Physics*, 56(2):243–379, 2007.

[29] Immanuel Bloch, Jean Dalibard, and Wilhelm Zwerger. Many-body physics with ultra-cold gases. *Rev. Mod. Phys.*, 80:885, 2008.

[30] J. Ignacio Cirac and Peter Zoller. Goals and opportunities in quantum simulation. *Nature Physics*, 8(4):264–266, Apr 2012.

[31] Simon Braun, Mathis Friesdorf, Sean S. Hodgman, Michael Schreiber, Jens Philipp Ronzheimer, Arnau Riera, Marco del Rey, Immanuel Bloch, Jens Eisert, and Ulrich Schneider. Emergence of coherence and the dynamics of quantum phase transitions. *Proceedings of the National Academy of Sciences*, 112(12):3641–3646, 2015.

[32] W Hofstetter and T Qin. Quantum simulation of strongly correlated condensed matter systems. *Journal of Physics B: Atomic, Molecular and Optical Physics*, 51(8):082001, 2018.

[33] Florian Schäfer, Takeshi Fukuhara, Seiji Sugawa, Yosuke Takasu, and Yoshiro Takahashi. Tools for quantum simulation with ultracold atoms in optical lattices. *Nature Reviews Physics*, 2(8):411–425, Aug 2020.

[34] M. Greiner, O. Mandel, T. Esslinger, T. W. Hänsch, and I. Bloch. Quantum phase transition from a superfluid to a Mott insulator in a gas of ultracold atoms. *Nature*, 415:39, 2002.

[35] J. K. Freericks and H. Monien. Phase diagram of the Bose-Hubbard Model. *Europhys. Lett.*, 26(7):551–556, 1994.

[36] T. D. Kühner and H. Monien. Phases of the one-dimensional Bose-Hubbard model. *Phys. Rev. B*, 58(22):14741, 1998.

[37] Jean Dalibard, Fabrice Gerbier, Gediminas Juzeliūnas, and Patrik Öhberg. Colloquium. *Rev. Mod. Phys.*, 83:1523–1543, Nov 2011.

[38] Nathan Goldman, G Juzeliūnas, Patrik Öhberg, and Ian B Spielman. Light-induced gauge fields for ultracold atoms. *Reports on Progress in Physics*, 77(12):126401, 2014.

[39] N. Goldman, J. C. Budich, and P. Zoller. Topological quantum matter with ultracold gases in optical lattices. *Nature Physics*, 12(7):639–645, Jul 2016.

[40] M. Greiner, O. Mandel, T. W. Hänsch, and I. Bloch. Collapse and revival of the matter wave field of a Bose-Einstein condensate. *Nature*, 419:51, 2002.

[41] W. S. Bakr, A. Peng, M. E. Tai, R. Ma, J. Simon, J. I. Gillen, S. Fölling, L. Pollet, and M. Greiner. Probing the Superfluid–to–Mott Insulator Transition at the Single-Atom Level. *Science*, 329(5991):547–550, 2010.

[42] David Chen, Matthew White, Cecilia Borries, and Brian DeMarco. Quantum Quench of an Atomic Mott Insulator. *Phys. Rev. Lett.*, 106:235304, Jun 2011.

[43] S. Trotzky, Y.-A. Chen, A. Flesch, I. P. McCulloch, U. Schollwöck, J. Eisert, and I. Bloch. Probing the relaxation towards equilibrium in an isolated strongly correlated one-dimensional Bose gas. *Nature Physics*, 8(4):325–330, Apr 2012.

[44] M. Cheneau, P. Barmettler, D. Poletti, M. Endres, P. Schauß, T. Fukuhara, C. Gross, I. Bloch, C. Kollath, and S. Kuhr. Light-cone-like spreading of correlations in a quantum many-body system. *Nature*, 481:484, 2012.

Bibliography

[45] Ulrich Schneider, Lucia Hackermüller, Jens Philipp Ronzheimer, Sebastian Will, Simon Braun, Thorsten Best, Immanuel Bloch, Eugene Demler, Stephan Mandt, David Rasch, and Achim Rosch. Fermionic transport and out-of-equilibrium dynamics in a homogeneous Hubbard model with ultracold atoms. *Nature Physics*, 8(3):213–218, Mar 2012.

[46] T. Esslinger. Fermi-Hubbard physics with atoms in an optical lattice. *Annual Revies of Condensed Matter Physics*, 1:129, 2010.

[47] Immanuel Bloch, Jean Dalibard, and Sylvain Nascimbène. Quantum simulations with ultracold quantum gases. *Nature Physics*, 8(4):267–276, Apr 2012.

[48] Abigail Klopper. Topics in non-equilibrium physics. *Nature Physics*, 11(2):103–103, Feb 2015.

[49] C. Kollath, A.M. Läuchli, and E. Altman. Quench dynamics and non-equilibrium phase diagram of the Bose-Hubbard model. *Phys. Rev. Lett.*, 98:180601, 2007.

[50] Frank Verstraete, Michael M. Wolf, and J. Ignacio Cirac. Quantum computation and quantum-state engineering driven by dissipation. *Nature Physics*, 5:633, 2009.

[51] Hendrik Weimer, Markus Müller, Igor Lesanovsky, Peter Zoller, and Hans Peter Büchler. A Rydberg quantum simulator. *Nature Physics*, 6(5):382–388, May 2010.

[52] Julio T. Barreiro, Markus Müller, Philipp Schindler, Daniel Nigg, Thomas Monz, Michael Chwalla, Markus Hennrich, Christian F. Roos, Peter Zoller, and Rainer Blatt. An open-system quantum simulator with trapped ions. *Nature*, 470:486, 2010.

[53] M. Müller, S. Diehl, G. Pupillo, and P. Zoller. Engineered Open Systems and Quantum Simulations with Atoms and Ions. *Advances in Atomic, Molecular, and Optical Physics*, 61:1–80, 2012.

[54] D. A. Lidar, I. L. Chuang, and K. B. Whaley. Decoherence-Free Subspaces for Quantum Computation. *Phys. Rev. Lett.*, 81:2594–2597, Sep 1998.

[55] Daniel A. Lidar and K. Birgitta Whaley. *Decoherence-Free Subspaces and Subsystems*, pages 83–120. Springer Berlin Heidelberg, Berlin, Heidelberg, 2003.

[56] H. P. Breuer and F. Petruccione. *The theory of open quantum systems*. Oxford University Press, Oxford, 2002.

[57] Sebastian Diehl, Enrique Rico, Mikhail A. Baranov, and Peter Zoller. Topology by dissipation in atomic quantum wires. *Nature Physics*, 7(12):971–977, Dec 2011.

[58] C-E Bardyn, M A Baranov, C V Kraus, E Rico, A İmamoğlu, P Zoller, and S Diehl. Topology by dissipation. *New Journal of Physics*, 15(8):085001, aug 2013.

[59] Jan Carl Budich, Peter Zoller, and Sebastian Diehl. Dissipative preparation of Chern insulators. *Phys. Rev. A*, 91:042117, Apr 2015.

[60] Fernando Iemini, Davide Rossini, Rosario Fazio, Sebastian Diehl, and Leonardo Mazza. Dissipative topological superconductors in number-conserving systems. *Phys. Rev. B*, 93:115113, Mar 2016.

[61] Ameneh Sheikhan, Ferdinand Brennecke, and Corinna Kollath. Cavity-induced generation of nontrivial topological states in a two-dimensional Fermi gas. *Phys. Rev. A*, 94:061603, Dec 2016.

[62] Zongping Gong, Sho Higashikawa, and Masahito Ueda. Zeno Hall Effect. *Phys. Rev. Lett.*, 118:200401, May 2017.

[63] Moshe Goldstein. Dissipation-induced topological insulators: A no-go theorem and a recipe. *SciPost Phys.*, 7:67, 2019.

[64] Hendrik Weimer, Augustine Kshetrimayum, and Román Orús. Simulation methods for open quantum many-body systems. *Rev. Mod. Phys.*, 93:015008, Mar 2021.

[65] Helmut Ritsch, Peter Domokos, Ferdinand Brennecke, and Tilman Esslinger. Cold atoms in cavity-generated dynamical optical potentials. *Rev. Mod. Phys.*, 85:553–601, Apr 2013.

[66] Farokh Mivehvar, Francesco Piazza, Tobias Donner, and Helmut Ritsch. Cavity QED with Quantum Gases: New Paradigms in Many-Body Physics. *arXiv:2102.04473*, 2021.

[67] K. Baumann, C. Guerlin, F. Brennecke, and T. Esslinger. Dicke quantum phase transition with a superfluid gas in an optical cavity. *Nature*, 464:1301, 2010.

[68] Igor B Mekhov and Helmut Ritsch. Quantum optics with ultracold quantum gases: towards the full quantum regime of the light–matter interaction. *Journal of Physics B: Atomic, Molecular and Optical Physics*, 45(10):102001, 2012.

[69] Wei Jiang, Wu Ming Liu, and Heng Fan. Exciton condensation in cavity quantum electrodynamics. *Journal of Physics B: Atomic, Molecular and Optical Physics*, 44(5):055302, 2011.

[70] J. Klinder, H. Keßler, M. Reza Bakhtiari, M. Thorwart, and A. Hemmerich. Observation of a Superradiant Mott Insulator in the Dicke-Hubbard Model. *Phys. Rev. Lett.*, 115:230403, Dec 2015.

[71] Renate Landig, Lorenz Hruby, Nishant Dogra, Manuele Landini, Rafael Mottl, Tobias Donner, and Tilman Esslinger. Quantum phases from competing short- and long-range interactions in an optical lattice. *Nature*, 532(7600):476–479, Apr 2016. Letter.

[72] Lorenz Hruby, Nishant Dogra, Manuele Landini, Tobias Donner, and Tilman Esslinger. Metastability and avalanche dynamics in strongly correlated gases with long-range interactions. *Proceedings of the National Academy of Sciences*, 115(13):3279–3284, 2018.

[73] Xiangliang Li, Davide Dreon, Philip Zupancic, Alexander Baumgärtner, Andrea Morales, Wei Zheng, Nigel R. Cooper, Tobias Donner, and Tilman Esslinger. First order phase transition between two centro-symmetric superradiant crystals. *Phys. Rev. Research*, 3:L012024, Mar 2021.

[74] Farokh Mivehvar, Helmut Ritsch, and Francesco Piazza. Cavity-Quantum-Electrodynamical Toolbox for Quantum Magnetism. *Phys. Rev. Lett.*, 122:113603, Mar 2019.

[75] S Ostermann, H-W Lau, H Ritsch, and F Mivehvar. Cavity-induced emergent topological spin textures in a Bose–Einstein condensate. *New Journal of Physics*, 21(1):013029, jan 2019.

[76] Martin Kiffner, Jonathan R. Coulthard, Frank Schlawin, Arzhang Ardavan, and Dieter Jaksch. Manipulating quantum materials with quantum light. *Phys. Rev. B*, 99:085116, Feb 2019.

Bibliography

[77] Frank Schlawin, Andrea Cavalleri, and Dieter Jaksch. Cavity-Mediated Electron-Photon Superconductivity. *Phys. Rev. Lett.*, 122:133602, Apr 2019.

[78] Corinna Kollath, Ameneh Sheikhan, Stefan Wolff, and Ferdinand Brennecke. Ultracold Fermions in a Cavity-Induced Artificial Magnetic Field. *Phys. Rev. Lett.*, 116:060401, Feb 2016.

[79] Stefan Wolff, Ameneh Sheikhan, and Corinna Kollath. Dissipative time evolution of a chiral state after a quantum quench. *Phys. Rev. A*, 94:043609, Oct 2016.

[80] A. Sheikhan, F. Brennecke, and C. Kollath. Cavity-induced chiral states of fermionic quantum gases. *Phys. Rev. A*, 93:043609, 2016.

[81] W. Zheng and N. R. Cooper. Superradiance Induced Particle Flow via Dynamical Gauge Coupling. *Phys. Rev. Lett.*, 117:175302, Oct 2016.

[82] Kyle E. Ballantine, Benjamin L. Lev, and Jonathan Keeling. Meissner-like Effect for a Synthetic Gauge Field in Multimode Cavity QED. *Phys. Rev. Lett.*, 118:045302, Jan 2017.

[83] Catalin-Mihai Halati, Ameneh Sheikhan, and Corinna Kollath. Cavity-induced artificial gauge field in a Bose-Hubbard ladder. *Phys. Rev. A*, 96:063621, Dec 2017.

[84] Farokh Mivehvar, Helmut Ritsch, and Francesco Piazza. Superradiant Topological Peierls Insulator inside an Optical Cavity. *Phys. Rev. Lett.*, 118:073602, Feb 2017.

[85] Elvia Colella, Farokh Mivehvar, Francesco Piazza, and Helmut Ritsch. Hofstadter butterfly in a cavity-induced dynamic synthetic magnetic field. *Phys. Rev. B*, 100:224306, Dec 2019.

[86] M. Landini, N. Dogra, K. Kroeger, L. Hruby, T. Donner, and T. Esslinger. Formation of a Spin Texture in a Quantum Gas Coupled to a Cavity. *Phys. Rev. Lett.*, 120:223602, May 2018.

[87] Ronen M. Kroeze, Yudan Guo, Varun D. Vaidya, Jonathan Keeling, and Benjamin L. Lev. Spinor Self-Ordering of a Quantum Gas in a Cavity. *Phys. Rev. Lett.*, 121:163601, Oct 2018.

[88] Farokh Mivehvar, Francesco Piazza, and Helmut Ritsch. Disorder-Driven Density and Spin Self-Ordering of a Bose-Einstein Condensate in a Cavity. *Phys. Rev. Lett.*, 119:063602, Aug 2017.

[89] Nishant Dogra, Manuele Landini, Katrin Kroeger, Lorenz Hruby, Tobias Donner, and Tilman Esslinger. Dissipation-induced structural instability and chiral dynamics in a quantum gas. *Science*, 366(6472):1496–1499, 2019.

[90] E. I. Rodríguez Chiacchio and A. Nunnenkamp. Dissipation-Induced Instabilities of a Spinor Bose-Einstein Condensate Inside an Optical Cavity. *Phys. Rev. Lett.*, 122:193605, May 2019.

[91] Berislav Buca and Dieter Jaksch. Dissipation Induced Nonstationarity in a Quantum Gas. *Phys. Rev. Lett.*, 123:260401, Dec 2019.

[92] Ronen M. Kroeze, Yudan Guo, and Benjamin L. Lev. Dynamical Spin-Orbit Coupling of a Quantum Gas. *Phys. Rev. Lett.*, 123:160404, Oct 2019.

[93] Catalin-Mihai Halati, Ameneh Sheikhan, and Corinna Kollath. Cavity-induced spin-orbit coupling in an interacting bosonic wire. *Phys. Rev. A*, 99:033604, Mar 2019.

[94] Francesco Piazza and Helmut Ritsch. Self-Ordered Limit Cycles, Chaos, and Phase Slippage with a Superfluid inside an Optical Resonator. *Phys. Rev. Lett.*, 115:163601, Oct 2015.

[95] Jayson G. Cosme, Christoph Georges, Andreas Hemmerich, and Ludwig Mathey. Dynamical Control of Order in a Cavity-BEC System. *Phys. Rev. Lett.*, 121:153001, Oct 2018.

[96] Hans Keßler, Jayson G. Cosme, Michal Hemmerling, Ludwig Mathey, and Andreas Hemmerich. Emergent limit cycles and time crystal dynamics in an atom-cavity system. *Phys. Rev. A*, 99:053605, May 2019.

[97] P. Zupancic, D. Dreon, X. Li, A. Baumgärtner, A. Morales, W. Zheng, N. R. Cooper, T. Esslinger, and T. Donner. P-Band Induced Self-Organization and Dynamics with Repulsively Driven Ultracold Atoms in an Optical Cavity. *Phys. Rev. Lett.*, 123:233601, Dec 2019.

[98] Hans Keßler, Jayson G Cosme, Christoph Georges, Ludwig Mathey, and Andreas Hemmerich. From a continuous to a discrete time crystal in a dissipative atom-cavity system. *New Journal of Physics*, 22(8):085002, 2020.

[99] Hans Keßler, Phatthamon Kongkhambut, Christoph Georges, Ludwig Mathey, Jayson G. Cosme, and Andreas Hemmerich. Observation of a dissipative time crystal. *arXiv:2012.08885*, 2021.

[100] C. Maschler, I. B. Mekhov, and H. Ritsch. Ultracold atoms in optical lattices generated by quantized light fields. *The European Physical Journal D*, 46(3):545–560, 2008.

[101] G. Szirmaia D. Nagy and P. Domokos. Self-organization of a Bose-Einstein condensate in an optical cavity. *Eur. Phys. J. D*, 48:127, 2008.

[102] András Vukics, Christoph Maschler, and Helmut Ritsch. Microscopic physics of quantum self-organization of optical lattices in cavities. *New Journal of Physics*, 9(8):255–255, aug 2007.

[103] Christoph Maschler, Helmut Ritsch, Andras Vukics, and Peter Domokos. Entanglement assisted fast reordering of atoms in an optical lattice within a cavity at T=0. *Optics Communications*, 273(2):446 – 450, 2007.

[104] J. M. Zhang, W. M. Liu, and D. L. Zhou. Cavity QED with cold atoms trapped in a double-well potential. *Phys. Rev. A*, 77:033620, Mar 2008.

[105] S. Krämer and H. Ritsch. Self-ordering dynamics of ultracold atoms in multicolored cavity fields. *Phys. Rev. A*, 90:033833, Sep 2014.

[106] Sandner, R. M., Niedenzu, W., Piazza, F., and Ritsch, H. Self-ordered stationary states of driven quantum degenerate gases in optical resonators. *EPL*, 111(5):53001, 2015.

[107] Stefan Ostermann, Wolfgang Niedenzu, and Helmut Ritsch. Unraveling the Quantum Nature of Atomic Self-Ordering in a Ring Cavity. *Phys. Rev. Lett.*, 124:033601, Jan 2020.

[108] Catalin-Mihai Halati, Ameneh Sheikhan, Helmut Ritsch, and Corinna Kollath. Numerically Exact Treatment of Many-Body Self-Organization in a Cavity. *Phys. Rev. Lett.*, 125:093604, Aug 2020.

[109] Catalin-Mihai Halati, Ameneh Sheikhan, and Corinna Kollath. Theoretical methods to treat a single dissipative bosonic mode coupled globally to an interacting many-body

system. *Phys. Rev. Research*, 2:043255, Nov 2020.

[110] Alla V. Bezvershenko, Catalin-Mihai Halati, Ameneh Sheikhan, Corinna Kollath, and Achim Rosch. Dicke transition in open many-body systems determined by fluctuation effects. *arXiv:2012.11823*, 2020.

[111] Catalin-Mihai Halati, Ameneh Sheikhan, and Corinna Kollath. Breaking strong symmetries in dissipative quantum systems: the (non-)interacting bosonic chain coupled to a cavity. *arXiv:2102.02537*, 2021.

[112] Z. Wang, C.-M. Halati, J.-S. Bernier, A. Ponomaryov, D. Kamenskyi, D. I. Gorbunov, S. Niesen, J. M. Klopf, S. Zvyagin, T. Lorenz, A. Loidl, and C. Kollath. Observation of many-body magnon bound states in a transverse-field Heisenberg-Ising chain. *in preparation*.

[113] G. Lindblad. *Commun. Math. Phys.*, 48:119, 1976.

[114] H. Carmichael. *An open systems approach to quantum optics*. Springer Verlag, Berlin Heidelberg, 1991.

[115] Victor V. Albert and Liang Jiang. Symmetries and conserved quantities in Lindblad master equations. *Phys. Rev. A*, 89:022118, Feb 2014.

[116] E. T. Jaynes and F. W. Cummings. Comparison of quantum and semiclassical radiation theories with application to the beam maser. *Proceedings of the IEEE*, 51(1):89–109, 1963.

[117] Berislav Buca and Tomaz Prosen. A note on symmetry reductions of the Lindblad equation: transport in constrained open spin chains. *New Journal of Physics*, 14(7):073007, jul 2012.

[118] Søren Gammelmark and Klaus Mølmer. Interacting spins in a cavity: Finite-size effects and symmetry-breaking dynamics. *Phys. Rev. A*, 85:042114, Apr 2012.

[119] Shojiro Kimura, Koichi Okunishi, Masayuki Hagiwara, Koichi Kindo, Zhangzhen He, Tomoyasu Taniyama, Mitsuru Itoh, Keiichi Koyama, and Kazuo Watanabe. Collapse of Magnetic Order of the Quasi One-Dimensional Ising-Like Antiferromagnet BaCo2V2O8 in Transverse Fields. *Journal of the Physical Society of Japan*, 82(3):033706, 2013.

[120] S. K. Niesen, G. Kolland, M. Seher, O. Breunig, M. Valldor, M. Braden, B. Grenier, and T. Lorenz. Magnetic phase diagrams, domain switching, and quantum phase transition of the quasi-one-dimensional Ising-like antiferromagnet $BaCo_2V_2O_8$. *Phys. Rev. B*, 87:224413, Jun 2013.

[121] H. J. Mikeska and A. Kolezhuk. One-dimensional magnetism. In U. Schollwöck, J. Richter, D. Farnell, and R. Bishop, editors, *Quantum magnetism*, volume 645, page 1. Springer, Lecture notes in Physics, 2004.

[122] T. Giamarchi. *Quantum Physics in One Dimension*. Oxford University Press, Oxford, 2004.

[123] T. Koma and B. Nachtergaele. The Spectral Gap of the Ferromagnetic XXZ Chain. *Lett. Math. Phys.*, 40:1, 1997.

[124] Ulrich Schollwöck. The density-matrix renormalization group in the age of matrix product states. *Annals of Physics*, 326(1):96 – 192, 2011. January 2011 Special Issue.

[125] M B Hastings. An area law for one-dimensional quantum systems. *Journal of Statistical*

Mechanics: Theory and Experiment, 2007(08):P08024–P08024, aug 2007.

[126] F. Verstraete and J. I. Cirac. Matrix product states represent ground states faithfully. *Phys. Rev. B*, 73:094423, Mar 2006.

[127] Ryotaro Arita, Kazuhiko Kuroki, Hideo Aoki, and Michele Fabrizio. Density-matrix renormalization-group study of the spin gap in a one-dimensional Hubbard model: Effect of the distant transfer and exchange coupling. *Phys. Rev. B*, 57:10324–10327, May 1998.

[128] T. D. Kühner, S. R. White, and H. Monien. One-dimensional Bose-Hubbard model with nearest-neighbor interaction. *Phys. Rev. B*, 61(18):12474, 2000.

[129] S. R. White. Density matrix formulation for quantum renormalization groups. *Phys. Rev. Lett.*, 69:2863, 1992.

[130] Tomotoshi Nishino, Yasuhiro Hieida, Kouichi Okunishi, Nobuya Maeshima, Yasuhiro Akutsu, and Andrej Gendiar. Two-Dimensional Tensor Product Variational Formulation. *Progress of Theoretical Physics*, 105(3):409–417, 03 2001.

[131] G. Vidal. Entanglement Renormalization. *Phys. Rev. Lett.*, 99:220405, Nov 2007.

[132] F. Verstraete, V. Murg, and J.I. Cirac. Matrix product states, projected entangled pair states, and variational renormalization group methods for quantum spin systems. *Advances in Physics*, 57(2):143–224, 2008.

[133] A. J. Daley, C. Kollath, U. Schollwöck, and G. Vidal. Time-dependent density-matrix renormalization-group using adaptive effective Hilbert spaces. *J. Stat. Mech.: Theor. Exp.* , P04005, 2004.

[134] S. R. White and A. E. Feiguin. Real time evolution using the density matrix renormalization group. *Phys. Rev. Lett.*, 93:076401, 2004.

[135] G. Vidal. Efficient simulation of one-dimensional quantum many-body systems. *Phys. Rev. Lett.*, 93:040502, 2004.

[136] Michele Dolfi, Bela Bauer, Sebastian Keller, Alexandr Kosenkov, Timothée Ewart, Adrian Kantian, Thierry Giamarchi, and Matthias Troyer. Matrix product state applications for the ALPS project. *Computer Physics Communications*, 185(12):3430–3440, 2014.

[137] Johannes Hauschild and Frank Pollmann. Efficient numerical simulations with Tensor Networks: Tensor Network Python (TeNPy). *SciPost Phys. Lect. Notes*, page 5, 2018.

[138] Daniel Jaschke, Michael L. Wall, and Lincoln D. Carr. Open source Matrix Product States: Opening ways to simulate entangled many-body quantum systems in one dimension. *Computer Physics Communications*, 225:59–91, 2018.

[139] Matthew Fishman, Steven R. White, and E. Miles Stoudenmire. The ITensor Software Library for Tensor Network Calculations. *arXiv:2007.14822*, 2020.

[140] J. Eisert, M. Cramer, and M. B. Plenio. Colloquium: Area laws for the entanglement entropy. *Rev. Mod. Phys.*, 82:277–306, Feb 2010.

[141] Michael M. Wolf, Frank Verstraete, Matthew B. Hastings, and J. Ignacio Cirac. Area Laws in Quantum Systems: Mutual Information and Correlations. *Phys. Rev. Lett.*, 100:070502, Feb 2008.

[142] H. F. Trotter. On the Product of Semi-Groups of Operators. *Proceedings of the American*

Mathematical Society, 10(4):545–551, 1959.

[143] M. Suzuki. Relationship between d-Dimensional Quantal Spin Systems and (d+1)-Dimensional Ising Systems — Equivalence, Critical Exponents and Systematic Approximants of the Partition Function and Spin Correlations —. *Prog. Theor. Phys.*, 56:1454, 1976.

[144] M. Suzuki. Decomposition formulas of exponential operators and Lie exponentials with some applications to quantum mechanics and statistical physics. *J. Math. Phys.*, 26(4):601, 1985.

[145] Pasquale Calabrese and John Cardy. Entanglement entropy and quantum field theory. *J. Stat. Mech.: Theor. Exp.* , P06002, 2004.

[146] E. H. Lieb and D. W. Robinson. The finite group velocity of quantum spin systems. *Communications in Mathematical Physics*, 28:251–257, 1972.

[147] Tobias J. Osborne. Efficient Approximation of the Dynamics of One-Dimensional Quantum Spin Systems. *Phys. Rev. Lett.*, 97:157202, Oct 2006.

[148] Jean Dalibard, Yvan Castin, and Klaus Mølmer. Wave-function approach to dissipative processes in quantum optics. *Phys. Rev. Lett.*, 68(5):580–583, Feb 1992.

[149] C. W. Gardiner, A. S. Parkins, and P. Zoller. Wave-function quantum stochastic differential equations and quantum-jump simulation methods. *Phys. Rev. A*, 46:4363–4381, Oct 1992.

[150] F. Verstraete, M. Popp, and J. I. Cirac. Entanglement versus Correlations in Spin Systems. *Phys. Rev. Lett.*, 92:027901, 2004.

[151] M. Zwolak and G. Vidal. Mixed-state dynamics in one-dimensional quantum lattice systems: a time-dependent superoperator renormalization algorithm. *Phys. Rev. Lett.*, 93:207205, 2004.

[152] Andrew J. Daley. Quantum trajectories and open many-body quantum systems. *Advances in Physics*, 63(2):77–149, 2014.

[153] Jean-Sébastien Bernier, Peter Barmettler, Dario Poletti, and Corinna Kollath. Emergence of spatially extended pair coherence through incoherent local environmental coupling. *Phys. Rev. A*, 87:063608, Jun 2013.

[154] Lars Bonnes and Andreas M. Läuchli. *arXiv:1411.4831*, 2014.

[155] Michael L. Wall, Arghavan Safavi-Naini, and Ana Maria Rey. Simulating generic spin-boson models with matrix product states. *Phys. Rev. A*, 94:053637, Nov 2016.

[156] Marco T. Manzoni, Darrick E. Chang, and James S. Douglas. Simulating quantum light propagation through atomic ensembles using matrix product states. *Nature Communications*, 8(1):1743, Nov 2017.

[157] Daniel Jaschke, Simone Montangero, and Lincoln D Carr. One-dimensional many-body entangled open quantum systems with tensor network methods. *Quantum Science and Technology*, 4(1):013001, nov 2018.

[158] J. Tindall, B. Buca, J. R. Coulthard, and D. Jaksch. Heating-Induced Long-Range η Pairing in the Hubbard Model. *Phys. Rev. Lett.*, 123:030603, Jul 2019.

[159] E M Stoudenmire and Steven R White. Minimally entangled typical thermal state algorithms. *New Journal of Physics*, 12(5):055026, may 2010.

[160] Michael L. Wall, Arghavan Safavi-Naini, and Ana Maria Rey. Boson-mediated quantum spin simulators in transverse fields: XY model and spin-boson entanglement. *Phys. Rev. A*, 95:013602, Jan 2017.

[161] C. Brockt, F. Dorfner, L. Vidmar, F. Heidrich-Meisner, and E. Jeckelmann. Matrix-product-state method with a dynamical local basis optimization for bosonic systems out of equilibrium. *Phys. Rev. B*, 92:241106, Dec 2015.

[162] Jan Stolpp, Jacek Herbrych, Florian Dorfner, Elbio Dagotto, and Fabian Heidrich-Meisner. Charge-density-wave melting in the one-dimensional Holstein model. *Phys. Rev. B*, 101:035134, Jan 2020.

[163] Chunli Zhang, Eric Jeckelmann, and Steven R. White. Density Matrix Approach to Local Hilbert Space Reduction. *Phys. Rev. Lett.*, 80:2661–2664, Mar 1998.

[164] J J García-Ripoll, S Dürr, N Syassen, D M Bauer, M Lettner, G Rempe, and J I Cirac. Dissipation-induced hard-core boson gas in an optical lattice. *New Journal of Physics*, 11(1):013053, 2009.

[165] Florentin Reiter and Anders S. Sørensen. Effective operator formalism for open quantum systems. *Phys. Rev. A*, 85:032111, Mar 2012.

[166] E. M. Kessler. Generalized Schrieffer-Wolff formalism for dissipative systems. *Phys. Rev. A*, 86:012126, Jul 2012.

[167] Dario Poletti, Peter Barmettler, Antoine Georges, and Corinna Kollath. Emergence of Glasslike Dynamics for Dissipative and Strongly Interacting Bosons. *Phys. Rev. Lett.*, 111:195301, Nov 2013.

[168] Bruno Sciolla, Dario Poletti, and Corinna Kollath. Two-Time Correlations Probing the Dynamics of Dissipative Many-Body Quantum Systems: Aging and Fast Relaxation. *Phys. Rev. Lett.*, 114:170401, Apr 2015.

[169] E. I. Rodríguez Chiacchio and A. Nunnenkamp. Tuning the relaxation dynamics of ultracold atoms in a lattice with an optical cavity. *Phys. Rev. A*, 97:033618, Mar 2018.

[170] Andy C. Y. Li, F. Petruccione, and Jens Koch. Perturbative approach to Markovian open quantum systems. *Scientific Reports*, 4(1):4887, May 2014.

[171] Jens Klinder, Hans Keßler, Matthias Wolke, Ludwig Mathey, and Andreas Hemmerich. Dynamical phase transition in the open Dicke model. *Proceedings of the National Academy of Sciences*, 112(11):3290–3295, 2015.

[172] G. Scalari, C. Maissen, D. Turcinková, D. Hagenmüller, S. De Liberato, C. Ciuti, C. Reichl, D. Schuh, W. Wegscheider, M. Beck, and J. Faist. Ultrastrong Coupling of the Cyclotron Transition of a 2D Electron Gas to a THz Metamaterial. *Science*, 335(6074):1323–1326, 2012.

[173] Xiaoze Liu, Tal Galfsky, Zheng Sun, Fengnian Xia, Erh-chen Lin, Yi-Hsien Lee, Stéphane Kéna-Cohen, and Vinod M. Menon. Strong light–matter coupling in two-dimensional atomic crystals. *Nature Photonics*, 9(1):30–34, Jan 2015.

Bibliography

[174] Qi Zhang, Minhan Lou, Xinwei Li, John L. Reno, Wei Pan, John D. Watson, Michael J. Manfra, and Junichiro Kono. Collective non-perturbative coupling of 2D electrons with high-quality-factor terahertz cavity photons. *Nature Physics*, 12(11):1005–1011, Nov 2016.

[175] Stephan Smolka, Wolf Wuester, Florian Haupt, Stefan Faelt, Werner Wegscheider, and Ataç Imamoglu. Cavity quantum electrodynamics with many-body states of a two-dimensional electron gas. *Science*, 346(6207):332–335, 2014.

[176] Andreas Bayer, Marcel Pozimski, Simon Schambeck, Dieter Schuh, Rupert Huber, Dominique Bougeard, and Christoph Lange. Terahertz Light–Matter Interaction beyond Unity Coupling Strength. *Nano Letters*, 17(10):6340–6344, Oct 2017.

[177] Christoph Maschler and Helmut Ritsch. Cold Atom Dynamics in a Quantum Optical Lattice Potential. *Phys. Rev. Lett.*, 95:260401, Dec 2005.

[178] Jonas Larson, Bogdan Damski, Giovanna Morigi, and Maciej Lewenstein. Mott-Insulator States of Ultracold Atoms in Optical Resonators. *Phys. Rev. Lett.*, 100:050401, Feb 2008.

[179] Wolfgang Niedenzu, Rainer Schulze, András Vukics, and Helmut Ritsch. Microscopic dynamics of ultracold particles in a ring-cavity optical lattice. *Phys. Rev. A*, 82:043605, Oct 2010.

[180] A. O. Silver, M. Hohenadler, M. J. Bhaseen, and B. D. Simons. Bose-Hubbard models coupled to cavity light fields. *Phys. Rev. A*, 81:023617, Feb 2010.

[181] Sonia Fernández-Vidal, Gabriele De Chiara, Jonas Larson, and Giovanna Morigi. Quantum ground state of self-organized atomic crystals in optical resonators. *Phys. Rev. A*, 81:043407, Apr 2010.

[182] Yongqiang Li, Liang He, and Walter Hofstetter. Lattice-supersolid phase of strongly correlated bosons in an optical cavity. *Phys. Rev. A*, 87:051604, May 2013.

[183] T. J. Elliott and I. B. Mekhov. Engineering many-body dynamics with quantum light potentials and measurements. *Phys. Rev. A*, 94:013614, Jul 2016.

[184] M. Reza Bakhtiari, A. Hemmerich, H. Ritsch, and M. Thorwart. Nonequilibrium Phase Transition of Interacting Bosons in an Intra-Cavity Optical Lattice. *Phys. Rev. Lett.*, 114:123601, Mar 2015.

[185] T. Flottat, L. de Forges de Parny, F. Hébert, V. G. Rousseau, and G. G. Batrouni. Phase diagram of bosons in a two-dimensional optical lattice with infinite-range cavity-mediated interactions. *Phys. Rev. B*, 95:144501, Apr 2017.

[186] Rui Lin, Luca Papariello, Paolo Molignini, R. Chitra, and Axel U. J. Lode. Superfluid–Mott-insulator transition of ultracold superradiant bosons in a cavity. *Phys. Rev. A*, 100:013611, Jul 2019.

[187] Fran çois Damanet, Andrew J. Daley, and Jonathan Keeling. Atom-only descriptions of the driven-dissipative Dicke model. *Phys. Rev. A*, 99:033845, Mar 2019.

[188] Michael Schuler, Daniele De Bernardis, Andreas M. Läuchli, and Peter Rabl. The Vacua of Dipolar Cavity Quantum Electrodynamics. *SciPost Phys.*, 9:66, 2020.

[189] Minghui Xu, D. A. Tieri, and M. J. Holland. Simulating open quantum systems by applying SU(4) to quantum master equations. *Phys. Rev. A*, 87:062101, Jun 2013.

[190] Peter Kirton and Jonathan Keeling. Superradiant and lasing states in driven-dissipative Dicke models. *New Journal of Physics*, 20(1):015009, jan 2018.

[191] Nathan Shammah, Shahnawaz Ahmed, Neill Lambert, Simone De Liberato, and Franco Nori. Open quantum systems with local and collective incoherent processes: Efficient numerical simulations using permutational invariance. *Phys. Rev. A*, 98:063815, Dec 2018.

[192] Francesco Piazza, Philipp Strack, and Wilhelm Zwerger. Bose–Einstein condensation versus Dicke–Hepp–Lieb transition in an optical cavity. *Annals of Physics*, 339:135–159, 2013.

[193] Alla V. Bezvershenko. Dicke transition in open many-body systems. Master's thesis, University of Cologne, 2020.

[194] J. K. Asbóth, P. Domokos, H. Ritsch, and A. Vukics. Self-organization of atoms in a cavity field: Threshold, bistability, and scaling laws. *Phys. Rev. A*, 72:053417, Nov 2005.

[195] Stefan Schütz and Giovanna Morigi. Prethermalization of Atoms Due to Photon-Mediated Long-Range Interactions. *Phys. Rev. Lett.*, 113:203002, Nov 2014.

[196] Francesco Piazza and Philipp Strack. Quantum kinetics of ultracold fermions coupled to an optical resonator. *Phys. Rev. A*, 90:043823, Oct 2014.

[197] Julian Léonard, Andrea Morales, Philip Zupancic, Tobias Donner, and Tilman Esslinger. Monitoring and manipulating Higgs and Goldstone modes in a supersolid quantum gas. *Science*, 358(6369):1415–1418, 2017.

[198] Christoph Georges, Jayson G. Cosme, Ludwig Mathey, and Andreas Hemmerich. Light-Induced Coherence in an Atom-Cavity System. *Phys. Rev. Lett.*, 121:220405, Nov 2018.

[199] Katrin Kroeger, Nishant Dogra, Rodrigo Rosa-Medina, Marcin Paluch, Francesco Ferri, Tobias Donner, and Tilman Esslinger. Continuous feedback on a quantum gas coupled to an optical cavity. *New Journal of Physics*, 22(3):033020, 2020.

[200] Christoph Georges, Jayson G. Cosme, Hans Keßler, Ludwig Mathey, and Andreas Hemmerich. Dynamical density wave order in an atom-cavity system. *arXiv:2003.14135*, 2021.

[201] R. Balian. *From Microphysics to Macrophysics.* Springer-Verlag Berlin Heidelberg, 2007.

[202] V. Yurovsky M. Rigol, V. Dunjko and M. Olshanii. *Phys. Rev. Lett.*, 98:050405, 2007.

[203] E. M. Kessler, G. Giedke, A. Imamoglu, S. F. Yelin, M. D. Lukin, and J. I. Cirac. Dissipative phase transition in a central spin system. *Phys. Rev. A*, 86:012116, Jul 2012.

[204] Fabrizio Minganti, Alberto Biella, Nicola Bartolo, and Cristiano Ciuti. Spectral theory of Liouvillians for dissipative phase transitions. *Phys. Rev. A*, 98:042118, Oct 2018.

[205] H. J. Carmichael. Breakdown of Photon Blockade: A Dissipative Quantum Phase Transition in Zero Dimensions. *Phys. Rev. X*, 5:031028, Sep 2015.

[206] Hendrik Weimer. Variational Principle for Steady States of Dissipative Quantum Many-Body Systems. *Phys. Rev. Lett.*, 114:040402, Jan 2015.

[207] Mónica Benito, Carlos Sánchez Muñoz, and Carlos Navarrete-Benlloch. Degenerate parametric oscillation in quantum membrane optomechanics. *Phys. Rev. A*, 93:023846, Feb 2016.

[208] L. M. Sieberer, S. D. Huber, E. Altman, and S. Diehl. Dynamical Critical Phenomena in

Driven-Dissipative Systems. *Phys. Rev. Lett.*, 110:195301, May 2013.

[209] Carlos Sánchez Muñoz, Antonio Lara, Jorge Puebla, and Franco Nori. Hybrid Systems for the Generation of Nonclassical Mechanical States via Quadratic Interactions. *Phys. Rev. Lett.*, 121:123604, Sep 2018.

[210] Matteo Biondi, Gianni Blatter, Hakan E. Türeci, and Sebastian Schmidt. Nonequilibrium gas-liquid transition in the driven-dissipative photonic lattice. *Phys. Rev. A*, 96:043809, Oct 2017.

[211] Myung-Joong Hwang, Peter Rabl, and Martin B. Plenio. Dissipative phase transition in the open quantum Rabi model. *Phys. Rev. A*, 97:013825, Jan 2018.

[212] J. J. Mendoza-Arenas, S. R. Clark, S. Felicetti, G. Romero, E. Solano, D. G. Angelakis, and D. Jaksch. Beyond mean-field bistability in driven-dissipative lattices: Bunching-antibunching transition and quantum simulation. *Phys. Rev. A*, 93:023821, Feb 2016.

[213] Henrik Wilming, Michael J. Kastoryano, Albert H. Werner, and Jens Eisert. Emergence of spontaneous symmetry breaking in dissipative lattice systems. *Journal of Mathematical Physics*, 58(3):033302, 2017.

[214] Julia Hannukainen and Jonas Larson. Dissipation-driven quantum phase transitions and symmetry breaking. *Phys. Rev. A*, 98:042113, Oct 2018.

[215] João S. Ferreira and Pedro Ribeiro. Lipkin-Meshkov-Glick model with Markovian dissipation: A description of a collective spin on a metallic surface. *Phys. Rev. B*, 100:184422, Nov 2019.

[216] Katarzyna Macieszczak, M Guţă, Igor Lesanovsky, and Juan P. Garrahan. Towards a Theory of Metastability in Open Quantum Dynamics. *Phys. Rev. Lett.*, 116:240404, Jun 2016.

[217] Thomas Fink, Anne Schade, Sven Höfling, Christian Schneider, and Ataç Imamoglu. Signatures of a dissipative phase transition in photon correlation measurements. *Nature Physics*, 14(4):365–369, Apr 2018.

[218] C. Carr, R. Ritter, C. G. Wade, C. S. Adams, and K. J. Weatherill. Nonequilibrium Phase Transition in a Dilute Rydberg Ensemble. *Phys. Rev. Lett.*, 111:113901, Sep 2013.

[219] Natalia R. de Melo, Christopher G. Wade, Nikola Šibalić, Jorge M. Kondo, Charles S. Adams, and Kevin J. Weatherill. Intrinsic optical bistability in a strongly driven Rydberg ensemble. *Phys. Rev. A*, 93:063863, Jun 2016.

[220] S. R. K. Rodriguez, W. Casteels, F. Storme, N. Carlon Zambon, I. Sagnes, L. Le Gratiet, E. Galopin, A. Lemaître, A. Amo, C. Ciuti, and J. Bloch. Probing a Dissipative Phase Transition via Dynamical Optical Hysteresis. *Phys. Rev. Lett.*, 118:247402, Jun 2017.

[221] F. Letscher, O. Thomas, T. Niederprüm, M. Fleischhauer, and H. Ott. Bistability Versus Metastability in Driven Dissipative Rydberg Gases. *Phys. Rev. X*, 7:021020, May 2017.

[222] P. R. Muppalla, O. Gargiulo, S. I. Mirzaei, B. Prasanna Venkatesh, M. L. Juan, L. Grünhaupt, I. M. Pop, and G. Kirchmair. Bistability in a mesoscopic Josephson junction array resonator. *Phys. Rev. B*, 97:024518, Jan 2018.

[223] M. J. A. Schuetz, E. M. Kessler, L. M. K. Vandersypen, J. I. Cirac, and G. Giedke. Steady-

State Entanglement in the Nuclear Spin Dynamics of a Double Quantum Dot. *Phys. Rev. Lett.*, 111:246802, Dec 2013.

[224] M. J. A. Schuetz, E. M. Kessler, L. M. K. Vandersypen, J. I. Cirac, and G. Giedke. Nuclear spin dynamics in double quantum dots: Multistability, dynamical polarization, criticality, and entanglement. *Phys. Rev. B*, 89:195310, May 2014.

[225] Mattias Fitzpatrick, Neereja M. Sundaresan, Andy C. Y. Li, Jens Koch, and Andrew A. Houck. Observation of a Dissipative Phase Transition in a One-Dimensional Circuit QED Lattice. *Phys. Rev. X*, 7:011016, Feb 2017.

[226] Carlos Sánchez Muñoz, Berislav Buca, Joseph Tindall, Alejandro González-Tudela, Dieter Jaksch, and Diego Porras. Symmetries and conservation laws in quantum trajectories: Dissipative freezing. *Phys. Rev. A*, 100:042113, Oct 2019.

[227] Daniel Manzano and Pablo I. Hurtado. Symmetry and the thermodynamics of currents in open quantum systems. *Phys. Rev. B*, 90:125138, Sep 2014.

[228] Florian Lange, Zala Lenarcic, and Achim Rosch. Pumping approximately integrable systems. *Nature Communications*, 8(1):15767, Jun 2017.

[229] Zala Lenarcic, Florian Lange, and Achim Rosch. Perturbative approach to weakly driven many-particle systems in the presence of approximate conservation laws. *Phys. Rev. B*, 97:024302, Jan 2018.

[230] Simon Lieu, Ron Belyansky, Jeremy T. Young, Rex Lundgren, Victor V. Albert, and Alexey V. Gorshkov. Symmetry Breaking and Error Correction in Open Quantum Systems. *Phys. Rev. Lett.*, 125:240405, Dec 2020.

[231] Shao-Liang Zhang and Qi Zhou. Manipulating novel quantum phenomena using synthetic gauge fields. *Journal of Physics B: Atomic, Molecular and Optical Physics*, 50(22):222001, nov 2017.

[232] Y.-J. Lin, R. L. Compton, A. R. Perry, W. D. Phillips, J. V. Porto, and I. B. Spielman. Bose-Einstein Condensate in a Uniform Light-Induced Vector Potential. *Phys. Rev. Lett.*, 102:130401, Mar 2009.

[233] Y.-J. Lin, R. L. Compton, K. Jiménez-García, J. V. Porto, and I. B. Spielman. Synthetic magnetic fields for ultracold neutral atoms. *Nature*, 462(7273):628–632, Dec 2009.

[234] J. Struck, C. Ölschläger, R. Le Targat, P. Soltan-Panahi, A. Eckardt, M. Lewenstein, P. Windpassinger, and K. Sengstock. Quantum Simulation of Frustrated Classical Magnetism in Triangular Optical Lattices. *Science*, 333(6045):996–999, 2011.

[235] Hirokazu Miyake, Georgios A. Siviloglou, Colin J. Kennedy, William Cody Burton, and Wolfgang Ketterle. Publisher's Note: Realizing the Harper Hamiltonian with Laser-Assisted Tunneling in Optical Lattices [Phys. Rev. Lett. 111, 185302 (2013)]. *Phys. Rev. Lett.*, 111:199903, Nov 2013.

[236] M. Aidelsburger, M. Atala, S. Nascimbène, S. Trotzky, Y.-A. Chen, and I. Bloch. Experimental Realization of Strong Effective Magnetic Fields in an Optical Lattice. *Phys. Rev. Lett.*, 107:255301, Dec 2011.

[237] M. Atala, M. Aidelsburger, M. Lohse, J. T. Barreiro, B. Paredes, and I. Bloch. Observation of the Meissner effect with ultracold atoms in bosonic ladders. *Nat. Phys.*, 10:588, 2014.

Bibliography

[238] M. Mancini, G. Pagano, G. Cappellini, L. Livi, M. Rider, J. Catani, C. Sias, P. Zoller, M. Inguscio, M. Dalmonte, and L. Fallani. Observation of chiral edge states with neutral fermions in synthetic Hall ribbons. *Science*, 349(6255):1510–1513, 2015.

[239] L. F. Livi, G. Cappellini, M. Diem, L. Franchi, C. Clivati, M. Frittelli, F. Levi, D. Calonico, J. Catani, M. Inguscio, and L. Fallani. Synthetic Dimensions and Spin-Orbit Coupling with an Optical Clock Transition. *Phys. Rev. Lett.*, 117:220401, Nov 2016.

[240] Logan W. Clark, Brandon M. Anderson, Lei Feng, Anita Gaj, K. Levin, and Cheng Chin. Observation of Density-Dependent Gauge Fields in a Bose-Einstein Condensate Based on Micromotion Control in a Shaken Two-Dimensional Lattice. *Phys. Rev. Lett.*, 121:030402, Jul 2018.

[241] Frederik Görg, Kilian Sandholzer, Joaquín Minguzzi, Rémi Desbuquois, Michael Messer, and Tilman Esslinger. Realization of density-dependent Peierls phases to engineer quantized gauge fields coupled to ultracold matter. *Nature Physics*, 15(11):1161–1167, Nov 2019.

[242] Christian Schweizer, Fabian Grusdt, Moritz Berngruber, Luca Barbiero, Eugene Demler, Nathan Goldman, Immanuel Bloch, and Monika Aidelsburger. Floquet approach to $\mathbb{Z}_2$ lattice gauge theories with ultracold atoms in optical lattices. *Nature Physics*, 15(11):1168–1173, Nov 2019.

[243] Y.-J. Lin, K. Jimènez-Garcia, and I.B. Spielman. Spin-orbit-coupled Bose-Einstein condensates. *Nature*, 471:83, 2011.

[244] Pengjun Wang, Zeng-Qiang Yu, Zhengkun Fu, Jiao Miao, Lianghui Huang, Shijie Chai, Hui Zhai, and Jing Zhang. Spin-Orbit Coupled Degenerate Fermi Gases. *Phys. Rev. Lett.*, 109:095301, Aug 2012.

[245] Lawrence W. Cheuk, Ariel T. Sommer, Zoran Hadzibabic, Tarik Yefsah, Waseem S. Bakr, and Martin W. Zwierlein. Spin-Injection Spectroscopy of a Spin-Orbit Coupled Fermi Gas. *Phys. Rev. Lett.*, 109:095302, Aug 2012.

[246] Victor Galitski and Ian B. Spielman. Spin–orbit coupling in quantum gases. *Nature*, 494(7435):49–54, Feb 2013.

[247] Yongping Zhang, Maren Elizabeth Mossman, Thomas Busch, Peter Engels, and Chuanwei Zhang. Properties of spin–orbit-coupled Bose–Einstein condensates. *Frontiers of Physics*, 11(3):118103, Jun 2016.

[248] Eyal Cornfeld and Eran Sela. Chiral currents in one-dimensional fractional quantum Hall states. *Phys. Rev. B*, 92:115446, Sep 2015.

[249] Yuval Oreg, Gil Refael, and Felix von Oppen. Helical Liquids and Majorana Bound States in Quantum Wires. *Phys. Rev. Lett.*, 105:177002, Oct 2010.

[250] Roman M. Lutchyn, Jay D. Sau, and S. Das Sarma. Majorana Fermions and a Topological Phase Transition in Semiconductor-Superconductor Heterostructures. *Phys. Rev. Lett.*, 105:077001, Aug 2010.

[251] George I. Japaridze, Henrik Johannesson, and Mariana Malard. Synthetic helical liquid in a quantum wire. *Phys. Rev. B*, 89:201403, May 2014.

[252] William S. Cole, Junhyun Lee, Khan W. Mahmud, Yahya Alavirad, I. B. Spielman, and

Jay D. Sau. Emergent gauge field and the Lifshitz transition of spin-orbit coupled bosons in one dimension. *Scientific Reports*, 9(1):7471, May 2019.

[253] Luca Barbiero, Christian Schweizer, Monika Aidelsburger, Eugene Demler, Nathan Goldman, and Fabian Grusdt. Coupling ultracold matter to dynamical gauge fields in optical lattices: From flux attachment to $\mathbb{Z}_2$ lattice gauge theories. *Science Advances*, 5(10), 2019.

[254] Y. Deng, J. Cheng, H. Jing, and S. Yi. Bose-Einstein Condensates with Cavity-Mediated Spin-Orbit Coupling. *Phys. Rev. Lett.*, 112:143007, Apr 2014.

[255] Lin Dong, Lu Zhou, Biao Wu, B. Ramachandhran, and Han Pu. Cavity-assisted dynamical spin-orbit coupling in cold atoms. *Phys. Rev. A*, 89:011602, Jan 2014.

[256] Jian-Song Pan, Xiong-Jun Liu, Wei Zhang, Wei Yi, and Guang-Can Guo. Topological Superradiant States in a Degenerate Fermi Gas. *Phys. Rev. Lett.*, 115:045303, Jul 2015.

[257] Bikash Padhi and Sankalpa Ghosh. Spin-orbit-coupled Bose-Einstein condensates in a cavity: Route to magnetic phases through cavity transmission. *Phys. Rev. A*, 90:023627, Aug 2014.

[258] Farokh Mivehvar and David L. Feder. Synthetic spin-orbit interactions and magnetic fields in ring-cavity QED. *Phys. Rev. A*, 89:013803, Jan 2014.

[259] Farokh Mivehvar and David L. Feder. Enhanced stripe phases in spin-orbit-coupled Bose-Einstein condensates in ring cavities. *Phys. Rev. A*, 92:023611, Aug 2015.

[260] F. Dimer, B. Estienne, A. S. Parkins, and H. J. Carmichael. Proposed realization of the Dicke-model quantum phase transition in an optical cavity QED system. *Phys. Rev. A*, 75:013804, Jan 2007.

[261] Lin Tian. Cavity-assisted dynamical quantum phase transition at bifurcation points. *Phys. Rev. A*, 93:043850, Apr 2016.

[262] E. Orignac and T. Giamarchi. Meissner effect in a bosonic ladder. *Phys. Rev. B*, 64:144515, Sep 2001.

[263] Alexandru Petrescu and Karyn Le Hur. Chiral Mott insulators, Meissner effect, and Laughlin states in quantum ladders. *Phys. Rev. B*, 91:054520, Feb 2015.

[264] Shun Uchino. Analytical approach to a bosonic ladder subject to a magnetic field. *Phys. Rev. A*, 93:053629, May 2016.

[265] S. Greschner, M. Piraud, F. Heidrich-Meisner, I. P. McCulloch, U. Schollwöck, and T. Vekua. Symmetry-broken states in a system of interacting bosons on a two-leg ladder with a uniform Abelian gauge field. *Phys. Rev. A*, 94:063628, Dec 2016.

[266] Marcello Calvanese Strinati, Eyal Cornfeld, Davide Rossini, Simone Barbarino, Marcello Dalmonte, Rosario Fazio, Eran Sela, and Leonardo Mazza. Laughlin-like States in Bosonic and Fermionic Atomic Synthetic Ladders. *Phys. Rev. X*, 7:021033, Jun 2017.

[267] G. Vidal, J. I. Latorre, E. Rico, and A. Kitaev. Entanglement in quantum critical phenomena. *Phys. Rev. Lett.*, 90:227902, 2003.

[268] C. Holzey, F. Larsen, and F. Wilczek. Geometric and renormalized entropy in conformal field theory. *Nucl. Phys. B*, 424:44, 1994.

[269] Nicolas Laflorencie, Erik S. Sorensen, Ming-Shyang Chang, and Ian Affleck. Boundary

Effects in the Critical Scaling of Entanglement Entropy in 1D Systems. *Physical Review Letters*, 96(10):100603, 2006.

[270] Ian Affleck and Andreas W. W. Ludwig. Universal noninteger "ground-state degeneracy" in critical quantum systems. *Phys. Rev. Lett.*, 67(2):161–164, Jul 1991.

[271] U. Schollwöck. The density-matrix renormalization group. *Rev. Mod. Phys.*, 77(1):259, 2005.

[272] Karen A. Hallberg. New trends in density matrix renormalization. *Advances in Physics*, 55(5-6):477–526, 2006.

[273] E. Jeckelmann. Dynamical density-matrix renormalization group method. *Phys. Rev. B*, 66:045114, 2002.

[274] C.-M. Halati. Cavity-induced artificial gauge field in a Bose-Hubbard ladder. Master's thesis, University of Bonn, 2017.

[275] Hoi Chun Po, Weiqiang Chen, and Qi Zhou. Non-Luttinger quantum liquid of one-dimensional spin-orbit-coupled bosons. *Phys. Rev. A*, 90:011602, Jul 2014.

[276] Matthias Wolke, Julian Klinner, Hans Keßler, and Andreas Hemmerich. Cavity Cooling Below the Recoil Limit. *Science*, 337(6090):75–78, 2012.

[277] Julian Léonard, Andrea Morales, Philip Zupancic, Tilman Esslinger, and Tobias Donner. Supersolid formation in a quantum gas breaking a continuous translational symmetry. *Nature*, 543(7643):87–90, Mar 2017.

[278] Peter Domokos and Helmut Ritsch. Collective Cooling and Self-Organization of Atoms in a Cavity. *Phys. Rev. Lett.*, 89:253003, Dec 2002.

[279] A. Widera, F. Gerbier, S. Foelling, T. Gericke, O. Mandel, and I. Bloch. Precision measurement of spin-dependent interaction strengths for spin-1 and spin-2 87Rb atoms. *New J. Phys.*, 8:152, 2006.

[280] B. Lake, D. A. Tennant, J.-S. Caux, T. Barthel, U. Schollwöck, S. E. Nagler, and C. D. Frost. Multispinon Continua at Zero and Finite Temperature in a Near-Ideal Heisenberg Chain. *Phys. Rev. Lett.*, 111:137205, Sep 2013.

[281] Martin Mourigal, Mechthild Enderle, Axel Klöpperpieper, Jean-Sébastien Caux, Anne Stunault, and Henrik M. Rønnow. Fractional spinon excitations in the quantum Heisenberg antiferromagnetic chain. *Nature Physics*, 9(7):435–441, Jul 2013.

[282] Vivien Zapf, Marcelo Jaime, and C. D. Batista. Bose-Einstein condensation in quantum magnets. *Rev. Mod. Phys.*, 86:563–614, May 2014.

[283] B. Dalla Piazza, M. Mourigal, N. B. Christensen, G. J. Nilsen, P. Tregenna-Piggott, T. G. Perring, M. Enderle, D. F. McMorrow, D. A. Ivanov, and H. M. Rønnow. Fractional excitations in the square-lattice quantum antiferromagnet. *Nature Physics*, 11(1):62–68, Jan 2015.

[284] R. Toskovic, R. van den Berg, A. Spinelli, I. S. Eliens, B. van den Toorn, B. Bryant, J.-S. Caux, and A. F. Otte. Atomic spin-chain realization of a model for quantum criticality. *Nature Physics*, 12(7):656–660, Jul 2016.

[285] L. S. Wu, W. J. Gannon, I. A. Zaliznyak, A. M. Tsvelik, M. Brockmann, J.-S. Caux, M. S. Kim,

Y. Qiu, J. R. D. Copley, G. Ehlers, A. Podlesnyak, and M. C. Aronson. Orbital-exchange and fractional quantum number excitations in an f-electron metal, Yb2Pt2Pb. *Science*, 352(6290):1206–1210, 2016.

[286] Zhe Wang, Jianda Wu, Shenglong Xu, Wang Yang, Congjun Wu, Anup Kumar Bera, A. T. M. Nazmul Islam, Bella Lake, Dmytro Kamenskyi, Papori Gogoi, Hans Engelkamp, Nanlin Wang, Joachim Deisenhofer, and Alois Loidl. From confined spinons to emergent fermions: Observation of elementary magnetic excitations in a transverse-field Ising chain. *Phys. Rev. B*, 94:125130, Sep 2016.

[287] Oliver Breunig, Markus Garst, Andreas Klümper, Jens Rohrkamp, Mark M. Turnbull, and Thomas Lorenz. Quantum criticality in the spin-1/2 Heisenberg chain system copper pyrazine dinitrate. *Science Advances*, 3(12), 2017.

[288] Zhe Wang, M. Schmidt, A. Loidl, Jianda Wu, Haiyuan Zou, Wang Yang, Chao Dong, Y. Kohama, K. Kindo, D. I. Gorbunov, S. Niesen, O. Breunig, J. Engelmayer, and T. Lorenz. Quantum Critical Dynamics of a Heisenberg-Ising Chain in a Longitudinal Field: Many-Body Strings versus Fractional Excitations. *Phys. Rev. Lett.*, 123:067202, Aug 2019.

[289] Matthias Vojta. Quantum phase transitions. *Reports on Progress in Physics*, 66(12):2069–2110, nov 2003.

[290] Subir Sachdev. Quantum magnetism and criticality. *Nature Physics*, 4(3):173–185, Mar 2008.

[291] Thierry Giamarchi, Christian Rüegg, and Oleg Tchernyshyov. Bose–Einstein condensation in magnetic insulators. *Nature Physics*, 4(3):198–204, Mar 2008.

[292] M. Klanjsek, H. Mayaffre, C. Berthier, M. Horvatić, B. Chiari, O. Piovesana, P. Bouillot, C. Kollath, E. Orignac, R. Citro, and T. Giamarchi. Controlling Luttinger Liquid Physics in Spin Ladders under a Magnetic Field. *Phys. Rev. Lett.*, 101:137207, Sep 2008.

[293] Pierre Bouillot, Corinna Kollath, Andreas M. Läuchli, Mikhail Zvonarev, Benedikt Thielemann, Christian Rüegg, Edmond Orignac, Roberta Citro, Martin Klanjsek, Claude Berthier, Mladen Horvatić, and Thierry Giamarchi. Statics and dynamics of weakly coupled antiferromagnetic spin-$\frac{1}{2}$ ladders in a magnetic field. *Phys. Rev. B*, 83:054407, Feb 2011.

[294] D. Schmidiger, P. Bouillot, T. Guidi, R. Bewley, C. Kollath, T. Giamarchi, and A. Zheludev. Spectrum of a Magnetized Strong-Leg Quantum Spin Ladder. *Phys. Rev. Lett.*, 111:107202, Sep 2013.

[295] D. Blosser, N. Kestin, K. Yu. Povarov, R. Bewley, E. Coira, T. Giamarchi, and A. Zheludev. Finite-temperature correlations in a quantum spin chain near saturation. *Phys. Rev. B*, 96:134406, Oct 2017.

[296] D. Blosser, V. K. Bhartiya, D. J. Voneshen, and A. Zheludev. $z = 2$ Quantum Critical Dynamics in a Spin Ladder. *Phys. Rev. Lett.*, 121:247201, Dec 2018.

[297] I. A. Zaliznyak, H. Woo, T. G. Perring, C. L. Broholm, C. D. Frost, and H. Takagi. Spinons in the Strongly Correlated Copper Oxide Chains in $SrCuO_2$. *Phys. Rev. Lett.*, 93:087202, Aug 2004.

[298] B. Thielemann, Ch. Rüegg, H. M. Rønnow, A. M. Läuchli, J.-S. Caux, B. Normand, D. Biner,

Bibliography

K. W. Krämer, H.-U. Güdel, J. Stahn, K. Habicht, K. Kiefer, M. Boehm, D. F. McMorrow, and J. Mesot. Direct Observation of Magnon Fractionalization in the Quantum Spin Ladder. *Phys. Rev. Lett.*, 102:107204, Mar 2009.

[299] D. Schmidiger, S. Mühlbauer, A. Zheludev, P. Bouillot, T. Giamarchi, C. Kollath, G. Ehlers, and A. M. Tsvelik. Symmetric and asymmetric excitations of a strong-leg quantum spin ladder. *Phys. Rev. B*, 88:094411, Sep 2013.

[300] A. K. Bera, B. Lake, F. H. L. Essler, L. Vanderstraeten, C. Hubig, U. Schollwöck, A. T. M. N. Islam, A. Schneidewind, and D. L. Quintero-Castro. Spinon confinement in a quasi-one-dimensional anisotropic Heisenberg magnet. *Phys. Rev. B*, 96:054423, Aug 2017.

[301] Zhangzhen He, Desheng Fu, Tôru Kyômen, Tomoyasu Taniyama, and Mitsuru Itoh. Crystal Growth and Magnetic Properties of BaCo2V2O8. *Chemistry of Materials*, 17(11):2924–2926, 2005.

[302] S. Kimura, T. Takeuchi, K. Okunishi, M. Hagiwara, Z. He, K Kindo, T. Taniyama, and M. Itoh. Novel Ordering of an $S = 1/2$ Quasi-1d Ising-Like Antiferromagnet in Magnetic Field. *Phys. Rev. Lett.*, 100:057202, Feb 2008.

[303] E. Canévet, B. Grenier, M. Klanjšek, C. Berthier, M. Horvatić, V. Simonet, and P. Lejay. Field-induced magnetic behavior in quasi-one-dimensional Ising-like antiferromagnet BaCo$_2$V$_2$O$_8$: A single-crystal neutron diffraction study. *Phys. Rev. B*, 87:054408, Feb 2013.

[304] B. Grenier, S. Petit, V. Simonet, E. Canévet, L.-P. Regnault, S. Raymond, B. Canals, C. Berthier, and P. Lejay. Longitudinal and Transverse Zeeman Ladders in the Ising-Like Chain Antiferromagnet BaCo$_2$V$_2$O$_8$. *Phys. Rev. Lett.*, 114:017201, Jan 2015.

[305] S. K. Niesen, O. Breunig, S. Salm, M. Seher, M. Valldor, P. Warzanowski, and T. Lorenz. Substitution effects on the temperature versus magnetic field phase diagrams of the quasi-one-dimensional effective Ising spin-$\frac{1}{2}$ chain system BaCo$_2$V$_2$O$_8$. *Phys. Rev. B*, 90:104419, Sep 2014.

[306] M. Klanjšek, M. Horvatić, S. Krämer, S. Mukhopadhyay, H. Mayaffre, C. Berthier, E. Canévet, B. Grenier, P. Lejay, and E. Orignac. Giant magnetic field dependence of the coupling between spin chains in BaCo$_2$V$_2$O$_8$. *Phys. Rev. B*, 92:060408, Aug 2015.

[307] Quentin Faure, Shintaro Takayoshi, Virginie Simonet, Béatrice Grenier, Martin Månsson, Jonathan S. White, Gregory S. Tucker, Christian Rüegg, Pascal Lejay, Thierry Giamarchi, and Sylvain Petit. Tomonaga-Luttinger Liquid Spin Dynamics in the Quasi-One-Dimensional Ising-Like Antiferromagnet BaCo$_2$V$_2$O$_8$. *Phys. Rev. Lett.*, 123:027204, Jul 2019.

[308] Wang Yang, Jianda Wu, Shenglong Xu, Zhe Wang, and Congjun Wu. One-dimensional quantum spin dynamics of Bethe string states. *Phys. Rev. B*, 100:184406, Nov 2019.

[309] M. Matsuda, H. Onishi, A. Okutani, J. Ma, H. Agrawal, T. Hong, D. M. Pajerowski, J. R. D. Copley, K. Okunishi, M. Mori, S. Kimura, and M. Hagiwara. Magnetic structure and dispersion relation of the $S = \frac{1}{2}$ quasi-one-dimensional Ising-like antiferromagnet BaCo$_2$V$_2$O$_8$ in a transverse magnetic field. *Phys. Rev. B*, 96:024439, Jul 2017.

[310] Shintaro Takayoshi, Shunsuke C. Furuya, and Thierry Giamarchi. Topological transition

between competing orders in quantum spin chains. *Phys. Rev. B*, 98:184429, Nov 2018.

[311] Akira Okutani, Hiroaki Onishi, Shojiro Kimura, Tetsuya Takeuchi, Takanori Kida, Michiyasu Mori, Atsushi Miyake, Masashi Tokunaga, Koichi Kindo, and Masayuki Hagiwara. Spin Excitations of the S= 1/2 One-Dimensional Ising-Like Antiferromagnet BaCo2V2O8 in Transverse Magnetic Fields. *Journal of the Physical Society of Japan*, 90(4):044704, 2021.

[312] D. V. Dmitriev, V. Ya. Krivnov, A. A. Ovchinnikov, and A. Langari. One-dimensional anisotropic Heisenberg model in the transverse magnetic field. *Journal of Experimental and Theoretical Physics*, 95(3):538–549, Sep 2002.

[313] Jean-Sébastien Caux, Fabian H. L. Essler, and Ute Löw. Dynamical structure factor of the anisotropic Heisenberg chain in a transverse field. *Phys. Rev. B*, 68:134431, Oct 2003.

[314] Benedikt Bruognolo, Andreas Weichselbaum, Jan von Delft, and Markus Garst. Dynamic structure factor of the spin-$\frac{1}{2}$ XXZ chain in a transverse field. *Phys. Rev. B*, 94:085136, Aug 2016.

[315] Zhangzhen He, Tomoyasu Taniyama, and Mitsuru Itoh. Large magnetic anisotropy in the quasi-one-dimensional system BaCo2V2O8. *Applied Physics Letters*, 88(13):132504, 2006.

[316] S Kimura, H Yashiro, M Hagiwara, K Okunishi, K Kindo, Z He, T Taniyama, and M Itoh. High field magnetism of the quasi one-dimensional anisotropic antiferromagnet BaCo2V2O8. *Journal of Physics: Conference Series*, 51:99–102, nov 2006.

[317] T. Giamarchi, A. Iucci, and C. Berthod. *Introduction to Many Body physics, Lecture notes.* University of Geneva, 2013.

[318] P. Jordan and E. Wigner. Über das Paulische Äquivalenzverbot. *Zeitschrift für Physik*, 47(9):631–651, Sep 1928.

[319] E. Lieb, T. Schultz, and D. Mattis. Antiferromagnetic chain. *Ann. Phys.*, 16:407, 1961.

[320] Daniel C. Mattis. *The Theory of Magnetism I.* Springer-Verlag Berlin Heidelberg, 1981.

[321] S. A. Zvyagin, M. Ozerov, E. Čizmár, D. Kamenskyi, S. Zherlitsyn, T. Herrmannsdörfer, J. Wosnitza, R. Wünsch, and W. Seidel. Terahertz-range free-electron laser electron spin resonance spectroscopy: Techniques and applications in high magnetic fields. *Review of Scientific Instruments*, 80(7):073102, 2009.

[322] S. A. Zvyagin. Spin dynamics of S=1/2 Heisenberg chains with a staggered transverse field: electron spin resonance studies (Review Article). *Low Temperature Physics*, 38(9):819–825, 2012.

[323] Shane P. Kelly, Ana Maria Rey, and Jamir Marino. Effect of Active Photons on Dynamical Frustration in Cavity QED. *Phys. Rev. Lett.*, 126:133603, Apr 2021.

[324] Kushal Seetharam, Alessio Lerose, Rosario Fazio, and Jamir Marino. Correlation engineering via non-local dissipation. *arXiv:2101.06445*, 2021.

[325] Yudan Guo, Varun D. Vaidya, Ronen M. Kroeze, Rhiannon A. Lunney, Benjamin L. Lev, and Jonathan Keeling. Emergent and broken symmetries of atomic self-organization arising from Gouy phase shifts in multimode cavity QED. *Phys. Rev. A*, 99:053818, May

2019.

[326] Yudan Guo, Ronen M. Kroeze, Varun D. Vaidya, Jonathan Keeling, and Benjamin L. Lev. Sign-Changing Photon-Mediated Atom Interactions in Multimode Cavity Quantum Electrodynamics. *Phys. Rev. Lett.*, 122:193601, May 2019.

[327] Yudan Guo, Ronen M. Kroeze, Brendan P. Marsh, Sarang Gopalakrishnan, Jonathan Keeling, and Benjamin L. Lev. An optical lattice with sound. *arXiv:2104.13922*, 2021.

[328] Colin Rylands, Yudan Guo, Benjamin L. Lev, Jonathan Keeling, and Victor Galitski. Photon-Mediated Peierls Transition of a 1D Gas in a Multimode Optical Cavity. *Phys. Rev. Lett.*, 125:010404, Jul 2020.

[329] Kevin Roux, Hideki Konishi, Victor Helson, and Jean-Philippe Brantut. Strongly correlated Fermions strongly coupled to light. *Nature Communications*, 11(1):2974, Jun 2020.

[330] Hideki Konishi, Kevin Roux, Victor Helson, and Jean-Philippe Brantut. Universal pair-polaritons in a strongly interacting Fermi gas. *arXiv:2103.02459*, 2021.

[331] K. W. Kim, A. Pashkin, H. Schäfer, M. Beyer, M. Porer, T. Wolf, C. Bernhard, J. Demsar, R. Huber, and A. Leitenstorfer. Ultrafast transient generation of spin-density-wave order in the normal state of BaFe2As2 driven by coherent lattice vibrations. *Nature Materials*, 11(6):497–501, Jun 2012.

[332] James Lloyd-Hughes, Peter Oppeneer, Tatiane Pereira dos Santos, Andre Schleife, Sheng Meng, Michael A Sentef, Michael Ruggenthaler, Angel Rubio, Ilie Radu, Margaret Murnane, Xun Shi, Henry Kapteyn, Benjamin Stadtmüller, Keshav M. Dani, Felipe da Jornada, Eva Prinz, Martin Aeschlimann, Rebecca Milot, Maria Burdanova, Jessica Boland, Tyler L. Cocker, and Frank A Hegmann. The 2021 Ultrafast Spectroscopic Probes of Condensed Matter Roadmap. *Journal of Physics: Condensed Matter*, 2021.

[333] A.L. Fetter and J.D. Walecka. *Quantum Theory of Many-Particle Systems*. Dover Books on Physics. Dover Publications, 2012.